

Spectroscopic Study of the Acetylene Species

by

Zicheng Duan

Submitted to the Department of Chemistry
in partial fulfillment of the requirements for the degree of

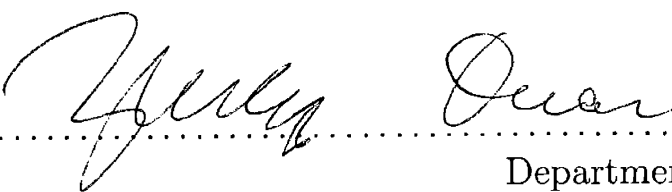
Doctor of Philosophy

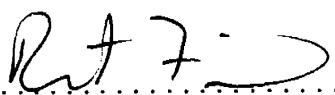
at the

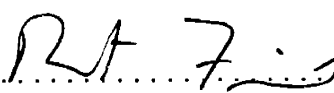
MASSACHUSETTS INSTITUTE OF TECHNOLOGY

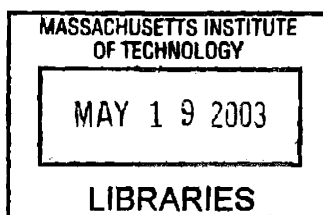
Feb 2003

© Massachusetts Institute of Technology 2003. All rights reserved.

Author 
Department of Chemistry
January 22, 2003

Certified by 
Robert W. Field
Haslam and Dewey Professor of Chemistry
Thesis Supervisor

Accepted by 
Robert W. Field
Chairman, Department Committee on Graduate Students



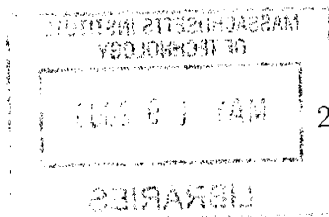
ARCHIVES

This doctoral thesis has been examined by a Committee of the Department of Chemistry that included

Professor Mounji G. Bawendi *M. G. Bawendi*
(Chairperson)

Professor Andrei Tokmakoff *Andrei Tokmakoff*

Professor Robert W. Field *Robert W. Field*
(Thesis Supervisor)



Spectroscopic Study of the Acetylene Species

by

Zicheng Duan

Submitted to the Department of Chemistry
on January 22, 2003, in partial fulfillment of the
requirements for the degree of
Doctor of Philosophy

Abstract

This thesis describes recent spectroscopic studies of acetylene and its HCCD isotopomer. Three different kinds of experiments have been performed: Laser-Induced Fluorescence (LIF), Dispersed Fluorescence (DF), and Stimulated Emission Pumping (SEP). Each experiment has yielded new discoveries in the vibrational and rotational dynamics of acetylene in its ground electronic state (\tilde{X}) state and its first excited singlet state (\tilde{A}) state.

The goal of my research at MIT has focused on making contributions to the investigation of isomerization processes in acetylene. These include the linear \leftrightarrow vinylidene isomerization process on the \tilde{X} state and the *trans* \leftrightarrow *cis* isomerization process on the \tilde{A} state. I have reasons to believe that the local bending motion is the major contributor in both processes.

LIF spectroscopic study of the \tilde{A} state of acetylene has led to new assignments of $2^2_03^1_0$ and $1^1_03^1_0$ bands which involve a_g symmetry. The frequency of the upper state symmetric CH stretch mode normal, ν'_1 , is determined to be 2880.5 cm^{-1} , 60 cm^{-1} lower than the presently-accepted value of 3040.6 cm^{-1} [104, 106].

DF spectroscopic study of the \tilde{X} state of acetylene has revealed a collisional K-changing process in the \tilde{A} state. In order to model theoretically the intensities measured from the present DF dataset, an local mode based Franck-Condon calculation scheme is given, and the results are shown to agree with the nodal structures exhibited in the experimental observations to within two quanta in both the CC stretch and the trans-bending coordinates. Improvements on the FC calculation are expected to aid in the direct assignment of the HCCD DF spectra, which are more complicated than those from the symmetric isotopomer, HCCH, due to reduced symmetry.

SEP spectroscopic study of the \tilde{X} state of acetylene has uncovered a Coriolis coupling between the $\nu''_2 + 4\nu''_4$ and $7\nu''_4$ vibrational states of acetylene. Modelling this coupling through a least-square fit gives a Coriolis coupling parameter, $\xi = 0.00057\text{ cm}^{-1}$, but such a coupling is expected to have negligible effects on the single-bright-state-per-polyad assumption in the overall vibrational dynamics in the \tilde{X} state, as sampled by DF as well as SEP spectra.

Thesis Supervisor: Robert W. Field
Title: Haslam and Dewey Professor of Chemistry

Acknowledgments

Isaac Newton said, “If I have seen further... it is because I have stood on the shoulders of giants.” I could not have done any of the research reported in this thesis without the help and support of many people.

First of all, I would like to thank my research advisor, Bob Field, and his wife, Susan, who gave me tremendous support during the difficult time spent completing this thesis. Bob made himself available to me on weekends, often right between grocery shopping and cooking dinner, and a lot of important discussions took place at his home. Over the years he has granted me the widest freedom to pursue my own research directions, and always insists that students’ names go first on the publications. Bob never waited for full recovery after a surgery before returning to work: his undying passion for molecules has inspired me to never stop learning.

I would like to thank my undergraduate advisor, Qingshi Zhu, and his wife, Lianzhi Tan. Professor Zhu introduced me to molecular spectroscopy, and it was in his laboratory that I decided to pursue a graduate degree in this field. Former USTC labmates, Xiaogang Wang, Shengfu Yang, Jinhui Zhang, Fuge Sun, Jixin Chen, Jiaxiang Han, Jielou Liao, Shuimin Hu, Dong Wang, Ke Deng, Qiang Shi, and Feng Shuang all gave me tremendous help establishing me in the field. Thank you all. I would like to thank Shengfu especially, not only for the basketball, but also for all of his help on my oral exams at MIT.

Hal Abelson said, “If I have not seen as far as others, it is because giants were standing on my shoulders.” This precisely describes my relation to my immediate predecessor on the project, Matthew Jacobson. Every idea that I raised, Matt had thought about, often many times as deep. Without Matt’s constant help and his brilliant work on XCC and the effective Hamiltonian, the Franck-Condon project could not have been done.

Thank you, Peter Giunta, for all that you have done for everybody in the group.

Throughout the years at MIT, I worked with a group of great people besides Matt. Jon O’Brien, Stephen Drucker, Sergey Panov, and Jian Li were the senior students

and postdocs who were always ready to teach when I came to them with questions. The rest are my peers, who provided many unforgettable moments. I would like to thank:

- Michelle Silva, for your trust in me and my LIF programs.
- Jason Clevenger, what a toastmaster for a decade!
- David Oertel, for your corrections of my English and the constant challenges for a perfect solution to problems.
- Ryan Thom, for the wonderful discussions we had on theology, literature, languages and many more...
- Xing Jiang, for helping me to stay true to my roots.
- Selen Altunata and Serhan Altunata, for your counselling in facing difficulties.
- Leah Ruslen, who is the only one who told me that I had “a good sense of humor” – big surprise!
- Kyle Bittinger, for helping with the group webpage and for your help in my preparation for the thesis defense.
- Jeff Kay, for your help in setting up for my defense talk, especially the keystone on the LCD projector.
- Daniel Byun, for your sense of humor and for all the good questions that you ease people with.
- Adya Mishra, for your presence.

I am also grateful to Professor Jeffery I. Steinfeld, for his constant discussion with me on my research progress, and for his help in my oral exams; to Professor Robert J. Silbey, who offered me several appointments on vibronic coupling, despite his busy schedule; to Professor Mounji G. Bawendi, who was my lecturer on first-year

Quantum Mechanics, and who introduced me to the level of research at MIT. Also, I thank Professor Jianshu Cao for his constant encouragement.

Thank you, Geng Wu, Guobin Sha, Song Gao, Peng Pan, your help in the last few months means a lot to me.

I would like to thank Mr. Tim Reynolds, for his understandings while patiently waiting for me to get my degree. I am thankful to Tim for sharing my anxieties and joys in the whole process.

Rao and Marilyn Lindsay, who are the first American couple I met in China, thank you for your support, and for the tutorial on America.

Thank you, Chau-Wen Chiou, for teaching me to be a forthright person, and to be faithful despite others. Thank you, Fred Chen, for your spiritual support. All friends at the Chinese Bible Church of Greater Boston and the Young Professional Fellowship, thank you for your support.

Finally, I would like to thank my parents for raising me, and for nurturing my passion for science. For that matter, to many of my dearest relatives, too, I extend thanks.

In writing the acknowledgement, I am sure that I have left out some people. I could not have finished my graduate study alone, and I would like to say "thank you" to all the others who have enriched my life and my graduate studies.

For My Parents

Contents

1	Introduction	33
1.1	Motivations and Objectives	33
1.2	Acetylene	36
1.3	Experimental Overview	37
1.3.1	Laser Induced Fluorescence (LIF)	37
1.3.2	Dispersed Fluorescence (DF)	41
1.3.3	Stimulated Emission Pumping (SEP)	41
1.4	Outline of the Thesis	42
2	Differential Temperature Laser Induced Fluorescence Spectroscopy	47
2.1	Introduction	47
2.2	Experimental	49
2.2.1	Production of Light	49
2.2.2	Temperature Control	51
2.2.3	Detection	52
2.3	Results and Analysis	52
2.3.1	Initial Data Processing	52
2.3.2	Theoretical Basis	53
2.3.3	Analysis by Structure Based Cross Correlation (SBCC)	60
2.4	Discussion	71
2.5	Conclusion	74

3	New Assignments in the $\tilde{A}^1A_u - \tilde{X}^1\Sigma_g^+$ Electronic Transition of C_2H_2	75
3.1	Introduction	75
3.2	Experiments	77
3.3	Results	79
3.3.1	Appearance of the spectra	79
3.3.2	Rotational analysis	82
3.3.3	Vibrational assignments	90
3.4	Discussion	91
4	Observation of Collision-Induced Population Transfer in the $S_1 \tilde{A}^1A_u$ State of Acetylene	95
4.1	Introduction	95
4.2	Experimental	96
4.2.1	Dispersed Fluorescence	96
4.2.2	Power Study	98
4.2.3	Exposure Study	98
4.2.4	Rotational-J Study	98
4.2.5	Gating Study	99
4.2.6	Pressure Study	102
4.2.7	Rotational-K Study	102
4.3	Analysis	104
4.3.1	Pattern Recognition	104
4.4	Conclusion	108
5	Franck-Condon Calculation in Lack of Good Potentials: <i>gerade</i> Bending Modes	109
5.1	Introduction	109
5.2	Overview	112
5.3	Algorithm	116
5.3.1	RKR-like Semiclassical Inversion	116
5.3.2	Local \leftrightarrow Normal Conversion	121

5.3.3	Treatment of Vibrational Angular Momentum	124
5.3.4	Treatment of Torsion	127
5.4	Results	134
5.5	Conclusion	138
6	Franck-Condon Calculation in Lack of Good Potentials: Multi-Dimensional	
	139	
6.1	Introduction	139
6.2	Overview	139
6.3	Algorithm	141
6.3.1	Normal Mode Analysis	142
6.3.2	Function Consideration of the Transition Moment	154
6.3.3	Dushinsky Rotation	155
6.4	Results	158
6.5	Comparison with Watson's FC Calculation on Acetylene	162
6.6	Conclusion	168
7	Observation of Coriolis Coupling between $\nu_2 + 4\nu_4$ and $7\nu_4$ in Acety-	
	lene $\widetilde{X}^1\Sigma_g^+$ by Stimulated Emission Pumping Spectroscopy	169
7.1	Introduction	169
7.2	Experimental Details	173
7.3	Results	175
7.4	Analysis	181
7.4.1	Frequency Analysis	181
7.4.2	Relative Intensity Calculations	185
7.5	Discussion	188
8	Ongoing Projects	193
8.1	Introduction	193
8.2	Dispersed Fluorescence of HCCD	194
8.2.1	Background and Motivation	194

8.2.2	Experimental	195
8.2.3	Spectra	198
8.2.4	Assignment	199
8.3	A Proposal on Investigation of the <i>cis</i> -well of S_1 state of C_2H_2	205
8.3.1	Overview	205
8.3.2	Experiment	207
8.3.3	Feasibility	209
8.3.4	Ringdown Signal	213
8.3.5	Discussion	213
8.4	Study of Perturbations in the $3\nu'_3$ State of C_2H_2	216
8.4.1	Goal	216
8.4.2	Experiments	217
8.4.3	Conclusion	223
	Bibliography	225

List of Figures

1-1	The \tilde{X} state and \tilde{A} state electronic potential surfaces of acetylene. The ground electronic state has two local minima corresponding to the familiar linear geometry and the vinylidene geometry, where both hydrogen nuclei are located on the same side of the CC bond. The first excited state has three local minima corresponding to the <i>trans</i> , <i>cis</i> , and vinylidene geometries. The linear geometry in the \tilde{X} state and the <i>trans</i> geometry in the \tilde{A} state are the two commonly accessible wells. Our objective is focused on experimentally observing and theoretically predicting identifiable patterns associated with the linear \leftrightarrow vinylidene isomerization in the \tilde{X} state, and <i>trans</i> \leftrightarrow <i>cis</i> in the \tilde{A} state. The critical point energies contained in this figure were reported by Stanton and coworkers [89, 97].	38
1-2	Normal modes and normal frequencies for linear-, <i>cis</i> - and <i>trans</i> - Acetylene. The linear configuration belongs to the \tilde{X} state while the <i>trans</i> and <i>cis</i> belong to the \tilde{A} state (Figure 1-1). Point group symmetry labels are added belong each normal mode.	39
1-3	Overview of the excitation and signal collection schemes of three basic experimental techniques employed in our studies of acetylene and its isotopomers. From left to right, they are: Laser-Induced Fluorescence (LIF), Dispersed Fluorescence (DF), and Stimulated Emission Pumping (SEP). A sample segment of spectrum is attached below each excitation scheme. For simplicity, the vinylidene well on the \tilde{A} state potential is not drawn.	40

2-1	<p>The Experimental Setup. A xenon chloride excimer laser, operating at 20 Hz, produces 250-350 mJ of light at 308 nm, of which about 100 mJ is used to pump the dye laser. While the dye laser output is ~ 10-15 mJ, only 5 mJ is sent into the BBO crystal, to produce around 500 μJ of UV output. The amplifiers used have input impedance of 1 kohm and a fixed gain of 10. The gate for the boxcars is switched on at ~ 30 ns after the laser pulse, with a width of ~ 100 ns. The “H”-shaped gas cell enables simultaneous collection of LIF spectra at two different temperatures.</p>	50
2-2	<p>Top: Two adjacent LIF spectral segments with 1/3 overlap. Middle: Recursion map of the spectral overlap region. A fit is performed to determine the optimum intensity scaling from one scan to the other. Bottom: A concatenated spectrum constructed from the two spectral segments, properly scaled by the tangent of the slope of the line on the recursion map.</p>	54
2-3	<p>Top: Two Frequency/Intensity calibrated LIF spectra of 60 cm^{-1} length from acetylene. This pair of spectra is used as an example in this chapter to demonstrate the DT-LIF and SBCC techniques. Bottom Left: Recursion map of the spectra in the top panel. The axes of the recursion map represent intensity values in each of the two spectra, and each dot on the recursion map is obtained from corresponding resolution element on the original spectra. Bottom Right: XCC merit function computed with a large V_d for the spectra set in the top panel and the recursion map on the bottom left panel. The two local maxima indicate two apparent vibrational bands with distinctively different intensity ratios.</p>	55

2-4 Theoretically predicted pattern of the recursion map for acetylene vibrational levels $v'' = 0 - 9$, at $T_1 = 300K$ and $T_2 = 273.15K$. Top: Recursion map, a plot of the intensity of the T_1 spectrum versus that of T_2 . Bottom: Tilt angle of the recursion rays with respect to lower state vibrational quantum number. The dotted line in both panels is the *instrument response ratio*, $\left(\frac{C'_1}{C'_2}\right)\left(\frac{T_2}{T_1}\right)$. Notice that for the cold band ($v'' = 0$), the tilt angle is insensitive to temperature, and therefore its intensity ratio approximates the *instrument response ratio*. For this reason, in a T_1, T_2 pair of LIF spectra, the band with the least temperature variance originates from the $v'' = 0$ level. 58

2-5 Theoretically predicted pattern of the recursion map for acetylene rotational-vibrational $v''=0,1,2$ bands. Each vibrational band contains multiple rays, each of which corresponds to a rotational line, the slope of which is determined by its rotational-vibrational energy. The length of ray clusters from different vibrational bands have been normalized. The observation that high-J lines of a low- v'' vibrational band have similar slope as low-J lines of a high- v'' vibrational band indicates that rotational effects are not ignorable. 61

2-6 Merit Function: illustrations of the definitions of d and R for two classes of points. For ray A, the perpendicular projection of point P lies beyond the ray terminus; for ray B, the projection of point P lies within the length of the ray. The distances between point P and rays A and B, d_A and d_B , and the *intercept length*, R_A and R_B , are defined differently. 65

- 2-7 Surface plot of weight function, g_i , for every point on the 2D recursion surface ($I(T_1)$ vs. $I(T_2)$). The function value is also projected onto the top plane to form contour traces. On the left panel, g_i is constructed using a small variance, V , thus its contour exactly repeats the ray cluster pattern predicted in Figure 2-5. On the right panel, g_i is constructed with a larger variance, allowing for more adjacent points to contribute to the merit function. Use of a large V is appropriate when the intensity ratio is measured with large uncertainty, when the fitter searches for an “overall” pattern that most resembles the theoretical patterns. The weight function counts more credit to intense features, as is demonstrated by the steadily rising ridges on the surface. 66
- 2-8 Merit function constructed for the reduced dimension fit of the hot band (band B) in Figure 2-3. The merit function, G , takes on the same pattern with respect to T_1 , as it does with T_2 , due to the correlation relations used to reduce the dimensionality in the fit. Only the maximum occurring at $T_1 = 314 \pm 4$ K, $T_2 = 263 \pm 3$ K is consistent with the experimental conditions under which the spectra were recorded. 70
- 2-9 Agreement of the fit results with the spectral recursion map. On the top panel are plotted recursion map in intensity coordinates, fitted pattern for band B and predicted pattern for band A. The bottom panel contains the same plot in polar coordinates. The hot band patterns fit well at $T_1 = 310$ K and $T_2 = 274$ K. The predicted cold band pattern captures a small number of low-J lines, while most other J’s were missing from the original spectra. 72
- 2-10 Patterns identified with the *SBCC Weights Method*. All patterns are normalized to the same scale for convenience of comparison. Band A corresponds to a cold band ($v'' = 0$), while band B corresponds to a hot band ($v'' = 1$). 73

3-1 Top: The JWU spectrum: laser-induced fluorescence spectrum of C_2H_2 in the region $43200 - 48600 \text{ cm}^{-1}$ recorded using supersonic jet-cooling. The intensities of bands to the short wavelength side of 45500 cm^{-1} have been magnified by a factor of $\times 10$, in order to enhance the weaker bands. The new bands, which form the subject of this chapter, lie near 46000 cm^{-1} , between the $2_0^1 3_0^2$ and 3_0^4 bands. New vibrational assignments are written sideways. Bottom: The MIT spectra. Solid line: laser-induced fluorescence spectrum of C_2H_2 at the higher temperature in the selected regions of interest $43595 - 43742$, $44647 - 44754$, $44988 - 45579$ and $45685 - 46316 \text{ cm}^{-1}$ recorded using DT-LIF. The intensities of these spectral segments have been scaled to match those of the JWU spectrum. Dashed line: the JWU spectrum shown as on the top plot. For comparison, the two experimental LIF spectra are frequency aligned in the bottom plot. As expected, spectral patterns are consistent between them. 80

3-2 Laser-induced fluorescence spectra of C_2H_2 in the regions $45080 - 45580$ and $45740 - 46310 \text{ cm}^{-1}$ recorded with the sample at below 0°C . The two spectra have been displaced by the ground state ν_4'' vibrational frequency (612 cm^{-1}) in order to allow a direct comparison of “cold” bands in the lower trace with their corresponding ν_4'' “hot” bands in the upper trace. All the bands in the lower trace are “cold”, and all the bands in the upper trace are “hot” except for the intense 3_0^3 band. The vibrational notation for the “hot” bands indicates the lower level as 4_n ; for example, the $3^4 4_2$ band comes from the $\nu_4'' = 2$ level of the ground state. 81

3-3	<p>Vibrational manifold of the three a_g vibrations of the \tilde{A}^1A_u state of C_2H_2, as observed in Refs. [114, 11] (thick lines), or estimated by us from their data assuming that the undetermined anharmonicity constants, x'_{ij}, are zero (thin lines; energies in parentheses). The new vibrational levels analyzed in this work lie at 3798 and 3917 cm^{-1} of vibrational energy within the \tilde{A}^1A_u state; they are therefore assigned as 2^23^1 and 1^13^1, respectively. The latter assignment leads to a downward revision of the value of ν'_1 from 3040.6 cm^{-1} to 2880.5 cm^{-1}. A level lying at 4935 cm^{-1} is now assigned as 1^13^2 (see text).</p>	92
4-1	<p>Gate study of the quasi continuous baseline. Each trace is recorded with a 100 ns gate.</p>	100
4-2	<p>Dispersed Fluorescence resulting from pumping the Q(1) rotational line of the $2\nu'_3$ band at different time windows following the laser pulse. The intensities are normalized to the tallest peak. The peaks of the extra sharp features show intensity dependency which are different from those of the main fractionated bright state features.</p>	101
4-3	<p>Pressure study of the sharp “extra” feature. There are a group of collisional partners whose unique ratio of increase in intensity with respect to pressure help identify them as the collisional induced $K'_a = 2$ structure.</p>	103
4-4	<p>Excitation via the hot band $V_1^2K_1^0$ results in DF spectral patterns distinctively different from those excited via cold band $V_0^2K_0^1$. In the hot band DF, the patterns arising from $K'_a = 0$ (assignment shown in Fig. 4-5) acquire more intensity and become the “main” feature. The internal energies of the peaks between the two excitation schemes match exactly, with the $K'_a = 0$ peaks being the “extra” patterns in the cold band DF. This observation confirms that the sharp “extra” feature are induced by K'_a-changing collisional processes.</p>	105

4-5 Top: Dispersed Fluorescence spectra recorded via the Q(1) rotational line of the $2\nu'_3$ band, at various pressures. The intensity is normalized to that of the tallest peak. The arrows point to features whose intensities change differently relative to the “main” features as a function of pressure. Second: The “main” features from the top panel extracted by XCC are the expected bright state fractionation patterns from $K'_a = 1$ intermediate states. The $l''_4 = 0$ and $l''_4 = 2$ levels in the \tilde{X} state are not resolved. Third: The unexpected sharp “extra” features of the top panel, extracted by XCC. The most intense features in this pattern can be accounted for by emission from $K'_a = 0$ or $K'_a = 2$ intermediate states. The $l''_4 = 1$ and $l''_4 = 3$ lines are not resolved. Bottom: Dispersed fluorescence 200ns (expected bright state fluorescence lifetime) after the laser pulse, the similarity between this spectral segment and the “extra” patterns in the third panel indicate that the extra features are due to a prolonged process, confirming the hypothesis derived from the gate study of the local “extra” features. 106

5-1 Illustration of the definitions of the bond angle coordinate, α , and the Jacobi angle, γ . While the Jacobi angle facilitates calculations, as it reasonably describes the motion of the Hydrogen as it moves from one end of the CC bond to the other, the bond-angle representation is more realistic for small or medium amplitude bending motions (*e.g.* $\frac{1}{2}\pi \leq \alpha \leq \frac{3}{2}\pi$). 120

5-2 Comparison between the local bending potential and the cut along the isomerization pathway on the Halonen-Child-Carter surface. The top panel depicts the dependence of the rotational energy on the CCH bending angle along the isomerization pathway, and the bottom panel depicts the dependence on the CC bond length. In both cases, the potential obtained by the semi-classical RKR-inversion resembles the Halonen-Child-Carter potential to within 5% difference. In the course of RKR, we assume that the CC bond length is independent of the CCH bending angle. 122

5-3 Left: \tilde{X} state $l_L = 0$ local bending wavefunctions obtained from RKR inversion. As expected for $l_L = 0$ levels, only the even quanta levels are plotted. Right: The local bending wavefunctions plotted for the \tilde{A} state. These wavefunctions are obtained using the \tilde{A} state force constants from Crim *et al.* Notice that the equilibrium geometry on the \tilde{A} state is not linear, but rather at a *trans* bending angle of 1 rad . 123

5-4 Four geometries involved in the torsional treatment of the \tilde{A} state. Each geometry is represented in the perpendicular view (top) and the transverse view (bottom). On the left and the right are the *trans*-acetylene and *cis*-acetylene structures that correspond to the local minima on the \tilde{A} state electronic potential. Both the in-plane local bend (top geometry) and the out-of-plane torsion serve as pathways between the two isomers. However, we have sufficient reasons to believe that the torsional saddle point is higher than the local bend saddle point. . 130

- 5-5 Torsional potential. The cyclic potential is modelled as the sum of two trigonometric functions V_1 (blue) and V_2 (red). The torsional barrier thus constructed exceeds the isomerization saddle point (green), which is consistent with the half-linear transition state calculated by Stanton and coworkers [89]. The purple potential is harmonic, drawn with values reported by Tobiasson *et al* [106, 104]. My potential is in good agreement with the Tobiasson harmonic potential at low energy. The four stacks of levels shown are eigenenergies obtained from truncating the basis set at 15, 20, 30, and 40 spherical harmonics. All levels converge. 132
- 5-6 Torsional eigenfunctions drawn at their eigen energy levels. Two sets of levels, localized in the *trans* and *cis* wells initially, eventually tunnel with each other significantly at $v'_4 \geq 10$. At high enough energies above the torsional barrier, they becomes degenerate pairs of state, similar to degenerated free rotor wavefunctions. 133
- 5-7 The local bending wavefunction Franck-Condon factors. The x-axis is the quantum number for the local bending wavefunctions on the \tilde{X} state from 0 to 30 ($l_L = 0$). These FC factors do not by themselves contain any meaningful information, at least not directly. However, they are intermediate results from which the normal mode FC factors can be derived, either by a local \longleftrightarrow normal conversion, or by using the expansion coefficients of the eigenstates obtained via the local mode effective Hamiltonian. Notice that only even quanta of the ground state local bending quantum numbers are included, due to the $l_L = 0$ restriction. 135
- 5-8 Torsional Overlap plotted for the torsional zero-point level, $v'_4 = 0$, on the \tilde{A} state to the counter-rotating levels on the \tilde{X} state ($l''_A + l''_B = 0$). These factors are particularly useful, as the local \longleftrightarrow normal conversion contains multiple l''_A terms (*e.g.* Table 5.2). 136

5-9 The 1D FC results for normal modes after local \longleftrightarrow normal conversion. Results plotted include the Franck-Condon factors from the 0^0 level, the $2\nu'_3$, $\nu'_2 + \nu'_3$ and $\nu'_2 + 2\nu'_3$ levels. The line represents the calculated Franck-Condon factors, while the dots are the experimentally measured Franck-Condon factors. Most calculated nodes lie within one to two quanta of the observed position along a vibrational progression. Given the absence of an accurate potential, the calculation and the observation agree surprisingly well. 137

6-1 Illustration of the principles behind the Multi-Dimensional Franck-Condon factor calculation. The calculation is mainly based on local mode wavefunction overlap integral. However, to compare with the intensities in the experimental dataset, which has been found to be consistent with the single-bright-state-per-polyad assumption, bright state intensities must be obtained in normal mode representations. In order to do a global conversion between the local and the normal modes, normal mode analysis must be performed via FG matrix diagonalization. 141

6-2 Cartesian Displacement Coordinates for *trans*-bent (\tilde{A} -state) Acetylene. 142

6-3 Internal Coordinates used for FG matrix analysis for Acetylene. r_1 and r_2 describe the local stretches of the CH bonds, R defines the CC bond length displacement, θ_1 and θ_2 describe the CCH bond angle changes, and τ is the out-of-plane torsional angle. 144

6-4 Surface plots for the calculated multi-dimensional FC factors. On all graphs, the x axis represents the \tilde{X} state CC stretch quantum number, ν_2'' , the y axis represents the \tilde{X} state trans-bending quantum number, ν_4'' . The z axis is the calculated FC factor . The four graphs are plotted for the zero-point level (upper left), $2\nu_3'$ (upper right), $\nu_2' + \nu_3'$ (bottom left) and $\nu_2' + 2\nu_3'$ vibrational states in the \tilde{A} state. Each grid point on the 2D xy surface stands for one vibrational level, and the ground state levels are the same for all four graphs. However, different excitation patterns in the \tilde{A} state light up these states with different 2D Franck-Condon patterns. For example, the two parallel grooves on the $2\nu_3'$ graph stand for the two nodes in the trans-bending coordinate , while the two perpendicular grooves on the $\nu_2' + \nu_3'$ graph stand for one node in the CC-stretch and one node along the trans-bending. 160

6-5 Comparison of the multidimensional FC calculation with the experimentally measured FC factors. On each of the twelve plots, the x axis represents the \tilde{X} -state CC-stretch quantum number, v_2'' , while the y axis represents the \tilde{X} -state trans-bending quantum number, v_4'' . These plots are contours of the FC factor, in other words, they correspond to the projection of the surfaces in Figure 6-4 onto the xy plane. The left column is the calculated FC factors without considering Dushinsky rotation. The right column depicts the calculated FC factors, taking into account Dushinsky rotations discussed in this chapter. The middle column is the experimentally measured FC factors. The sloping cut off of the experimental contour is due to the absence of measured data above a certain internal energy level. Each row stands for a certain vibrational level in the upper \tilde{A} state. They are, respectively from top to bottom, the zero-point state, $2\nu_3'$, $\nu_2' + \nu_3'$, $\nu_2' + 2\nu_3'$. Judging from the appearance of these contour plots, the contours in the left column are more consistent with the experimental measurements, with every nodal point within two quanta from the minima on the contours in the middle column. 161

6-6 Comparison of the simulated origin band DF spectrum with the experimental DF spectrum. The spectrum is simulated frequency-wise by the normal mode effective Hamiltonian model, and intensity-wise by the FC factors reported in this chapter. Up to $8,000\text{ cm}^{-1}$ the simulated spectrum agrees well with the origin band DF spectrum, however, more discrepancies appear in higher internal energies. 163

- 7-1 Q-branch region of $N_{res} = 7$ SEP spectra recorded after pumping several Q-branch rotational transitions in the $V_0^2K_0^1$ vibronic band of acetylene: bottom, Q(5) PUMP; middle, Q(9) PUMP; top, Q(13) PUMP. For ease of display, traces have been shifted horizontally by $B_0J(J+1)$ ($B_0 = 1.176646 \text{ cm}^{-1}[102]$) and vertically by an arbitrary offset. 177
- 7-2 Q-branch region of $N_{res} = 7$ SEP spectra recorded after pumping Q(11) rotational transition of two vibronic bands in acetylene: bottom, $K' = 0$ ($V_1^2K_1^0$ vibronic band); top, $K' = 1$ ($V_0^2K_0^1$ vibronic band). Intermediate levels differ only in value of K' . Horizontal scale here has not been offset as in Fig. 7-1; to compare, subtract 155.3 cm^{-1} from this horizontal scale. 179
- 7-3 P-branch region of $N_{res} = 7$ SEP spectra recorded after pumping Q(11) rotational transition of two vibronic bands in acetylene: bottom, $K' = 0$ ($V_1^2K_1^0$ vibronic band); top, $K' = 1$ ($V_0^2K_0^1$ vibronic band). Intermediate levels differ only in value of K' . As in Fig. 7-2, horizontal scale has not been offset. 181
- 7-4 Observed (symbols) and calculated (curves) term values (reduced by $B_0J(J+1)$, $B_0 = 1.176646 \text{ cm}^{-1}[102]$) for eigenstates in the $N_{res} = 7$ region of acetylene. Also shown (dotted lines) are deperturbed zero-order energies for the basis states $\nu_2 + 4\nu_4$ and $7\nu_4$ in the absence of rotational l resonance and Coriolis coupling. Filled symbols are e -parity levels and open symbols are f -parity levels with nominal l assignments as indicated in the legend. 183
- 7-5 Observed (symbols) and calculated (curves) relative intensities for SEP transitions to eigenstates in the $N_{res} = 7$ region of acetylene: top, higher energy pair of e -parity levels (columns 3 and 4 of Table 7.1); middle, lower energy pair of e -parity levels (columns 1 and 2 of Table 7.1); bottom, f -parity levels. Symbols correspond to those in Fig. 7-4. 187

8-1	Raw DF spectra at 18 cm^{-1} resolution recorded from the $4\nu'_3$, $\nu'_2 + 2\nu'_3$, $\nu'_1 + \nu'_3$, $2\nu'_3 + \nu'_6$, $\nu'_2 + \nu'_3$, and $2\nu'_3$ levels of the \tilde{A} state of <i>HCCD</i> . The undulating baseline is the Quasi continuous baseline described in Chapter 4. All spectra are carefully calibrated and concatenated. Therefore, the frequency information contained in every spectrum is identical, while the intensity information contained in each spectrum is related to the Franck-Condon factor from the individual upper vibrational states.	195
8-2	HCCD DF spectra with baseline correction. The baseline removal tool is listed in the appendix, the algorithm for which is based on a paper by Ruckstuhl <i>et al</i> [81].	198
8-3	A subset of assignments for the $4\nu'_3$ DF spectrum of <i>HCCD</i> . The repeated clusters of four or three close lying peaks are unique features in HCCD. These are the result of exchange of one quantum of dominant CD bending with one quantum in dominant CH bending. Notice that the strongest peak in the cluster is always the one with most quanta in mode 4 (dominant CD bending), and zero in mode 5 (dominant CH bending). Notice also that the quantum number in mode 5, ν''_5 , never exceeds 3, giving no more than four members for every cluster, no matter how many quanta in mode 4 to start with. Both of these observations suggest that the CH bending mode has smaller Franck-Condon factor than CD bending mode, when the excitation is via $4\nu'_3$ in the \tilde{A} state. This seems counter-intuitive, because the ν'_3 mode in the \tilde{A} -state is dominant CH bending. A qualitative Franck-Condon explanation of this phenomenon is given in Fig 8-4.	201

8-4	A qualitative account for the spectral observation in HCCD. In the plot, the black nuclei stand for Carbons, red stands for the Deuterium nucleus, and green stands for the Hydrogen nucleus. The top row depicts the two turning points while <i>HCCD</i> in the \tilde{A} state is undergoing dominant CH bend, while the bottom depicts for the CD-bend. While neither the hard turning point for the CH bend nor that for the CD bend resembles the geometry of the ground state, the soft turning point for the dominant CH bend resembles an extreme, half-linear, local CD bend geometry downstairs, and <i>vice versa</i> . This is the reason why I believe in the observations made in the $4\nu'_3$ DF spectral analysis for HCCD.	202
8-5	In order to uncover as many unassigned features as possible, a synthetic “known” spectrum (green) is subtracted from the original, baseline-removed, $4\nu'_3$ DF spectrum. The red trace in the top panel is the result after the subtraction. The spectrum in the bottom panel contains a zoom-in view of the residual “unknown” features (the red trace in the top panel). Spectral congestion in the residual is high, and there are unexplainable lines as low as $4,000\text{ cm}^{-1}$, where not too many vibrational states ought to be present. The spectral congestion exceeds that expectation.	204
8-6	IR-UV double-resonance transition diagram	206
8-7	IR-UV double-resonance CRD setup	208
8-8	Principal-axes vs. body-fixed Cartesian axes	214
8-9	The $3\nu'_3$ LIF spectrum. The peaks at 45305.3 cm^{-1} and 45306.0 cm^{-1} were assigned as the R(1) “main” and the R(1) “extra” features, respectively. Utz et al [110] suggested that this perturbation pair is caused by a singlet perturber which is a member of the $4\nu'_6$ polyad.	219

8-10 The top two DF spectra were recorded from the R(1) “main” line and the R(1) “extra” lines. From 0 to 7500 cm^{-1} of internal energy, these two DF spectra look similar, however, the “extra” line DF spectrum starts to display extra vibrational features above 7500 cm^{-1} . A simple subtraction of the two DF spectra results in the third trace, which indicates that there is virtually no Franck-Condon overlap between the singlet perturber of the $3\nu'_3$ state and the linear geometry (manifested in the low internal energy region of the DF spectrum) from the \tilde{X} state. The bottom trace is a gaussian-convoluted, lower resolution version of the third trace. Its pattern manifests a strong similarity to the “ $6\nu'_3$ ” DF pattern reported by Tsuji *et al* (Fig. 3 from [108]), which led us to the belief that what was assigned as “ $6\nu'_3$ ” should instead be a member of some $n\nu'_b$ polyad. (n=7-9) 220

List of Tables

3.1	Comparison of the laser-induced fluorescence experiments at Japan Women's University (JWU) and Massachusetts Institute of Technology (MIT).	79
3.2	Rotational constants for the 2^23^1 and 1^13^1 vibrational levels of the \tilde{A}^1A_u state of C_2H_2 . Values in cm^{-1}	83
3.3	Assigned lines of the $2^23^1-4_0$ band, $K'_a = 0$ and 1, of the $\tilde{A}^1A_u - \tilde{X}^1\Sigma_g^+$ system of C_2H_2 , in cm^{-1} . The asterisk, *, denotes a line that is blended or otherwise uncertain.	84
3.4	Assigned lines of the $2^23^1-4_1$ band, $K'_a = 0$ and 1, of the $\tilde{A}^1A_u - \tilde{X}^1\Sigma_g^+$ system of C_2H_2 , in cm^{-1} . The asterisk, *, denotes a line that is blended or otherwise uncertain.	85
3.5	Assigned lines of the $2^23^1-4_1$ band, $K'_a = 2$, of the $\tilde{A}^1A_u - \tilde{X}^1\Sigma_g^+$ system of C_2H_2 , in cm^{-1} . The asterisk, *, denotes a line that is blended or otherwise uncertain.	86
3.6	Assigned lines of the $1^13^1-4_0$ band, $K'_a = 0$ and 1, of the $\tilde{A}^1A_u - \tilde{X}^1\Sigma_g^+$ system of C_2H_2 , in cm^{-1} . The asterisk, *, denotes a line that is blended or otherwise uncertain. The question mark, ?, denotes a line whose assignment is uncertain.	87
3.7	Assigned lines of the $1^13^1-4_1$ band, $K'_a = 0$ and 1, of the $\tilde{A}^1A_u - \tilde{X}^1\Sigma_g^+$ system of C_2H_2 , in cm^{-1} . The asterisk, *, denotes a line that is blended or otherwise uncertain. The question mark, ?, denotes a line whose assignment is uncertain.	88

3.8	Assigned lines of the $1^13^1 - 4_1$ band, $K'_a = 2$, of the $\tilde{A}^1A_u - \tilde{X}^1\Sigma_g^+$ system of C_2H_2 , in cm^{-1} . The asterisk, *, denotes a line that is blended or otherwise uncertain.	89
4.1	Integrated intensity of “expected” fractionated bright state (FBS) fluorescence signals vs. the “unexpected” quasi-continuous baseline signal, measured for various time gates.	100
5.1	A comparison between traditional Franck-Condon calculations and our method of Semi-Classical RKR-inversion.	116
5.2	Expansion for the $(0,0,0,10^0,0^0)$ bright state into local modes. We use A and B to symbolize two different CCH bending motions. The listed values given are expansion coefficients.	125
6.1	F matrix of the \tilde{X} state	150
6.2	F matrix of the \tilde{A} state	150
6.3	G matrix of the \tilde{X} state for $HCCH$	150
6.4	T matrix of the \tilde{X} state for $HCCH$	151
6.5	G matrix of the \tilde{X} state for $H^{13}C^{13}CH$	151
6.6	T -matrix of the \tilde{X} state for $H^{13}C^{13}CH$	151
6.7	G matrix of the \tilde{X} state for $HCCD$	151
6.8	T matrix of the \tilde{X} state for $HCCD$	152
6.9	G matrix of the \tilde{A} state for $HCCH$	152
6.10	T matrix of the \tilde{A} state for $HCCH$	152
6.11	G matrix of the \tilde{A} state for $H^{13}C^{13}CH$	153
6.12	T matrix of the \tilde{A} state for $H^{13}C^{13}CH$	153
6.13	G matrix of the \tilde{A} state for $HCCD$	153
6.14	T matrix of the \tilde{A} state for $HCCD$	154
6.15	Normal Mode Frequencies Obtained from the FG matrix analysis and their comparison with the experimental measurement	154

6.16	Comparison between Watson's calculated value and our program for the absorption series, $n\nu'_3 \leftarrow 0$ progression, of the $\tilde{A} \leftarrow \tilde{X}$ system of C_2H_2 . The results reach satisfactory agreement.	165
6.17	Comparison between Watson's calculated value and our program for the emission series, $0 \leftarrow n\nu''_4$ progression, of the $\tilde{A} \leftarrow \tilde{X}$ system of C_2H_2 . Results also reach satisfactory agreement.	166
6.18	Discrepancy in the 0_0^0 Band. our program based on Watson's FC algorithm using his Dushinsky matrices is predicting another series of bright states $1, 0, 0, \nu''_4, 0$ beside the only series of bright states that are experimentally confirmed, the $0, 1, 0, \nu''_4, 0$ series.	166
7.1	Observed (Observed - Calculated) Term Values (cm^{-1}) for States Observed in the $N_{res} = 7$ Region of Acetylene SEP Spectra. Columns correspond to symbols connected by curves in Fig. 7-4; nominal l values decrease from left to right beginning with $l = 3$. If no state was observed experimentally, the calculated term value is shown in <i>italics</i>	180
7.2	Model Fit Parameters (Defined in Text) for Coriolis-Coupled Levels $\nu_2 + 4\nu_4$ (Bright) and $7\nu_4$ (Perturber) in $\tilde{X}^1\Sigma_g^+$ Acetylene. The last digit in parentheses specifies 2σ errors.	184
8.1	Assignments of the $HCCD$ DF Spectrum Recorded from $4\nu'_3$ in the 5,000-10,000 cm^{-1} Range. The calculation is performed according to constants published by Herman and coworkers [59]. Of the states that have been observed, although 2-11 quanta of CD bend are present, very few (0-3) quanta of CH bend are observable. This effect can be accounted for by a simple Franck-Condon argument.	200
8.2	The rotational constants of <i>cis</i> and <i>trans</i>	209
8.3	The character table for C_{2v} point group (<i>cis</i> \tilde{A}^1A_2)	214
8.4	The character table for C_{2h} point group (<i>trans</i> \tilde{A}^1A_u)	214
8.5	The character table for $D_{\infty h}$ point group (<i>linear</i> $\tilde{X}^1\Sigma_g^+$)	214

Chapter 1

Introduction

In this chapter I describe the motivations for the research and the objective of this thesis, and outline the organization of the various chapters in this thesis.

1.1 Motivations and Objectives

My interest in spectroscopic studies of acetylene derives from two convictions. First is my interest in molecular spectroscopy, and the second is that acetylene is a well-suited molecule for the study, as is described below.

My specific research field can be best described as laser-excited, gas-phase molecular spectroscopy. Even before coming to MIT, I was exposed to concepts such as the normal modes of vibration, molecular symmetry, point groups, Lie algebra, etc., and found these concepts extremely interesting ¹. When I came to MIT in 1996, molecular spectroscopy was already a mature field. For one thing, tremendous resources are available for this field of study. Literature-wise, classic books have been written by Herzberg [24], Levine [58], Townes and Schawlow [107], and so on. Research journals, such as the Journal of Molecular Spectroscopy, and the frequent spectroscopic publications in Journal of Physical Chemistry A and Journal of Chemical Physics, contain new progress made in modern spectroscopy every month. Experimental-wise,

¹I owe thanks to my undergraduate advisor, Qingshi Zhu, and labmates, Xiaogang Wang, Shengfu Yang, Jixin Chen, and Jinhui Zhang for introducing me into this great field of study

many classes of spectroscopic equipment have become commercially available, such as the Fourier Transform Spectrometer. Laser technology is advancing on a day-to-day basis to provide more powerful excitation sources throughout the spectrum from the Far-InfraRed to the eXtreme Ultra-Violet. Many great scientists in this field of study are constantly and patiently helping students to better understand molecular structure and dynamics. Just as Classical Mechanics led people into understanding the physical principles underlying every daily activity, with the advances in molecular spectroscopy, I found myself exposed to an environment in which most processes in small molecules have been very well described and understood. Given such an academic setting, a natural question would be, what is not yet understood in molecular spectroscopy that is worth studying? Over the course of my graduate school study, I was guided by the conviction that there is a regularity by which molecules must behave at excitation energies above the normal mode energy realm. There is a set of rules that the molecules follow as they vibrate, rotate and isomerize, which go beyond the current understanding of the simple anharmonically corrected force fields. With the current understanding of such rules, I would like to explore realms where the rules have not yet been speculated, and at the very least, find out where limits lie. In this thesis, I hope to introduce some new findings about the molecule acetylene, C_2H_2 , and its isotopomer mono-deuterated acetylene, C_2HD .

When the laser was first discovered, physical chemists had a dream of doing bond-selective chemistry. The idea was to use the laser photon as a blade to cut a specific bond of the molecule, generate molecular fragments, and recombine them to form a new molecule. Because a laser photon is monochromatic, and the vibrational frequency of any bond in the molecule can be well calculated, this method was expected to revolutionize wet-lab based chemical reactions, and “create molecules that even God has never dreamed of making”. However, as people understood more about molecules, they found that intramolecular vibrational energy redistribution (IVR) would upset this dream, as excitation energies are quickly dissipated into other bonds, and before the monochromatic excitation source could break any bond, the entire molecule would start, perhaps even chaotically, to vibrate. However, later a specific

type of molecular behavior, local mode behavior, was observed at relatively high vibrational energies. This type of molecular behavior exhibits surprisingly slow IVR, with most of the excitation energy remaining localized in certain bonds. This is where my interest in acetylene began:

Why acetylene?

There are three size-related reasons we pick this molecule. First of all, because it is a small molecule, intramolecular vibrational redistribution (IVR) in acetylene can be described by the coupling of a small number (≤ 6) of vibrational modes. This means, the tool of Quantum Mechanical Perturbation Theory can be applied to the study of molecular dynamics, without the necessity to step into the world of Statistical Mechanics. Secondly, we like acetylene because it is a four-nuclei molecule, which has some symmetry properties that diatomic or triatomic molecules do not have. These symmetry properties of acetylene can be taken advantage of in the analysis (*e.g.* the resulting single-bright-state-per-polyad assumption [42, 47, 48, 35]). The last reason we like its size is because although acetylene is sufficiently small so that diagnostically important effects are not concealed by spectral congestion, it has many physical properties that is directly transferable to the studies of many-atom molecules. These physical properties include local mode vibrational characters, isomerization pathway mechanisms, Franck-Condon overlap principles, etc. There are only a few physical properties from bigger size molecules that is not contained in acetylene, namely, those of a molecular ring, such as the aromatic species, or the C_{60} molecule, etc..

There are other reasons we prefer acetylene. First of all, over the years, acetylene has been well studied by many spectroscopy groups around the world. This results in an abundant knowledge database for us. Secondly, when acetylene isomerizes into vinylidene, the vinyl group in vinylidene is an active and preferred ligand for organic chemists. Finally, Stanton and coworkers [97] have calculated the equilibrium and isomerization geometries (later on in this thesis would be referred to as the “critical” geometries) of acetylene in both the ground electronic state and the first excited electronic state, making some qualitative predictions about the molecular potential,

which is necessary for feasible and meaningful designs of experiments.

1.2 Acetylene

The topics presented in this thesis are almost exclusively studies on the singlet states of acetylene. Within the realm where the Born-Oppenheimer approximation is valid, electronic potential surfaces can be drawn as a function of the nuclear configuration. Figure 1-1 depicts the electronic potential surfaces of the ground state (\tilde{X} state or S_0 surface) and the first excited singlet state (\tilde{A} state or S_1 surface) electronic potential of acetylene. The ground electronic state has two local minima corresponding to the familiar linear and inversion-symmetric geometry and the vinylidene geometry, where both hydrogen nuclei are located on the same side of the CC bond. The first excited singlet state has three local minima, corresponding to the *trans*, *cis*, and vinylidene geometries. The critical energies were calculated by Stanton and coworkers [89, 97]. The linear geometry in the \tilde{X} state and *trans*-bent geometry in the \tilde{A} state are the two commonly accessible and spectroscopically well characterized wells. Our objective is to experimentally observe and theoretically predict identifiable patterns associated with the linear \leftrightarrow vinylidene isomerization in the \tilde{X} state, and *trans* \leftrightarrow *cis* in the \tilde{A} state. As will be described in this thesis, sufficient evidence exists that these two isomerization processes have a similar transition state geometry, the half-linear half-bent structure. Because of this, it is my strong belief, based on the Franck-Condon principle, that access to *either* isomerization barrier would lead to the ability to observe the other.

On the \tilde{A} state potential surface, although the vinylidene well is located at relatively low energy, 39610 cm^{-1} ², its isomerization barrier to either the *trans* or the *cis* isomer lies as high as 57880 cm^{-1} . In addition, since the vinylidene geometry has virtually zero Franck-Condon overlap with the linear well of the electronic ground state, it is presently of little interest to us. In the future, when it becomes possible

²These wavenumber measurement are relative to the zero-point minimum of the \tilde{X} state unless otherwise specified.

to access the vinylidene well in the \tilde{X} state, interest in the *trans* \leftrightarrow vinylidene and *cis* \leftrightarrow vinylidene isomerization processes will be rekindled.

Figure 1-2 depicts the normal modes of the acetylene molecule ($^{12}C_2H_2$) and their harmonic frequencies in the \tilde{X} and \tilde{A} state. The term normal mode describes the molecular eigenstate in a harmonic force field. In terms of classical mechanics, a normal mode corresponds to synchronized stable motions of the overall 4-balls-and-3-springs system.

1.3 Experimental Overview

Figure 1-3 depicts the experimental excitation and signal collection schemes for the three basic experimental schemes employed in our studies of acetylene. They are the Laser Induced Fluorescence (LIF), the Dispersed Fluorescence (DF) and the Stimulated Emission Pumping (SEP).

1.3.1 Laser Induced Fluorescence (LIF)

Shown on the left of Figure 1-3, the LIF method is to collect the optical emission from molecules that have been excited to higher energy levels via laser absorption. As we scan the laser frequency into resonance with transition into an upper state ro-vibrational level, the intensity of fluorescence increases. By plotting the emission intensity collected by the photomultiplier with respect to the laser frequency, we can get a LIF spectrum on the upper electronic state.

Advantages of LIF include:

1. greater sensitivity of fluorescence detection relative to absorption measurements,
2. the capability to selective excite a single ro-vibronic level on the \tilde{A} state.

Chapter 2 includes a detailed description of the LIF experiment. The resolution in our LIF spectra can usually reach the order of 0.05 cm^{-1} .

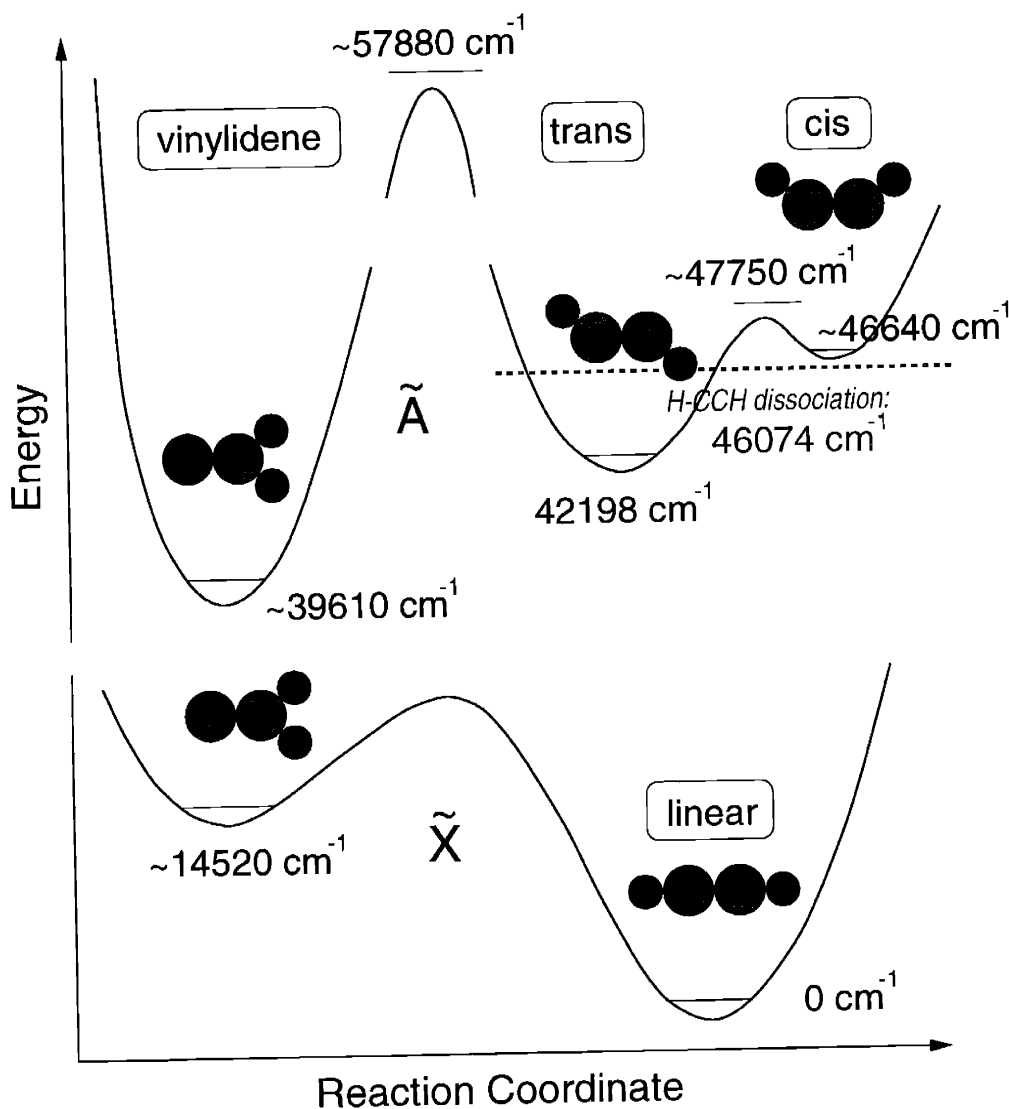


Figure 1-1: The \tilde{X} state and \tilde{A} state electronic potential surfaces of acetylene. The ground electronic state has two local minima corresponding to the familiar linear geometry and the vinylidene geometry, where both hydrogen nuclei are located on the same side of the CC bond. The first excited state has three local minima corresponding to the *trans*, *cis*, and vinylidene geometries. The linear geometry in the \tilde{X} state and the *trans* geometry in the \tilde{A} state are the two commonly accessible wells. Our objective is focused on experimentally observing and theoretically predicting identifiable patterns associated with the linear \leftrightarrow vinylidene isomerization in the \tilde{X} state, and *trans* \leftrightarrow *cis* in the \tilde{A} state. The critical point energies contained in this figure were reported by Stanton and coworkers [89, 97].

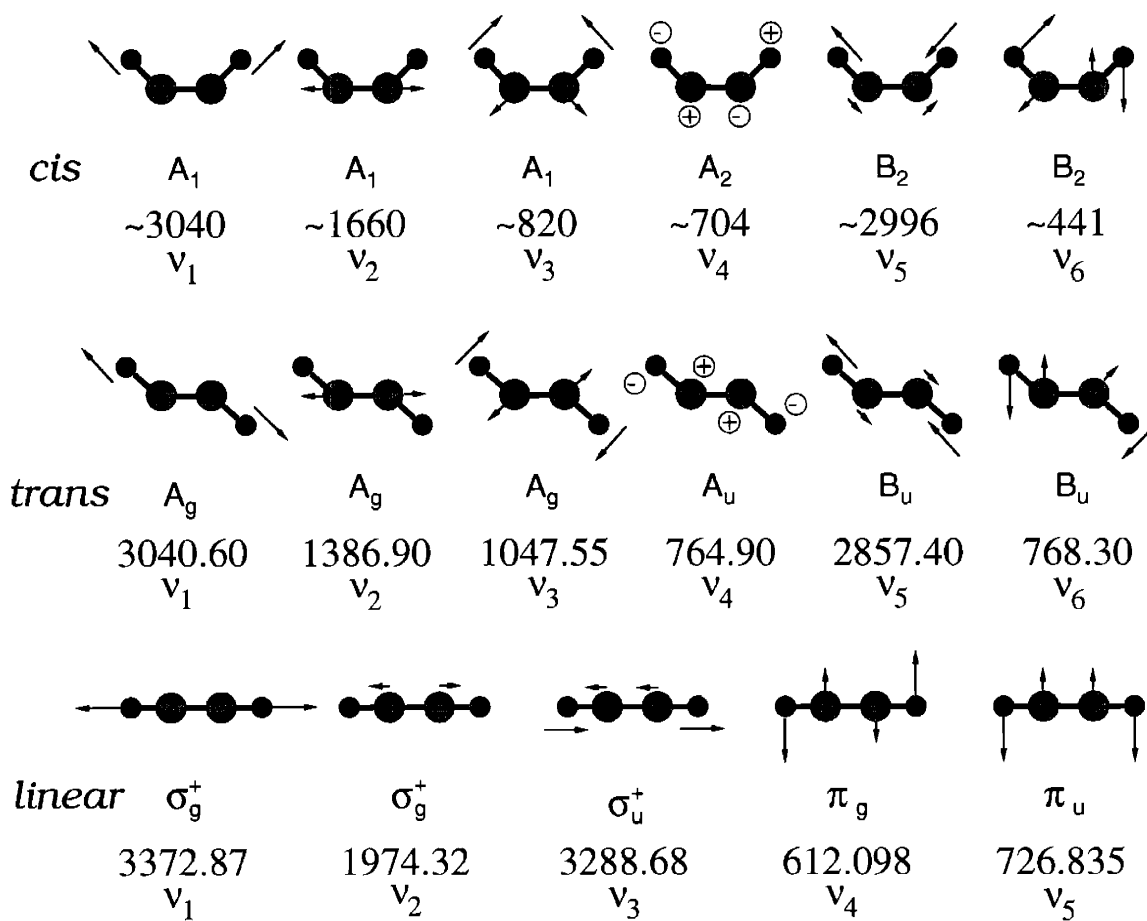


Figure 1-2: Normal modes and normal frequencies for linear-, *cis*- and *trans*- Acetylene. The linear configuration belongs to the \tilde{X} state while the *trans* and *cis* belong to the \tilde{A} state (Figure 1-1). Point group symmetry labels are added along each normal mode.

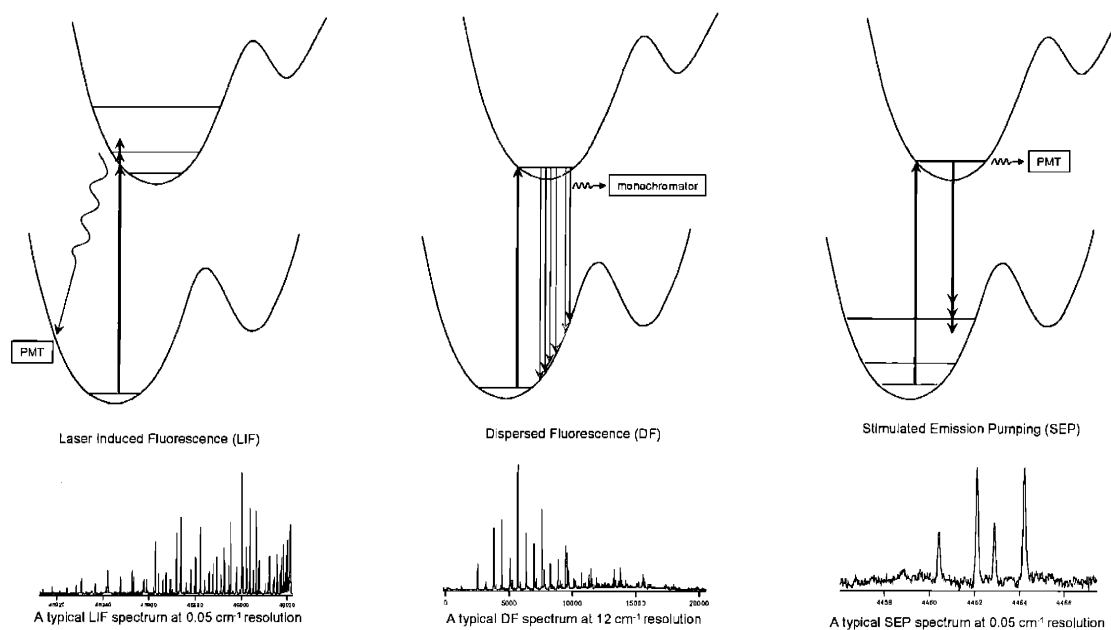


Figure 1-3: Overview of the excitation and signal collection schemes of three basic experimental techniques employed in our studies of acetylene and its isotopomers. From left to right, they are: Laser-Induced Fluorescence (LIF), Dispersed Fluorescence (DF), and Stimulated Emission Pumping (SEP). A sample segment of spectrum is attached below each excitation scheme. For simplicity, the vinylidene well on the \tilde{A} state potential is not drawn.

1.3.2 Dispersed Fluorescence (DF)

Dispersed Fluorescence (DF) spectroscopy is designed to probe a wide range of \tilde{X} state vibrational levels relatively quickly. Tuning one laser to lock onto a single ro-vibronic level of the \tilde{A} state, a monochromator is employed to disperse the spontaneous fluorescence into the ground state energy region of interest. The dispersed fluorescence signal is then collected by an ICCD camera to form a spectral segment. By adjusting the tilt of the grating in the monochromator, we obtain spectral segments on the order of 500 cm^{-1} wide for each grating position. Depending on the grating that is used by the monochromator, its length, the grating constant, the order of the grating being used, and the width of the ICCD array, we typically achieve 12 cm^{-1} resolution or better on the DF spectrum. Therefore, transitions that terminate in ground state vibrational levels usually show up as a single resolved peak.

Advantages of DF include:

1. very detailed information about the \tilde{X} state potential revealed by vibrational frequencies, anharmonicities and Franck-Condon intensities,
2. availability of an experimental Franck-Condon profile, which can provide details about the \tilde{A} state ro-vibronic wavefunctions. For an example in C_2H_2 , the symmetric bending modes in the \tilde{A} state have good Franck-Condon overlap with the trans-bend and CC stretch modes in the \tilde{X} state. If an observation is made on the DF spectrum that the trans-bend and CC stretch is the bright state, the launch state would very likely contain excitations in the symmetric bending levels.

In this thesis, Section 8.2 briefly describes the experimental details of the DF experiment.

1.3.3 Stimulated Emission Pumping (SEP)

Stimulated Emission Pumping (SEP) differs from DF by exploiting a second laser photon. The first laser beam (the PUMP beam) starts from a thermally populated

level of the ground state, and excites into a chosen ro-vibronic level of the \tilde{A} state. Therefore, that excited state fluoresces, and a PMT is used to monitor the fluorescence intensity while the frequency of a second laser (the DUMP) is scanned. When the frequency of the DUMP beam is resonant with a transition into the \tilde{X} state, most of fluorescence collapses onto that transition frequency, and the total detected fluorescence intensity from the intermediate state decreases. When that happens, we see a dip in the PMT signal.

Advantages of SEP include:

1. an enhanced probability of observing a weak Franck-Condon transition because the second transition is laser induced,
2. simplified rotational structure owing to rotational selection rule restrictions,
3. much (250 \times) higher resolution ($.05\text{ cm}^{-1}$) compared to DF (12 cm^{-1}).

1.4 Outline of the Thesis

Exploiting the three experimental building blocks, LIF, DF and SEP, we are capable of investigating the \tilde{X} and \tilde{A} state isomerization processes in acetylene and its *HCCD* isotopomer.

A major challenge in characterizing the \tilde{A} state via LIF is to distinguish hot bands (vibrational band structures originating from ground state $v'' > 0$) from cold bands ($v'' = 0$). Since the only optical control parameter we have that is directly related to the molecule is the color of the laser photon, we may not necessarily be exciting molecules from the vibrational ground level of the \tilde{X} state. Although the $\nu'_4 = 1$ state would usually have only one percent of the ground state thermal population, under room temperature there will be sufficient molecules in the ν'_4 fundamental and overtones to be excited into the \tilde{A} state. Furthermore, the hot band transition has a Franck-Condon advantage over the cold bands, therefore their intensities will not be negligible relative to that from the cold band. Chapter 2 describes a slightly modified version of LIF, the Differential Temperature LIF (DT-LIF) scheme, that enables hot

band transitions to be distinguished from cold band transitions. A numerical tool that accompanies this experimental scheme, the Structure-Based Cross Correlation (SBCC) method, will also be described in Chapter 2.

A direct application of DT-LIF to the studies of the \tilde{A} state is described in Chapter 3. New laser-induced fluorescence spectra of supersonic jet-cooled acetylene (C_2H_2), recorded by Dr. Nami Yamakita in Japan Women’s University in the wavelength region 230 - 205 nm have led to the need to apply DT-LIF to the same region. Nami and I recorded a higher-resolution, rotationally-resolved, cell-based spectrum, hoping to obtain improved understanding of the vibrational structure of the \tilde{A}^1A_u state. Among the new bands observed are two weak perturbed bands at 46008 and 46116 cm^{-1} . Rotational analyses of these bands on the DT-LIF dataset, together with the corresponding “hot” bands arising from the ground state ν_4 fundamental, have shown that the upper states have asymmetric top K -structure that is unaffected by a -axis Coriolis coupling; this means that they do not involve overtones of the low-frequency asymmetric bending (ν'_6 , b_u symmetry) and torsional vibrations (ν'_4 , a_u symmetry) and must therefore be combinations of a_g vibrational normal modes (ν'_1 symmetric CH stretch, ν'_2 CC stretch and ν'_3 symmetric bending). From their energy positions in the vibrational manifold, their vibrational assignments can only be $2^2_03^1_0$ and $1^1_03^1_0$. These assignments lead to values of x'_{22} , x'_{13} , and a revised value for the symmetric CH stretching frequency, $\nu'_1 = 2880.5 cm^{-1}$; this revised value is $160 cm^{-1}$ lower than the previously-accepted value, but consistent with new *ab initio* calculations that Stanton has performed at the EOM-CCSD level using a TZ2P (triple-zeta plus double polarisation) basis set.

Chapter 4 switches the topic to Dispersed Fluorescence spectroscopy. This is a chapter which is devoted to the understanding of previously unknown spectral features in DF spectra. Two types of mysterious features, the Quasi-Continuous baseline (QCB), and certain sharp features which are not observed by the higher-resolution SEP in the same region (the “ghost” features), have been studied through a systematic elimination scheme. We now understand that the “ghost” feature is due to K -changing collisions, and have eliminated several assumptions about the origin of

the QCB and confirmed that it is indeed a molecular feature.

Chapters 5 and 6 describe a new scheme to calculate Franck-Condon factors, which is the most lengthy theoretical calculation that I have performed. Franck-Condon factor calculations are important because they explain the intensities in the various DF spectra that we have observed, they are difficult to perform for a polyatomic molecule due to the lack of a theoretically precise potential up to the isomerization region. For this reason, a polyatomic RKR scheme [36] is used to obtain a local bending potential, and from this potential, wavefunctions, and overlap integral between the upper state and lower state wavefunctions can then be calculated. Chapter 5 described the core of the calculation, the FC calculation for the singlet *gerade* bending modes, while Chapter 6 describes how the results in Chapter 5 can be extended to a global six-mode FC calculation. A comparison between my FC calculation and that of J. K. G. Watson's [113] is given, and discussions as to why I disagree with Watson's Dushinsky displacement matrix are described.

Chapter 7 describes a SEP experiment that I performed with David Moss in my early years at MIT. Although the main goal of the SEP experiment was to probe into regions where QCB and "ghost" features are present in the DF spectrum, a surprising discovery was made about the Coriolis Coupling between $\nu_2'' + 4\nu_4''$ and $7\nu_4''$ in the \widetilde{X} state of acetylene. SEP was used to examine a low energy region (4400 cm^{-1}) of the \widetilde{X} state of acetylene at higher resolution than was possible in previous dispersed fluorescence studies. A least-squares analysis yields values for zero-order vibrational energies, rotational constants, and a Coriolis-coupling coefficient that are all consistent with expectations. Calculated relative intensities of SEP transitions, accounting for interference due to axis-switching effects, are also consistent with observations. The implications of the observed Coriolis resonance with regard to the global \widetilde{X} -state acetylene vibrational dynamics are also discussed.

Chapter 8 is devoted to several ongoing projects that I consider worthy pursuits in the future. In order to understand the local mode behavior in non-symmetric molecules, six DF spectra of HCCD have been recorded, and preliminary assignments and analysis are described. Reasons for why a precise FC calculation is necessary for

the progress in this project are given. A second project is still at proposal stage, in which I designed a scheme to directly probe into the \bar{A} state of acetylene through double-resonance CRD spectroscopy. Feasibility calculations, as well as group theoretical predictions of whether the designed transition is optically accessible, are described in detail.

Chapter 2

Differential Temperature Laser Induced Fluorescence Spectroscopy

2.1 Introduction

Since 1973 [13], the Laser Induced Fluorescence (LIF) technique has been widely used to record spectra, monitor species, and measure internal state distributions. Despite its resolution and sensitivity, the interpretation of ordinary LIF spectra is often made difficult by the thermal rotation-vibration distribution in the electronic ground state. A LIF spectrum recorded in a static gas cell often contains several overlapping rotation-vibration bands. Consequently, decoding the information contained in a LIF spectrum often depends on the ability to distinguish cold band transitions ($v'' = 0$) from the hot bands ($v'' > 0$).

One way to minimize band overlap is by jet-cooling, by which only the lowest few rotational and vibrational state populations are significant, thus largely simplifying the assignments of features in the spectrum. However, jet-cooled spectra have limitations. Structurally and dynamically interesting molecular phenomena, such as Coriolis interactions and other spectroscopic perturbations, often reveal their pres-

ence in frequency and intensity patterns that appear at relatively high rotational quantum numbers. Due to the effectiveness of rotational cooling, jet-cooled spectra contain only the lowest J lines in any band, and therefore are ill suited for detecting or surveying these effects.

A traditional way to distinguish hot from cold bands is by comparing the spectra recorded at different temperatures[24]. It is the method upon which this chapter is based. The underlying principle is, as the lower state vibrational quantum number v'' increases, the band intensity becomes more sensitive to a change in temperature. In this chapter we present a method capable of distinguishing hot band transitions from the usually more intense cold bands in a cell-recorded spectrum. Two spectra, at two different cell temperatures, are recorded simultaneously. The numerically measured, line-by-line intensity ratio provides diagnostic information about whether a line belongs to a hot or cold band. We name this technique DT-LIF, which stands for Differential Temperature Laser Induced Fluorescence. The present form of this technique is predicated on complete and accurate prior knowledge of the ro-vibrational structure of the lowest few vibrational levels of the electronic ground state.

Although DT-LIF is designed to separate overlapping bands according to the lower state vibrational quantum number, there are several other advantages. By recording the same band at two different temperatures, each spectral feature is recorded twice, minimizing spurious features introduced by random factors (e.g. voltage surge, cosmic rays). In addition, as the intensities in one spectrum are divided by those in the other, intrinsic properties such as Franck-Condon ratios and Hönl-London factors, and extrinsic effects such as laser intensity fluctuations cancel out, revealing only lower state population ratios. Frequency information becomes important only after the overlapped patterns are disentangled.

The numerical tool used to analyze DT-LIF datasets is called Structure-Based Cross-Correlation (SBCC). The method will be described here with a set of DT-LIF data from acetylene. As the purpose of this chapter is to demonstrate the DT-LIF/SBCC scheme, no rotational assignments are mentioned.

2.2 Experimental

2.2.1 Production of Light

The experimental apparatus is slightly modified from that used for Stimulated Emission Pumping (SEP) described previously [68, 44]. Specific modifications of the SEP setup for the purpose of DT-LIF data acquisition are described here.

Figure 2-1 depicts the experimental setup. A Lambda Physik LPX210icc xenon chloride excimer laser, operating at 20 Hz, produces 250-350 mJ of light at 308 nm. About 100 mJ of the excimer laser output is used to pump a Lambda Physik FL2002 dye laser. To achieve $\leq 0.05 \text{ cm}^{-1}$ spectral width, an etalon of 1 cm^{-1} free spectral range is inserted in the dye laser oscillator cavity. For the spectrum discussed in this chapter, Coumarin 440 (Lambda Physik LC120) laser dye is used. The fundamental output from the dye laser, at around 440 nm, is measured to be 10-15 mJ, of which 5 mJ is used to generate the doubled UV output through a β -BBO crystal. The pump beam input into the dye amplifier cuvette is partially blocked in order to keep the UV beam power below the damage threshold of the S1 UV optics. Nitrogen gas of grade 4.0 (99.99% minimum purity with 100ppm total impurity) from BOC Gases, Inc., is used to pressure scan [52] the dye laser. A CSK Crystals β -Barium Borate crystal (BBO) is used to frequency double the dye laser radiation to $\sim 220 \text{ nm}$ at a measured pulse energy of $500 \mu\text{J}$.

After passing through the doubling crystal, the fundamental and the frequency doubled UV beams are spatially separated by two 60° S1UV fused silica prisms. The fundamental beam is split and a $< 1\%$ portion of it is passed through a tellurium ($^{130}\text{Te}_2$) calibration oven (temperature equilibrated at around 780 K), and a monitor etalon manifold. Absorption in the $^{130}\text{Te}_2$ cell is monitored on a photodiode. The monitor etalon manifold is composed of a biconcave lens of focal length -5 cm, and a monitor etalon of finesse 10 and free spectral range of 30 GHz. The interference pattern from the monitor etalon manifold is used to tune the dye laser grating spectral profile into coincidence with a single longitudinal mode of the intracavity etalon. In one typical scan cycle, nitrogen pressure would range from vacuum to one atmosphere

DT-LIF Experimental Setup

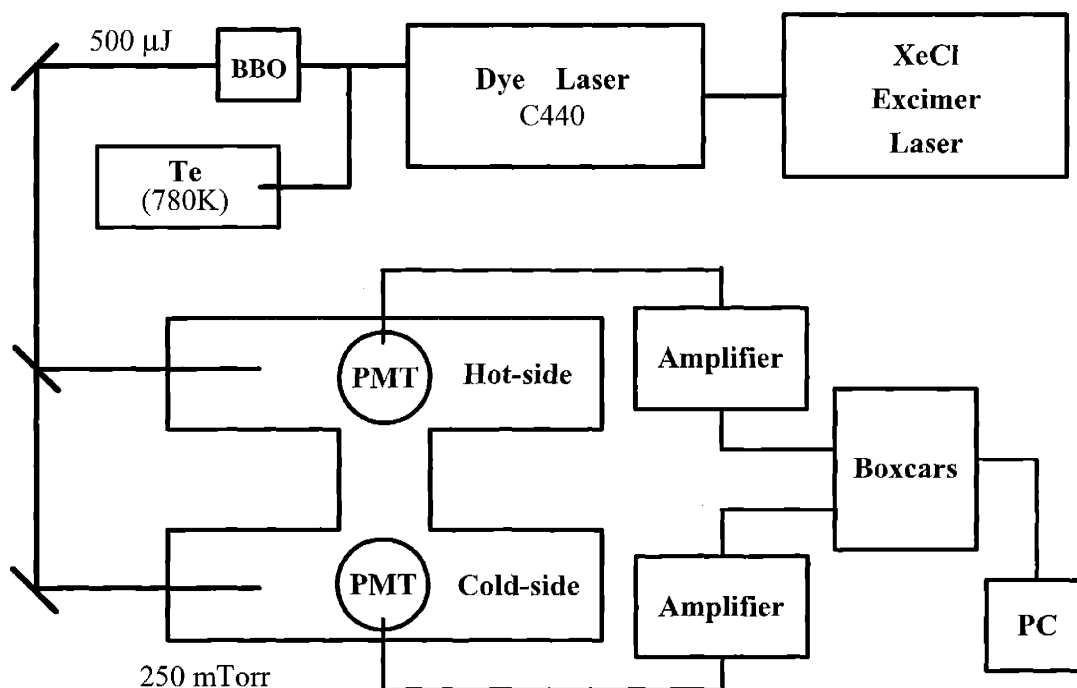


Figure 2-1: The Experimental Setup. A xenon chloride excimer laser, operating at 20 Hz, produces 250-350 mJ of light at 308 nm, of which about 100 mJ is used to pump the dye laser. While the dye laser output is ~ 10 -15 mJ, only 5 mJ is sent into the BBO crystal, to produce around $500 \mu\text{J}$ of UV output. The amplifiers used have input impedance of 1 kohm and a fixed gain of 10. The gate for the boxcars is switched on at ~ 30 ns after the laser pulse, with a width of ~ 100 ns. The “H”-shaped gas cell enables simultaneous collection of LIF spectra at two different temperatures.

in the dye laser oscillator cavity, covering a 12 cm^{-1} segment of LIF spectrum, at a resolution of the frequency doubled output of $\sim 0.05\text{ cm}^{-1}$. Adjacent spectral segments are designed to overlap by one third ($\sim 4\text{ cm}^{-1}$), for the purpose of keeping the intensity uniformly consistent throughout the concatenated frequency range of the entire spectrum.

2.2.2 Temperature Control

The static gas cell used for this experiment is a pair of parallel, linear, interconnected stainless steel cells[68]. The two arms of the cell resemble an H configuration (Figure 2-1), and in order to minimize outgassing, is pumped by a diffusion pump to 10^{-6} Torr for at least half an hour before the gas-fill procedure. Acetylene (BOC, atomic absorption grade 2.6, 99.6% purity) is used, which comes in cylinders containing acetone as a stabilizer. A few freeze-pump-thaw cycles are performed in order to minimize water vapor and oxygen impurities introduced at the time of transfer. A pentane-liquid nitrogen mixture was applied to the cylinder at the time of the fill in order to condense the acetone in the mixture. Before recording a spectrum, 250 mTorr of acetylene gas is filled into the cell.

One arm of the cell is warmed by a hot plate, while the other is cooled by a liquid nitrogen / pentane mixture. In order to prevent the window seals (Torr Seal) from overheating and leaking, the hot plate is set to $\sim 75^{\circ}\text{C}$, and raised to within a few millimeters of contact with the gas cell. The cooling mixture is made by leaving a thin layer of pentane over a bath of liquid nitrogen. The mixture is also raised to within a few millimeters of contact with the gas cell, and the cell temperature is selected to avoid condensing acetylene onto the inner walls and windows of the cell. Cooling water coils are installed around both fluorescence viewing windows to protect the photomultiplier and the hot cell from overheating, and to prevent moisture from condensing on the viewing window of the cold cell.

2.2.3 Detection

The UV beam is split by a 222 nm 50%/50% beam-splitter, and directed into both arms of the cell. Fluorescence from the hot and cold cells is imaged by S1UV f/1.9 collection optics onto matched Hamamatsu R166 solar-blind photomultipliers (PMTs). SCHOTT UG5 filters, which transmit over 80% in the 280-380 nm region, less than 7% at 220 nm, and less than 17% at 440 nm, are used to minimize scattered light from the laser beams. The outputs of the PMTs are amplified by LeCroy VV100BTB amplifiers, with $1k\Omega$ input impedance and $10\times$ fixed gain, and then input into two SRS 250 boxcar integrators. The gates for both boxcars are switched on at ~ 30 ns after every laser pulse, with a width of around 100 ns. The signal from the $^{130}\text{Te}_2$ wavelength calibration photodiode is directed into a third boxcar. The integrated analog signal outputs from the the boxcars are converted into digital signals by a 12-bit A/D converter and sent to a National Instrument NI-DAQ PC-LAB data acquisition board, to be stored and processed by Labview software on a personal computer.

2.3 Results and Analysis

2.3.1 Initial Data Processing

In the Coumarin 440 dye region, a single typical nitrogen pressure scan from vacuum to one atmosphere provides a 12 cm^{-1} LIF spectral segment after frequency doubling. Before starting the next scan, the grating position is shifted about 4 free spectral ranges of the 2 cm^{-1} free-spectral-range intracavity etalon.

Frequency calibration of the LIF spectrum is achieved by a quadratic fit through strong lines in the $^{130}\text{Te}_2$ spectral atlas. Although the lines in the $^{130}\text{Te}_2$ atlas are listed to 0.01 cm^{-1} precision, in certain regions where the $^{130}\text{Te}_2$ lines are sparse, the frequency calibration achieves an accuracy no poorer than 0.1 cm^{-1} .

In order to optimize the signal to noise ratio for each spectral segment, the boxcar sensitivity and the PMT voltage are adjusted between scans. To compare the LIF intensity patterns from the two different temperature cells, relative intensity calibra-

tions of adjacent spectral segments must be accurately made. The scan arrangement is depicted in the top panel of Figure 2-2.

Once the segments are frequency calibrated, a *recursion map* is constructed for the overlapping portions of adjacent spectral segments (Figure 2-2, middle panel). A detailed description of the *recursion map* will be given in the data analysis portion of this chapter. The recursion map consists of a plot of the intensity of segment 1 versus that of segment 2, one point for each element of the frequency grid. If the frequency calibration for consecutive spectral segments were perfect, the recursion map for each overlapping spectral region would consist of a straight line that passes through the origin. The $\leq 0.1 \text{ cm}^{-1}$ inaccuracy of the frequency calibration results in clusters of points which gather around a straight line at an angle that reflects the intensity ratio of the two segments. The slope of the line in the recursion map indicates how the intensities of adjacent spectral segments should be scaled. A linear fit is performed on the recursion map to determine the optimal intensity scaling ratios between scans. By scaling the adjacent spectral segments in this way, intensity calibration to $\pm 1\%$ is secured throughout the entire data range. This concatenation procedure also preserves the relative intensity information (Figure 2-2, bottom panel) for the high- and low-temperature spectra. As SBCC is based on accurate numerical measurement of intensity ratios, such an intensity calibration is essential.

After frequency and intensity calibration, one obtains a pair of concatenated LIF spectra, one from the hot cell, the other from the cold cell, recorded over the same 60 cm^{-1} frequency range (Figure 2-3, top panel). The spectra are then normalized using a strong line that is believed to belong to a cold band, for reasons that will become clear when we describe the SBCC method.

2.3.2 Theoretical Basis

The DT-LIF technique is designed to separate a spectrum into transitions that originate from different lower state vibrational levels. Given a spectrum without any initial knowledge of the upper state, DT-LIF makes it possible to distinguish hot from cold bands by observing the temperature dependence of the transition intensity

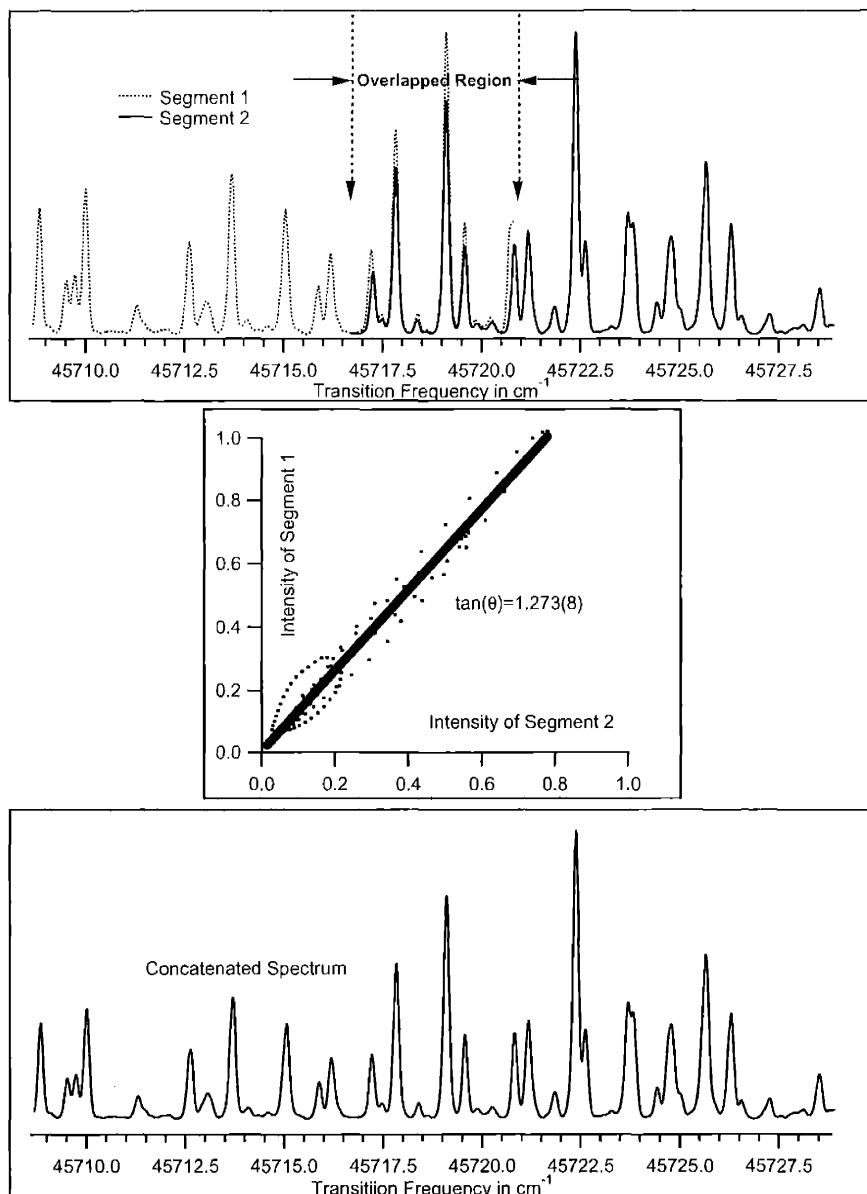


Figure 2-2: Top: Two adjacent LIF spectral segments with 1/3 overlap. Middle: Recursion map of the spectral overlap region. A fit is performed to determine the optimum intensity scaling from one scan to the other. Bottom: A concatenated spectrum constructed from the two spectral segments, properly scaled by the tangent of the slope of the line on the recursion map.

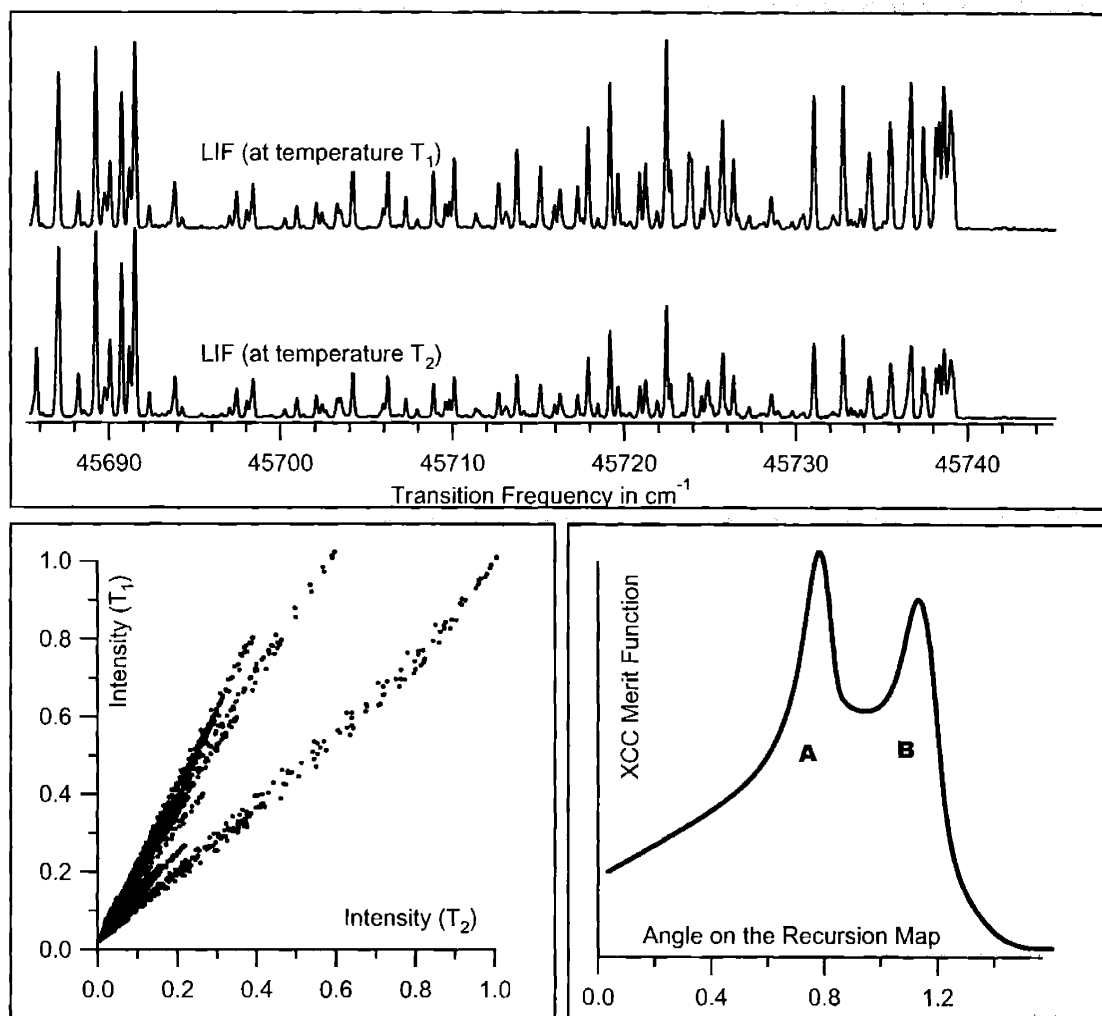


Figure 2-3: Top: Two Frequency/Intensity calibrated LIF spectra of 60 cm^{-1} length from acetylene. This pair of spectra is used as an example in this chapter to demonstrate the DT-LIF and SBCC techniques. Bottom Left: Recursion map of the spectra in the top panel. The axes of the recursion map represent intensity values in each of the two spectra, and each dot on the recursion map is obtained from corresponding resolution element on the original spectra. Bottom Right: XCC merit function computed with a large V_d for the spectra set in the top panel and the recursion map on the bottom left panel. The two local maxima indicate two apparent vibrational bands with distinctively different intensity ratios.

ratio. The physical principle of DT-LIF is based on thermal population derived from canonical partition functions.

The spectral intensity is observed to be almost proportional to the laser power. This implies that the transitions of interest are not saturated. Therefore, the intensities of the transitions in an LIF spectrum are mostly determined by the lower state population, N'' , and the squared transition moment $|\mu_{e'v'J',e''v''J''}|^2$. Since the transition moment is an intrinsic property of the molecule, thermal population is the only molecular property related to the hot:cold line intensity ratio.

To simplify, consider a non-degenerate, harmonic vibrational mode. Degenerate modes can be treated in similar fashions, and would yield almost exactly the same results. Let $\bar{\nu}$ specify the wavenumber (cm^{-1}) of the vibrational mode involved, and define $\beta = \frac{hc\bar{\nu}}{k_B}$. The spectral intensity scales with temperature according to the fractional vibrational population, obtained from the vibrational partition function[64]:

$$I_{v'v''}(T_1) = \frac{C'_1}{T_1} \bullet |\mu_{e'v'J',e''v''J''}|^2 \bullet e^{-\frac{\beta v''}{T_1}} (1 - e^{-\frac{\beta}{T_1}}) \quad (2.1)$$

$$I_{v'v''}(T_2) = \frac{C'_2}{T_2} \bullet |\mu_{e'v'J',e''v''J''}|^2 \bullet e^{-\frac{\beta v''}{T_2}} (1 - e^{-\frac{\beta}{T_2}}) \quad (2.2)$$

, where v' and v'' are the upper and lower state vibrational quantum numbers, and C'_1 and C'_2 are constants proportional to the detection efficiencies for the T_1 and T_2 optical systems, respectively. Pressure equilibrium for two cells implies that the absolute molecular density is lower for the hot cell than the cold cell. According to the ideal gas law, molecular density is proportional to $1/T$, reflected in the $\frac{1}{T_1}$ and $\frac{1}{T_2}$ factors. The $T_1:T_2$ intensity ratio for any particular vibrational band is independent of transition moment:

$$\frac{I_{v'v''}(T_1)}{I_{v'v''}(T_2)} = \left(\frac{C'_1}{C'_2}\right) \left(\frac{T_2}{T_1}\right) \left(\frac{1 - e^{-\frac{\beta}{T_1}}}{1 - e^{-\frac{\beta}{T_2}}}\right) e^{-\beta v'' \left(\frac{1}{T_1} - \frac{1}{T_2}\right)} \quad (2.3)$$

The intensity ratio is independent of upper state vibrational quantum number, v' , which is of special utility if spectroscopic perturbations occur in the upper state

of interest. We define $I.R.=\left(\frac{C'_1}{C'_2}\right)\left(\frac{T_2}{T_1}\right)$ as the *instrument response ratio*. For the $\tilde{A} - \tilde{X}$ electronic transition of acetylene, most bands originate from $v''_4=0, 1$, or 2 of the trans-bend normal mode in the ground state, with $\bar{\nu}_4=608.6 \text{ cm}^{-1}$ and $\beta=875.7 \text{ K}$. For a small temperature difference, such as $T_1 = 300\text{K}$ and $T_2 = 273.15\text{K}$, the intensity ratio is 0.99 I.R. for $v'' = 0$, 1.31 I.R. for $v'' = 1$, and 1.75 I.R. for $v'' = 2$. That is, simply by raising the temperature 27 degrees, one enhances the $v'' = 1$ hot band intensity by one third, the $v'' = 2$ hot band by 75% and decreases the cold band intensity by only one percent.

Figure 2-4 illustrates how the intensity ratio varies with lower state vibrational quantum numbers for acetylene at $T_1 = 300\text{K}$ and $T_2 = 273\text{K}$. The top panel of Figure 2-4 displays the predicted $T_1 : T_2$ intensity ratios, for vibrational bands originating from $v'' = 0 - 9$, although only low v'' ($v'' < 4$) have appreciable intensity due to the rapid decrease in thermal population with v'' . The top panel is a theoretical recursion map of the vibrational structure. The bottom panel of Figure 2-4 is a plot of the tilt angle for each v'' recursion ray. The dotted line in both panels is the instrument response ratio from Eq. (2.3), which lies very close to the intensity ratio line for the cold band. Only the cold band intensity ratio decreases as the temperature is increased. For this reason, in a spectral region where bands with various v'' coexist, the band with the smallest intensity dependence may be assigned as a cold band.

By normalizing the T_1 and T_2 spectra to the intensity of a line in the cold band, one can approximate the instrument response ratio by 1 ($\frac{C'_1}{C'_2} = \frac{T_1}{T_2}$). This approximation is accurate to about one percent for $T_1 = 300\text{K}$ and $T_2 = 273.15\text{K}$. The intensity ratio between vibrational transitions A and B is:

$$\mathfrak{R} = \frac{I_{v'_A v''_A}(T_1)/I_{v'_A v''_A}(T_2)}{I_{v'_B v''_B}(T_1)/I_{v'_B v''_B}(T_2)} = e^{-\beta(v''_A - v''_B)\left(\frac{1}{T_1} - \frac{1}{T_2}\right)} \quad (2.4)$$

Eq. (2.4) provides a correlation among temperatures, vibrational assignments and the spectral intensity ratio, independent of detection efficiencies and transition moments. This ratio of ratios from two bands is only determined by T_1 , T_2 and the difference in term value of the lower states. Although, for the sample spectra in Figure

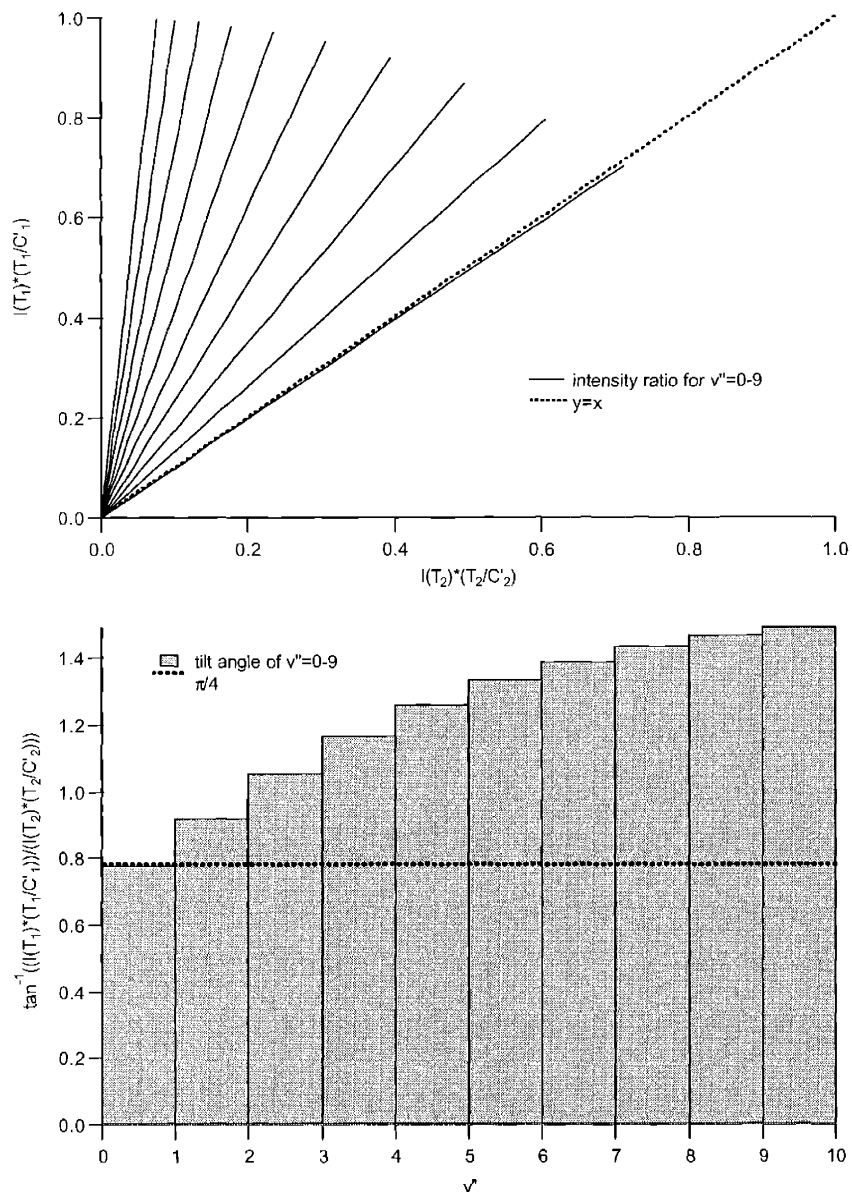


Figure 2-4: Theoretically predicted pattern of the recursion map for acetylene vibrational levels $v'' = 0 - 9$, at $T_1 = 300K$ and $T_2 = 273.15K$. Top: Recursion map, a plot of the intensity of the T_1 spectrum versus that of T_2 . Bottom: Tilt angle of the recursion rays with respect to lower state vibrational quantum number. The dotted line in both panels is the *instrument response ratio*, $\left(\frac{C_1}{C_2}\right)\left(\frac{T_2}{T_1}\right)$. Notice that for the cold band ($v'' = 0$), the tilt angle is insensitive to temperature, and therefore its intensity ratio approximates the *instrument response ratio*. For this reason, in a T_1 , T_2 pair of LIF spectra, the band with the least temperature variance originates from the $v'' = 0$ level.

2-3, the temperatures were not precisely measured, improvements could be made by adding accurate temperature control units to the setup. If T_1 and T_2 are accurately measured, \mathfrak{R} can be obtained from the XCC merit function[37] (bottom right panel of Figure 2-3), and assignments of lower state vibrational quantum number, v''_A and v''_B , can be made for specific transitions.

Rotational population effects can be incorporated into the model. A rigid, linear rotator is assumed. B is the rotational constant and $\theta_R = \frac{hcB}{k_B}$. C_1 and C_2 specify the ratio of the *absolute* spectral intensity to the relative population of the lower vibrational state, respectively at T_1 and T_2 . Disregarding Hönl-London factors¹, the intensity formulae take the following form:

$$I_{v',J',v'',J''}(T_1) = \frac{C_1}{T_1} \bullet g_{J''} \bullet \frac{\theta_R}{T_1} (2J'' + 1) e^{-\frac{\theta_R J''(J''+1)}{T_1}} \bullet |\mu_{e'v',e''v'',J''}|^2 \bullet e^{-\frac{\beta v''}{T_1}} (1 - e^{-\frac{\beta}{T_1}}) \quad (2.5)$$

$$I_{v',J',v'',J''}(T_2) = \frac{C_2}{T_2} \bullet g_{J''} \bullet \frac{\theta_R}{T_2} (2J'' + 1) e^{-\frac{\theta_R J''(J''+1)}{T_2}} \bullet |\mu_{e'v',e''v'',J''}|^2 \bullet e^{-\frac{\beta v''}{T_2}} (1 - e^{-\frac{\beta}{T_2}}) \quad (2.6)$$

, where v and J are the vibrational and rotational quantum numbers, and $g_{J''}$ the nuclear spin degeneracy factor for the J'' rotational level. For $^{12}C_2H_2$, $g_{J''}$ is 1 when J'' is even, and 3 when J'' is odd, $B=1.177 \text{ cm}^{-1}$ and $\theta_R=1.69 \text{ K}$. The theoretically predicted patterns from Eqs. (2.5) and (2.6) are plotted in Figure 2-5. If we plot a point for each J'' at the coordinates $(I(T_1), I(T_2))$, for $J''=1-25$ according to Eqs. (2.5) and (2.6), and connect each point to the origin to simulate the line shape of every rotational transition of a certain width, we obtain a *cluster* of rays in Figure 2-5 for *each* vibrational band. For every vibrational ray cluster, one rotational ray has a maximum length for J''_{max} . The overall length of the cluster of rays in each vibrational cluster is determined by a Franck-Condon factor, as well as by the lower state vibrational population. Within each vibrational ray cluster, the length of each

¹Since Hönl-London factors rapidly approach a limiting value as J increases[24], it is sensible to neglect this J -dependence in defining the structurally based pattern.

rotational ray is determined by the rotational thermal population, as well as some minor effects from Hönl-London factors, which have not been taken into account. To first approximation, the tilt of the rays in each vibrational cluster is determined by the lower state vibrational term value, and the tilt of each rotational member within a vibrational cluster is determined by the rotational term value. This rotation-specific ratio is:

$$\frac{I_{v' J' v'' J''}(T_1)}{I_{v' J' v'' J''}(T_2)} = \left(\frac{C_1}{C_2}\right) \left(\frac{T_2}{T_1}\right)^2 \left(\frac{1 - e^{-\frac{\beta}{T_1}}}{1 - e^{-\frac{\beta}{T_2}}}\right) e^{-\frac{\beta v'' + \theta_R J''(J''+1)}{k_B} \left(\frac{1}{T_1} - \frac{1}{T_2}\right)} \quad (2.7)$$

Given T_1 and T_2 , the ratio direction is determined by $e^{-\frac{\beta v'' + \theta_R J''(J''+1)}{k_B} \left(\frac{1}{T_1} - \frac{1}{T_2}\right)}$, wherein each J'' possesses its own tilt angle on the recursion map. An observation from Figure 2-5 is that high- J'' lines of a vibrational cold band have similar ratio directions as lower- J'' lines of a vibrational hot band. Thus it is insufficient to consider only vibrational effects in Eq. (2.1) and (2.2). The intensity ratio for any specific ro-vibrational transition cannot determine whether the lower state belongs to a high rotational level of a low vibrational level, or *vice versa*. This forces us to define a way to treat the overall vibrational ray cluster structure (such as in Figure 2-5) as a single pattern in order to obtain an optimal band-extracting statistic.

2.3.3 Analysis by Structure Based Cross Correlation (SBCC)

The above discussion provides a basis for improving on a simple vibrational XCC procedure: “Structure-Based Cross Correlation” (XBCC). SBCC is based on the XCC method, which has been reported previously [37, 10]. The relevant features of XCC will be discussed briefly, in the context of an improved method for processing DT-LIF spectra.

SBCC, like XCC, treats a spectroscopic data set as a series of discrete measurements, each of which is made in two or more at a single measurement element (i.e. a resolution element). In order to compare intensities from different spectra, they

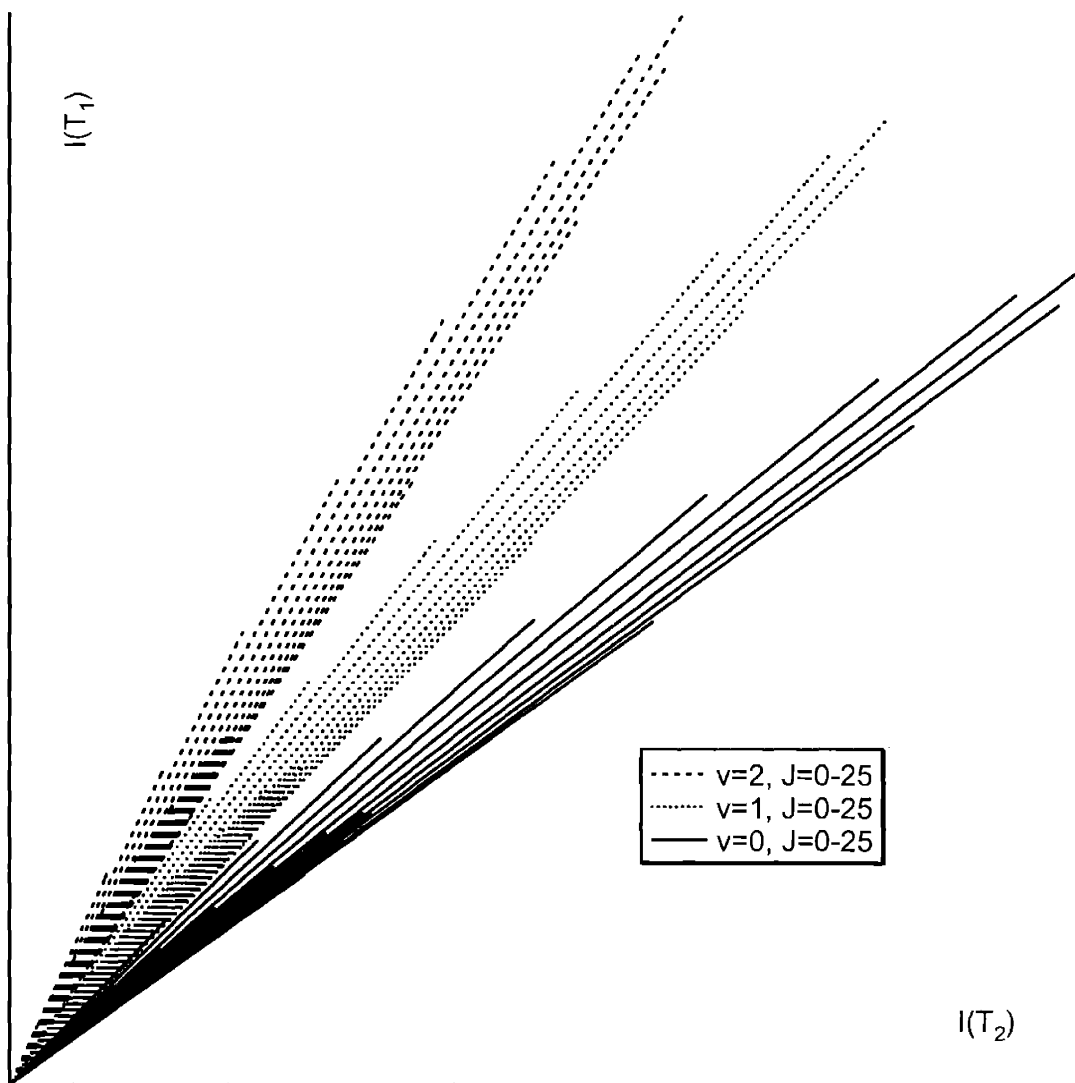


Figure 2-5: Theoretically predicted pattern of the recursion map for acetylene rotational-vibrational $v''=0,1,2$ bands. Each vibrational band contains multiple rays, each of which corresponds to a rotational line, the slope of which is determined by its rotational-vibrational energy. The length of ray clusters from different vibrational bands have been normalized. The observation that high- J lines of a low- v'' vibrational band have similar slope as low- J lines of a high- v'' vibrational band indicates that rotational effects are not ignorable.

must be *interpolated* onto identical frequency grids, the elements of which are usually chosen to be a small fraction of the spectral resolution.

Once the concatenated and calibrated spectra have been interpolated onto a common frequency grid, a *recursion map* is constructed for each T_1 , T_2 pair of spectra. The *recursion map* is constructed with its x and y axes representing the measured intensity in the LIF spectra recorded at the two different temperatures. Each frequency element appears on the recursion map as a point, the x and y coordinates of which are respectively its intensities in the T_1 and T_2 LIF spectra. No frequency information about each spectral element appears on the recursion map. The recursion map constructed for the sample T_1 , T_2 pair of acetylene spectra is shown on the bottom left panel of Figure 2-3.

The points on the *recursion map* can be organized into three categories:

1. *Points near the origin.* These points correspond to low intensity spectral elements. The scatter of these points around the origin is due to random noise.
2. *Points that form clusters of "rays" that pass through the origin.* These rays are the signatures of the T_1 , T_2 temperature dependence of the various rotational transitions. As Eqs. (2.5) and (2.6) indicate, each cluster of rays contains transitions originating from the same lower state v'' -level. Rotation, being a "finer" effect than vibration, converts each vibrational "ray" into a cluster of rotational rays. In other words, each rotational line in a single vibrational band has its own *ratio direction*, and therefore the collection of rotational rays in a vibrational band generates a cluster of rays.
3. *A sequence of points that crosses between, or possibly through rays.* This kind of feature is not present in the bottom left panel of Figure 2-3, but such points do appear when spectral lines belonging to hot and cold band overlap.

Of primary interest are the points in category 2. The absolute length of each rotational ray is determined by the intensity of the transition originating from that particular J'' in both bands. Since the vibration-rotation ray patterns are known *a*

priori (Figure 2-5), it is necessary for us to devise a scheme, without assigning any rotational lines, by which entire ray cluster patterns can be identified as in a real spectral recursion map, such as those that appear in the bottom left panel of Figure 2-3. While the XCC procedure treats a certain ratio direction as a pattern by itself, SBCC embodies the goal of identifying entire clusters of rotational rays associated with one vibrational band. To accomplish this, an appropriate merit function, G , must be devised.

The merit function, G , is designed to be large when a real spectral pattern on the recursion map is similar to a theoretical ray cluster pattern. G is a sum of individual weight functions, g_i , over all of the resolution elements in the $\{i\}$ ensemble. The *weight function*, g_i , similar to the g_i function used in XCC[37], denotes how close each point, i , lies to the theoretical pattern (in this case, the cluster of rotational rays) as the ratio direction of the entire theoretical pattern is scanned. The theoretical pattern is built from a set of lower state rotation-vibration term values, and is scanned by varying the variables that define the pattern,

$$G = \sum_i g_i = \sum_i R_i e^{-\frac{d_i^2}{2V}} \quad (2.8)$$

The weight function g_i in Eq. (2.8) is a product of two terms. The second term is a Gaussian function of d_i , which is the distance of the i th experimental point to the fit pattern (the vibrational cluster of rotational rays). This Gaussian term weights points according to their distance from the fit pattern. In order to define a useful d_i , an important judgement must be made numerically explicit. Given any point on the 2D surface of the recursion map, what is the distance between this point and the theoretical fit pattern, which consists of a cluster of rays of different lengths? The following definition of d_i provides a useful basis for specifying g_i . As Figure 2-6 illustrates, given any rotational J'' ray member of the theoretical vibrational ray cluster, there are two classes of relative positions that the experimental points, i , can take. If the perpendicular projection of the point on the ray lies beyond the terminus of the ray, d_{iJ} is defined as the distance between the experimental point and the

terminus; otherwise, d_{iJ} is the perpendicular distance between the experimental point and the ray. In the former case, the *intercept distance*, R_{iJ} , is defined as the length of the rotational ray itself; in the latter case, it is defined as the distance between the origin and the projection of the point i onto the ray. Thus, for each experimental point, i , d_{iJ} and R_{iJ} can be defined for each rotational ray associated with a particular rotational quantum number, J , in the theoretical pattern. In constructing the merit function, the distance of the point of interest, i , to the cluster of rays, d_i , is taken as the minimum from that group of d values ($d_i = \min_J d_{iJ}$), and R_i , the corresponding R_{iJ} .

V is a variance, which expresses how close the point must lie to the theoretical pattern, in order to contribute significantly to the merit function. This parameter should express the noise amplitude in the experimental spectra [37]. The first factor of g_i reflects the expectation that intense peaks provide a more accurate sample of the T_1 , T_2 intensity ratio. For extreme cases, where V is very small (i.e. good signal:noise ratio) relative to the distance between consecutive rotational rays, g_i ought to provide truthful representation of the ray cluster pattern, in that only points very close to the theoretical pattern will contribute to the weight function. A surface-contour plot of such a weight function g_i is depicted in the left panel of Figure 2-7. As shown in the plot, smaller V values are more restrictive; while larger V values (right panel) assign meaningful values to more adjacent points. In the case of larger variance, V , SBCC treats the theoretical patterns as a bundle, ignoring the finer details in the rotational ray patterns. When the g_i values are summed over all resolution elements in the “real” spectral recursion for one set of pattern-defining parameters, a value is obtained for the merit function, G , for this set of parameters. One expects that the merit function will achieve a maximum value when the theoretical pattern best matches the experimental spectral recursion map, as shown in the bottom left panel of Figure 2-3. Maximum finding routines can then be used on G to find the optimal set of parameters.

SBCC is applied to the T_1 , T_2 pair of acetylene spectra shown in the top panel of Figure 2-3. The goal is to identify patterns, such as those of Figure 2-5, that are

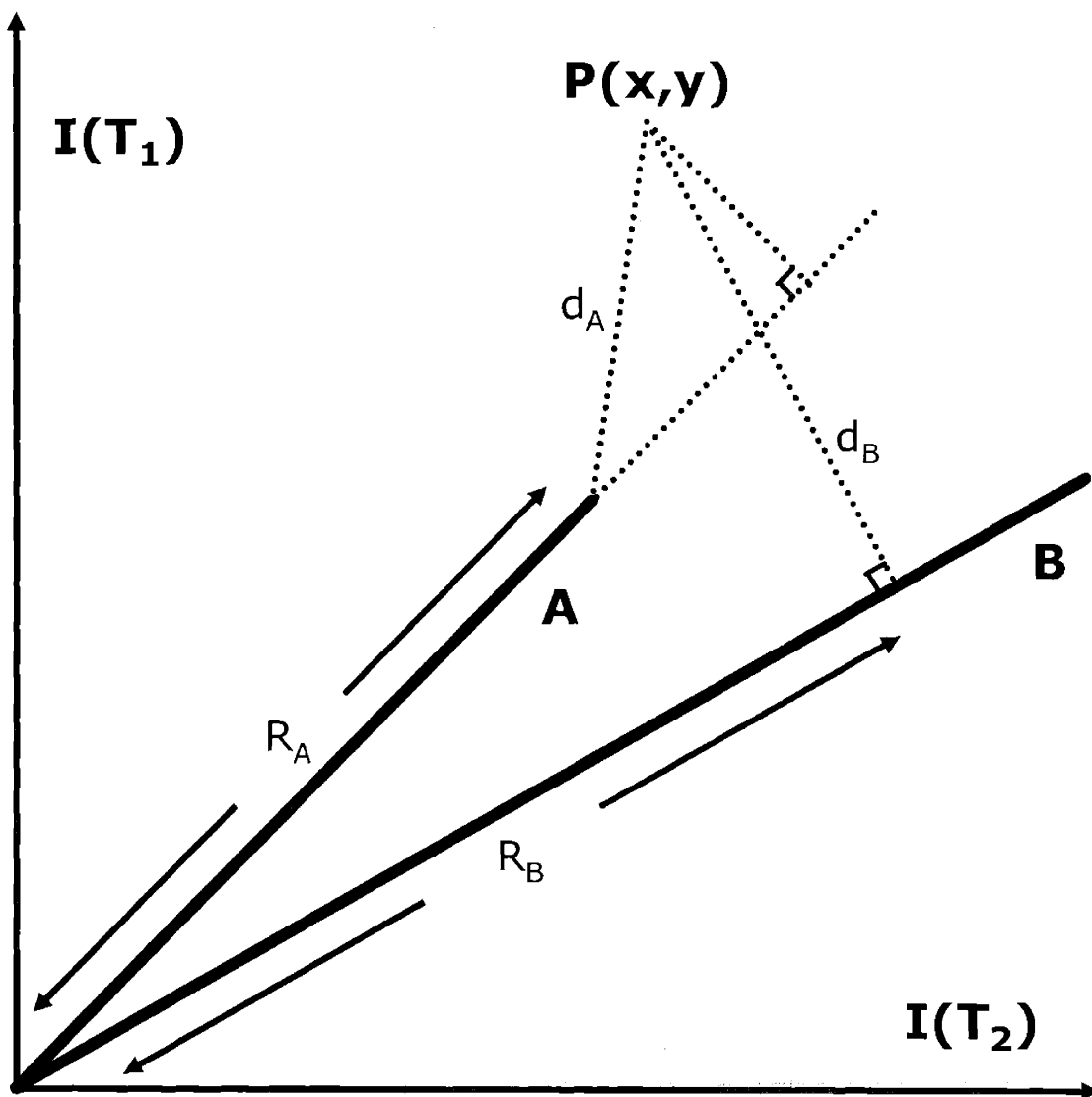


Figure 2-6: Merit Function: illustrations of the definitions of d and R for two classes of points. For ray A, the perpendicular projection of point P lies beyond the ray terminus; for ray B, the projection of point P lies within the length of the ray. The distances between point P and rays A and B, d_A and d_B , and the *intercept length*, R_A and R_B , are defined differently.

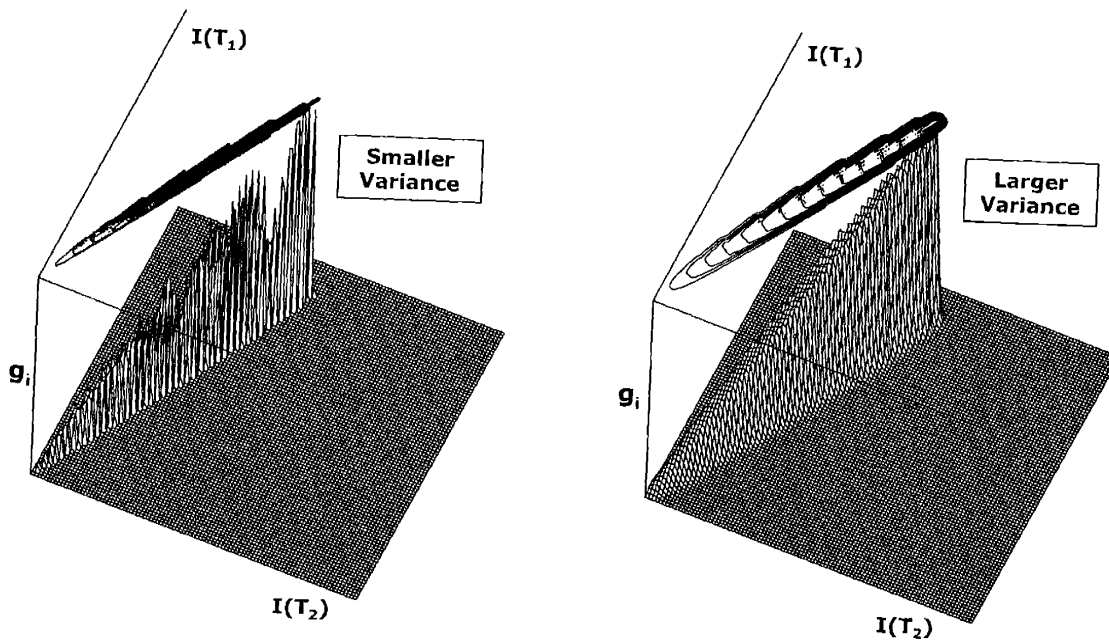


Figure 2-7: Surface plot of weight function, g_i , for every point on the 2D recursion surface ($I(T_1)$ vs. $I(T_2)$). The function value is also projected onto the top plane to form contour traces. On the left panel, g_i is constructed using a small variance, V , thus its contour exactly repeats the ray cluster pattern predicted in Figure 2-5. On the right panel, g_i is constructed with a larger variance, allowing for more adjacent points to contribute to the merit function. Use of a large V is appropriate when the intensity ratio is measured with large uncertainty, when the fitter searches for an “overall” pattern that most resembles the theoretical patterns. The weight function counts more credit to intense features, as is demonstrated by the steadily rising ridges on the surface.

present in the experimental recursion map, shown as the bottom left panel of Figure 2-3. While XCC can be applied to identify the overall vibrational features (bottom right panel of Figure 2-3), SBCC incorporates the well-known rotational intensity structure in order to optimally fit the entire cluster of rotational lines to a single vibrational band. By incorporating the known rotational term values into SBCC, the recursion patterns are more precisely defined and more accurately recovered. SBCC differs from XCC in that the former seeks a predicted structure, while the latter is better suited for situations where no *a priori* knowledge of the pattern is required.

A simple fit involves a scan of the overall ratio direction, the merit function for which locates patterns, as indicated by Eqs. (2.5) and (2.6). While a multi-dimensional fit, consisting of simultaneous optimization of C_1 , C_2 , T_1 , T_2 , v''_A and v''_B may seem feasible, it is unnecessary. For the following discussion, the pattern search is simplified to a simple one-dimensional fit along either the T_1 or the T_2 direction. A six-dimensional merit function G is simplified to a one-dimensional function, $G(T_1)$ or $G(T_2)$, thereby eliminating five degrees of freedom.

Because the two arms of the detection cell are not uniformly heated or cooled, the T_1 and T_2 temperatures to be obtained are effective values. It is easy to identify a cold band from the recursion map, because the intensities in that band are least affected by the T_1 - T_2 temperature difference. The more bands that are contained in the T_1 , T_2 pair of spectra, the more certainly is it possible to identify lines that belong to cold bands. In the sample pair of spectra shown in Figure 2-3, we already know that feature A on the vibrational merit function belongs to a cold band ($v''_A = 0$). Although knowledge of v''_A eliminates one degree of freedom in the fit, the pair of T_1 , T_2 LIF spectra contain only a small portion of the cold band A, namely, a few rotational lines. In the absence of their assignments, a small number of such lines are insufficient to fit reliably this band within the entire ray cluster pattern shown in Figure 2-5. In addition, as a cold band is least sensitive to temperature change, it is also least suitable for pattern recognition in a fit in which T_1 or T_2 is scanned. Therefore, we should only attempt to fit band B with a hot band pattern.

After the features are associated with $v''_A = 0$, a second degree of freedom may

be eliminated by making use of the correlation between T_1 and T_2 established in Eq. (2.4). This can be achieved by simple XCC. A large variance [37] V_d is used to encompass the entire bundle of rotational rays to obtain a merit function, as shown in the bottom right panel of Figure 2-3. The ratio of intensity ratios, \mathfrak{R} (Eq. 2.4), is obtained from the XCC merit function itself, recognizing that $\tan(\theta_A) = I_{v'_A v''_A}(T_1)/I_{v'_A v''_A}(T_2)$, and $\tan(\theta_B) = I_{v'_B v''_B}(T_1)/I_{v'_B v''_B}(T_2)$, with θ_A and θ_B being the average tilt angles of the two entire vibrational clusters. Simple XCC provides a convenient method to measure θ_A and θ_B . Two *ratio directions* at $\theta_A = 0.74 \pm 0.05$ rad and $\theta_B = 1.09 \pm 0.01$ rad are measured. Notice that θ_A is less precisely measured due to the fact that only a few rotational lines are included in the original spectrum. From the XCC merit function, $\mathfrak{R} = \frac{\tan(\theta_A)}{\tan(\theta_B)} = 0.48 \pm 0.03$. With Eq. (2.4), we obtain the following relation between T_1 and T_2 , thus eliminating the second degree of freedom in the fit:

$$\frac{1}{T_1} - \frac{1}{T_2} = -\frac{\ln \mathfrak{R}}{\beta(v''_A - v''_B)} \quad (2.9)$$

It is not surprising, as the T_1, T_2 LIF spectra have been normalized relative to a strong line in the cold band, A, that θ_A is determined to be very close to $\frac{\pi}{4}$. This can be used to advantage in the fit. We can simply constrain $\left(\frac{C_1}{C_2}\right) \left(\frac{T_2}{T_1}\right)^2 = 1$ in Eq. (2.7), to eliminate the third dimension in the fit.

At this stage, $v''_A - v''_B$ is not precisely known. If one examines multiple sets of LIF spectra recorded for various vibronic bands, all bands with the same vibrational quantum number will fall into vibrational clusters with the same tilt angle on the recursion map. Therefore, one would be able to pick out lower state vibrational quantum numbers merely by counting among the possible ratio directions. In Figure 2-3, which is based on only two major bands, v''_A is already known to be zero, while v''_B may only have a few plausible values ($v''_B = 1, 2, 3, 4$). Examination of the patterns resulting from discrete variation of v''_B , $v''_B = 1$ is shown to be the most consistent with the relation between T_1 and T_2 . The cold band pattern thus predicted is consistent with the few lines of band A sampled in the spectra. Knowing v''_B , we have eliminated

the fourth degree of freedom in the fit.

As discussed previously, the hot band pattern on the recursion map on the bottom left panel of Figure 2-3 contains a nearly complete set of rotational lines, and is well suited for a fit based on Eq. (2.9). For every pair of T_1 and T_2 that satisfies Eq. 2.3, the constant factors, $\frac{C_1}{T_1} \cdot \frac{\theta_R}{T_1} \cdot |\mu_{e'v'J',e''v''J''}|^2$ and $\frac{C_2}{T_2} \cdot \frac{\theta_R}{T_2} \cdot |\mu_{e'v'J',e''v''J''}|^2$ are scaled so that the maximum length of the theoretical ray cluster is equal to that of the experimental hot band ray cluster. This determines the fifth degree of freedom, and $G(T_1)$ and $G(T_2)$ can be obtained. As maximum in G corresponds a closest matching pattern on the spectral recursion map, these theoretical patterns can be plotted and used iteratively to construct another XCC merit function (such as the bottom right panel in Figure 2-3), thus producing a modified value in Eq. (2.4). Such iterations are repeated a few times, until the patterns converge. $G(T_1)$ and $G(T_2)$ from the final iteration are shown in Figure 2-8. The occurrence of multiple maxima is not surprising, as the tilt angle of the entire ray cluster could be shifted up or down by one J'' , thereby producing another close-match for the pattern. Despite this, we have the constraints that the cold trap prevents T_2 from rising above room temperature or below the temperature of the cold trap itself, $143 \text{ K} \leq T_2 \leq 300 \text{ K}$, while the hot plate requires that $300 \text{ K} \leq T_1 \leq 348 \text{ K}$. The merit function, G, whether plotted against T_1 or T_2 , has the same functional values, due to the correlation relations of T_1 and T_2 applied previously to reduce the second degrees of freedom in the fit.

Using the one-dimensional merit function, we measured one pair of temperatures that satisfy the constraints, $T_1 = 314 \pm 4 \text{ K}$, $T_2 = 263 \pm 3 \text{ K}$. The uncertainties arise from the following estimate: every rotational line intensity ratio has 10% measurement uncertainty, and there are ~ 25 rotational lines in each of the P, Q and R branches, thus measurement uncertainty is reduced to $\frac{10\%}{\sqrt{25 \times 3}} = 1.15\%$.

With T_1 and T_2 determined, the band A and band B patterns determined by Eq. (2.5) and (2.6) may be plotted, for comparison with the experimental recursion map. Figure 2-9 depicts the fit result for the hot band B, and the theoretical prediction for the cold band A, as a function of the fitted temperatures, T_1 and T_2 . The hot band structure is almost precisely reproduced by the rotation-vibration ray cluster pattern,

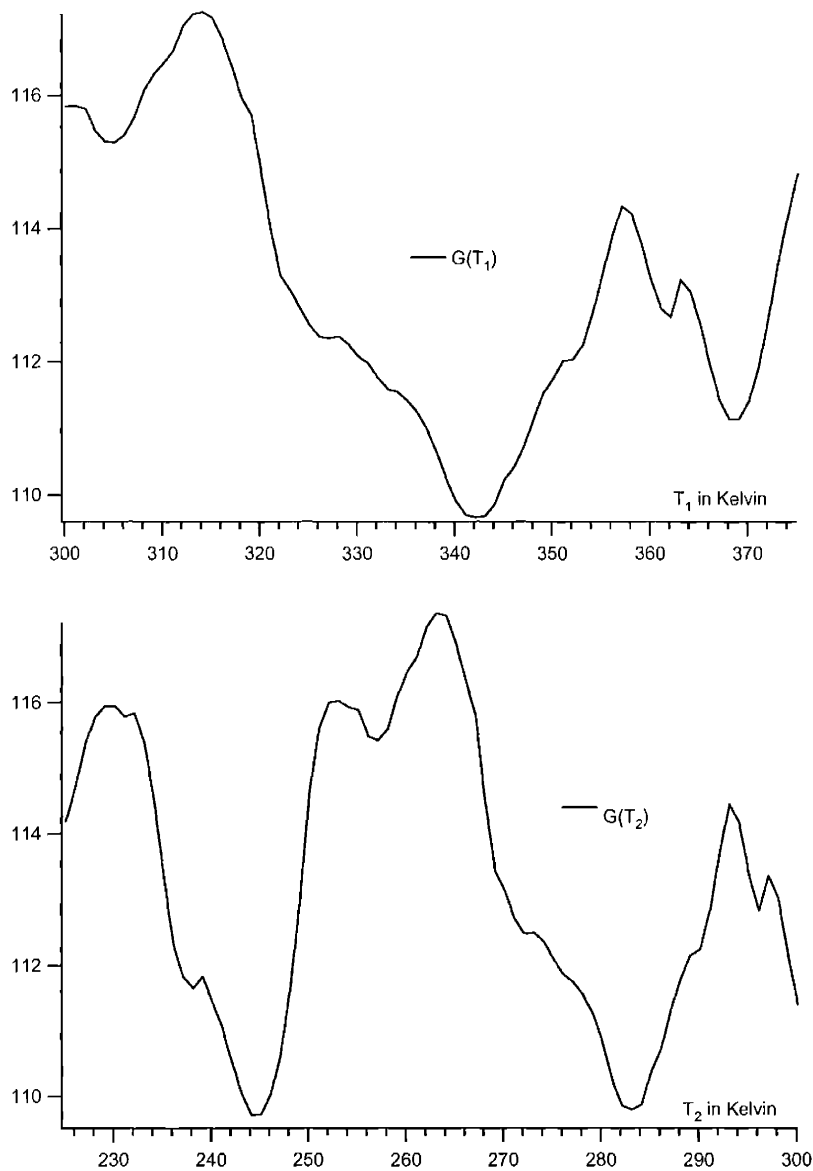


Figure 2-8: Merit function constructed for the reduced dimension fit of the hot band (band B) in Figure 2-3. The merit function, G , takes on the same pattern with respect to T_1 , as it does with T_2 , due to the correlation relations used to reduce the dimensionality in the fit. Only the maximum occurring at $T_1 = 314 \pm 4$ K, $T_2 = 263 \pm 3$ K is consistent with the experimental conditions under which the spectra were recorded.

while the cold band, albeit only a few rotational lines sampled in the original pair of spectra, agrees satisfactorily with the pattern predicted by the fitted parameters.

At this point, once both patterns are defined through fitted values of T_1 and T_2 , we can adopt a method similar to the *XCC Weights Method* [37] to extract the hot band and the cold band from the original spectra. Using a large variance V_i , the value of the weight function for every spectral element has a specific value for both the fitted hot band g_{iB} and the predicted cold band patterns g_{iA} . Because the values of the weight functions are largest for those spectral elements that are well identified as one pattern, and almost zero for those spectral elements that lie outside of any patterns, g_{iA} and g_{iB} identify all resolution elements that belong to the cold and hot band, respectively. A Plot of g_{iA} and g_{iB} against the frequencies of the original T_1 and T_2 spectra reproduces crude spectra of only the cold and hot band. Smoothing the weight functions reduces noise-induced fluctuations in the weights. The results of the smoothed g_{iA} and g_{iB} are depicted in Figure 2-10, as extracted patterns, A and B. In the sample spectra (top traces of Figure 2-10), the frequencies of the two bands of interest are well separated, to demonstrate that band A and B have been clearly separated in the middle traces of Figure 2-10. However, the SBCC technique is expected to be most valuable in cases where extensive entanglement exists between cold and hot bands, where SBCC must apportion the lines into vibrational bands prior to any rotational assignments.

2.4 Discussion

In the course of numerically treating DT-LIF datasets with SBCC, it is found that DT-LIF datasets have an important advantage over XCC datasets. The suitability of applying XCC to different spectral datasets depends on the quality of the frequency calibration[37]. Therefore, a major limitation of the XCC datasets occurs when the tellurium absorption lines (used for calibration) are sparse in a certain portion of a scan, resulting in a local frequency error, sometimes on the order of 0.1 cm^{-1} . A direct consequence of imprecise calibration is shifts of the same peak sampled by

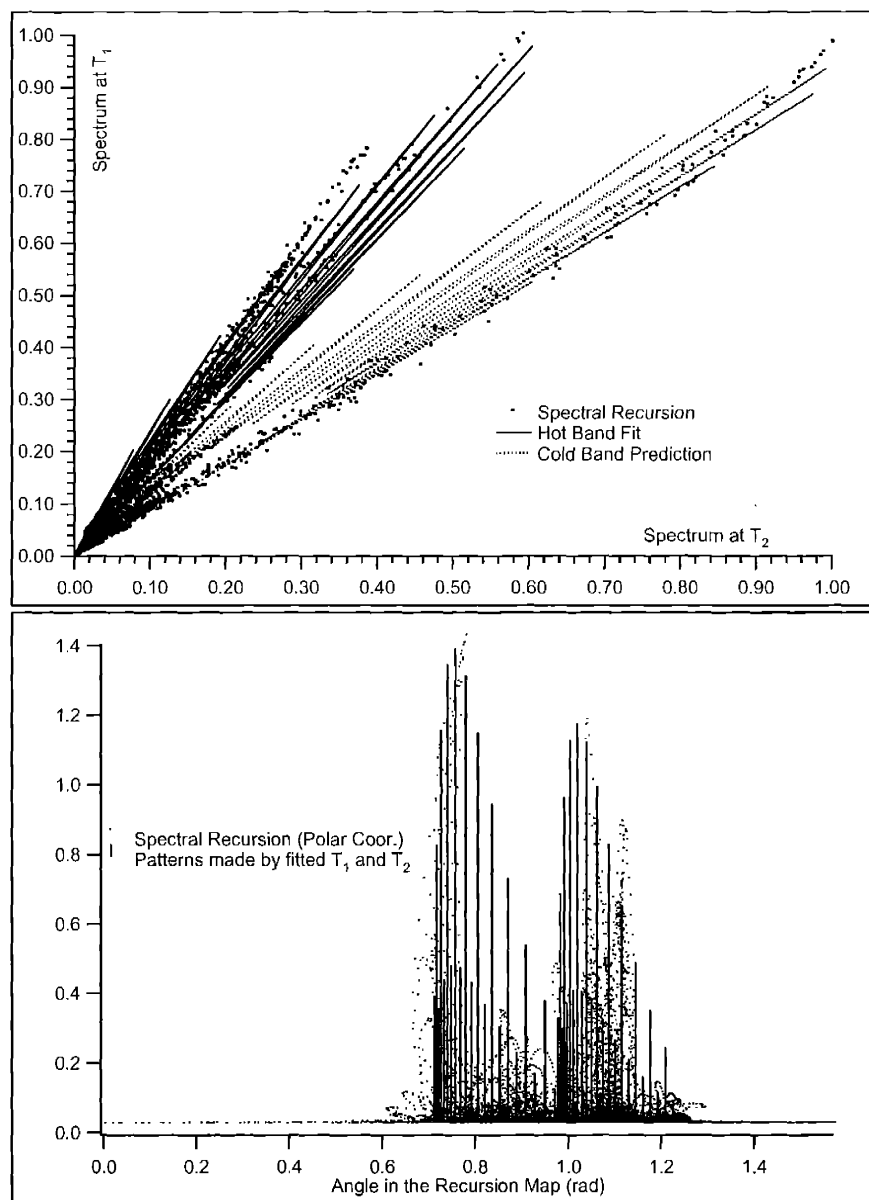


Figure 2-9: Agreement of the fit results with the spectral recursion map. On the top panel are plotted recursion map in intensity coordinates, fitted pattern for band B and predicted pattern for band A. The bottom panel contains the same plot in polar coordinates. The hot band patterns fit well at $T_1 = 310\text{K}$ and $T_2 = 274\text{ K}$. The predicted cold band pattern captures a small number of low- J lines, while most other J 's were missing from the original spectra.

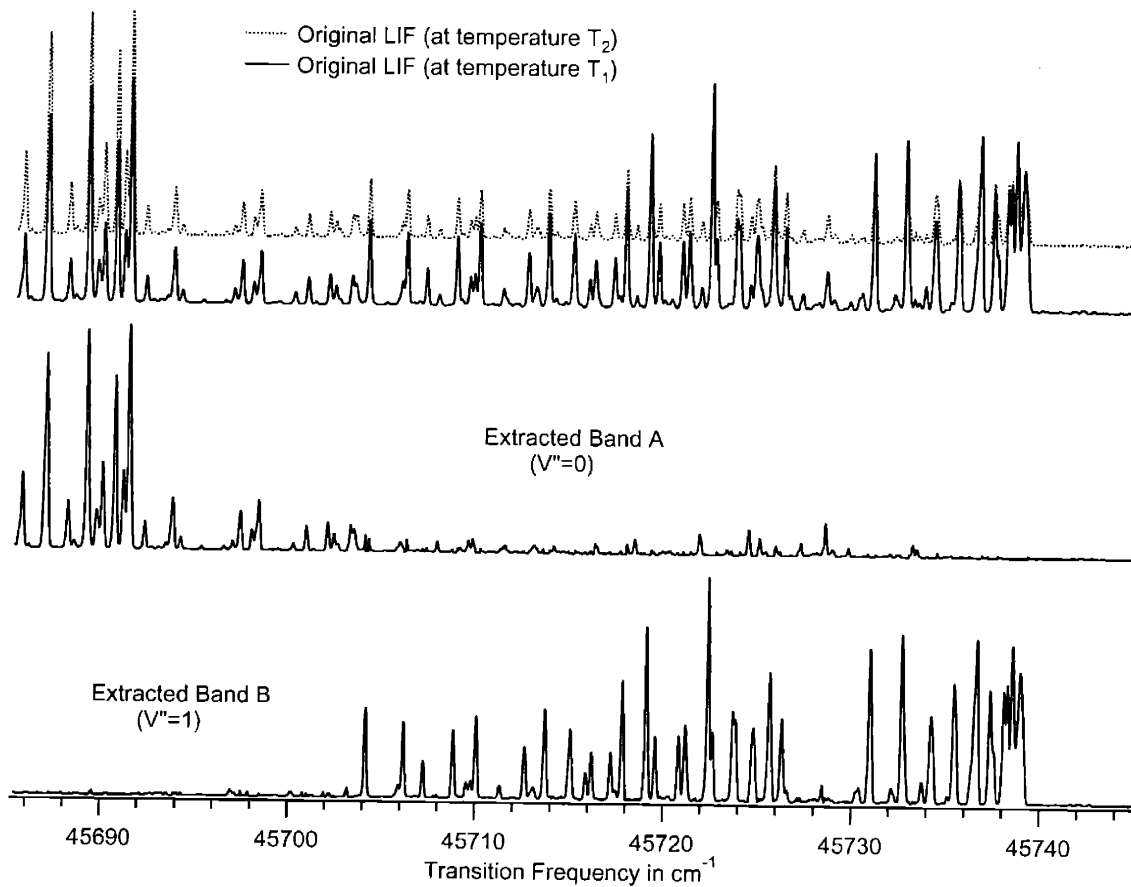


Figure 2-10: Patterns identified with the *SBC* Weights Method. All patterns are normalized to the same scale for convenience of comparison. Band A corresponds to a cold band ($v'' = 0$), while band B corresponds to a hot band ($v'' = 1$).

different spectra. This causes rays on the *recursion map* to be deformed into an elongated loop passing through the origin, which makes it difficult to determine an accurate *ratio direction* from the merit function. However, in DT-LIF, spectra of two temperature channels are recorded simultaneously. Both channels sample the same spectral resolution elements at every pulse of the excitation laser. This simultaneous collection scheme allows one to apply SBCC *prior to* frequency calibration, and therefore eliminates the requirement for nearly-perfect (<10% of a peak width) frequency calibration.

The model for SBCC, Eqs. (2.5) and (2.6), is based on an assumption that there are no upper state perturbations. In the case of an upper state perturbation, although the length of the ray may change, the ratio direction of the rays will not. Local perturbation usually does not eliminate SBCC from being the appropriate analysis tool, due to the fact that there is a series of well-defined maxima from the unperturbed rotational lines, maintaining an overall vibrational ray cluster shape on the recursion map. However, if the local perturbation happens accidentally on the J''_{max} rotational line, which has maximum intensity on that vibrational band, it may result in shift of the local maxima on the merit function by a number of rotational quantum numbers. This effect would lead to a few percent inaccuracy on the fit from the merit function. However, as prior discussion indicates, all bands with the same lower vibrational state shares the same overall vibrational ratio direction, therefore SBCC's capability to extract bands with perturbations in the upper state remains unaffected.

2.5 Conclusion

We have discussed a way to record LIF spectra, DT-LIF, recording simultaneously LIF spectra at two different temperatures. This technique, in combination with the SBCC algorithm, provides a method to distinguish and extract hot bands from cold bands with no *a priori* knowledge of the upper state molecular constants. SBCC enables precise fitting and extraction of rotation-vibration levels, based on accurate knowledge of the rotation-vibration term values of the lower electronic state.

Chapter 3

New Assignments in the

$\tilde{A}^1A_u - \tilde{X}^1\Sigma_g^+$ Electronic Transition of C_2H_2

3.1 Introduction

Acetylene (C_2H_2) is the simplest hydrocarbon containing a $C\equiv C$ triple bond and, as such, its spectra at all wavelengths have received very considerable amounts of attention over the past half century [23, 32, 34, 25, 76, 5, 85, 1, 114, 11, 12]. Its electronic spectrum is particularly interesting because the molecule, though linear in its $^1\Sigma_g^+$ ground state, becomes *trans*-bent in its first excited singlet electronic state, \tilde{A}^1A_u [32, 34, 114, 11, 12]. The first few vibrational levels of the \tilde{A}^1A_u state lie below the dissociation limit, $D_0^0 = 46074 \text{ cm}^{-1}$ [67] and, since the effects of predissociation are minimal until quite far up in the vibrational manifold, the $\tilde{A}^1A_u - \tilde{X}^1\Sigma_g^+$ electronic transition provides superb examples of resolved rotational structure in a situation where the point group changes on electronic excitation. Strong laser-induced fluorescence (LIF) can also be excited which, in addition to information about the \tilde{A} state, gives an enormous amount of information about the higher vibrational levels of the ground state, especially those involving overtones and combinations of

the ν_2'' C-C stretch and ν_4'' *trans*-bending vibrations [38].

The higher vibrational levels of the \tilde{A}^1A_u state offer excellent opportunities for study of the dynamics of inter-system crossing caused by spin-orbit interactions with the lower-lying triplet electronic states, and especially also the dynamics of *trans* \longleftrightarrow *cis* isomerization. Anharmonic effects associated with the *trans* \longleftrightarrow *cis* isomerization cause the vibrational structure of the $\tilde{A}^1A_u - \tilde{X}^1\Sigma_g^+$ system to become increasingly dense and complicated at higher vibrational energy. As a result, bands, which would not be expected to appear according to simple Franck-Condon arguments, systematically start to gain substantial intensity as a result of anharmonic resonances, while their positions diverge rapidly from what would be calculated in harmonic approximation. To understand these higher vibrational levels one needs to work methodically up from lower energy, establishing the assignments and the anharmonicity coefficients, and making sure that no obvious bands are left unexplained.

As part of an investigation of the *trans* \longleftrightarrow *cis* isomerization dynamics in the \tilde{A}^1A_u state of acetylene, we have recorded laser-induced fluorescence spectra of jet-cooled C_2H_2 in the region 43000–48500 cm^{-1} . The principal bands that appear in our spectra are the $n\nu_3'$ and $\nu_2' + n\nu_3'$ progressions, which have been previously analyzed in absorption by Watson *et al.* [114] and Van Craen *et al.* [11, 12]. In our spectra they are much simplified because nearly all the “hot” bands seen in their spectra, which arise from excited levels of the ν_4'' vibration, have disappeared as a result of the vibrational cooling. A number of weaker bands, which were not analyzed in Refs. [114] and [11], can be seen in our excitation spectra. The four longest-wavelength new bands lie in the region 45800 – 46200 cm^{-1} . Rotational analyses of excitation spectra of these bands, taken with acetylene samples near room temperature, have shown that two of them involve combinations of a_g vibrational normal modes of the \tilde{A}^1A_u state, while the other two involve double quanta of one of the low-frequency bending vibrations. The present chapter describes the analysis of the combination bands formed from the a_g vibrations, the assignments of the upper levels of which turn out to be $2_0^23_0^1$ and $1_0^13_0^1$. Given these assignments, together with other evidence, we deduce the frequency of the upper state ν_1' vibration to be 2880.5 cm^{-1} , somewhat

lower than the presently-accepted value of 3040.6 cm^{-1} from Ref. [11], but more consistent with the force field calculations of Tobiason *et al.* [106], which include data from C_2HD and C_2D_2 .

3.2 Experiments

The supersonic jet-cooled LIF spectra of acetylene were recorded at Japan Womens University (JWU). Acetylene in its $^1\Sigma_g^+$ ground state was excited to the \tilde{A}^1A_u state by ultraviolet laser irradiation. Two sources of laser radiation were employed. One was the frequency-doubled output of a Lambda Physik Scanmate 2EY dye laser, operating with Coumarin 120 or Stilbene 3 in the wavelength region 235-209 nm and pumped by the third harmonic of a Nd:YAG laser (Continuum Surelite III-10). The other was the frequency-doubled output of a Lambda Physik Scanmate 2EX dye laser, operating with Exalite dye in the region 210-206 nm and pumped by a xenon chloride excimer laser (Lambda Physik Compex 201). The line width of the ultraviolet lasers was 0.5 cm^{-1} when operating in grating scan mode, and their pulse energy was on the order of $100\ \mu\text{J}$ at 10 Hz repetition rate. The jet was produced by expanding acetylene gas (Takachiho Chem. Co.) into vacuum through a pulsed nozzle with an orifice diameter of 0.8 mm and a stagnation pressure of 0.8 atm. The laser beam intersected the jet approximately 20 mm downstream from the nozzle orifice, and the observed rotational temperature in the jet was about 30 K.

Fluorescence from the excited acetylene was observed in a direction perpendicular to both the laser beam and the jet axis. It was collected by a lens system, passed through a short wavelength cut-off filter (Sigma Koki, U28) and detected by a Hamamatsu R928 photomultiplier. As the laser wavelength was scanned, the signal from the photomultiplier was amplified by an NF, BX-31A amplifier and sent to a boxcar integrator (Stanford Research Systems, SR 250), which sampled the integrated fluorescence signal with a gate-width of $1\ \mu\text{s}$, producing the laser induced fluorescence (LIF) spectrum. The laser wavelength was calibrated by simultaneous measurement of the optogalvanic spectrum of neon from a hollow-cathode lamp (Hamamatsu, L2783-

26KNE-FE), using part of the dye laser output before frequency-doubling; the calibration accuracy given by the neon lines is estimated to be within $\pm 0.1 \text{ cm}^{-1}$. The LIF and optogalvanic spectra were digitized and stored in a personal computer.

At MIT, my goal was to record a similar spectrum using a static cell. The detailed spectral acquisition and pre-process procedures have been described in Chapter 2. Therefore only concise description will be given below. A Lambda Physik LPX210icc XeCl excimer laser, operating at 20 Hz, produced 250-350 mJ of light at 308 nm. As shown in Fig. 2-1, the excimer laser was used as the pump source for a Lambda Physik model FL2002 dye laser, operating with Coumarin 120. The output power of the dye laser, at its fundamental near 440 nm, was measured to be about 10 mJ/pulse; its wavelength was varied by pressure tuning, using N_2 gas. Part of the output was sent to an oven containing $^{130}\text{Te}_2$, for frequency calibration ($\pm 0.02 \text{ cm}^{-1}$ accuracy), and the remainder was frequency-doubled by a β -barium borate crystal (BBO) to give approximately 500 mJ/pulse of laser radiation at 220 nm.

The fluorescence cell used for the experiments had two parallel stainless steel arms, joined at their centres and arranged in a configuration like a letter "H". One of the arms was warmed to about 70°C by a hot plate, and the other was cooled to below 0°C by a liquid nitrogen/pentane mixture. The acetylene pressure in the cell was about 250 mTorr. Using a 50% beam-splitter optimized for 222 nm, the UV output from the doubling crystal was split into two beams, which were each directed into an arm of the cell. The fluorescences from the hot and cold regions of the cell were separately imaged by two sets of S1UV f/1.9 collection optics, through Schott RG5 filters to minimize scattered light, onto two Hamamatsu R166 solar-blind photomultipliers. The resulting outputs were sent through LeCroy VV100BTB amplifiers, SRS 250 boxcar integrators, a home-built A/D converter and a National Instrument NI-DAQ data acquisition device, before being collected as high resolution LIF spectra (0.05 cm^{-1} linewidth) on a personal computer.

A comparison of the experimental apparatus at JWU and MIT is given in Table 3.1.

Experiment	JWU	MIT
Type	supersonic jet	static cell
Scan	grating scan	pressure scan
Mode ¹		
Resolution	0.5 cm ⁻¹	0.05 cm ⁻¹
Highest J observed	4	25
Data Range ²	42,540 - 48,635 cm ⁻¹	43595 - 43742, 44647 - 44754, 44988 - 45579 and 45685 - 46316 cm ⁻¹
Goal	to obtain an overview of the $\tilde{A}^1A_u - \tilde{X}^1\Sigma_g^+$ system of C ₂ H ₂	to obtain rotational constants which provide the evidence for vibrational assignments

Table 3.1: Comparison of the laser-induced fluorescence experiments at Japan Women’s University (JWU) and Massachusetts Institute of Technology (MIT).

3.3 Results

3.3.1 Appearance of the spectra

The top plot of Figure 3-1 shows an LIF spectrum of jet-cooled C₂H₂ in the region 43200 - 48600 cm⁻¹ recorded at JWU. The bands at the long wavelength end are the $n\nu'_3$ and $\nu'_2 + n\nu'_3$ progressions, which are the only ones expected according to the Franck-Condon principle. The intensity scale has been magnified by a factor of $\times 10$ at 45500 cm⁻¹, in order to bring up the weaker bands at higher energy. Five of these weaker bands can be seen between the $2_0^1 3_0^2$ and 3_0^4 bands. The first of these, at 45727 cm⁻¹, is the only “hot” band of any significant intensity that appears in the jet-cooled spectrum; it has been analyzed rotationally in Ref. [11], where it was shown to be a $\Delta - \Pi$ band going from the ν_4'' fundamental to the $K = 2$ levels of $4\nu_3'$. Its assignment is not marked in Fig. 3-1. The other four bands are shown by DT-LIF to be “cold” bands, which have not been reported before.

Figure 3-2 illustrates these four “cold” bands, as seen in the LIF spectra recorded at MIT. The figure is in two parts. The lower trace covers the region 45740 - 46310 cm⁻¹, and shows the rotational structure of these four bands as it appears at a temperature of below 0°C. The upper trace covers the region 45080 - 45580 cm⁻¹. The two traces have been positioned in the figure such that their wavenumber scales

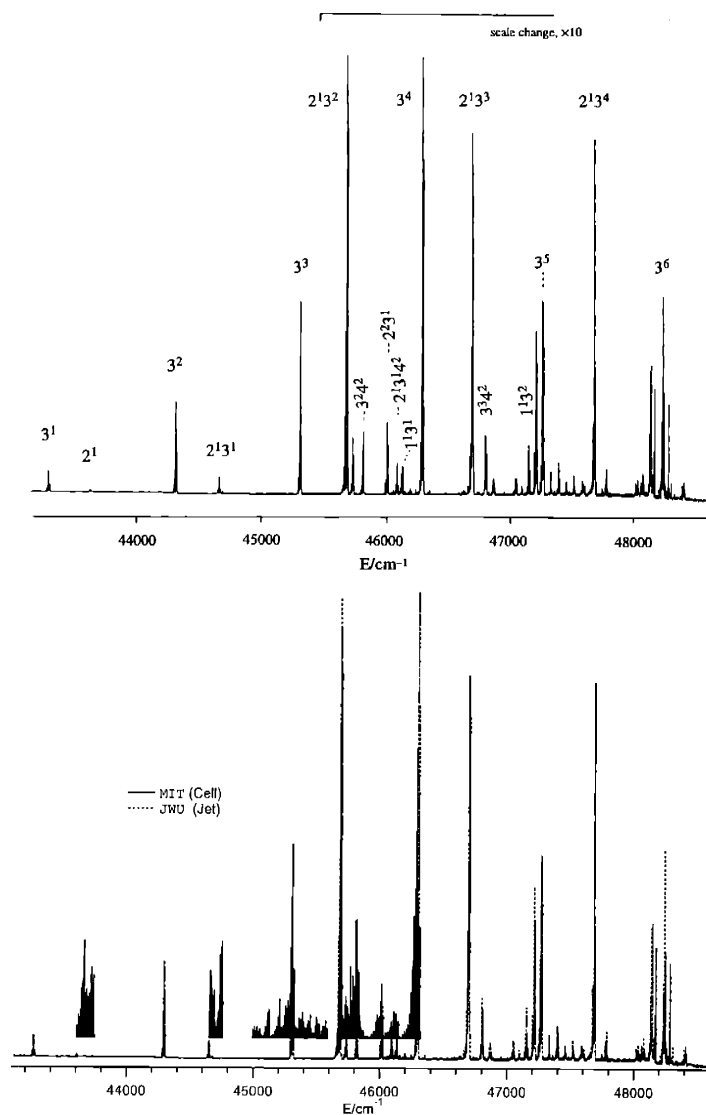


Figure 3-1: Top: The JWU spectrum: laser-induced fluorescence spectrum of C_2H_2 in the region $43200 - 48600 \text{ cm}^{-1}$ recorded using supersonic jet-cooling. The intensities of bands to the short wavelength side of 45500 cm^{-1} have been magnified by a factor of $\times 10$, in order to enhance the weaker bands. The new bands, which form the subject of this chapter, lie near 46000 cm^{-1} , between the $2_0^1 3_0^2$ and 3_0^4 bands. New vibrational assignments are written sideways. Bottom: The MIT spectra. Solid line: laser-induced fluorescence spectrum of C_2H_2 at the higher temperature in the selected regions of interest $43595 - 43742$, $44647 - 44754$, $44988 - 45579$ and $45685 - 46316 \text{ cm}^{-1}$ recorded using DT-LIF. The intensities of these spectral segments have been scaled to match those of the JWU spectrum. Dashed line: the JWU spectrum shown as on the top plot. For comparison, the two experimental LIF spectra are frequency aligned in the bottom plot. As expected, spectral patterns are consistent between them.

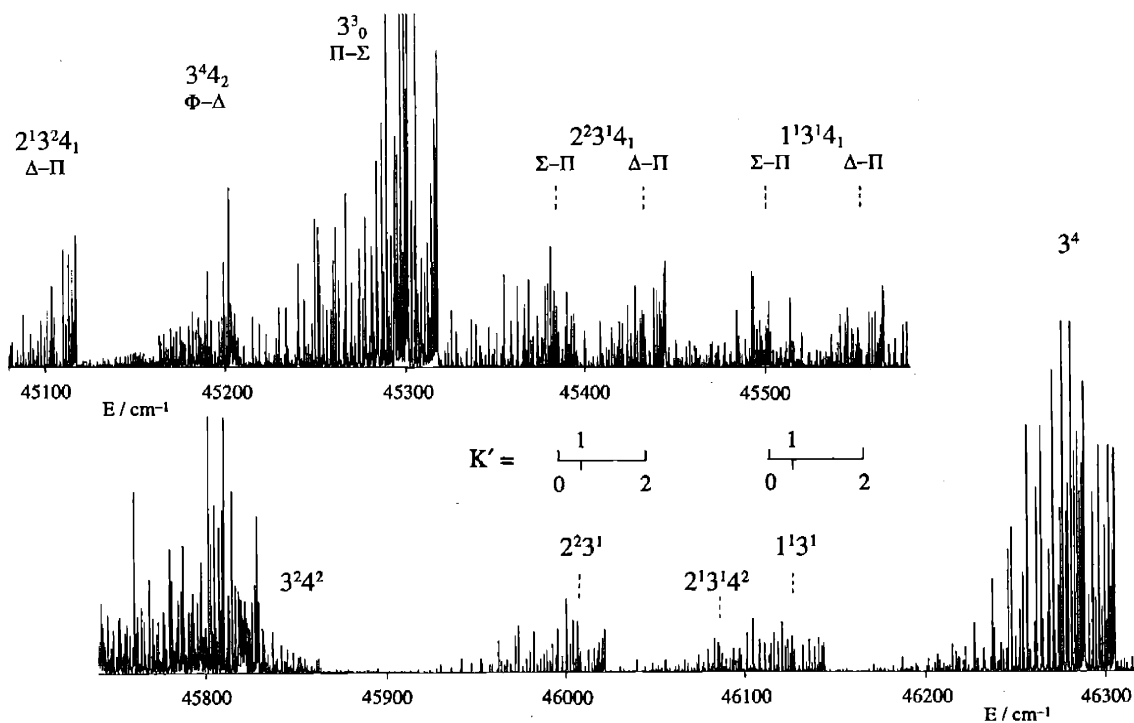


Figure 3-2: Laser-induced fluorescence spectra of C_2H_2 in the regions 45080 - 45580 and 45740 - 46310 cm^{-1} recorded with the sample at below $0^\circ C$. The two spectra have been displaced by the ground state ν_4'' vibrational frequency (612 cm^{-1}) in order to allow a direct comparison of “cold” bands in the lower trace with their corresponding ν_4'' “hot” bands in the upper trace. All the bands in the lower trace are “cold”, and all the bands in the upper trace are “hot” except for the intense 3_0^3 band. The vibrational notation for the “hot” bands indicates the lower level as 4_n ; for example, the 3_4^4 band comes from the $\nu_4'' = 2$ level of the ground state.

are displaced by 612 cm^{-1} , which is the ground state ν_4'' vibrational frequency. This means that any “hot” bands coming from the ν_4'' level which have sufficient intensity will lie directly above their corresponding “cold” bands in the figure, and allow the K -structures of the upper vibrational levels to be picked out at once.

The rationale for this follows from the $\Delta K_a = \pm 1$ (type C) rotational selection rules for the electronic transition. Bands arising from the zero point vibrational level of the $\tilde{X}^1\Sigma_g^+$ ground state, where $|l| = K_a = 0$, go to the $K_a = 1$ asymmetric top levels of the \tilde{A}^1A_u upper state, giving bands of $\Pi - \Sigma$ type, while bands from the ν_4'' fundamental, where $|l| = K_a = 1$, go to the $K_a = 0$ and 2 upper state levels, giving

$\Sigma - \Pi$ and $\Delta - \Pi$ bands; therefore, if allowance is made for the energy of the ν_4'' (Π) level, the K_a^2 -dependence of the energies of the upper state K_a -sub-bands becomes apparent when the two parts of the figure are compared.

Only two of the new “cold” bands, namely those at 46008 and 46127 cm^{-1} , show clear “hot” bands which can be assigned in terms of unperturbed asymmetric top K -structure in the upper state. As we show below, these bands can be assigned as $2_0^2 3_0^1$ and $1_0^1 3_0^1$, respectively, where the upper states involve only stretching vibrations in combination with the “straightening” vibration, ν_3' . The upper states of the other two new “cold” bands, at 45811 and 46087 cm^{-1} , are combinations involving the higher of the two overtones of the low-frequency bending vibrations. We have labelled this as $2\nu_4'$ in Figs. 3-1 and 3-2 though, since these two vibrations, the torsional vibration ν_4' and the antisymmetric in-plane bending vibration ν_6' , are so very strongly Coriolis-coupled [112, 110], a specific assignment such as this must be viewed with caution. The intensity of these bands comes from anharmonic resonances, and they will be described in more detail in a future publication.

3.3.2 Rotational analysis

Rotational analyses have been carried out for the sub-bands corresponding to the K_a' = 0, 1 and 2 rotational levels of the $2_0^2 3_0^1$ and $1_0^1 3_0^1$ vibrational levels, as sampled by the new DT-LIF spectra recorded at MIT. The analysis of the $2_0^2 3_0^1$ level, at 45995.65 cm^{-1} , was straight-forward, although a minor perturbation occurs in the $K_a' = 2$ levels for $J \geq 12$, where the structure is pushed down by up to 0.3 cm^{-1} . The assignments are confirmed by the observation of axis-switching induced Q_{fe} branches, for both $K = 0 - 0$ and $1 - 1$. The upper state rotational constants, as derived by least squares from the measured lines with $K_a' = 0, 1$ and 2 , are given in Table 3.2, and the assigned lines are listed in Tables 3.3, 3.4 and 3.5; the centrifugal distortion constants are those of Watsons A -reduced Hamiltonian [12]. No attempt was made to refine the constants for the ground state, which are known to great precision from many infra-red studies [23]. Nevertheless we treated the ν_4'' vibrational energy as a floating parameter in the fit, to allow for a possible calibration shift between our “cold” and “hot” band

Constants	2^23^1	1^13^1
T_0	45995.654 ± 0.023	46114.654 ± 0.059
A	13.617 ± 0.030	13.578 ± 0.078
B	1.10696 ± 0.00032	1.12677 ± 0.00101
C	1.01140 ± 0.00016	1.02252 ± 0.00066
Δ_K	0.0202 ± 0.0071	0.0034 ± 0.0160
Δ_{JK}	0.00030 ± 0.00002	0.0002 (fixed)
$\Delta_J \times 10^5$	0.240 ± 0.029	0.287 ± 0.215
$\delta_J \times 10^6$	0.37 ± 0.25	6.0 ± 1.8
E_4	611.693 ± 0.007	611.70 (fixed)
r.m.s. error	0.0205	0.0279

Table 3.2: Rotational constants for the 2^23^1 and 1^13^1 vibrational levels of the \tilde{A}^1A_u state of C_2H_2 . Values in cm^{-1} .

spectra; in the end this turned out to be unnecessary, since the difference between the literature value and our value was less than one standard deviation in the latter.

Assigned lines of the 2^23^1 $4_{0,1}$ and 1^13^1 $4_{0,1}^3$ bands of the $\tilde{A}^1A_u - \tilde{X}^1\Sigma_g^+$ system of C_2H_2 , in cm^{-1} . The asterisk, *, denotes a line that is blended or otherwise uncertain.

The 1^13^1 level, at 46114.65 cm^{-1} , has at least three perturbations. Two of the perturbations occur in the $K'_a = 0$ levels at comparatively low J : an avoided crossing with a vibrational level with a slightly higher B value occurs between $J = 5$ and 6, while a line-doubling occurs at $J = 11$. The $K'_a = 1$ (e -parity) levels are perturbed beyond $J = 13$, but the $K'_a = 2$ levels appear to be unperturbed, as far as we can follow them. Accordingly we fitted a restricted data set consisting of measurements for the $J = 1$ level of $K'_a = 0$, the $K'_a = 1$ (e -parity) levels up to $J = 13$ and the $K'_a = 1$ (f -parity) and 2 (both parity) levels up to $J = 18$. The fit was not as good as that for the 2^23^1 level, but this is not surprising in view of the perturbations. As before, the upper state rotational constants are given in Table 3.2 and the assigned lines in Tables 3.6, 3.7 and 3.8.

³The notation $4_{0,1}$ means that bands with zero and one quantum of the ground state *trans*-bending vibration ν_4' are included in the table.

J	$\Pi - \Sigma$			$\Sigma - \Sigma$
	R	Q	P	Q_{fe}
0	46010.36			
1	46012.32	46007.88		
2	46014.10	46007.31	46003.30	
3	46015.71	46006.45	46000.58	
4	46017.12	46005.32	45997.65	
5	46018.35	46003.91	45994.54	
6	46019.37	46002.25	45991.22	
7	46020.21	46000.25	45987.79	45988.98
8	46020.86	45997.97	45984.13	45987.12
9	46021.31	45995.40	45980.21	45984.95
10	46021.60*	45992.53	45976.15	45982.44*
11	46021.60*	45989.38	45971.91	45979.75
12		45986.00	45967.44	45976.76
13	46021.12	45982.24	45962.84	45973.50
14	46020.55	45978.19	45957.96	45969.97
15	46019.77	45973.86	45952.89*	45966.12
16	46018.77	45969.25	45947.71*	45962.04
17	46017.58	45964.34	45942.16	45957.59
18	46016.15	45959.12	45936.49	45952.89*
19	46014.48	45953.58	45930.60*	45947.71*
20	46012.59	45947.71*	45924.46*	45942.41
21	46010.40*	45941.59	45918.10	45936.72
22		45935.14	45911.53	45930.60*
23		45928.39	45904.70	45924.39
24		45921.32		45917.63
25		45913.91		45910.59
26		45906.16		
27		45898.19		

Table 3.3: Assigned lines of the $2^23^1 - 4_0$ band, $K'_a = 0$ and 1, of the $\tilde{A}^1A_u - \tilde{X}^1\Sigma_g^+$ system of C_2H_2 , in cm^{-1} . The asterisk, *, denotes a line that is blended or otherwise uncertain.

J	$\Sigma - \Pi$			$\Pi - \Pi$
	R	Q	P	Q_{fe}
1	45387.95	45383.75		
2	45389.63*	45383.29	45379.00*	
3	45390.99	45382.59	45376.16	
4	45392.11	45381.66	45373.05	
5	45392.79*	45380.47	45369.69	
6	45393.51*	45379.00*	45366.15	
7	45393.94*	45377.41		
8	45393.96*	45375.50	45358.22	
9	45393.94*	45373.33	45353.86	
10	45393.51*	45370.87	45349.26	
11	45392.79*	45368.24*	45344.37	45377.87
12	45391.82	45365.29	45339.20	45374.46
13	45390.53	45362.05	45333.96	45370.77
14	45388.92	45358.56	45328.10	45366.80
15	45387.02	45354.75	45322.04	45362.49
16	45384.87	45350.71		45357.92
17	45382.32	45346.28		45353.05
18	45379.45*	45341.61		45347.86
19	45376.16*	45336.64		45342.41
20	45372.75*	45331.28		45336.64*
21	45368.91	45325.66		45330.51
22	45364.73	45319.71		45324.13
23				
24				
25				
26				
27				

Table 3.4: Assigned lines of the $2^23^1 - 4_1$ band, $K'_a = 0$ and 1, of the $\tilde{A}^1A_u - \tilde{X}^1\Sigma_g^+$ system of C_2H_2 , in cm^{-1} . The asterisk, *, denotes a line that is blended or otherwise uncertain.

J	$\Delta - \Pi$					
	R_{ee}	R_{ff}	Q_{fe}	Q_{ef}	P_{ee}	P_{ff}
1	45437.89					
2	45439.53		45433.15			
3	45440.94		45432.47		45426.11	
4	45441.99		45431.44		45422.97	
5	45442.96		45430.35		45419.80	
6	45443.59		45428.97	45428.72	45416.27	45416.02
7	45443.94		45427.35	45427.00	45412.46	45408.24
8	45444.22*		45425.54	45425.04	45408.49	45408.24
9	45444.40	45444.22*	45423.46	45422.81	45404.26	45403.91
10	45444.22*	45443.94	45421.18	45420.34	45399.79	45399.38
11	45443.59		45418.70	45417.67*	45395.01	45394.58
12		45442.74	45416.02*	45414.63	45390.10	45389.63*
13	45441.82		45413.00	45411.34*	45384.46	
14		45440.66	45409.73	45407.94		45379.45
15	45439.10		45406.56		45373.73	
16		45437.89*		45399.99		45367.50
17	45435.22		45399.38*		45361.54	
18				45391.18		45355.32
19					45348.35	

Table 3.5: Assigned lines of the $2^23^1 - 4_1$ band, $K'_a = 2$, of the $\tilde{A}^1A_u - \tilde{X}^1\Sigma_g^+$ system of C_2H_2 , in cm^{-1} . The asterisk, *, denotes a line that is blended or otherwise uncertain.

J	$\Pi - \Sigma$			$\Sigma - \Sigma$
	R	Q	P	Q_{fe}
0	46129.37			
1	46131.46	46126.93		
2	46133.37	46126.43	46122.30	
3	46135.09	46125.64	46119.63	
4	46136.60	46124.61	46116.80	
5	46138.03	46123.30	46113.85	
6	46139.29	46121.73	46110.78	
7	46140.40	46119.94	46107.48	46108.47
8	46141.35*	46117.88	46104.05	46106.79
9	46142.14*	46115.55	46100.43	46104.83
10	46142.76*	46113.03	46096.67	
11	46143.16*	46110.24	46092.80	46100.44*
12	46143.16	46107.13	46088.65*	46098.33
13	46143.76	46103.77	46084.34	46095.19*
14	46143.55*	46100.14	46079.86	46092.25*
15	46143.16	46096.31	46075.56	46088.65*
16	46142.76	46092.95	46070.65	46085.03*
17	46142.14	46087.84?	46065.61	46081.05
18	46141.35	46083.22?	46060.55	46076.87
19			46055.21	46072.29
20			46049.63	46067.33*
21				46062.28

Table 3.6: Assigned lines of the $1^13^1 - 4_0$ band, $K'_a = 0$ and 1, of the $\tilde{A}^1A_u - \tilde{X}^1\Sigma_g^+$ system of C_2H_2 , in cm^{-1} . The asterisk, *, denotes a line that is blended or otherwise uncertain. The question mark, ?, denotes a line whose assignment is uncertain.

J	$\Sigma - \Pi$			$\Pi - \Pi$
	R	Q	P	Q_{fe}
1	45506.95*	45502.76		
2	45508.78	45502.38	45498.01	
3	45510.34	45501.79	45495.20*	
4	45511.55	45501.05	45492.29	
5	45512.16	45500.00	45489.05	
6	45513.04	45498.18	45485.66	
7	45513.70	45496.83	45481.45	45508.32
8	45514.07*	45495.20*	45477.62	
9	45514.07*	45493.29	45473.69*	45503.97
10		45491.08	45469.23	45501.51
11		45488.62, 45489.51	45464.54	45498.70
12		45486.65	45459.58, 45460.54	45495.64
13		45483.92	45455.35	45492.29*
14		45480.80	45449.90	45488.70*
15		45477.38		45484.91
16		45473.69*		45480.80*
17		45469.84		45477.38*?
18		45465.58		45472.00
19		45461.10		
20		45456.29		
21		45451.15		

Table 3.7: Assigned lines of the $1^13^1 - 4_1$ band, $K'_a = 0$ and 1, of the $\tilde{A}^1A_u - \tilde{X}^1\Sigma_g^+$ system of C_2H_2 , in cm^{-1} . The asterisk, *, denotes a line that is blended or otherwise uncertain. The question mark, ?, denotes a line whose assignment is uncertain.

J	$\Delta - \Pi$					
	R_{ee}	R_{ff}	Q_{fe}	Q_{ef}	P_{ee}	P_{ff}
1	45557.01					
2	45558.74		45552.26			
3	45560.27		45551.69			
4	45561.51		45550.78		45542.18	
5	45562.69	45549.86	45549.72		45539.10	
6	45563.51	45548.66	45548.41	45535.78	45535.57	
7	45564.39	45547.29	45546.91	45532.18	45531.89	
8	45564.74	45545.71	45545.24	45528.41	45528.12	
9	45565.19	45543.99	45543.32	45524.46	45524.10	
10		45542.04	45541.17	45520.27	45519.89*	
11		45539.88	45538.77	45515.87	45515.50	
12		45537.88	45535.21		45510.88	
13		45535.09	45533.39*	45506.44		
14			45530.30		45501.05*	
15				45496.15		
16			45523.56			
17						
18			45515.87*			

Table 3.8: Assigned lines of the $1^{13^1} - 4_1$ band, $K'_a = 2$, of the $\tilde{A}^1A_u - \tilde{X}^1\Sigma_g^+$ system of C_2H_2 , in cm^{-1} . The asterisk, *, denotes a line that is blended or otherwise uncertain.

3.3.3 Vibrational assignments

The rotational analyses just described show that the upper states of the new vibrational levels at 45996 and 46115 cm^{-1} are vibrationally totally symmetric. Since the zero-point level of the \tilde{A}^1A_u state lies nearly 4000 cm^{-1} below, at 42198 cm^{-1} the upper vibrational levels must be combination levels. The question then arises of whether they are combinations formed just from the three a_g vibrations, or whether they involve overtones of the low-lying bending vibrations ν'_4 and ν'_6 , which are of species a_u and b_u , respectively. The answer is provided by their K -structures. As can be seen in Table 3.2, the A rotational constants of the new levels are about 13.5 cm^{-1} , and their centrifugal distortion constants Δ_K are in the range 0.02 to 0.003 cm^{-1} . These are very similar to what is found [114] in the lowest members of the $n\nu'_3$ and $\nu'_2 + n\nu'_3$ progressions, and may be considered “normal”. By contrast, it is known that extremely strong a-axis Coriolis interaction occurs between the levels of the two low-frequency bending vibrations, ν'_4 and ν'_6 , which causes their K -structures to be highly irregular [112, 110]. The apparent values of A , inasmuch as they are defined for such strongly interacting levels, lie in the range 5 to 30 cm^{-1} , while the values of Δ_K are as large as 1 cm^{-1} . The strength of the Coriolis interaction increases with excitation of the bending vibrations, so that it is extremely unlikely that any vibrational levels in which the bending (namely ν'_4 and ν'_6) vibrations are involved will show “normal” values of A and Δ_K . This means that the values of A and Δ_K provide a diagnostic test for whether the Coriolis-coupled bending levels are excited in any particular vibrational level, and it seems clear in the present case that they are not.

Given that the new bands do not involve the low-lying bending vibrations, they must be assigned in terms of the totally symmetric vibrations ν'_1 (the symmetric CH stretch), ν'_2 (the CC stretch) and ν'_3 (the *trans*-bend or symmetric bending, or as Anthony Merer calls it, the “straightening” vibration). The positions of the $n\nu'_3$ levels with $n = 1-6$ and the $\nu'_2 + n\nu'_3$ levels with $n = 1-5$ have been established by the rotational analyses of Refs. [114, 11]; they are shown in Fig. 3-1 for reference. The currently-accepted value of ν'_1 (3040.6 cm^{-1}) was derived from the assignment of the

level at 47195 cm^{-1} as $\nu'_1 + 2\nu'_3$ in Ref. [11]. Using the data from Refs. [114, 11], we have calculated the energies of the manifold of ν'_1 , ν'_2 and ν'_3 vibrational levels up to about 5000 cm^{-1} of vibrational energy in the \tilde{A}^1A_u state; these are shown in Fig. 3-3. Since the only anharmonicity constants available for these three vibrations are x'_{23} and x'_{33} , we have set all the other x'_{ij} to zero in drawing the figure. Our new vibrational levels at 45996 and 46115 cm^{-1} lie at vibrational energies of 3798 and 3917 cm^{-1} within the \tilde{A}^1A_u state. Comparison with Fig. 3-3 shows that there is a good match for the 3798 cm^{-1} level with $2^2_03^1_0$, allowing for anharmonicity, but that there is nothing predicted near the position of the 3917 cm^{-1} level.

The 3917 cm^{-1} level can only be understood if it is assigned as $1^1_03^1_0$, with the value of ν'_1 reduced by about 160 cm^{-1} from the currently-accepted value. This lowering of ν'_1 is not unreasonable considering that the assignment leading to the higher value was made before the discovery of the strong Coriolis interaction in the low-lying bending vibrations [112, 110], and the recognition in the present work that levels involving these bending vibrations would always have anomalous K -structure. We note that, in Table XI of Ref. [11], the A constant of the 47195 cm^{-1} level (assigned there as $\nu'_1 + 2\nu'_3$) is given as 11.51 cm^{-1} ; with hindsight we suggest that this is lower than the “normal” value, and that this level is probably a bending level involving ν'_4 or ν'_6 .

3.4 Discussion

The identification of the 1^13^1 and 2^23^1 levels in the \tilde{A}^1A_u state of C_2H_2 allows us to derive values for the anharmonicity constants x'_{13} and x'_{22} and, even though the level ν'_1 itself has not been found, to estimate its frequency.

The constant x'_{22} is obtained at once from application of the vibrational energy formula

$$G(v'_2, v'_3) = \omega_2 \left(v'_2 + \frac{1}{2} \right) + \omega_3 \left(v'_3 + \frac{1}{2} \right) + x'_{22} \left(v'_2 + \frac{1}{2} \right)^2 + x'_{33} \left(v'_3 + \frac{1}{2} \right)^2 + x'_{23} \left(v'_2 + \frac{1}{2} \right) \left(v'_3 + \frac{1}{2} \right) \quad (3.1)$$

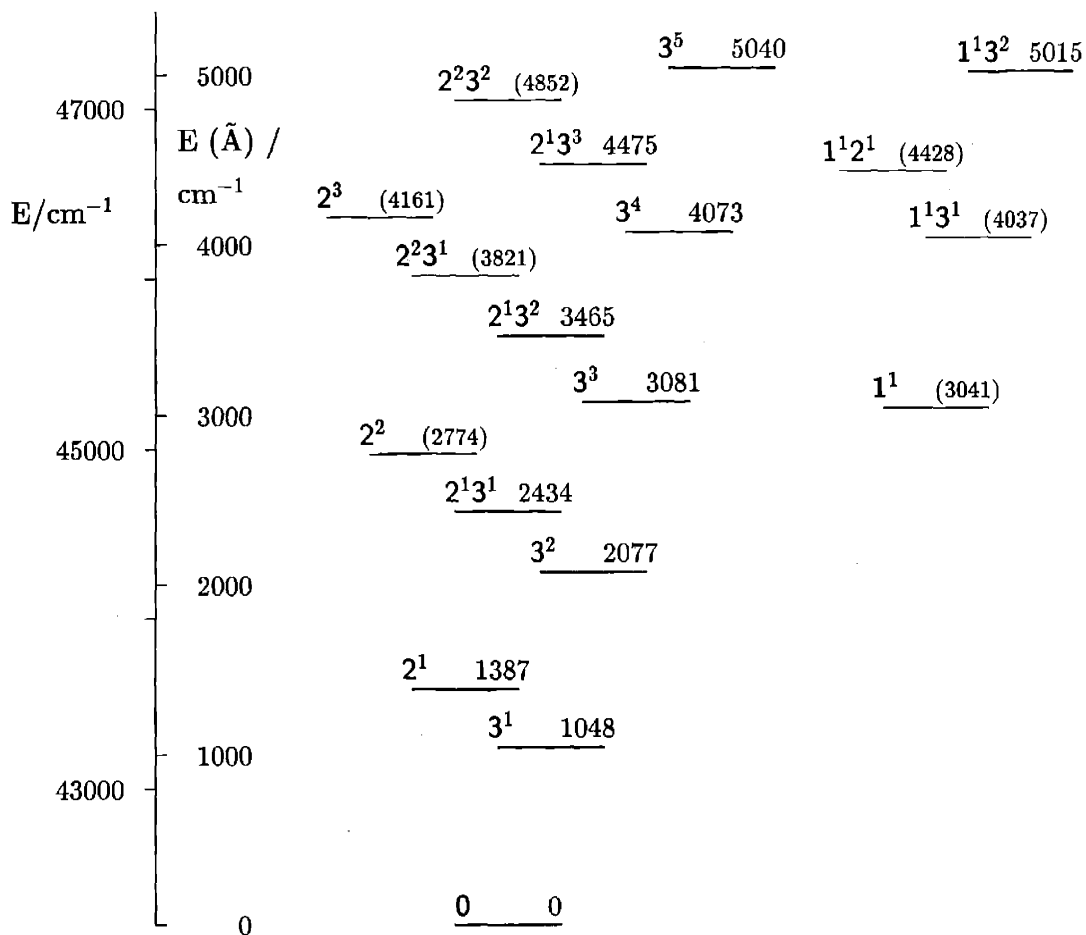


Figure 3-3: Vibrational manifold of the three a_g vibrations of the \tilde{A}^1A_u state of C_2H_2 , as observed in Refs. [114, 11] (thick lines), or estimated by us from their data assuming that the undetermined anharmonicity constants, x'_{ij} , are zero (thin lines; energies in parentheses). The new vibrational levels analyzed in this work lie at 3798 and 3917 cm^{-1} of vibrational energy within the \tilde{A}^1A_u state; they are therefore assigned as 2^23^1 and 1^13^1 , respectively. The latter assignment leads to a downward revision of the value of ν'_1 from 3040.6 cm^{-1} to 2880.5 cm^{-1} . A level lying at 4935 cm^{-1} is now assigned as 1^13^2 (see text).

to the observed levels with up to two quanta of ν'_2 and ν'_3 ; the derived value is

$$x'_{22} = -12.13\text{cm}^{-1}. \quad (3.2)$$

There are no previous experimental numbers against which to compare this value, since no levels with two quanta of ν'_2 have been observed prior to this work, but the *ab initio* calculations recently conducted by Stanton and coworkers are in exact agreement.

The position of the level 1^13^1 alone does not carry enough information to give both ν'_1 and x'_{13} , but using our calculated *ab initio* value, $x'_{13} = -6.7 \text{ cm}^{-1}$, together with the experimental value $x'_{33} = -8.95 \text{ cm}^{-1}$, we estimate that the level 1^13^2 , $K'_a = 0$ should lie near 47137.6 cm^{-1} . Now this region of the spectrum has been investigated at jet-cooled rotational resolution by Yamakita *et al.* [116]. They find a $K = 1-0$ subband, of about twice the strength of the $1_0^13_0^1$ band, with origin (defined as $T_0 + A$) at 47148.01 cm^{-1} . To compare the two energies, the upper state rotational constant A must be subtracted from the energy of the $K'_a = 1$ origin. Assuming that the level in question is 1^13^2 , for which we extrapolate that A should be 14.72 cm^{-1} (using data from Refs. [114, 11]), the $K'_a = 0$ origin is calculated to lie at 47133.29 cm^{-1} . The agreement seems good enough for us to be reasonably certain of the assignment because, as Fig. 3-1 shows, the nearest band with any significant intensity lies over 40 cm^{-1} away, at 47107.32 cm^{-1} . Working backwards from the 1^13^2 origin, we estimate the parameter x'_{13} to be 11.0 cm^{-1} ; the agreement with the *ab initio* calculation is not as good as with x'_{22} , but the experimental value includes the extrapolation of A .

Given this value of x'_{13} , we estimate the value of ν'_1 to be

$$\nu'_1 = 2880.5\text{cm}^{-1}, \quad (3.3)$$

with a probable error of the order of 2 cm^{-1} . This value is considerably lower than the previous value of 3040.6 cm^{-1} [11], but there are strong arguments to support it. The ν'_1 fundamental of the \tilde{A}^1A_u state has been observed directly in C_2D_2 [29], though not in C_2HD [2]. The reason appears to be that in the heavier isotopomer the vibra-

tional normal coordinates q_1 and q_3 are not purely CD stretching and *trans*-bending internal coordinates, but mixtures of the two; this has the result of transferring some of the Franck-Condon activity of ν'_3 to ν'_1 . Using the observed values of all the frequencies that had been observed in C_2H_2 , C_2HD and C_2D_2 , Tobiasson *et al.* [106] carried out a detailed normal mode analysis for the \tilde{A}^1A_u state. They found that it was impossible to get a set of force constants that successfully fitted the values of ν'_1 in both C_2H_2 and C_2D_2 simultaneously, and concluded that “the frequency for ν'_1 in C_2H_2 of 3040.6 cm^{-1} that Van Craen *et al.* extracted is too large.”

Further support comes from Stanton’s new *ab initio* calculations. These predict that the symmetric and antisymmetric CH stretching vibrations of C_2H_2 , \tilde{A}^1A_u , which are numbered ν'_1 and ν'_5 , should have frequencies of 2940 and 2914 cm^{-1} . These are to be compared to the experimental values of 2880 cm^{-1} (this work) and 2857 cm^{-1} [105]. It is seen that the *ab initio* calculations predict clearly that the two CH stretching vibrations of C_2H_2 should lie below 3000 cm^{-1} , with ν'_1 lying about 25 cm^{-1} above ν'_5 (as is observed).

With the new value of ν'_1 obtained in this work we are in a better position to assign the higher vibrational levels observed in the \tilde{A}^1A_u state of C_2H_2 . Already we can make definite vibrational assignments of the *ungerade* levels appearing in the infrared-ultraviolet double resonance spectra of C_2H_2 in the vibrational energy region of 3600–4800 cm^{-1} [117]; we expect that these will permit assignments of both *ungerade* and *gerade* levels at yet higher energies, which will give information on the dynamics of the *trans* \longleftrightarrow *cis* isomerization in the \tilde{A}^1A_u state.

Chapter 4

Observation of Collision-Induced Population Transfer in the $S_1 \bar{A}^1 A_u$ State of Acetylene

4.1 Introduction

Unexpected spectral patterns in the Dispersed Fluorescence (DF) spectra recorded of the molecule acetylene in its gas phase, are universally present in many independent studies. Although no such patterns were reported when Brus [4] and Stephenson *et al* [98] acquired the first acetylene DF spectra recorded at low resolution ($>200 \text{ cm}^{-1}$), they became visible in many recent DF experiments. When a photomultiplier and monochromator were employed into the DF study, Scherer *et al* launched DF to study an \bar{A} -state perturbation, and unambiguously visible was a strong quasi-continuous baseline (QCB) in the collected spectrum (Fig. 4 of [84]). With similar experimental setup, Yamanouchi *et al* recorded DF at $50\text{-}80 \text{ cm}^{-1}$ resolution, and quasi-continuous baseline features were also found (see figures in [118]). More recently, Solina *et al* recorded DF of the acetylene origin band [96], and the extra patterns have unmistakable transition intensities¹.

¹I doubt the reality of such observations in Jet-cooled DF, but both O'Brien and Jacobson claimed that they had been observed [73, 35] — this is worth precaution!

O'Brien [73] initiated a series of experiments to investigate these observations of QCB, and these experiments established that the baseline was a molecular feature, not an experimental artifact. The question is, does it belong to acetylene, or its impurities? Of particular interest is the widely varying amplitudes of the QCB in the DF spectra recorded via different \tilde{A} -state vibrational levels. Although the QCB is a subject of ongoing investigation, Jacobson [35] identified another unexpected pattern, which tends to lie close in internal energy to the normally expected fractionated bright states. Using a numerical pattern recognition algorithm [37, 10, 74], such extra patterns were identified and their intensities were measured quantitatively for the first time.

Moss and I carried out Stimulated Emission Pumping experiments which probed the acetylene S_0 state from 7,000 to 10,000 cm^{-1} . In those studies, no SEP transitions were observed that corresponded to any of the extra features in the DF spectra, despite the greater dynamic range of SEP than DF. The SEP studies confirm that the extra features do not arise from emission from the single rovibrational levels in the S_1 state that are initially populated by the laser in the DF studies. This chapter presents a series of DF studies performed to identify the collisional mechanism responsible for these previously unknown patterns.

4.2 Experimental

In this section we discuss the methodologies adopted to characterize the “extra patterns”. Dispersed Fluorescence being the crucial technique, we have examined many experimentally controllable parameters, including laser power study, exposure study, rotational-J study, gating study, pressure study, and rotational-K study via hotband excitation.

4.2.1 Dispersed Fluorescence

A Xenon-Chloride Excimer Laser (Lambda Physik LPX-210icc), running at 20-65 Hz, was used to pump a pressure-tuned dye laser (Coherent FL2002) operated with

Coumarin 440, 450, or 460 dye. The dye laser beam was frequency doubled in BBO to produce $750 \mu\text{J}$ of tunable, 215-240 nm, radiation with a spectral width of $\leq 0.05 \text{ cm}^{-1}$. The frequency doubled laser light was spatially separated from the residual fundamental by two 60° prisms. The residual fundamental laser beam was passed through a frequency-calibration cell containing $^{130}\text{Te}_2$, and the dye laser was scanned and locked onto the $^{12}\text{C}_2\text{H}_2$ $S_1 \leftarrow S_0$ rovibronic transition of interest.

The frequency doubled dye laser output was passed through a static gas cell charged with 0.04-5.0 Torr of acetylene. The fluorescence from the static gas cell was imaged onto a monochromator entrance slit. The emission was imaged by $f/5.8$ fused silica optics onto the entrance slit of a Jobin-Yvon HR 640 mm monochromator equipped with a ruled grating (1200 gr/mm, blazed for 500 nm), used in first order. The entrance slit on the monochromator is set to $100 \mu\text{m}$, which corresponding to a spectral resolution of 0.1 nm.

The dispersed fluorescence was then recorded on a Princeton Instruments Intensified Charge Coupled Device (ICCD), Model 1024-M059413, which has 256×700 active pixels. The number of laser shots recorded on the ICCD was on the order of $10^4 - 10^5$. In order to discriminate against spurious noise spikes caused by cosmic rays, the DF spectrum at any grating position was recorded twice. Since cosmic rays rarely repeat on the same pixel of the ICCD, comparison of the consecutive recordings allows removal of such artifacts.

Frequency calibration was achieved by recording, for each grating position, the emission from a series of wavelength calibration lamps. Iron, Krypton, Argon, Xenon, Mercury, and Neon calibration lamps were placed in the beam path immediately after recording the acetylene emission. This calibration methodology [73, 96] permits compensation for systematic errors in calibration, as well as the non-linearity that is inherent in the dispersion of the grating. The frequency calibration errors were estimated to be 5 cm^{-1} .

4.2.2 Power Study

By partially blocking the pump beam before it entered the amplifier dye cuvette, we adjusted the average power of the excitation beam from 120 μJ to 750 μJ . Since the oscillator strength of these transitions is on the order of 8×10^{-5} [32], we are far below from the saturation limit. The factor of six range of intensity results in no perceptible change in the relative intensities of the lines observed in the DF spectrum. This result rules out, as an explanation for the extra patterns, emission from some photofragment species (C_2H or C_2 , for example) created through a multi-photon absorption process.

4.2.3 Exposure Study

By adjusting the accumulation time for the ICCD controller, which in turn triggers the lasers, we changed the irradiation time from 1 sec to 10 sec. The 1 sec exposure was accumulated 300 times, while the 10 sec exposure was accumulated 30 times, in order to achieve good signal to noise ratios. The amplitudes of the extra patterns did not change as a function of the exposure time window. Therefore, it is unlikely that the extra patterns are due to emission from a stable molecule that is formed photochemically upon irradiation of acetylene at 225 nm.

4.2.4 Rotational-J Study

If the extra patterns manifest unexpected rotational transitions in emission due to either S_1 state b-axis Coriolis couplings or $S_1 \leftarrow S_0$ axis-switching transitions [44, 114], their intensity would scale as J^2 . We recorded DF from intermediate $J' = 1$ to $J' = 9$ rotational lines, which showed no increase in the amplitude of the extra features relative to the normal assignable features. The fact that the relative amplitude of the extra patterns is insensitive to the intermediate rotational state chosen, eliminates the possibility that the extra patterns are due to J-state-specific phenomena.

4.2.5 Gating Study

Quasi-Continuous Baseline

The fluorescence lifetime for any known bright state is estimated to be around 250 ns. As part of the effort to compare the upper state fluorescence lifetimes between transition terminated in the fractionated bright states and the quasi-continuous baseline, we gated the fluorescence with various time windows after the laser excitation pulse, and recorded DF spectral segments (Table 4.1). Although the charge coupled device is not optimized for observing time profiles, the difference of lifetimes is clearly manifested in Fig. 4-1. The intensity of the QCB relative to the FBS does vary as a function of the time delay relative to the entrance of the laser pulse into the sample cell. The intensity of the QCB emission varies with time differently than the emission to the sharp features, with the QCB emission dominant at later times. Particularly, in the DF segment recorded at 171-271 ns, where the fractional bright state signals have almost disappeared, the QCB features have same intensity as observed in the earlier segments. This indicates that the lifetime of the upper state QCB transitions is longer than the upper state of the fractional bright state fluorescence. Using the DF segment recorded at 171-271 ns to represent the QCB character, we can integrate the intensity of both features, and measure the fraction of “expected” fluorescence signal vs. the “unexpected”. In integration, only pixels no. 65-705 are taken into account to avoid image intensifier and edge effects. Such results are included in Table 4.1. This trial identifies the quasi-continuous baseline as arising from an “extra” feature, with a much longer lifetime (1 ms) than that of the normal bright state fluorescence decay (200 ns).

Unexpected Sharp Features

In addition to the quasi-continuous baseline feature, there are also sharp “extra” features, which can be extracted by XCC as independent patterns². In the gate position study of these local features, efforts are made to detect the fluorescence

²see the “Introduction” section

Detection Gate (ns)	Total Int.	FBS Int.	QCB Int.	QCB%
0-100	270,666,000	184,639,000	86,027,300	31.8%
100-200	184,184,000	98,156,600	86,027,300	46.7%
121-221	114,139,000	60,483,400	53,655,200	47.0%
150-250	86,597,800	38,682,300	47,915,500	55.3%
171-271	48,137,700	13,478,000	34,659,700	72.0%
200-300	29,208,700	1,415,100	27,793,600	95.1%
300-400	8,602,730	n/a	8,602,730	100%
400-500	1,920,420	n/a	1,920,420	100%
505-1505	852,005	n/a	852,005	100%

Table 4.1: Integrated intensity of “expected” fractionated bright state (FBS) fluorescence signals vs. the “unexpected” quasi-continuous baseline signal, measured for various time gates.

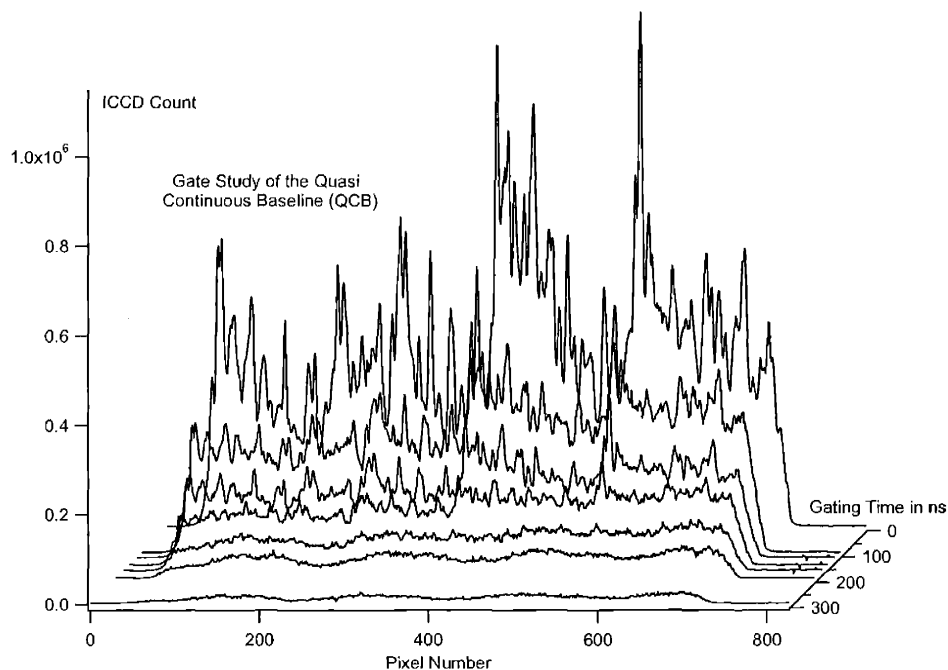


Figure 4-1: Gate study of the quasi continuous baseline. Each trace is recorded with a 100 ns gate.

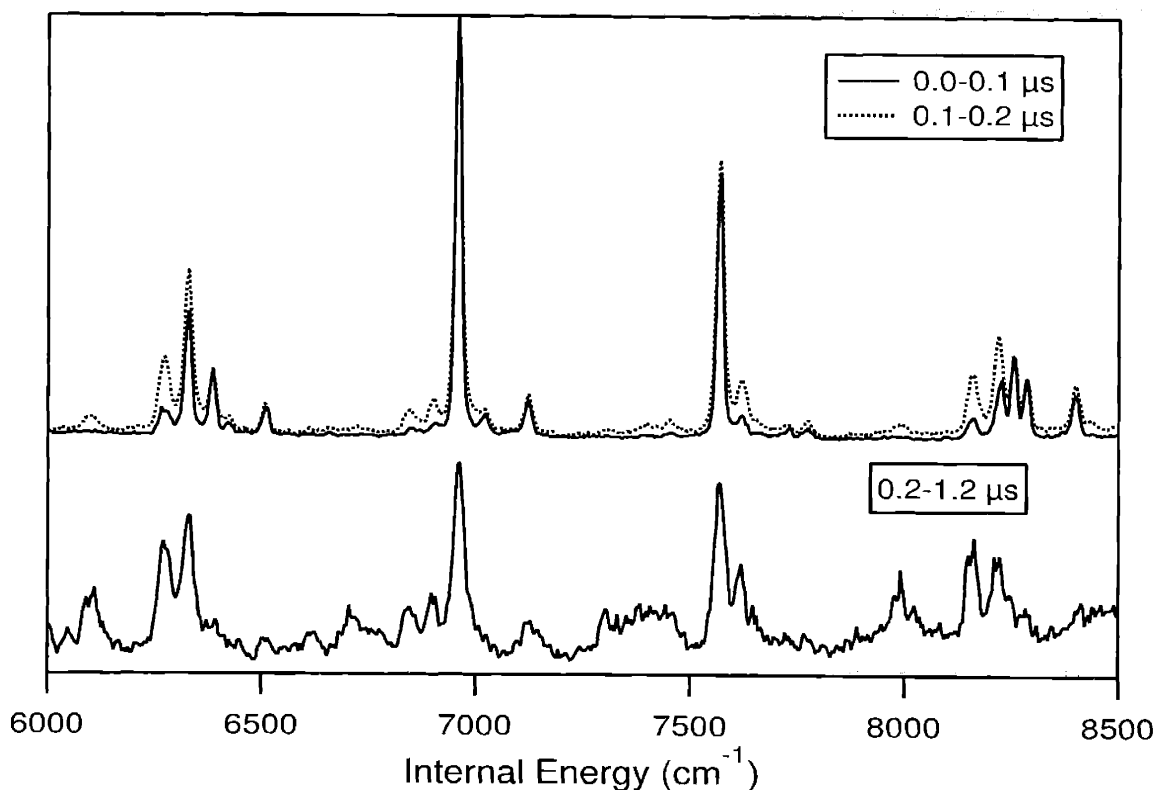


Figure 4-2: Dispersed Fluorescence resulting from pumping the Q(1) rotational line of the $2\nu'_3$ band at different time windows following the laser pulse. The intensities are normalized to the tallest peak. The peaks of the extra sharp features show intensity dependency which are different from those of the main fractionated bright state features.

decay rate of the upper state responsible for these sharp features.

In Fig. 4-2 are depicted a segment of a dispersed fluorescence spectrum recorded in two time windows via the Q(1) rotational line of the $2\nu'_3$ band. The amplitudes of the extra patterns have a different dependence upon the time window relative to that of the normal fractional bright state fluorescence, which is used to normalize the spectra acquired at different time windows. It is evident that the intensities of the unexpected patterns are relatively larger at later times. It appears that these extra sharp patterns do not arise directly from laser excitation, but from processes which follow the laser pulse. Collision-induced population is a candidate to explain such processes.

4.2.6 Pressure Study

The pressure study is performed exclusively for the extra sharp features. By observing the pressure dependence of their fluorescence intensities, the hypothesis that the extra sharp features are induced by collisional processes is confirmed.

Fig. 4-3 depicts the pressure study of the fluorescence spectrum excited via the Q(1) line of $2\nu'_3$. The ICCD acquisition system is gated with a fixed width of 200 ns immediately after the laser excitation pulse. Eight pressures were used in this study, 0.040, 0.080, 0.159, 0.247, 0.505, 1.018, 2.000, and 3.575 Torr, respectively. The pressure dependencies of several weak peaks in the dispersed fluorescence spectrum differ from those of the expected fractionated bright state characters. The pressure dependence of these extra sharp features suggests that both collisional energy transfer in C_2H_2 and new molecular species formed via collisions could play a role in their origin. From the internal energy separations of the extra features, it is found that the former hypothesis is more probable³, however, this assertion must be confirmed by further experimental evidence as follows.

4.2.7 Rotational-K Study

We have described the rotational-J study, which led us to believe that the sharp extra patterns do not arise from the laser-populated rotational state. Both the gate study and the pressure study raise the possibility of collisionally induced population transfer. In order to test whether this is due to a collisional process that changes the K'_a quantum number, a rotational-K study must be performed. The normal excitation is via a cold band, where the lower state is the ground state $(0,0,0,0^0,0^0)$ in the S^0 transition state, with $l''_{total} = 0$. This excitation scheme allows only transitions into $K'_a=1$ levels, due to the propensity rule, $K'_a - l'' = \pm 1$. The expectation in the rotational-K study is that if the sharp extra features are induced by K-changing collisions, by exciting levels with $K'_a \neq 1$, patterns will be seen in the DF spectrum at *exactly* the same frequencies as those excited via the normal $K'_a=1$ intermediate state,

³see the "Analysis" section

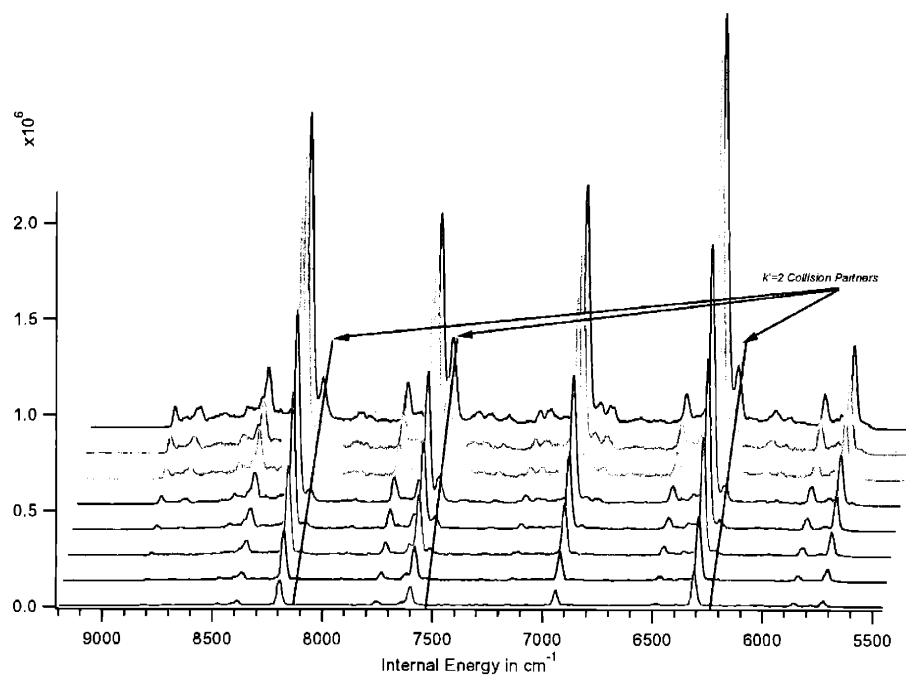


Figure 4-3: Pressure study of the sharp “extra” feature. There are a group of collisional partners whose unique ratio of increase in intensity with respect to pressure help identify them as the collisional induced $K'_a = 2$ structure.

yet the intensity patterns in those DF spectra would be almost the opposite as far as direct and collisionally induced features are concerned. That is, if we directly excite the state formerly collisionally populated from $K'_a=1$, the “extra” features would now become the “main” features, and *vice versa*. Excitation via a hotband, whose lower state satisfies $l''_{total} = 1$, will lead to $K'_a \neq 1$. Depicted in Fig. 4-4 are two DF spectral segments recorded via the Q(1) line of the $2\nu'_3$ cold band and hot band, respectively. The vibrational patterns match the signatures described above, and thus confirm that the sharp “extra” feature is induced by K'_a -changing collisional processes.

4.3 Analysis

As the interpreted intensities of the sharp extra features are more easily measured than the quasi-continuous baseline features, numerical analysis in this section only deals with the sharp features. We try to answer two questions, “What process do these extra features come from?” and “Can this process be theoretically modelled?”

4.3.1 Pattern Recognition

To identify the origin of the collision induced sharp extra patterns, it is helpful to separate them from the usual fractionated bright state patterns. The XCC [37, 10, 74] pattern recognition technique is adopted for this purpose. In doing so, no attempt is made to identify individual bright state fractionation patterns, but only to extract all of the extra features from the spectra.

The analysis is based on the pressure study, which has yielded the most complete quantitatively measurable data. The assumption underlying this approach is that the amplitudes of all of the extra patterns vary in the same way with pressure. Within the pressure study dataset, XCC identifies all of the fractionated bright state features as a single pattern, and all of the unexpected sharp features as a second pattern, as is depicted in Fig. 4-5, second and third panels, respectively.

The “main” features, as expected, are identified as fractionated bright state patterns. The spectral features extracted can be assigned as emission from a $K'_a = 1$

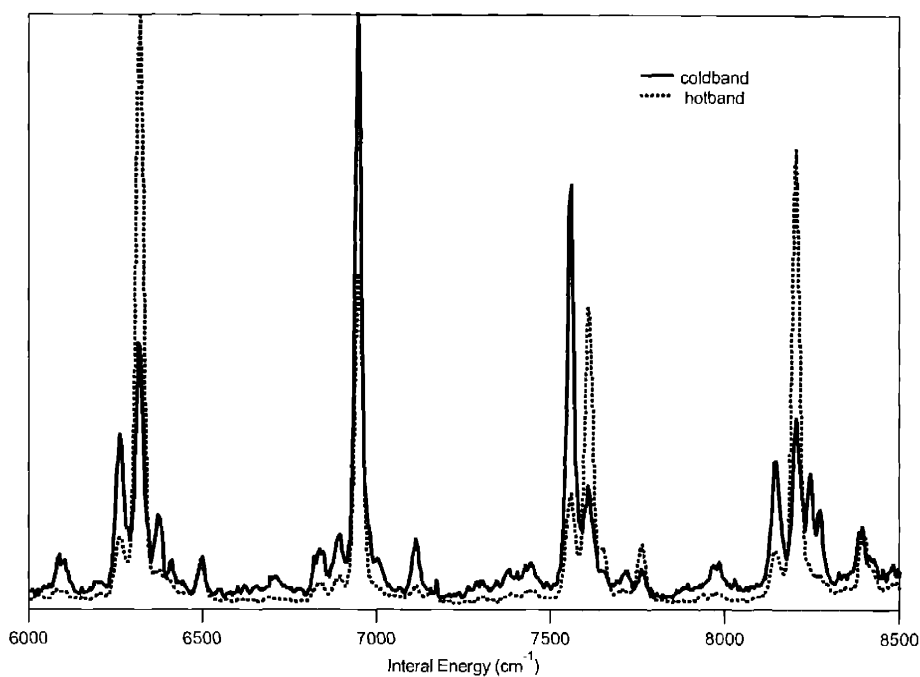


Figure 4-4: Excitation via the hot band $V_1^2 K_1^0$ results in DF spectral patterns distinctively different from those excited via cold band $V_0^2 K_0^1$. In the hot band DF, the patterns arising from $K'_a = 0$ (assignment shown in Fig. 4-5) acquire more intensity and become the “main” feature. The internal energies of the peaks between the two excitation schemes match exactly, with the $K'_a = 0$ peaks being the “extra” patterns in the cold band DF. This observation confirms that the sharp “extra” feature are induced by K'_a -changing collisional processes.

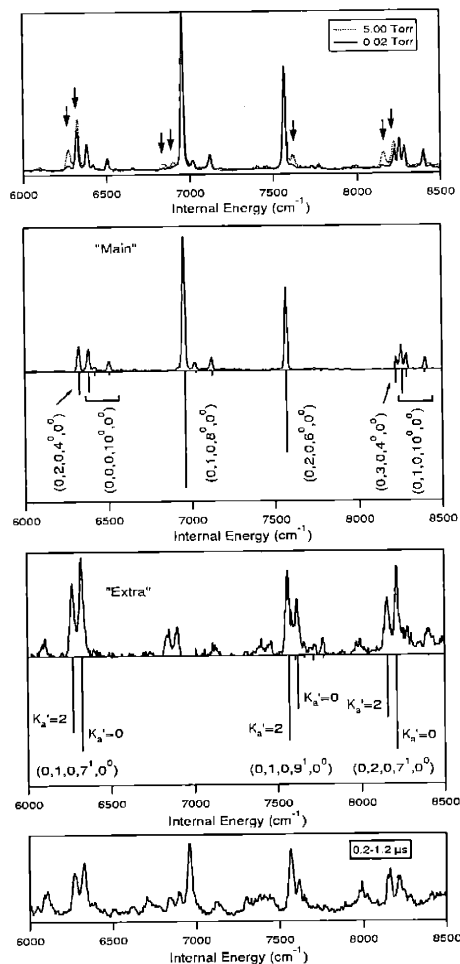


Figure 4-5: Top: Dispersed Fluorescence spectra recorded via the Q(1) rotational line of the $2\nu_3$ band, at various pressures. The intensity is normalized to that of the tallest peak. The arrows point to features whose intensities change differently relative to the “main” features as a function of pressure. Second: The “main” features from the top panel extracted by XCC are the expected bright state fractionation patterns from $K'_a = 1$ intermediate states. The $l''_4 = 0$ and $l''_4 = 2$ levels in the \tilde{X} state are not resolved. Third: The unexpected sharp “extra” features of the top panel, extracted by XCC. The most intense features in this pattern can be accounted for by emission from $K'_a = 0$ or $K'_a = 2$ intermediate states. The $l''_4 = 1$ and $l''_4 = 3$ lines are not resolved. Bottom: Dispersed fluorescence 200ns (expected bright state fluorescence lifetime) after the laser pulse, the similarity between this spectral segment and the “extra” patterns in the third panel indicate that the extra features are due to a prolonged process, confirming the hypothesis derived from the gate study of the local “extra” features.

intermediate state to $(0, v_2, 0, v_4^{0/2}, 0^0)$ bright states with even quanta in the trans bend mode, ν_4'' [27, 39, 31, 23]. Depicted in Fig. 4-5 are only the predicted $l_4'' = 0$ patterns, from which the $l_4'' = 2$ patterns were not resolved.

The sharp “extra” features generally appear as doublets with a spacing of 56 cm^{-1} . This energy is nearly equal to the splitting between the $K'_a=0$ and 2 manifolds of the $2\nu_3'$ vibrational level in the $^{12}\text{C}_2\text{H}_2 S_1$ state. It is established [43, 96, 35] that, by exciting the totally symmetric in-plane bending modes on the \tilde{A} state, only zero-order states of the form $(0, v_2, 0, v_4^l, 0^0)$ are bright in emission. Thus, $l_4'' = l_{total}''$, and if l_{total}'' is even, v_4 must also be even. Since the lower state from which the laser excites is the ground state, $(0, 0, 0, 0^0, 0^0)$ with $l_{total}'' = 0$, the propensity rule of $K'_a - l'' = \pm 1$ determines that only S_1 states of $K'_a=1$ can be excited. On the other hand, although thermal population at room temperature of $v_4'' \geq 1$ states is non-negligible, the hot band transition frequencies are separated by at least 600 cm^{-1} from the cold band transition adopted in the excitation scheme, and because of the dye laser’s spectral width of 0.05 cm^{-1} , the hot band is not directly excited, and thus the excitation photon exclusively populates the $(J'=1, K'_a=1)$ level. The only possibility by which $K'_a=0$ or 2 levels can be populated is through collisional redistribution from the $K'_a=1$ level.

Using an effective Hamiltonian model [35, 40], the hypothesis of K-collisional population transfer can be tested numerically against peak frequencies measured from the extracted patterns. According to the propensity rule, both $K'_a=0$ and 2 levels can emit to $l''=1$ levels; $K'_a=2$ levels can also emit to $l''=3$ levels. The emission from a pair of $K'_a=0$ and 2 levels to the same $l''=1$ level, are separated by $4A' \approx 56 \text{ cm}^{-1}$ due to the upper state term value difference, and thus can be resolved at the 14 cm^{-1} DF spectral resolution. Nine polyad positions predicted by the effective Hamiltonian model match the observed frequencies in both the extracted main feature pattern and the extra patterns, indicated by negative-going sticks in the middle two panels of Fig. 4-5. It is clear that the K'_a -changing collisions account for all of the most intense sharp unexpected features in the DF spectra.

4.4 Conclusion

We now understand that the unknown sharp features accompanying the well-characterized polyad structures are due to a collisional k -changing process. This has answered a long-term mystery which was first reported by O’Brien [73]. The SEP study reported in Chapter 7 was designed to answer the question about the origin of the DF “ghost” features, but did not identify any spectral features corresponding to these features. However, a carefully designed excitation scheme through the hot band has identified the mechanism.

Chapter 5

Franck-Condon Calculation in Lack of Good Potentials: *gerade* Bending Modes

5.1 Introduction

Given any spectrum, or any segments of a spectrum, there are three important classes of information that they contain:

1. *Frequency*: Frequency information is the most helpful diagnostic tool for uncovering the level structures of the molecule of interest. After Schawlow and Townes published their paper on the possibility of laser action in the infrared and visible region, ruby was soon discovered as the first lasing medium [62] in 1960. After that, the development in laser technology became closely correlated to developments in frequency measurement, and therefore, spectroscopy. Spectroscopists used Quantum Mechanics in the interpretation and understanding of frequency information contained in spectra. Commercially available spectrometers (*e.g.* FTIR, FT-NIR, FT-Raman, etc.), some of which measure to $< 0.0001 \text{ cm}^{-1}$ precision, lead to precise understanding of the lower internal energy region of small molecules in the gas phase. Obviously, as one goes to higher frequency,

the more difficult it is to understand the spectra.

2. *Intensity*: Intensity of any transition is a direct consequence of the level of resonance the molecules find with the excitation frequency. Quantum mechanically, time-dependent perturbation theory has proved the direct relationship between intensity and transition moment integrals, $\langle \Psi' | \mu | \Psi'' \rangle$. Thus, the quality of theoretical interpretation of the intensity information contained in any spectra, is simply determined by how accurately the scientists can calculate the wavefunction integrals.
3. *Line Shape*: Line shape is the functional form of the shape of peaks with frequency. Line width, the full-width-at-half-maximum of any peak in the spectrum, contains the most descriptive quantity in each lineshape. An ideal experiment would produce stick spectra as a representative of transitions between molecular energy levels. Line shapes are largely dependent on the experimental conditions under which particular spectra are recorded. Four major contributions to lineshapes are, *natural lineshape*, *collisional lineshape*, *Doppler lineshape* and *Saturation*. *Natural lineshape* is a consequence of the uncertainty principle. Because the transition lifetime is finite, The transition spans a range of frequencies. *Natural lineshape* is Lorentzian. *Collision-broadened lineshape* is also Lorentzian, but it reflects the shortening of the lifetimes of both upper and lower states due to collisions. The *Doppler lineshape* is due to Doppler effects, and its lineshape is Gaussian. When Lorentzian and Gaussian lineshapes are convoluted, the lineshape usually takes on a *Voigt* profile. Saturation of the transition may lead to more complicated lineshapes. To a large degree, lineshapes are very important to experimentalists, and are indispensable parts of any feasibility calculation upon design of a molecular spectroscopy experiment.

As far as the set of DF spectra from Acetylene and its isotopomers are concerned, the frequency information has been studied extensively [35, 74, 27, 39, 40, 38, 92, 93]. Results from the DF frequency analysis include:

1. a confirmation of the validity of the polyad model at the 7 cm^{-1} resolution of the DF spectra at internal energies up to at least $15,000\text{ cm}^{-1}$ [74],
2. the observation and interpretation of bending dynamics which is simpler at $15,000\text{ cm}^{-1}$ than $10,000\text{ cm}^{-1}$ [40],
3. construction and validation of a global effective Hamiltonian, \mathbf{H}^{eff} , up to $15,000\text{ cm}^{-1}$ of internal energy [39], which is also capable of predicting about intensity distributions within a polyad,
4. documentation of the anomalously slow Intramolecular Vibrational Redistribution for the CC stretching levels up to $15,000\text{ cm}^{-1}$ [39],
5. observation of a transition to local mode behavior in the acetylene bending system above $10,000\text{ cm}^{-1}$ – the *trans* and *cis* normal modes evolve into local bendings and counter-rotations as internal energy increases, [41],
6. generally slower Intramolecular Vibrational Redistribution (IVR) in $^{13}\text{C}_2\text{H}_2$, particularly with nonzero quanta of CC stretch excitation [92, 93].

Given all the results from the frequency analysis, there remain a number of unaddressed questions. Most of these questions can be answered by analysis of intensity. To name a few:

1. As frequency analysis successfully simulates the intra-polyad intensity distribution based on the assumption of a single bright state per polyad, what then is the inter-polyad intensity distribution? The ability to predict the relative intensities of entire polyads would enhance our understanding of the potential energy function used in the the effective Hamiltonian \mathbf{H}^{eff} .
2. Of the perturbations observed in the $3\nu'_3$ state of $^{12}\text{C}_2\text{H}_2$ Acetylene, does the DF spectrum recorded from the perturbed levels reveal unambiguous assignments of the perturbation? As a continuation of the former question, how would the Franck-Condon intensity profile of the \tilde{A} state *gerade* vibrational levels differ from that of the *ungerade* levels?

3. While the torsional frequency, ν'_4 , and the asymmetric bending frequency, ν'_6 , are nearly identical, would the Franck-Condon intensity profile provide diagnostic tools for determining the ν'_4 and ν'_6 mixing coefficients in the $n\nu'_{bend}$ polyads?
4. In C_2HD , where the single-bright-state-per-polyad assumption breaks down, the DF spectra are vastly more complicated (due to the fact that the nominal *cis* vibrational mode, or the dominant CH bend, now turns bright). How would the intensity information contained in these DF spectra aid in the ground state vibrational assignments?

It is obvious that the remaining questions can only be addressed by an accurate Franck-Condon calculation, which would account for the intensity information contained in the $^{12}C_2H_2$, $^{12}C_2H_2$, C_2HD , and in the future, $^{12}C_2D_2$ dispersed fluorescence spectra.

5.2 Overview

The calculation of Franck-Condon factors for polyatomic molecules has a long history. Among recent publications, Vaccaro and coworkers [30, 71, 70, 69] have published a series of papers on the FC calculation for S_2O . Watson [113] has published an FC calculation for the acetylene $\tilde{A} - \tilde{X}$ bend system. Guo and coworkers [115, 7] have calculated vibrational energy levels of acetylene and are modeling relative intensities assembled in the DF spectrum as well.

Why is the intensity calculation of acetylene so interesting to theoreticians and experimentalists alike? What is the major difficulty in the intensity calculation for acetylene?

The practical difficulties in performing the Franck-Condon calculation in acetylene molecule include:

1. Experimentally, DF spectra have been recorded up to $18,000\text{ cm}^{-1}$, which is above the isomerization barrier between the linear and vinylidene isomers. This implies that the experimentally recorded data is accessing a very anharmonic

- part of the electronic potential. Traditional harmonic force field and normal mode representations are not applicable in this barrier region.
2. No experiments directly measure wavefunctions. In the course of calculating wavefunction overlaps, it is especially difficult to determine whether certain wavefunctions have been miscalculated due to the lack of experimental backup. Intensity, and therefore Franck-Condon factor, provides the only “calibration” in determine the quality of the wavefunction calculations. However, it is an indirect “calibration” in that although one can be certain of a wavefunction miscalculation from a mismatch of the calculated and observed intensities; even if there is a perfect match, no conclusions can be drawn as to how accurate the wavefunctions have been obtained.
 3. Although *ab initio* calculations can calculate frequencies well up to satisfactory precision, wavefunction calculation proves to be a much more difficult task for *ab initio* calculations. Relatively easy-to-perform Semi-classical calculations are able to calculate the wavefunctions qualitatively, they too lack the capability in reproducing wavefunctions to a quantitatively satisfying precision.
 4. Experimental intensities will help to refine the potentials. However, due to the lack of knowledge and description of the multidimensional potential up to 18,000 cm^{-1} , calculated wavefunctions up to that energy range runs short of accuracy to reproduce the experimentally acquired intensity profiles.
 5. The equilibrium geometry of the ground electronic state of acetylene is linear and has seven vibrational dimensions. Among these, the *trans* bending mode and *cis* bending mode are both doubly degenerate. In contrast, in the first excited singlet state of acetylene, the \tilde{A} state, or the S_1 state, has the trans bend equilibrium geometry, which leads to six, non-degenerate vibrational dimensions. The mismatched numbers of dimensions is a source of difficulty for the calculations.
 6. Although Franck-Condon calculations for diatomic molecules are one dimen-

sional, it is unlikely that a polyatomic molecule with fairly dissimilar geometrical configuration, in its upper and lower electronic states such as acetylene, would possess such a convenience for theoreticians. That is, no apparent normal modes from the upper and lower state could be incorporated into the same dimension.

7. Despite the experimental observation that, at 7 cm^{-1} resolution, no sign of polyad breakdown has been noticed up to $18,000\text{ cm}^{-1}$, it is my belief that the DF spectra have not directly sampled the isomerization pathway. Along the isomerization pathway, there will be extremely strong diagonal and off-diagonal anharmonicity, as well as numerous perturbations between states approximately localized in the acetylene and vinylidene wells (tunneling).
8. The transition moment will be a strong function of the nuclear geometry, especially in the large-amplitude bending coordinates. To my best knowledge, there is no precise functional form of the global transition moment available for acetylene as of present.

I am not claiming that the method described in this chapter is the only approach to solve the above difficulties. However, it provides one possible solution. My goal is to simply work with the expected difficulties, and find the best possible approach within our limits. As a first attempt, my expectation is to obtain a qualitatively correct Franck-Condon profile, and as better knowledge of the acetylene potential becomes available, to incorporate those into the calculation in the future. The sketch of my approach contains the following methods:

1. We use the local mode basis in place of the traditional, normal mode basis set to describe the wavefunctions. The goal of doing so is to reconcile the inherently different definitions of normal mode coordinates in the upper and lower electronic states. A byproduct of the local mode basis set is the evenly matched numbers of dimensions used to describe the vibrational wavefunctions. However, the indispensable feature needed to generate the local mode wavefunctions is a local-mode potential along the bending coordinates.

2. To obtain a local mode potential, we take advantage of a local mode based effective Hamiltonian which accounts well for the frequency information observed in our DF spectral data sets. In addition, the diagonal part of the potential along the local bending coordinates embedded in this effective Hamiltonian would then be obtained from a semiclassical RKR-like algorithm to obtain the effective local bending potential.
3. The kinetic energy part of the local bending effective Hamiltonian uses a semi-rigid bender assumption which will be described later in this chapter. Once we have the kinetic energy part of the Hamiltonian and the effective potential, solving the Schrodinger equation along the local mode direction would yields the local mode wavefunctions.
4. The description above is mainly used for the bending modes in the ground electronic state. A much simpler method is used to generate the wavefunctions for the stretching modes in the ground state, as well as all the vibrational modes in the first excited state. Since the number of quanta in the CC stretch and symmetric bending mode from which the DF spectrum is recorded is relatively low, we use the harmonic force field published by Crim and coworkers [106]. Because the maximum excitation energy in the \tilde{A} state sampled in the DF spectra is 4000 cm^{-1} , a harmonic representation for the \tilde{A} state vibration is expected to be sufficiently accurate.
5. Once the stretching and bending wavefunctions from both the upper and lower electronic states are computed, the Franck-Condon overlap integrals in this representation are calculated. The final step is to express the eigenstates in terms of the local mode basis set for both the upper and lower electronic states. The Franck-Condon overlap between the eigenstates can then be obtained as a linear combination of the local mode Franck-Condon overlaps.

This chapter describes the detailed approach to treat the local bending overlaps, as well as the resulting eigenstate Franck-Condon factors and their comparison to

Classical Method	Our Method
Based on normal mode/harmonic oscillator approximation	Curvilinear, anharmonic local modes
Difficult to incorporate anharmonicity	Same set of coordinates for both states
Cannot do a good job at high energies	Use normal \leftrightarrow local transformation for normal mode Franck-Condon factors
Technical difficulties associated with linear \leftrightarrow nonlinear transitions	High energy is built in the wavefunctions

Table 5.1: A comparison between traditional Franck-Condon calculations and our method of Semi-Classical RKR-inversion.

experimentally recorded intensities. This part is treated as a stand alone chapter, because it is my belief that this method is innovative, especially lacking an accurate, *ab initio* electronic potential. Despite the above sketch of the algorithm, there are several minor details awaiting solution. For example, how does one map the vibrational angular momentum in the ground electronic state to K-rotation on the upper state? What is a good functional form for the transition dipole moment, μ ? In the following portions of this chapter, we intend to address these questions, as details of the algorithms are presented. To summarize, Table 5.1 lists some distinctive features of our method compared to traditional Franck-Condon calculations.

5.3 Algorithm

5.3.1 RKR-like Semiclassical Inversion

Matthew Jacobson [35] has constructed a local mode Hamiltonian, \mathbf{H}^{eff} , that fits the acetylene dispersed fluorescence data set up to $15,000 \text{ cm}^{-1}$. It is not my intention to describe the Jacobson Hamiltonian in detail other than to quote four crucial parameters from his fit, which is required to perform the RKR-like inversion to obtain the one-dimensional effective local bending potential. These parameters, w , x , y and g describe the diagonal portion of the local bending Hamiltonian, with the cubic polynomial expansion form of $\omega v + xv^2 + yv^3 + gl^2$, where v is the local bending quantum number, and l is the vibrational angular momentum quantum number.

The eigenstates of this diagonal portion of the local bending potential are essentially the “bright” states in the local mode representation. From the local mode Hamiltonian fit to the DF dataset of acetylene, $\omega=668.000(34)$ cm^{-1} , $x=-1.688(13)$ cm^{-1} , $y=0.00585(72)$ cm^{-1} and $g=5.0307(326)$ cm^{-1} with the numbers in parentheses being 2σ uncertainties in the last digits.

As is true for most semi-empirical models, the RKR-inversion algorithm provides a computationally simple scheme to describe the large-amplitude vibrational dynamics of small molecules. The RKR inversion does not have the disadvantages of some common semi-empirical approaches, such as the spectroscopic effective Hamiltonian, which has been shown to encounter serious deficiency above or near the energy of a saddle point [36]. However, the RKR-inversion algorithm has its own limitations. Because RKR is based on the JWKB quantization integral, where the curvature of the potential surface is assumed to be a slowly varying quantity, areas of the true local bending potential near the isomerization saddle point *do not* belong to this description. Furthermore, when internal energy goes up to the bottom of the vinylidene well, the potential possesses multiple turning points, RKR would not be capable of treating the potential. Therefore, above a certain CCH bond angle, RKR-inversion loses its capability to derive the potential from vibrational data. Nevertheless, before the bending amplitude exceeds this critical bond angle, the potential should be trustworthy. For the application to acetylene, we choose this angle to be around 1.1 *rad*, which corresponds to $n_{localbend} < 22$ internal energy region.

The RKR (Rydberg-Klein-Rees) method [82, 83, 50, 77], is usually only applied to diatomic molecules. It derives, from spectroscopic data, the difference between the two classical one-dimensional turning points as well as the difference between the reciprocals of these two turning points. The difference between the two turning points depends only upon the vibrational energies, whereas the difference between the reciprocals of the two turning points is dependent on both the vibrational energies and the rotational constants, B . I am grateful to Professor Robert J. Le Roy from University of Waterloo, who distributes free programs using the RKR algorithm. Most recent publications by Le Roy and coworkers using RKR is performed on the

potential surface for Na_2 in the $1^3\Sigma_g^-$ State [60, 61]. However, for polyatomic potentials, calculating the difference between the reciprocals of the two turning points is not possible, because not only the molecular geometry but also the Coriolis effects contribute substantially to the effective rotational constants. However, Ratner and coworkers [79] have demonstrated that inversion of spectroscopic data to obtain a potential energy surface can be conducted by a SCF method. Furthermore, they have also successfully applied RKR to two-dimensional polyatomic surfaces of the form $W(q_1, q_2) = V_1(q_1) + V_2(q_2) + V_{12}(q_1, q_2)$ [80]. However, there are distinctive differences between the Ratner's method and ours.

We only employ the first of the two equations in the RKR method, i.e., calculating the difference between the two turning points. This is normally insufficient to determine the potential, because we are attempting to obtain the locations of two turning points by one equation. However, the local bending potential of the acetylene molecule is symmetric, and $x_1 = -x_2$, with x_1 and x_2 being the two classical turning points. Therefore, in this case, it becomes feasible to only use one RKR equation to obtain the effective local bending potential.

In the case of the total vibrational angular momentum quantum number $l_{tot} = l_A + l_B = 0$ (notice that the local bending vibrational quantum number l_A or l_B may not be zero themselves), the adiabatic local bending Hamiltonian has the form

$$\hat{H}^{bend} = f(\gamma)\hat{l}^2 + V^{eff}(\gamma) \quad (5.1)$$

$$= -\hbar^2 f(\gamma) \frac{d^2}{d\gamma^2} + V^{eff}(\gamma), \quad (5.2)$$

where l specify either local bend vibrational angular momentum, l_A or l_B , V^{eff} is the effective bending potential, and $f(\gamma)$ is the kinetic energy factor, determined by

$$f(\gamma) = \langle \Psi_0(\gamma) | \left[\frac{1}{2\mu_r r^2} + \frac{1}{2\mu_R R^2} \right] | \Psi_0(\gamma) \rangle, \quad (5.3)$$

We can then write down the RKR-like inversion equation as

$$\int_{-x(U)}^{x(U)} \frac{1}{\sqrt{f(\gamma)}} d\gamma = \int_{-\frac{1}{2}}^{v(U)} \frac{1}{\sqrt{U - E(v)}} dv, \quad (5.4)$$

where $x(U)$ is the classical turning point, U is a given vibrational energy, and $E(v)$ is the internal energy of the “bright” local mode vibrational levels determined by fitting the local mode effective Hamiltonian to the DF dataset.

For the factor $f(\gamma)$ in the kinetic energy term of the bending Hamiltonian, r specifies the distance of the hydrogen nucleus from the center of the CC bond (Jacobi length), and R is the Jacobi CC bond length. γ is the Jacobi bend angle for the Hydrogen nucleus, which uses the center of the CC bond as the origin, and is the angle between the position of the Hydrogen nucleus and the CC bond. Among them, r and R are actually length operators. However, we can use the semi-rigid bender approximation, which would greatly simplify the way the kinetic energy operator matrix elements are calculated. The semi-rigid approximation assumes that r and R have parametric dependence upon the Jacobi angle, γ , along the isomerization pathway. Therefore, Eq. (5.3) can be simplified as

$$f(\gamma) = \frac{1}{2\mu_r r(\gamma)^2} + \frac{1}{2\mu_R R(\gamma)^2}, \quad (5.5)$$

Although the Jacobi angle is frequently used in calculations, as it reasonably connects the Hydrogen from one end of the CC bond to the other, it is my belief that for small amplitude bending motions along the isomerization pathway, the CH bond length hardly changes. Therefore, I prefer to use the CCH bond angle to substitute for the Jacobi angle, γ , to describe the parametric dependence of r and R upon the bend. The definitions of bond angle and Jacobi angle are compared in Figure 5-1. The advantage of substituting the bond angle for the Jacobi angle is that along the local bending coordinate in the isomerization pathway, before the Hydrogen bends to above its closer carbon nucleus, $\frac{1}{2}\pi \leq \alpha \leq \frac{3}{2}\pi$, the CH bond length does not change appreciably. However, if we describe this bending in terms of the Jacobi angle, it necessarily involves a large change in the CH bond length. In short, in the bond angle representation, because there is less parametric dependence of the bond length

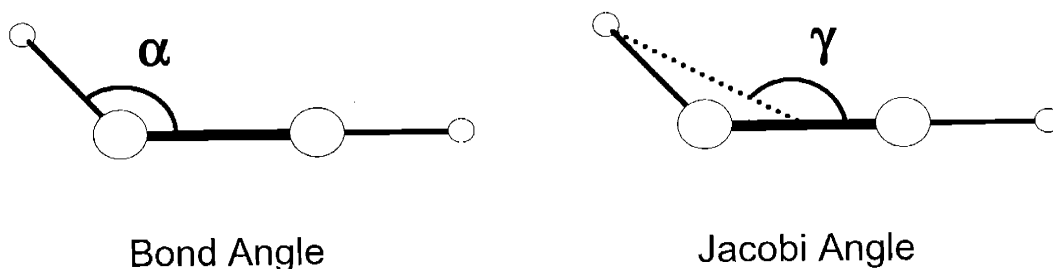


Figure 5-1: Illustration of the definitions of the bond angle coordinate, α , and the Jacobi angle, γ . While the Jacobi angle facilitates calculations, as it reasonably describes the motion of the Hydrogen as it moves from one end of the CC bond to the other, the bond-angle representation is more realistic for small or medium amplitude bending motions (*e.g.* $\frac{1}{2}\pi \leq \alpha \leq \frac{3}{2}\pi$).

on bond angle, the semi-rigid bender model will be accurate.

By adopting the CCH bond angle, α , we have switched the basis to curvilinear local mode. Simple trigonometric relationships can be used to derive the $\alpha \longleftrightarrow \gamma$ conversions,

$$\sin^2 \gamma = \frac{r_{CH}^2 \sin^2 \alpha}{r_{CH}^2 + \frac{r_{CC}^2}{4} - r_{CH}r_{CC} \cos \alpha} \quad (5.6)$$

Combining Eqs. (5.5) and (5.6), we obtain the parametric dependence of the kinetic energy factor, f , upon the bond angle, α :

$$f(\alpha) = \frac{1}{2\mu_r r(\alpha)^2} + \frac{1}{2\mu_R R(\alpha)^2}, \quad (5.7)$$

In this way, the kinetic and potential energy parts for the 1D effective bending Hamiltonian are obtained (notice that the potential part of the Hamiltonian is still expressed in the Jacobi angle). Compared with the method of calculating and fitting the global potential energy surface, our approach of considering only a small number of points along the minimum energy isomerization pathway is computationally much less demanding and practically sufficient to calculate the changes in bond lengths with bond angle. Our molecule tells us about a specific cut through the potential surface,

a slice along the isomerization pathway. We use RKR to invert the spectrum to this cut. As we believe that most anharmonicity occurs at the isomerization pathway, we use more standard harmonic or morse oscillator approximations for other modes.

Figure 5-2 displays a comparison between the local bending potential derived for our RKR inversion of DF data and the cut along the isomerization pathway on the Halonen-Child-Carter surface. The top panel depicts the dependence of the bending potential energy on the CCH bending angle along the isomerization pathway, and the bottom panel depicts the dependence on the CC bond length. In both cases, the potential obtained by the semi-classical RKR-inversion resembles the Halonen-Child-Carter potential to $< 5\%$. The consistency confirms that our method is legitimate to the largest degree.

For the purpose of calculating Hamiltonian matrix elements, we use a spherical harmonics basis set, and express the local bending potential as a cosine Fourier series. In this way, the matrix elements of both the kinetic and potential parts of the Hamiltonian are easily computed analytically using the Wigner-Eckart theorem [55]. Therefore, the obtained eigenstates are also expressed in a spherical harmonics basis set.

For a simple illustration of the \widetilde{X} state local bending wavefunctions obtained with the semi-classical RKR-like inversion, we plot a subset of the wavefunctions, the $l_L = 0$ wavefunctions in the left panel of Figure 5-3.

5.3.2 Local \leftrightarrow Normal Conversion

At low internal energy, the eigenstates resemble normal mode basis states. Therefore, there are two ways to compare the FC factors calculated in the local mode basis set with the experimentally observed FC factors. One way is by using the local mode effective Hamiltonian, expressing the eigenstates in terms of the local mode basis states, and directly applying the local mode FC factors to the comparison. This implementation is still being developed in collaboration with Matthew Jacobson. The other way is by converting the local mode basis states into normal mode basis states, obtain the normal mode bright state intensity, and then use the normal mode effective

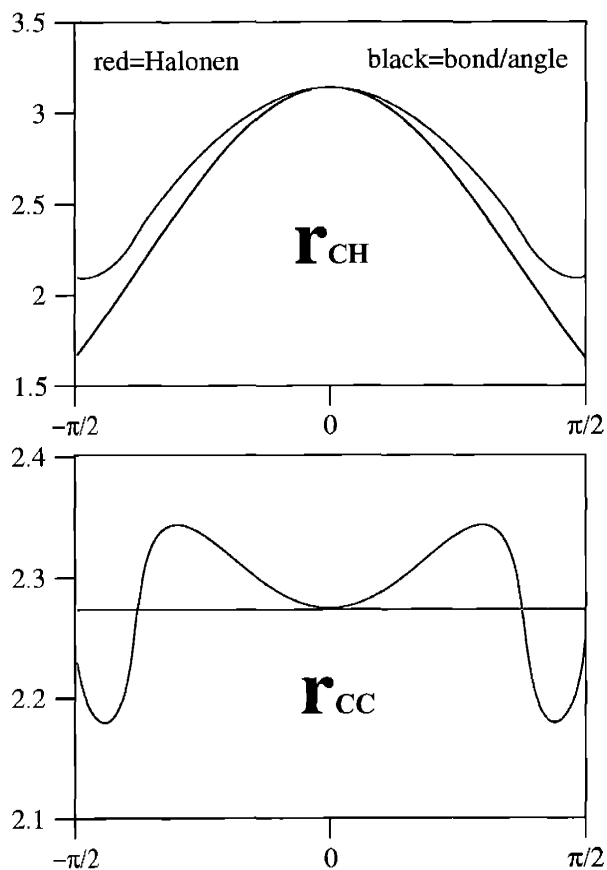


Figure 5-2: Comparison between the local bending potential and the cut along the isomerization pathway on the Halonen-Child-Carter surface. The top panel depicts the dependence of the rotational energy on the CCH bending angle along the isomerization pathway, and the bottom panel depicts the dependence on the CC bond length. In both cases, the potential obtained by the semi-classical RKR-inversion resembles the Halonen-Child-Carter potential to within 5% difference. In the course of RKR, we assume that the CC bond length is independent of the CCH bending angle.

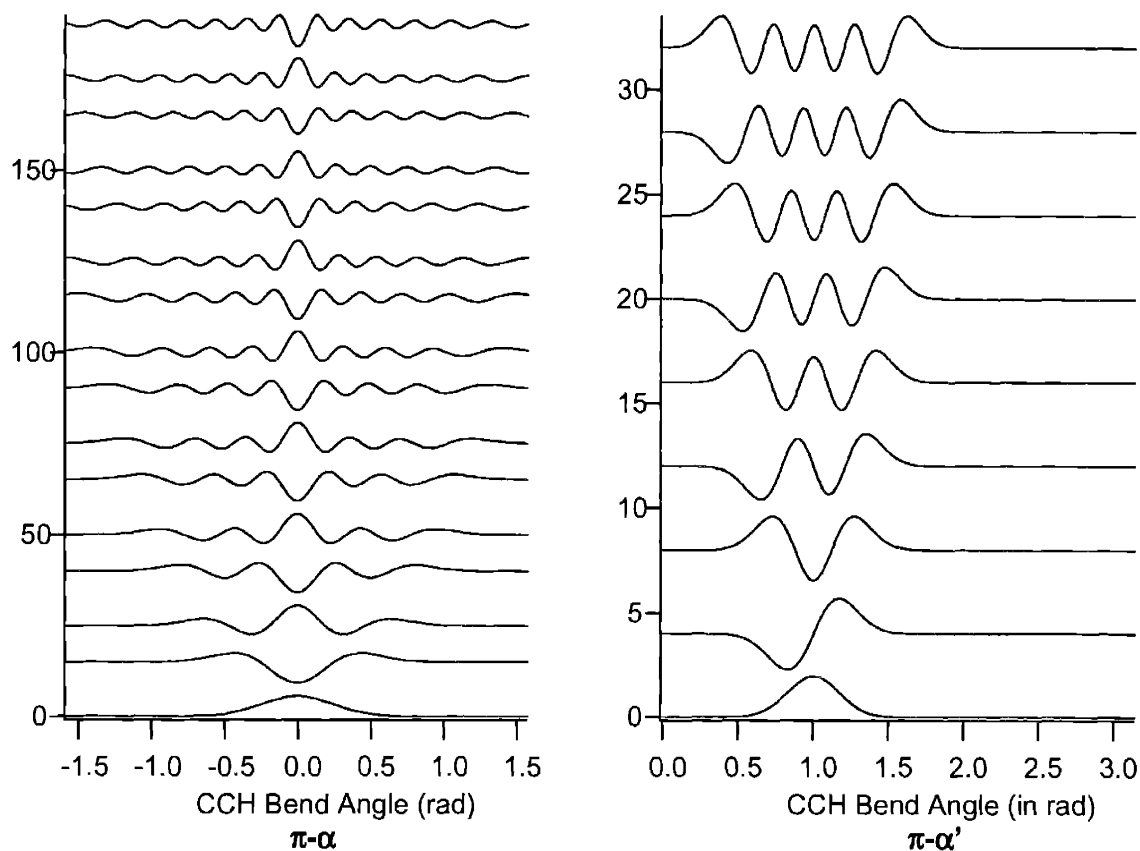


Figure 5-3: Left: \tilde{X} state $l_L = 0$ local bending wavefunctions obtained from RKR inversion. As expected for $l_L = 0$ levels, only the even quanta levels are plotted. Right: The local bending wavefunctions plotted for the \tilde{A} state. These wavefunctions are obtained using the \tilde{A} state force constants from Crim *et al.* Notice that the equilibrium geometry on the \tilde{A} state is not linear, but rather at a *trans* bending angle of 1 *rad*.

Hamiltonian to model the intensity distribution within every polyad. The local \leftrightarrow normal conversion can be accomplished by first recognizing that the vibrationless level is the same in both representations:

$$|0^0, 0^0\rangle_N = |0^0, 0^0\rangle_L \quad (5.8)$$

Applying the 2D harmonic ladder operators as defined by Cohen-Tannoudji *et al.* [9], we expand the normal mode bright states in the local mode basis set on the \widetilde{X} state:

$$|v_4^0, 0^0\rangle_N = (\hat{a}_{4d}^\dagger)^{\frac{v_4}{2}} (\hat{a}_{4g}^\dagger)^{\frac{v_4}{2}} |0^0, 0^0\rangle_N \quad (5.9)$$

$$= (\hat{a}_{4d}^\dagger)^{\frac{v_4}{2}} (\hat{a}_{4g}^\dagger)^{\frac{v_4}{2}} |0^0, 0^0\rangle_L \quad (5.10)$$

$$= \frac{1}{2^{\frac{v_4}{2}}} (\hat{a}_{Ad}^\dagger - \hat{a}_{Bd}^\dagger)^{\frac{v_4}{2}} (\hat{a}_{Ag}^\dagger - \hat{a}_{Bg}^\dagger)^{\frac{v_4}{2}} |0^0, 0^0\rangle_L \quad (5.11)$$

Table 5.2 gives the expansion for the $(0,0,0,10^0,0^0)$ bright state in the local mode basis, using the ladder operator method described above.

There is, however, a limitation of the suitability for applying this expansion method with the ladder operators. The ladder operators, \hat{a}_d^\dagger and \hat{a}_g^\dagger , are appropriate for a 2D Harmonic Oscillator potential force field. The ground state potential above 8,000 cm^{-1} of internal energy, starts to be anharmonic. Thus, the local \leftrightarrow normal conversion method is expected to be only good to that energy range. Direct application of the local mode effective Hamiltonian to the conversion between the eigenstates and the local mode basis states, on the other hand, should be good to as far as the local bend Hamiltonian fits the DF dataset.

5.3.3 Treatment of Vibrational Angular Momentum

As previously mentioned, in this chapter I will only describe the calculation for the bending wavefunctions. FC factors for stretching modes, as well as a global FC calculation for all the modes, is described in the next chapter.

v_A	l_A	v_B	l_B	<i>Expansion</i>
0	0	10	0	0.031250
1	-1	9	1	0.069877
1	1	9	-1	0.069877
2	-2	8	2	0.098821
2	0	8	0	0.156250
2	2	8	-2	0.098821
3	-3	7	3	0.098821
3	-1	7	1	0.220971
3	1	7	-1	0.220971
3	3	7	-3	0.098821
4	-4	6	4	0.069877
4	-2	6	2	0.220971
4	0	6	0	0.312500
4	2	6	-2	0.220971
4	4	6	-4	0.069877
5	-5	5	5	0.031250
5	-3	5	3	0.156250
5	-1	5	1	0.312500
5	1	5	-1	0.312500
5	3	5	-3	0.156250
5	5	5	-5	0.031250
6	-4	4	4	0.069877
6	-2	4	2	0.220971
6	0	4	0	0.312500
6	2	4	-2	0.220971
6	4	4	-4	0.069877
7	-3	3	3	0.098821
7	-1	3	1	0.220971
7	1	3	-1	0.220971
7	3	3	-3	0.098821
8	-2	2	2	0.098821
8	0	2	0	0.156250
8	2	2	-2	0.098821
9	-1	1	1	0.069877
9	1	1	-1	0.069877
10	0	0	0	0.031250

Table 5.2: Expansion for the $(0,0,0,10^0,0^0)$ bright state into local modes. We use A and B to symbolize two different CCH bending motions. The listed values given are expansion coefficients.

In considering the bending coordinates, solutions must be provided for two problems. Namely, the treatment of vibrational angular momentum in the \widetilde{X} state, and the mismatched numbers of vibrational degrees of freedom between the \widetilde{A} state and the \widetilde{X} state.

We label the two CH bonds as A and B , the CCH bond angle as γ , and the azimuthal angle as ϕ . The \widetilde{X} state bending wavefunctions (in local mode representation) can be written as:

$$\Psi_A(v_A; \alpha_A) \psi_A(l_A; \phi_A) \Psi_B(v_B; \alpha_B) \psi_B(l_B; \phi_B), \quad (5.12)$$

while the \widetilde{A} state bending wavefunctions (in local mode representation) can be written as:

$$\Psi'_A(v'_A; \alpha'_A) \Psi'_B(v'_B; \alpha'_B) \psi'_{tot}(K_a; \phi'_A + \phi'_B) \psi'_{tor}(\phi'_A - \phi'_B). \quad (5.13)$$

These two equations suggest a symmetrization of ϕ_A and ϕ_B on the \widetilde{X} state:

$$\Psi_A(v_A; \alpha_A) \Psi_B(v_B; \alpha_B) \psi_{tot}(\phi_A + \phi_B) \psi_{cnt.rot.}(\phi_A - \phi_B). \quad (5.14)$$

With the above established consistency in the dimensionality for the two electronic states, the transition moment overlap between these wavefunctions can be factored into four one-dimensional integrals:

$$\langle \Psi'_A(v'_A; \alpha'_A) | \mu | \Psi_A(v_A; \alpha_A) \rangle \quad (5.15)$$

$$\langle \Psi'_B(v'_B; \alpha'_B) | \mu | \Psi_B(v_B; \alpha_B) \rangle \quad (5.16)$$

$$\langle \psi'_{tot}(K_a; \phi'_A + \phi'_B) | \mu | \psi_{tot}(\phi_A + \phi_B) \rangle \quad (5.17)$$

$$\langle \psi'_{tor}(\phi'_A - \phi'_B) | \mu | \psi_{cnt.rot.}(\phi_A - \phi_B) \rangle \quad (5.18)$$

Among these matrix elements, 5.15 and 5.16 are one-dimensional, local mode bending wavefunction overlap integrals, 5.18 is the overlap between the torsional

wavefunction in the \tilde{A} state and the counter-rotating state in the \tilde{X} state, while 5.17 leads to the total angular momentum selection rule (when we consider only transitions of the $(K' = 1) \leftarrow (L'' = 0)$ type, this is a constant factor throughout the spectrum and does not affect the relative intensities). As a first approximation in this chapter, we will not consider the dependence of the transition moment operator, μ , upon molecular geometry. This approximation is due to the fact that we lack the knowledge of the transition moment operator itself. Furthermore, since the transition moment is a property of the entire molecule, we find it un-physical to define μ for the local bending mode which only involve three nuclei. Therefore, μ is treated as a constant throughout the rest of this calculation.

As a necessity in the entire calculation, by treating the overlap between torsion (a normal mode in the \tilde{A} state) and counter-rotating (a derivative of the local bending in the \tilde{X} state), we have answered the problem of the mismatched normal modes between the two electronic states. Calculation of torsional overlap will also provide the key phase factors that will permit assignment of \tilde{A} state *nu'end* polyad components.

5.3.4 Treatment of Torsion

For $l''_{total} = l''_A + l''_B = 0$, the freely counter-rotating basis state wavefunction in the \tilde{X} state is simply $e^{il''_A(\phi_A - \phi_B)}$. However, obtaining the torsional vibrational wavefunction for the \tilde{A} state is not as straightforward. First of all, torsion by π leads from the *trans* geometry to the *cis* geometry, and *vice versa*. This means the potential is cyclic. However, the same problem exists for bending as for torsion, the torsional barrier between *trans* and *cis* in the \tilde{A} state has not been observed, nor has the in-plane *cis-trans* barrier been observed. Can we create a model potential which reasonably well describes the torsion? How can we treat the cyclic potential in a way that most resembles the truth before we know what it is?

The natural coordinate used to describe the torsion is the dihedral angle τ , or equivalently, the azimuthal angle difference between the two CH bonds. Collecting every known about the \tilde{A} state geometry, we have the following information:

1. There are two local minima on the \tilde{A} state electronic potential. The vibrational ground level of the *trans* minimum has been well known experimentally to lie at 42198 cm^{-1} . The *cis* minimum, however, has never been measured experimentally. However, John Stanton calculated the vibrational ground state of the *cis* minimum to be 45248 cm^{-1} . This gives us roughly $45248 - 42198 = 3050 \text{ cm}^{-1}$ difference between the two vibrationless levels in the local minima.
2. The isomerization barrier is also calculated by Stanton to be 46508 cm^{-1} . This is $46508 - 42198 = 4310 \text{ cm}^{-1}$ above the *trans* well vibrationless level, just about $46508 - 45248 = 1260 \text{ cm}^{-1}$ above the zero point level in the *cis* well.
3. As Figure 5-4 demonstrates, both the in-plane local bend and the out-of-plane torsional motions would take the *trans* geometry to *cis*, and *vice versa*. Therefore, as far as the torsional potential is concerned, we are dealing with a cyclic potential, whose barrier should exceed or at least be equal to the minimization energy isomerization barrier of 4310 cm^{-1} .

Further information has led me to the belief that the in-plane local bend is the isomerization motion. I have two strong reasons to believe that the saddle point between the *trans* and the *cis* wells is mostly in-plane:

1. The normal mode frequency on the *cis* well suggests so. As Figure 1-2 indicates, although the torsional mode ν'_4 (764.90 cm^{-1}) and in-plane asymmetric bending ν'_6 (768.30 cm^{-1}) fundamental frequencies in the *trans* well in the \tilde{A} state are very close in value, the corresponding difference in the \tilde{A} state *cis* well is large. ν'_4 , the torsional mode frequency in the *cis* well is 704 cm^{-1} , while ν'_6 , the in-plane asymmetric bending mode is only 441 cm^{-1} . Considering that the *cis* well is very shallow (1100 cm^{-1} in Figure 1-1), and that the isomerization mode is always the floppiest mode, ν'_6 is certainly more likely to follow along the isomerization pathway than the torsion.
2. The *cis* \leftrightarrow *trans* transition state geometry from the Stanton *et al* calculations [97, 89] resembles a half-linear bent nuclear configuration. This is consistent

with the bottom path in Figure 5-4 – in-plane local bend.

Summarizing the above two points, it is my belief that although both the torsion and the in-plane bending would lead the *trans* geometry to isomerize into the *cis* geometry, the out-of-plane torsion is *not* along the minimum-energy-pathway. Therefore, the torsional barrier should be higher in energy than the saddle point between *trans* and *cis*. As to whether it is the in-plane local bend or the in-plane asymmetric bending that is most similar to the isomerization pathway, I would intuitively argue for the local bend, since the other CCH bond only changes about 10° [89] between *trans* and *cis* equilibrium geometry, although there is no proof yet that this must be true.

Gathering all the information we have about the torsional mode in the \tilde{A} state, we can make a reasonable hypothesis for the functional form of the cyclic torsional barrier. Based on the stationary points calculated by Stanton and coworkers [97], the difference between the lowest point of the potential (instead of the zero point level) is:

$$\begin{aligned}
 & [T_0(cis) - ZPE(cis)] - [T_0(trans) - ZPE(trans)] \\
 & = [46640 - 4833] - [43830 - 5065] \\
 & = 3042(\text{cm}^{-1}) \approx 3050(\text{cm}^{-1})
 \end{aligned} \tag{5.19}$$

Therefore, the simplest assumption for a cyclic potential would be ¹

$$V_{tor} = 3050 \cos^2 \left(\frac{\tau}{2} \right) + V_x \sin^2 \tau, \tag{5.20}$$

where V_x is a constant whose value is not yet known. However, since the torsional fundamental frequency is known [110] to be 768.26 cm^{-1} , V_x can be adjusted so that the $v=1$ level would be so much away from the zero point in the *trans* well.

Now that I have a hypothesis for the potential, the kinetic energy part is easily

¹I would like to thank David C. Oertel for a helpful discussion on this topic.

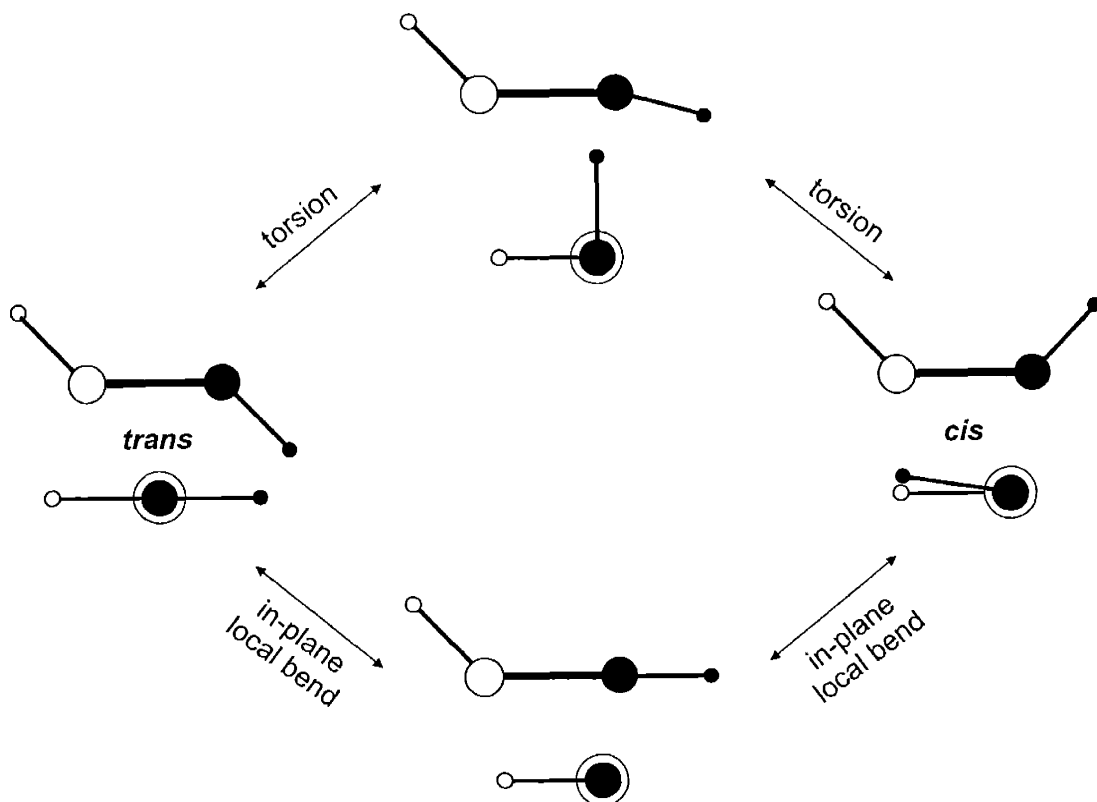


Figure 5-4: Four geometries involved in the torsional treatment of the \tilde{A} state. Each geometry is represented in the perpendicular view (top) and the transverse view (bottom). On the left and the right are the *trans*-acetylene and *cis*-acetylene structures that correspond to the local minima on the \tilde{A} state electronic potential. Both the in-plane local bend (top geometry) and the out-of-plane torsion serve as pathways between the two isomers. However, we have sufficient reasons to believe that the torsional saddle point is higher than the local bend saddle point.

obtained according to a formula provided in Townes and Schawlow [107]:

$$\hat{H}_{tor}\psi'_{tor} = \hat{T}_{tor}\psi'_{tor} + \hat{V}_{tor}\psi'_{tor} = \left(\frac{I_A + I_B}{2I_A I_B}\right) \frac{\partial^2 \psi'_{tor}}{\partial \tau^2} + V_{tor}\psi'_{tor}. \quad (5.21)$$

In Eq. (5.21), in our case, the moments of inertia, I_A and I_B , are simply:

$$\begin{aligned} I_A &= m_{H_A} \times (r_{CH} \sin \theta_{CCH})^2 \\ I_B &= m_{H_B} \times (r_{CH} \sin \theta_{CCH})^2; \end{aligned} \quad (5.22)$$

I wrote the Hydrogen nuclei as H_A and H_B for the purpose of subsequent calculations for acetylene isotopomers.

The time-independent Schrödinger equation for a Hamiltonian such as in Eq. (5.21) is called the Mathieu Equation. There are standard procedures to follow to solve the equation, and Professor Randall Shirts from Brigham Young University kindly provided me with a program which calculates eigenfunctions for the Mathieu Equation. However, as my goal is to obtain these wavefunctions numerically, I adopted a simple treatment of the Mathieu equation, described as follows:

Because the potential is cyclic and is in trigonometric functional form, a spherical harmonics basis set is ideal for obtaining matrix elements. Truncating such a basis set at 15, 20, 30, and 40 basis functions, I obtained four series of eigen-energy levels (Figure 5-5) and their corresponding eigenfunctions (Figure 5-6). The calculation converges at what I believe to be the true torsional energy levels. In order to arrive at the correct fundamental frequency spacing between $v'_4 = 1$ and $v'_4 = 0$, V_x is determined to be 3332 cm^{-1} .

There are a number of ways to determine whether $V_x = 3332 \text{ cm}^{-1}$ is a reasonable number and whether the potential is realistic. The first confirmation comes from the fact that the torsional barrier constructed as in Equation (5.20) exceeds the isomerization saddle point, drawn as a green line across in Figure 5-5), which is consistent with the above discussion. The next confirmation comes when we draw a harmonic potential according to the $F'_{\tau\tau}$ constant provided by Tobiason *et al.* At

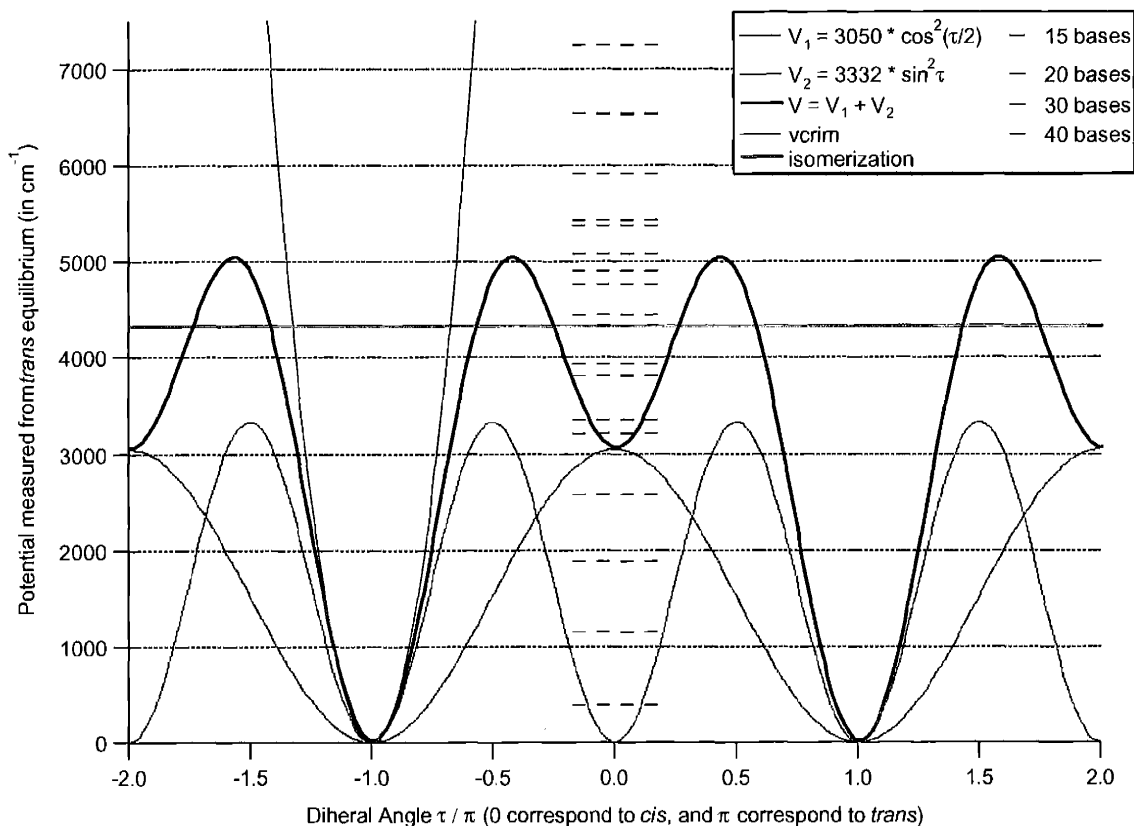


Figure 5-5: Torsional potential. The cyclic potential is modelled as the sum of two trigonometric functions V_1 (blue) and V_2 (red). The torsional barrier thus constructed exceeds the isomerization saddle point (green), which is consistent with the half-linear transition state calculated by Stanton and coworkers [89]. The purple potential is harmonic, drawn with values reported by Tobiason *et al* [106, 104]. My potential is in good agreement with the Tobiason harmonic potential at low energy. The four stacks of levels shown are eigenenergies obtained from truncating the basis set at 15, 20, 30, and 40 spherical harmonics. All levels converge.

relatively low energy in the *trans* well, my potential is in good agreement with the Tobiason harmonic potential. The final confirmation is when all the torsional eigenlevels converge, whether we truncate the spherical harmonic basis set at 15, 20, 30, or 40 levels.

Upon obtaining the torsional wavefunctions, an interesting observation is that although all the spherical harmonic basis functions are complex functions ($|e^{ik\tau}\rangle$), the eigen wavefunctions are real eigenvalue. We do not intend to lengthen this chapter to prove this, but in fact it is necessary for the torsional wavefunctions to be real.

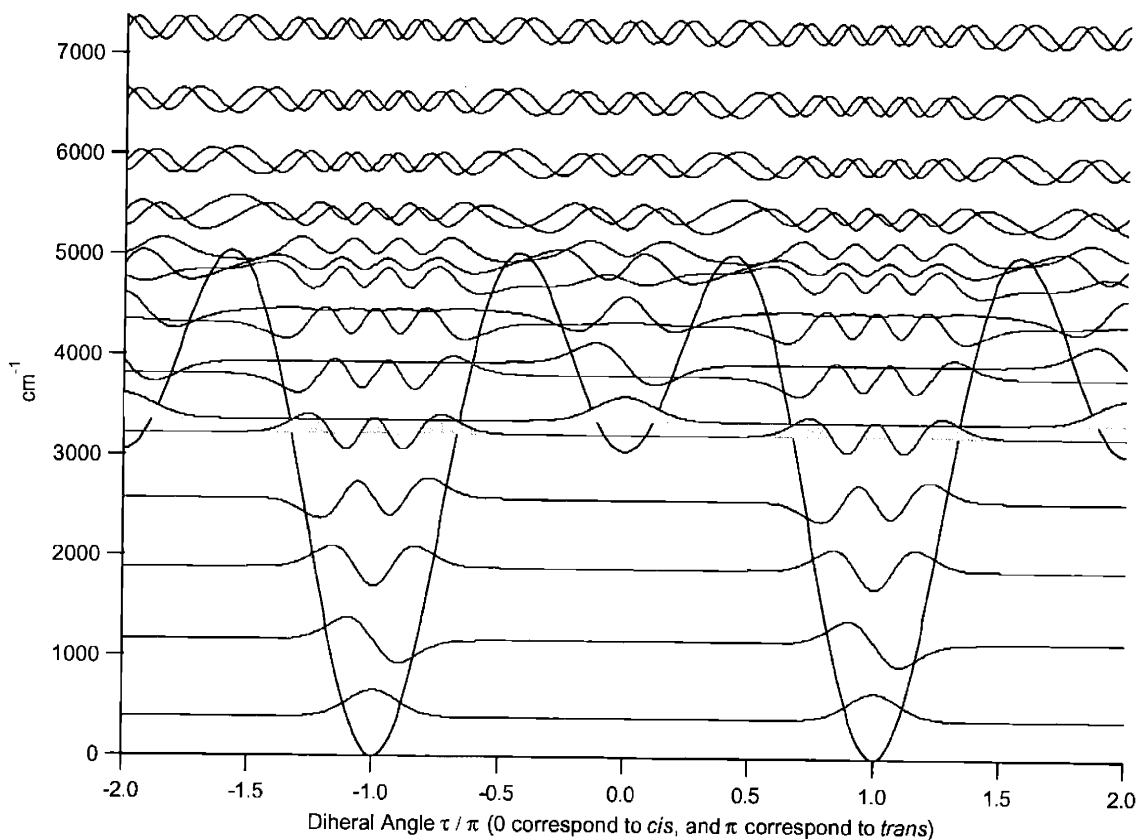


Figure 5-6: Torsional eigenfunctions drawn at their eigen energy levels. Two sets of levels, localized in the *trans* and *cis* wells initially, eventually tunnel with each other significantly at $\nu'_4 \geq 10$. At high enough energies above the torsional barrier, they become degenerate pairs of state, similar to degenerated free rotor wavefunctions.

Judging from the wavefunction diagram in Figure 5-6, we see two sets of levels, localized in the *trans* and *cis* wells respectively. They eventually tunnel into each other significantly at $\nu'_4 \geq 10$, and, at sufficiently high energies above the torsional barrier, become degenerate pairs of states, similar to doubly degenerate free rotor wavefunction. In other words, at sufficiently high energies, the wavefunctions no longer “feel” the existence of a low-lying potential barrier. In classical mechanical terms, one can think of the degenerate pair of free-rotor functions as a clockwise rotor and a counter-clockwise rotor.

Despite the observations derived from the torsional wavefunction calculations, for our purpose of comparing the torsional wavefunction FC factors with intensities derived from experimentally observed spectra, a few quanta in the *trans* well is all

that is asked for. Sufficient numerical descriptions of the torsional wavefunctions have been obtained. For the Franck-Condon factors described in this chapter, we are only concerned with the torsional ground state. Future studies of the $n\nu'_{bend}$ polyad will make much more usage of these wavefunctions. For this purpose, a Matlab code is attached in the Appendix for future reference.

5.4 Results

There are several intermediate outputs from the RKR inversion algorithm. Namely, the local bending and torsional wavefunctions (the bending wavefunctions shown in Figure 5-3), and the local bending and torsional wavefunction overlap integrals shown in Figures 5-7 and 5-8. These intermediate outputs are a step along the way to the final complete eigenstate overlap integrals, which can be directly compared to experimental intensity measurements.

The local bending wavefunction Franck-Condon factors are displayed in Figure 5-7. These FC factors are calculated between $\nu'_L = 0 - 4$ of the \tilde{A} state, and ν_A or $\nu_B = 0 - 30$ on the \tilde{X} state, with $l_A = l_B = 0$. In other words, these are squares of factors specified by Eqs. (5.15) and (5.16). The reason I chose to depict the square of these factors instead of the factors themselves is first to make the nodes more pronounced, and secondly, the intensity profile is what we would have seen, if the eigenstates in the \tilde{X} state and \tilde{A} state were pure local bends. However, in the lower internal energy region, the eigenstates resemble normal modes rather than local modes. Therefore, the local mode FC factors cannot, by themselves, contain any directly meaningful intensity information. However, they are important intermediate results from which the normal mode FC factors can be derived, either by a local \leftrightarrow normal conversion, or by using the expansion coefficients of the eigenstates obtained from the local mode effective Hamiltonian.

In the current DF dataset on acetylene, no upper state with any excitation in the torsional mode is directly excited. Therefore, it is sufficient to calculate overlap between the torsional ground state wavefunction in the \tilde{A} state and the counter-

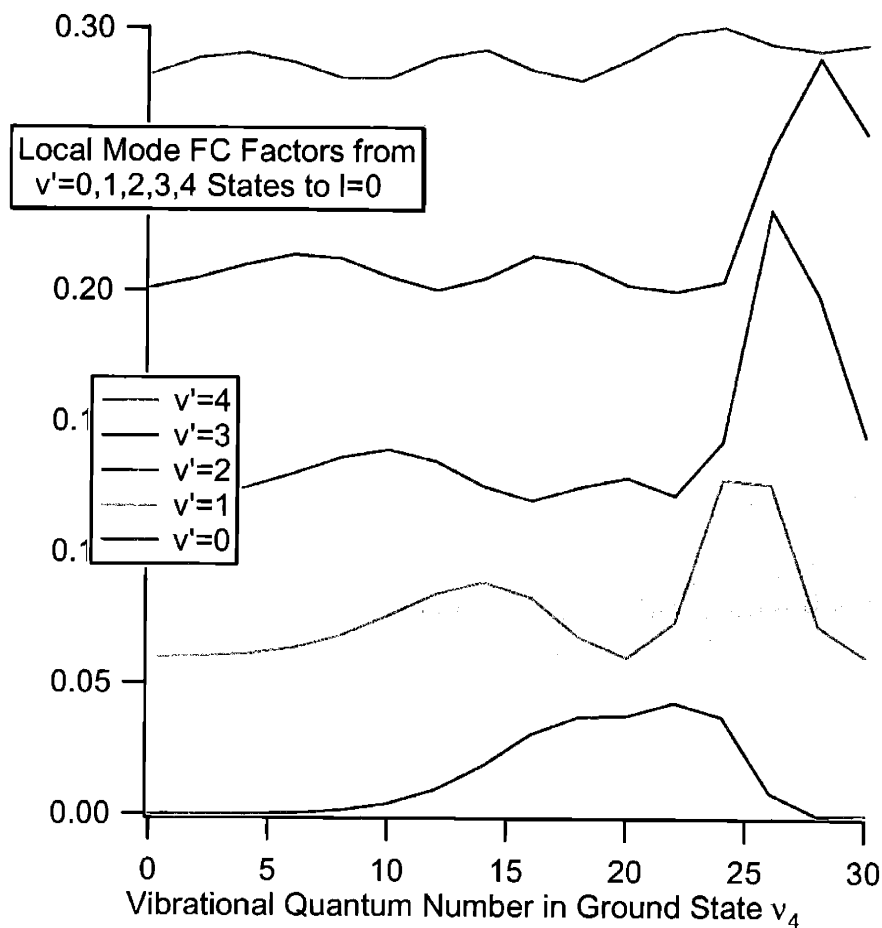


Figure 5-7: The local bending wavefunction Franck-Condon factors. The x-axis is the quantum number for the local bending wavefunctions on the \tilde{X} state from 0 to 30 ($l_L = 0$). These FC factors do not by themselves contain any meaningful information, at least not directly. However, they are intermediate results from which the normal mode FC factors can be derived, either by a local \longleftrightarrow normal conversion, or by using the expansion coefficients of the eigenstates obtained via the local mode effective Hamiltonian. Notice that only even quanta of the ground state local bending quantum numbers are included, due to the $l_L = 0$ restriction.

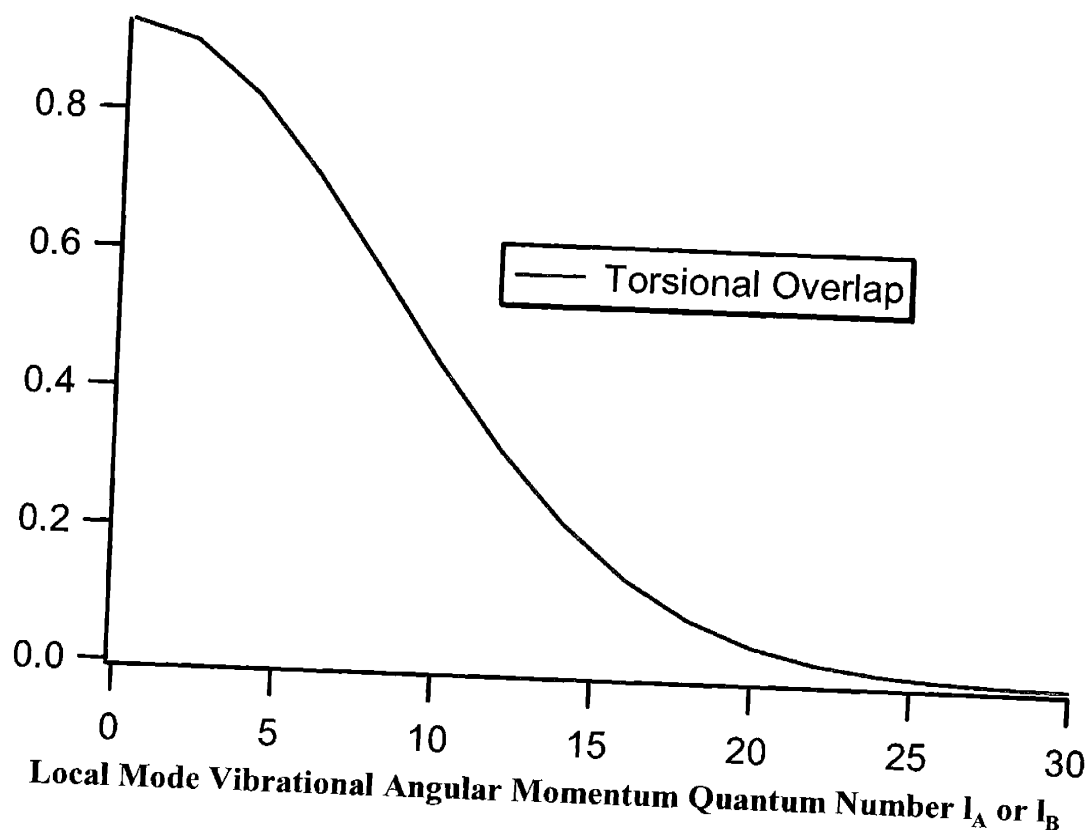


Figure 5-8: Torsional Overlap plotted for the torsional zero-point level, $v'_4 = 0$, on the \tilde{A} state to the counter-rotating levels on the \tilde{X} state ($l''_A + l''_B = 0$). These factors are particularly useful, as the local \longleftrightarrow normal conversion contains multiple l''_A terms (e.g. Table 5.2).

rotating wavefunctions of the \tilde{X} state in Eq. (5.18). As expansions of the normal mode bright states on the X electronic state contain multiple l''_A terms, the accuracy of this torsional overlap factor contributes greatly to the accumulative sums.

Finally, in Figure 5-9 we plot the normal mode FC factors obtained by combining all intermediate results. Results plotted include the Franck-Condon factors from the 0^0 level, the $2\nu'_3$, $\nu'_2 + \nu'_3$ and $\nu'_2 + 2\nu'_3$ levels. The line represents the calculated Franck-Condon factors, while the dots are the experimentally measured Franck-Condon factors. Most calculated nodes lie within one or two quanta of their observed position. Given the absence of an accurate potential, the calculation and observations are reasonably consistent.

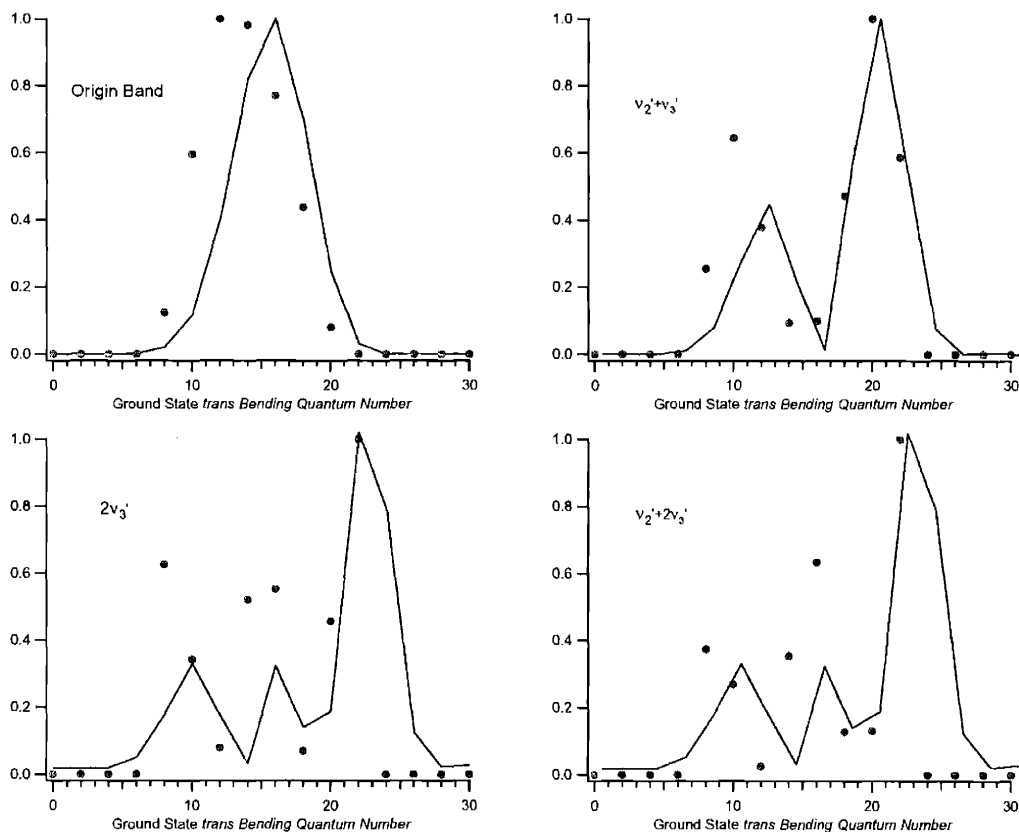


Figure 5-9: The 1D FC results for normal modes after local \longleftrightarrow normal conversion. Results plotted include the Franck-Condon factors from the 0^0 level, the $2\nu_3'$, $\nu_2' + \nu_3'$ and $\nu_2' + 2\nu_3'$ levels. The line represents the calculated Franck-Condon factors, while the dots are the experimentally measured Franck-Condon factors. Most calculated nodes lie within one to two quanta of the observed position along a vibrational progression. Given the absence of an accurate potential, the calculation and the observation agree surprisingly well.

5.5 Conclusion

In this chapter I have described a Franck-Condon calculation algorithm based on RKR inversion. A semi-empirical local bending potential for the \widetilde{X} state is constructed with the “observed” local mode bright states (that is, the diagonal terms of the local bending effective Hamiltonian which globally fits our DF dataset). The eigenstates from this semi-empirical local bending potential are believed to have captured the key features of the true bending wavefunctions of acetylene, as the resulting FC factors agree with the corresponding experimental measurement to within two vibrational quanta.

Chapter 6

Franck-Condon Calculation in Lack of Good Potentials: Multi-Dimensional

6.1 Introduction

This chapter is focused on two objectives. A Multi-Dimensional Franck-Condon calculation will be described, using the *gerade* bending mode FC factors that are reported in Chapter 5. In addition, a comparison between our Franck-Condon algorithm with several existing FC algorithms will be given, the most important among which is Watson's Franck-Condon calculation on Acetylene [113].

6.2 Overview

As Figure 6-1 depicts, the multi-dimensional Franck-Condon factor calculation comprises of the following steps:

1. *Local Mode Wavefunction Overlaps*: The local mode is convenient, in that it most faithfully represents the dynamical motions of the H nucleus as it moves to the other side of the CC bond to form vinylidene. In fact, Jacobson *et. al.*

have demonstrated that local bends and counter-rotations are the dominant characters of the eigenstates along the isomerization pathway. For this reason, by exploiting local mode wavefunctions, I hope to extend the validity of the FC calculation to as high internal energy as possible. The bending and torsional portions of the local mode vibrational wavefunctions have been described in Chap. 5. The stretching treatment is simpler, because bends involving $v > 0$ of CH stretch are absent from our DF dataset, therefore the CH stretch can be treated as harmonic, and the CC stretch is virtually the same whether in the normal mode representation or in the local mode representation, we treat it in two ways, as harmonic oscillators and as morse oscillators. To obtain the overlap integrals between the two sets of wavefunctions, in the \tilde{A} state and \tilde{X} state respectively, we use a simple Newton integration algorithm. After these procedures, the local mode wavefunction overlap integrals are obtained.

2. *Normal Mode Observations:* Measurement of the Franck-Condon intensity profile from the C_2H_2 DF dataset is available, by simply integrating the overall intensity of all transitions within any polyad, and to associate the intensity to the single bright state from that polyad. To compare this measurement with the local mode FC calculation, a connection must be established between the normal modes and the local modes. In the one-dimensional case described in the previous chapter, we use the laddering operator to perform the transformation. The multi-dimensional case is more complicated. Because of the single-bright-state-per-polyad assumption, the local mode overlaps must be transformed into normal mode overlaps through normal mode analysis, and then we will be able to compare the calculated FC factors with the experimental findings.
3. *FG Matrix Analysis:* This is the normal mode analysis, by which the transformation between the eigenstate and the internal coordinates of the molecule is determined. The internal coordinates of the molecule are expressed as displacement coordinates of a single bond or bond angle, and therefore are naturally expressed in terms of local mode displacements. Because the FG matrix method

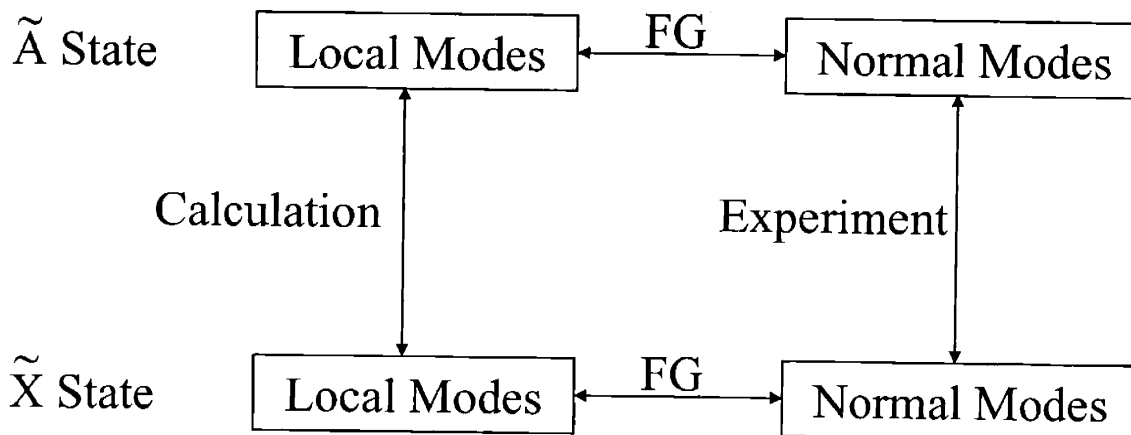


Figure 6-1: Illustration of the principles behind the Multi-Dimensional Franck-Condon factor calculation. The calculation is mainly based on local mode wavefunction overlap integral. However, to compare with the intensities in the experimental dataset, which has been found to be consistent with the single-bright-state-per-polyad assumption, bright state intensities must be obtained in normal mode representations. In order to do a global conversion between the local and the normal modes, normal mode analysis must be performed via FG matrix diagonalization.

is based on a harmonic force field, the eigenstates obtained are in the normal mode basis set. The FG matrix method would define the transformation matrix between the local mode and the normal mode for both the \tilde{A} state and \tilde{X} state of acetylene.

In addition to the above steps, we have also attempted to find a suitable functional form for the transition dipole moment. This was suggested by Kevin Lehmann and Hue Guo at the Telluride Conference in the year 2000. There are several clues as to how the transition moment ought to behave, and these will be described in Section 6.3.

6.3 Algorithm

In this section, we will describe two major routes of the multi-dimensional FC calculation: As the normal mode analysis and the transition moment function. Greater emphasis will be put on the normal mode analysis, as it is my belief that this part

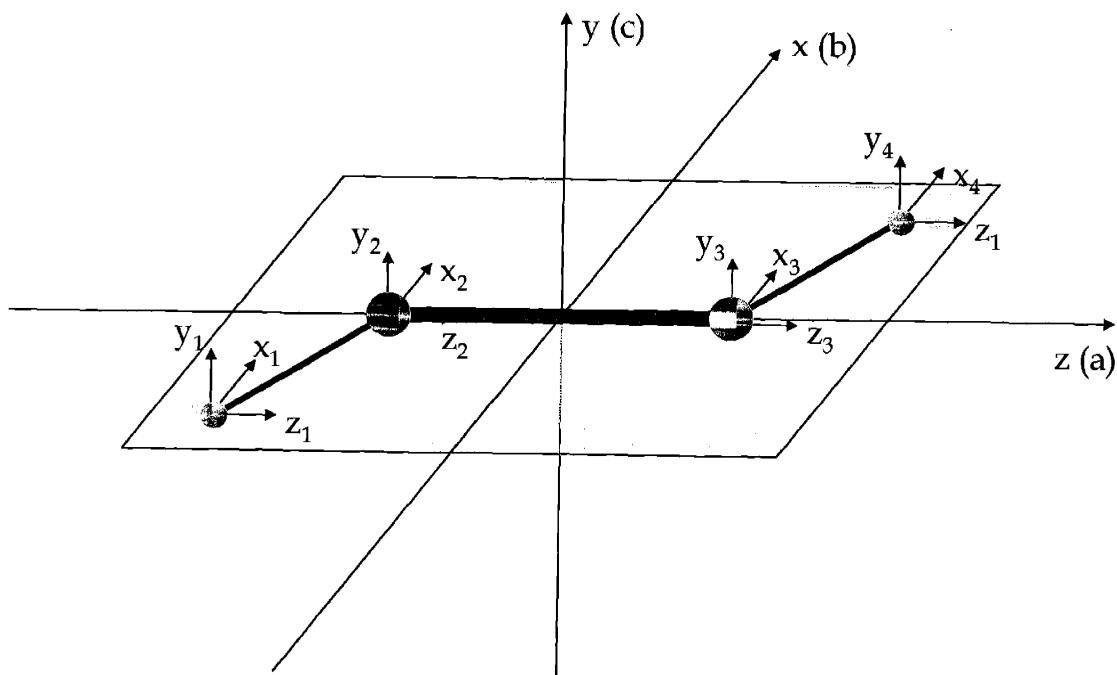


Figure 6-2: Cartesian Displacement Coordinates for *trans*-bent (\tilde{A} -state) Acetylene.

of the calculation can be transplanted into many projects in the future. In addition, I would like to describe my analysis of Dushinsky Rotation effects in acetylene. This part is highly relevant to our FC calculation. Essentially, in considering the Dushinsky rotation, we have considered the dependence of bond length on bending angle, etc. Additionally, studies of Dushinsky Rotation help making direct connections between our calculation and Watson's FC calculation.

6.3.1 Normal Mode Analysis

The most fundamental coordinates by which the molecule acetylene can be described are the Cartesian displacement coordinates (Figure 6-2), where each nuclear position is described by three Cartesian coordinates with origin at the equilibrium position of the nuclei. The kinetic energy, expressed in this coordinate system, is

$$T = \frac{1}{2} \sum_{i=1}^N m_i (\dot{x}_i^2 + \dot{y}_i^2 + \dot{z}_i^2). \quad (6.1)$$

Hence, we can express the kinetic energy part of the Lagrangian in matrix format:

$$2T = \dot{\mathbf{X}}^\dagger \mathbf{M} \dot{\mathbf{X}}, \quad (6.2)$$

in which \mathbf{X} is a column vector consisting of $3N$ elements, N being the number of nuclei in the molecule ($N = 4$ for acetylene). \mathbf{X}^\dagger is the conjugate transpose of \mathbf{X} , and \mathbf{M} is a diagonal matrix consisting of the masses of the nuclei m_i , each m_i is listed three times. If we use mass-weighted Cartesian displacement coordinates: $q_1 = \sqrt{m_1}x_1$, $q_2 = \sqrt{m_1}y_1$, $q_3 = \sqrt{m_1}z_1$, $q_4 = \sqrt{m_2}x_2$, $q_5 = \sqrt{m_2}y_2$, $q_6 = \sqrt{m_2}z_2$, ..., then the kinetic energy can be written as

$$T = \frac{1}{2} \sum_{i=1}^{3N} \dot{q}_i^2. \quad (6.3)$$

To express the entire Lagrangian in mass-weighted Cartesian displacement coordinates, the potential energy should be expressed as a Taylor expansion on q_i relative to the equilibrium positions:

$$U = U_e + \sum_{i=1}^{3N} \left(\frac{\partial U}{\partial q_i} \right)_e q_i + \frac{1}{2} \sum_{i=1}^{3N} \sum_{j=1}^{3N} \left(\frac{\partial^2 U}{\partial q_i \partial q_j} \right)_e q_i q_j + \dots \quad (6.4)$$

At equilibrium,

$$\left(\frac{\partial U}{\partial q_i} \right)_e = 0 \quad (6.5)$$

for all i . If we define

$$u_{ij} = \left(\frac{\partial^2 U}{\partial q_i \partial q_j} \right)_e, \quad (6.6)$$

we obtain

$$U \approx U_e + \frac{1}{2} \sum_{i=1}^{3N} \sum_{j=1}^{3N} u_{ij} q_i q_j, \quad (6.7)$$

Substituting the kinetic energy T and U into the Lagrangian equation:

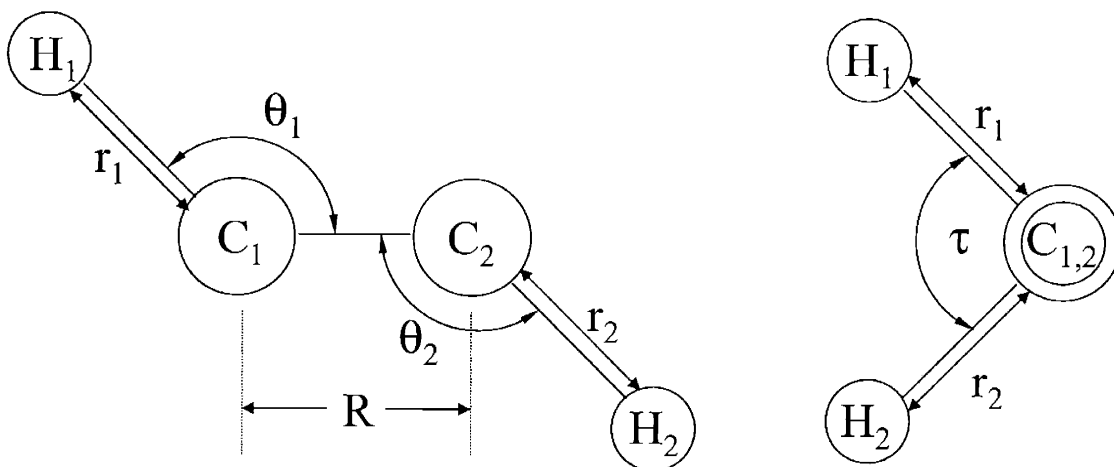


Figure 6-3: Internal Coordinates used for FG matrix analysis for Acetylene. r_1 and r_2 describe the local stretches of the CH bonds, R defines the CC bond length displacement, θ_1 and θ_2 describe the CCH bond angle changes, and τ is the out-of-plane torsional angle.

$$\frac{d}{dt}\left(\frac{\partial L}{\partial \dot{q}_j}\right) - \frac{\partial L}{\partial q_j} = \frac{d}{dt}\left(\frac{\partial T}{\partial \dot{q}_j}\right) + \frac{\partial V}{\partial q_j} = 0, \quad (6.8)$$

where $j = 1, 2, \dots, 3N$, we obtain the equations of motion.

In order to remove the translational and rotational motions from the kinetic energy, we can use internal coordinates, D_i , instead of the Cartesian displacements x_i . Figure 6-3 lists all of the internal coordinates that we have defined for the Acetylene molecule. Among them, r_1 and r_2 describe the local stretches of the CH bonds, R defines the CC bond stretch, θ_1 and θ_2 describe the CCH bond angle displacements, and τ is the out-of-plane torsional angle. We define \mathbf{B} as the matrix which transforms x_i into D_i : $\mathbf{D} = \mathbf{B}\mathbf{X}$, in which \mathbf{D} is a column vector consisting of $3N - 6$ elements. Obviously, \mathbf{B} is a matrix of $(3N - 6) \times 3N$ dimensions.

Now if we define the Wilson G matrix as $\mathbf{G} = \mathbf{B}\mathbf{M}^{-1}\mathbf{B}^\dagger$, then it can be proved that similarly to Eq. (6.2), we have

$$2T = \dot{\mathbf{D}}^\dagger \mathbf{G}^{-1} \dot{\mathbf{D}}, \quad (6.9)$$

in which \mathbf{G}^{-1} is a matrix of $(3N - 6) \times (3N - 6)$ dimensions. If we express the potential energy V in terms of the internal coordinates, then similarly to Eq. (6.7), we have

$$V = U - U_e = \frac{1}{2} \sum_{i=1}^{3N} \sum_{j=1}^{3N} F_{ij} D_i D_j, \quad (6.10)$$

where

$$F_{ij} = F_{ji} = \left(\frac{\partial^2 U}{\partial D_i \partial D_j} \right)_e. \quad (6.11)$$

Therefore, we have

$$2\mathbf{V} = \mathbf{D}^\dagger \mathbf{F} \mathbf{D}, \quad (6.12)$$

where \mathbf{F} is also a matrix of $(3N - 6) \times (3N - 6)$ dimensions.

We can also write Eq. (6.12) as

$$V = \frac{1}{2} \sum_{i,j} D_i F_{ij} D_j. \quad (6.13)$$

Hence,

$$\begin{aligned} \frac{\partial V}{\partial D_m} &= \frac{1}{2} \sum_{i,j} (\delta_{im} F_{ij} D_j + D_i F_{ij} \delta_{jm}) \\ &= \frac{1}{2} \left(\sum_j F_{mj} D_j + \sum_i D_i F_{im} \right) = \sum_j F_{mj} D_j. \end{aligned} \quad (6.14)$$

Similarly, from Eq. (6.9) we obtain

$$T = \frac{1}{2} \sum_{i,j} \dot{D}_i G_{ij}^{-1} \dot{D}_j. \quad (6.15)$$

Therefore,

$$\frac{\partial T}{\partial \dot{D}_m} = \sum_j G_{mj}^{-1} \dot{D}_j, \quad (6.16)$$

Substituting Eq. (6.14) and Eq. (6.16) into the Lagrangian equation of motion:

$$\frac{d}{dt} \left(\frac{\partial L}{\partial \dot{D}_m} \right) - \frac{\partial L}{\partial D_m} = \frac{d}{dt} \left(\frac{\partial T}{\partial \dot{D}_m} \right) + \frac{\partial V}{\partial D_m} = 0, \quad (6.17)$$

we obtain

$$\frac{d}{dt} \left(\sum_j G_{mj}^{-1} \dot{D}_j \right) + \sum_j F_{mj} D_j = \sum_j G_{mj}^{-1} \ddot{D}_j + \sum_j F_{mj} D_j = 0. \quad (6.18)$$

Suppose the solution for the internal coordinates, D_j , has the form

$$D_j = A_j \cos(\sqrt{\lambda}t + \epsilon), j = 1, 2, \dots, 3N - 6, \quad (6.19)$$

then

$$\ddot{D}_j = -\lambda D_j \quad (6.20)$$

Combining Eqs. (6.18) and (6.20), we get

$$\sum_j F_{mj} D_j - \sum_j \lambda G_{mj}^{-1} D_j = \sum_j \left(F_{mj} - \lambda G_{mj}^{-1} \right) D_j = 0 \quad (6.21)$$

If we write Eq. (6.21) in matrix form, we obtain

$$(\mathbf{F} - \lambda \mathbf{G}^{-1}) \mathbf{D} = 0. \quad (6.22)$$

The necessary and sufficient condition for D_j to have nontrivial form is that the determinant of the coefficients of \mathbf{D} in Eq. (6.22) must be zero:

$$\det|\mathbf{F} - \lambda\mathbf{G}^{-1}| = 0. \quad (6.23)$$

From Eq. (6.23), we obtain

$$\det|\mathbf{FG} - \lambda\mathbf{I}| = 0 \quad (6.24)$$

$$\det|\mathbf{GF} - \lambda\mathbf{I}| = 0 \quad (6.25)$$

where \mathbf{I} is the unit matrix. Eqs. (6.24) and (6.25) are alternative forms of the secular equation for the \mathbf{FG} matrix.

Up to this point, we have derived the methodology behind necessity to diagonalize the \mathbf{FG} matrix. However, we can develop this subject further by asking the following three questions:

1. How to obtain the \mathbf{F} and \mathbf{G} matrices?
2. Will \mathbf{FG} and \mathbf{GF} always be a symmetric matrix?
3. Does an alternative basis set exist that would simplify the \mathbf{FG} diagonalization?

We will address these questions in reverse order. For the last question, “Does an alternative basis set exist that would simplify the \mathbf{FG} diagonalization?”, the answer is yes, and that basis set is the symmetrized internal coordinates, S_j . Conversion between the internal coordinates and the symmetrized internal coordinates can be automatically performed by a point group projection operator. This topic can be found in many physical chemistry textbooks that treat point groups. For now, if we convert the internal coordinates, D_j to symmetry internal coordinates, S_j : $\mathbf{S} = \mathbf{UD}$, \mathbf{U} must be an orthogonal matrix due to the way the symmetry coordinates are constructed. Then it follows from Eq. (6.9) that we have

$$2T = \dot{\mathbf{D}}^\dagger \mathbf{G}^{-1} \dot{\mathbf{D}} = \dot{\mathbf{S}}^\dagger \mathbf{UG}^{-1} \mathbf{U}^\dagger \dot{\mathbf{S}} = \dot{\mathbf{S}}^\dagger \tilde{\mathbf{G}}^{-1} \dot{\mathbf{S}}, \quad (6.26)$$

where $\tilde{\mathbf{G}} = \mathbf{UGU}^\dagger$, which is a block-diagonal matrix.

We define $\tilde{\mathbf{F}} = \mathbf{U}\mathbf{F}\mathbf{U}^\dagger$, which is also a block-diagonal matrix. Then, following from Eqs. (6.24) and (6.25), we have

$$\det|\tilde{\mathbf{F}}\tilde{\mathbf{G}} - \lambda\mathbf{I}| = 0, \quad (6.27)$$

$$\det|\tilde{\mathbf{G}}\tilde{\mathbf{F}} - \lambda\mathbf{I}| = 0. \quad (6.28)$$

Eqs. (6.27) and (6.28) are the equivalent of Eqs. (6.24) and (6.25), expressed in the symmetrized internal coordinates. Although the coordinates we adopted to do the actual FG analysis for acetylene are the internal coordinates, we still consider the symmetrized coordinates to be an efficient way to perform the analysis.

The answer to the second question, “Will \mathbf{FG} or \mathbf{GF} always be a symmetric matrix?”, is simply no. Let us consider the following case where

$$\mathbf{F} = \begin{bmatrix} 1 & 0 \\ 0 & 2 \end{bmatrix} \quad \mathbf{G} = \begin{bmatrix} 1 & 2 \\ 2 & 1 \end{bmatrix}, \quad (6.29)$$

the resultant \mathbf{FG} and \mathbf{GF} matrixes are as the following:

$$\mathbf{FG} = \begin{bmatrix} 1 & 2 \\ 4 & 2 \end{bmatrix} \quad \mathbf{GF} = \begin{bmatrix} 1 & 4 \\ 2 & 2 \end{bmatrix}. \quad (6.30)$$

Therefore, instead of considering the \mathbf{FG} or the \mathbf{GF} matrix, it is best to consider the following matrix:

$$\left(\mathbf{G}^{\frac{1}{2}}\mathbf{F}\mathbf{G}^{\frac{1}{2}}\right) \left(\mathbf{G}^{\frac{1}{2}}\mathbf{L}\right) = \mathbf{\Lambda} \left(\mathbf{G}^{\frac{1}{2}}\mathbf{L}\right), \quad (6.31)$$

where \mathbf{L} is the transformation matrix between the internal coordinates and the normal coordinates:

$$\mathbf{D} = \mathbf{L}\mathbf{Q}, \quad (6.32)$$

and $\mathbf{\Lambda}$ is a diagonal matrix whose elements correspond to the values of λ_i used in

Eqs. (6.24), (6.25), (6.27) and (6.28), which are directly related to the harmonic frequencies of the normal modes. This symmetrized treatment of the FG matrix was suggested to me by Professor Anthony J. Merer from University of British Columbia.

As to the last question, “How to obtain the \mathbf{F} and \mathbf{G} matrices?”, the \mathbf{F} matrix can be constructed according to the known force constants from the harmonic potential, while the most common method to obtain the \mathbf{G} matrix elements is to look them up in the Wilson G-matrix table. Input in the Wilson G-matrix element formulae are equilibrium bond lengths, equilibrium bond angles, and the masses of individual nuclei. For the FG matrix analysis in the \tilde{X} state of acetylene, I used the force constants published by Strey and Mills [99]. For the \tilde{A} state, the force constants from Tobiasson *et al.* [106] are used. It is helpful to point out that there is a typo in Tobiasson’s paper [106], the values of the CH and CC bond lengths in the first paragraph have been interchanged. Force constants for the \tilde{X} and \tilde{A} states reported by these two papers have been constantly updated. However, for the purpose of determining the global transformation between the normal and local modes, these constants should be suitable.

We have obtained results from the FG normal mode analysis, for both the \tilde{A} state and the \tilde{X} state, for the molecules $^{12}\text{C}_2\text{H}_2$, $^{13}\text{C}_2\text{H}_2$ and HCCD . Fourteen tables will be used to summarize the results from my FG analysis. The purpose of performing the FG analysis for these three isotopomers is to meet the expectation that the multi-dimensional FC calculation, once completed for $^{12}\text{C}_2\text{H}_2$, can be transferred to $^{13}\text{C}_2\text{H}_2$ and HCCD , the DF dataset for which has been collected by Michelle Silva and me.

Obviously, the \mathbf{F} matrices for the \tilde{A} and \tilde{X} states for all three isotopomers are the same. Tables 6.2 and 6.1 are constructed using the force constants known for the \tilde{X} and \tilde{A} states of acetylene.

Tables 6.3 and 6.4 give the \mathbf{G} matrix elements and the transformation matrix, \mathbf{T} , for the \tilde{X} state of HCCH . The \mathbf{T} matrix is simply the eigenvalues that result from the FG matrix diagonalization, reflecting the transformation between the internal coordinates (local mode) and the low-internal-energy eigenstates (normal mode):

	r_1	r_2	R	θ_1	θ_2
r_1	6.370 $\frac{\text{mdyn}}{\text{Å}}$	-0.019 $\frac{\text{mdyn}}{\text{Å}}$	-0.095 $\frac{\text{mdyn}}{\text{Å}}$	0	0
r_2	-0.019 $\frac{\text{mdyn}}{\text{Å}}$	6.370 $\frac{\text{mdyn}}{\text{Å}}$	-0.095 $\frac{\text{mdyn}}{\text{Å}}$	0	0
R	-0.095 $\frac{\text{mdyn}}{\text{Å}}$	-0.095 $\frac{\text{mdyn}}{\text{Å}}$	16.341 $\frac{\text{mdyn}}{\text{Å}}$	0	0
θ_1	0	0	0	0.251 mdyn×Å	0.0925 mdyn×Å
θ_2	0	0	0	0.0925 mdyn×Å	0.251 mdyn×Å

Table 6.1: \mathbf{F} matrix of the \tilde{X} state

	r_1	r_2	R	θ_1	θ_2	τ
r_1	4.780 $\frac{\text{md}}{\text{Å}}$	0.138 $\frac{\text{md}}{\text{Å}}$	0	0.188 md	0	0
r_2	0.138 $\frac{\text{md}}{\text{Å}}$	4.780 $\frac{\text{md}}{\text{Å}}$	0	0	0.188 md	0
R	0	0	7.630 $\frac{\text{md}}{\text{Å}}$	0.583 md	0.583 md	0
θ_1	0.188 md	0	0.583 md	0.541 md×Å	0.127 md×Å	0
θ_2	0	0.188 md	0.583 md	0.127 md×Å	0.541 md×Å	0
τ	0	0	0	0	0	0.137 md×Å

Table 6.2: \mathbf{F} matrix of the \tilde{A} state

$$\mathbf{Q}^\dagger = \mathbf{D}^\dagger \mathbf{T} \quad (6.33)$$

Tables 6.5 and 6.6 give the \mathbf{G} matrix elements and the transformation matrix, \mathbf{T} , for the \tilde{X} state of $^{13}\text{C}_2\text{H}_2$.

Tables 6.7 and 6.8 give the \mathbf{G} matrix elements and the transformation matrix, \mathbf{T} , for the \tilde{X} state of C_2HD .

Tables 6.9 and 6.10 give the \mathbf{G} matrix elements and the transformation matrix,

	r_1	r_2	R	θ_1	θ_2
r_1	1.0756 amu ⁻¹	0	-0.0833 amu ⁻¹	0	0
r_2	0	1.0756 amu ⁻¹	-0.0833 amu ⁻¹	0	0
R	-0.0833 amu ⁻¹	-0.0833 amu ⁻¹	0.1667 amu ⁻¹	0	0
θ_1	0	0	0	1.2021 $\frac{\text{Å}}{\text{amu}^{\circ-2}}$	-0.2457 $\frac{\text{Å}}{\text{amu}^{\circ-2}}$
θ_2	0	0	0	-0.2457 $\frac{\text{Å}}{\text{amu}^{\circ-2}}$	1.2021 $\frac{\text{Å}}{\text{amu}^{\circ-2}}$

Table 6.3: \mathbf{G} matrix of the \tilde{X} state for HCCH

	ν_1	ν_2	ν_3	ν_4	ν_5
r_1	0.6415	0.1203	0.7071	0	0
r_2	0.6415	0.1203	-0.7071	0	0
R	-0.4207	0.9854	0	0	0
θ_1	0	0	0	0.7071	-0.7071
θ_2	0	0	0	0.7071	0.7071

Table 6.4: **T** matrix of the \tilde{X} state for $HCCH$

	r_1	r_2	R	θ_1	θ_2
r_1	1.0691 amu ⁻¹	0	-0.0769 amu ⁻¹	0	0
r_2	0	1.0691 amu ⁻¹	-0.0769 amu ⁻¹	0	0
R	-0.0769 amu ⁻¹	-0.0769 amu ⁻¹	0.1538 amu ⁻¹	0	0
θ_1	0	0	0	1.1774 $\frac{\text{\AA}}{\text{amu}^{0.5}}$	-0.2268 $\frac{\text{\AA}}{\text{amu}^{0.5}}$
θ_2	0	0	0	-0.2268 $\frac{\text{\AA}}{\text{amu}^{0.5}}$	1.1774 $\frac{\text{\AA}}{\text{amu}^{0.5}}$

Table 6.5: **G** matrix of the \tilde{X} state for $H^{13}C^{13}CH$

	ν_1	ν_2	ν_3	ν_4	ν_5
r_1	0.6520	0.1086	0.7071	0	0
r_2	0.6520	0.1086	-0.7071	0	0
R	-0.3871	0.9881	0	0	0
θ_1	0	0	0	0.7071	-0.7071
θ_2	0	0	0	0.7071	0.7071

Table 6.6: **T**-matrix of the \tilde{X} state for $H^{13}C^{13}CH$

	r_1	r_2	R	θ_1	θ_2
r_1	1.0756 amu ⁻¹	0	-0.0833 amu ⁻¹	0	0
r_2	0	0.5798 amu ⁻¹	-0.0833 amu ⁻¹	0	0
R	-0.0833 amu ⁻¹	-0.0833 amu ⁻¹	0.1667 amu ⁻¹	0	0
θ_1	0	0	0	1.2021 $\frac{\text{\AA}}{\text{amu}^{0.5}}$	-0.2457 $\frac{\text{\AA}}{\text{amu}^{0.5}}$
θ_2	0	0	0	-0.2457 $\frac{\text{\AA}}{\text{amu}^{0.5}}$	0.7613 $\frac{\text{\AA}}{\text{amu}^{0.5}}$

Table 6.7: **G** matrix of the \tilde{X} state for $HCCD$

	ν_1	ν_2	ν_3	ν_4	ν_5
r_1	0.9405	0.1078	0.1267	0	0
r_2	0.0511	0.3195	-0.7637	0	0
R	-0.3359	0.9414	0.6331	0	0
θ_1	0	0	0	-0.0762	0.9177
θ_2	0	0	0	0.9971	0.3972

Table 6.8: \mathbf{T} matrix of the \tilde{X} state for $HCCD$

	r_1	r_2	R	θ_1	θ_2	τ
r_1	1.076 amu ⁻¹	0	-0.045 amu ⁻¹	-0.051 $\frac{\text{\AA}}{\text{amu}}$	-0.051 $\frac{\text{\AA}}{\text{amu}}$	0
r_2	0	1.076 amu ⁻¹	-0.045 amu ⁻¹	-0.051 $\frac{\text{\AA}}{\text{amu}}$	-0.051 $\frac{\text{\AA}}{\text{amu}}$	0
R	-0.045 amu ⁻¹	-0.045 amu ⁻¹	0.167 amu ⁻¹	-0.064 $\frac{\text{\AA}}{\text{amu}}$	-0.064 $\frac{\text{\AA}}{\text{amu}}$	0
θ_1	-0.051 $\frac{\text{\AA}}{\text{amu}}$	-0.051 $\frac{\text{\AA}}{\text{amu}}$	-0.064 $\frac{\text{\AA}}{\text{amu}}$	1.041 $\frac{\text{\AA}}{\text{amu}}$	0.148 $\frac{\text{\AA}}{\text{amu}}$	0
θ_2	-0.051 $\frac{\text{\AA}}{\text{amu}}$	-0.051 $\frac{\text{\AA}}{\text{amu}}$	-0.064 $\frac{\text{\AA}}{\text{amu}}$	0.147 $\frac{\text{\AA}}{\text{amu}}$	1.041 $\frac{\text{\AA}}{\text{amu}}$	0
τ	0	0	0	0	0	2.559 $\frac{\text{\AA}}{\text{amu}}$

Table 6.9: \mathbf{G} matrix of the \tilde{A} state for $HCCH$

\mathbf{T} , for the \tilde{A} state of $^{12}C_2H_2$.

Tables 6.11 and 6.12 give the \mathbf{G} matrix elements and the transformation matrix, \mathbf{T} , for the \tilde{A} state of $^{13}C_2H_2$.

Tables 6.13 and 6.14 give the \mathbf{G} matrix elements and the transformation matrix, \mathbf{T} , for the \tilde{A} state of $HCCD$.

Table 6.15 enlists the harmonic frequencies obtained for both the \tilde{X} and \tilde{A} state of $^{12}C_2H_2$ and the \tilde{X} state of $HCCD$. Agreement between the calculation and the

	ν_1	ν_2	ν_3	ν_4	ν_5	ν_6
r_1	0.7005	0.0631	0.0148	0	0.7064	0.0256
r_2	0.7005	0.0631	0.0148	0	-0.7064	-0.0256
R	-0.1355	0.9853	-0.4612	0	0	0
θ_1	0.0111	0.1032	0.6272	0	0.0309	-0.7066
θ_2	0.0111	0.1032	0.6272	0	-0.0309	0.7066
τ	0	0	0	1	0	0

Table 6.10: \mathbf{T} matrix of the \tilde{A} state for $HCCH$

	r_1	r_2	R	θ_1	θ_2	τ
r_1	1.069 amu ⁻¹	0	-0.041 amu ⁻¹	-0.047 $\frac{\text{\AA}}{\text{amu}}$	-0.047 $\frac{\text{\AA}}{\text{amu}}$	0
r_2	0	1.069 amu ⁻¹	-0.041 amu ⁻¹	-0.047 $\frac{\text{\AA}}{\text{amu}}$	-0.047 $\frac{\text{\AA}}{\text{amu}}$	0
R	-0.041 amu ⁻¹	-0.041 amu ⁻¹	0.154 amu ⁻¹	-0.059 $\frac{\text{\AA}}{\text{amu}}$	-0.059 $\frac{\text{\AA}}{\text{amu}}$	0
θ_1	-0.047 $\frac{\text{\AA}}{\text{amu}}$	-0.047 $\frac{\text{\AA}}{\text{amu}}$	-0.059 $\frac{\text{\AA}}{\text{amu}}$	1.024 $\frac{\text{\AA}}{\text{amu}}$	0.136 $\frac{\text{\AA}}{\text{amu}}$	0
θ_2	-0.047 $\frac{\text{\AA}}{\text{amu}}$	-0.047 $\frac{\text{\AA}}{\text{amu}}$	-0.059 $\frac{\text{\AA}}{\text{amu}}$	0.136 $\frac{\text{\AA}}{\text{amu}}$	1.024 $\frac{\text{\AA}}{\text{amu}}$	0
τ	0	0	0	0	0	2.515 $\frac{\text{\AA}}{\text{amu}}$

Table 6.11: \mathbf{G} matrix of the \tilde{A} state for $H^{13}C^{13}CH$

	ν_1	ν_2	ν_3	ν_4	ν_5	ν_6
r_1	0.7016	0.0577	0.0047	0	0.7064	0.0256
r_2	0.7016	0.0577	0.0047	0	-0.7064	-0.0256
R	-0.1232	0.9843	-0.5669	0	0	0
θ_1	0.0126	0.1108	0.5825	0	0.0309	-0.7066
θ_2	0.0126	0.1108	0.5825	0	-0.0309	0.7066
τ	0	0	0	1	0	0

Table 6.12: \mathbf{T} matrix of the \tilde{A} state for $H^{13}C^{13}CH$

	r_1	r_2	R	θ_1	θ_2	τ
r_1	1.076 amu ⁻¹	0	-0.045 amu ⁻¹	-0.051 $\frac{\text{\AA}}{\text{amu}}$	-0.051 $\frac{\text{\AA}}{\text{amu}}$	0
r_2	0	0.580 amu ⁻¹	-0.045 amu ⁻¹	-0.051 $\frac{\text{\AA}}{\text{amu}}$	-0.051 $\frac{\text{\AA}}{\text{amu}}$	0
R	-0.045 amu ⁻¹	-0.045 amu ⁻¹	0.167 amu ⁻¹	-0.064 $\frac{\text{\AA}}{\text{amu}}$	-0.064 $\frac{\text{\AA}}{\text{amu}}$	0
θ_1	-0.051 $\frac{\text{\AA}}{\text{amu}}$	-0.051 $\frac{\text{\AA}}{\text{amu}}$	-0.064 $\frac{\text{\AA}}{\text{amu}}$	1.041 $\frac{\text{\AA}}{\text{amu}}$	0.147 $\frac{\text{\AA}}{\text{amu}}$	0
θ_2	-0.051 $\frac{\text{\AA}}{\text{amu}}$	-0.051 $\frac{\text{\AA}}{\text{amu}}$	-0.064 $\frac{\text{\AA}}{\text{amu}}$	0.147 $\frac{\text{\AA}}{\text{amu}}$	0.629 $\frac{\text{\AA}}{\text{amu}}$	0
τ	0	0	0	0	0	2.063 $\frac{\text{\AA}}{\text{amu}}$

Table 6.13: \mathbf{G} matrix of the \tilde{A} state for $HCCD$

	ν_1	ν_2	ν_3	ν_4	ν_5	ν_6
r_1	0.9918	0.0597	0.0241	0	-0.0522	0.0437
r_2	0.0656	0.1525	0.0971	0	0.9706	0.0241
R	-0.1054	0.9793	-0.1749	0	-0.2321	0.1475
θ_1	0.0282	0.0898	0.8479	0	-0.0329	-0.3937
θ_2	-0.0117	0.0782	0.4903	0	0.0137	0.9060
τ	0	0	0	1	0	0

Table 6.14: **T** matrix of the \tilde{A} state for *HCCD*

$^{12}\text{C}_2\text{H}_2$				<i>HCCD</i>	
<i>X</i> State		<i>A</i> State		<i>X</i> State	
Cal.	Exp.	Cal.	Exp.	Cal.	Exp.
3497	3495.1	3002	2880.5 ¹	3460	3383.91
3415	3415.2	2913	2857.4	2656	2606.83
2011	2007.6	1420	1386.9	1884	1859.34
747	746.7	1065	1047.6	693	677.19
624	624.0	785	768.3	528	516.65
		771	764.8		

Table 6.15: Normal Mode Frequencies Obtained from the FG matrix analysis and their comparison with the experimental measurement

observed value is high.

6.3.2 Function Consideration of the Transition Moment

Historically, the possibility of variation of the transition moment does not bother many people. The transition moment is often treated in one of two ways. Since transition dipole and permanent multipole moments typically depend very weakly on molecular geometry, if one considers a limited region of the energy space, in most cases it is sufficient to consider transition moment as a constant, and therefore it drops out of the transition moment wavefunction overlap. Watson, for example, treated the electronic transition moment as independent of the stretching coordinates [113]. In other cases, it is sufficient to treat the transition moment as a linear function of some of the geometric parameters describing the vibrational motion under investigation.

We have a very different case for acetylene. There are several reasons for this:

1. The present DF datasets cover up to 18,000 cm^{-1} of internal energy. The pure bending polyads in these datasets involve large amplitude bend ($N_b \geq 22$). This is certainly beyond the range where the Condon approximation is still valid. The question is, within what range is our FC calculation valid? If FC fails within the range where the constant dipole treatment is valid, there is no further motivation to improve the FC calculations by including a coordinate dependent transition moment.
2. Transition moment is intrinsically a property of an entire molecule has. As we are working in the local mode representation, it would be difficult to find a proper definition of the transition moment.

Acetylene itself has provided us with many clues as to how the transition moment ought to behave. We know that under three geometric conditions, the transition moment must go to zero. These zero-moment geometries are: linear ($D_{\infty h}$), *trans* (C_{2h}) and “diamond” (D_{2d}). “Diamond” is a nickname I use to describe the acetylene geometry under extreme *trans*-bend, when the two Hydrogens bend to the center of the CC bond, one on top, one on bottom, equal distance away from the CC bond.

Therefore,

6.3.3 Dushinsky Rotation

As discussed previously, consideration of the Dushinsky Rotation will establish a connection between our calculation and Watson’s. As we adopt Sharp and Rosenstock’s convention [88] in calculating the Dushinsky Rotation matrices, the Dushinsky Rotation matrices according to Sharp and Rosenstock’s convention must be converted to those following the Watson convention.

The scheme illustrated by Figure 6-1, excluding the FC part, is essentially a derivation of Dushinsky Rotation effects. The internal coordinates for two electronic states are fundamentally and uniquely related to each other. However, the normal mode coordinates in the two states are not related in any obvious way. However, by using the transformation matrices derived from the FG analysis, a connection can

be established. Therefore, Dushinsky Rotation effects are fundamentally important where FC calculations are performed in the normal mode basis. In our particular application, the Dushinsky Rotation brings in some mixing of the local stretch overlap with the local bending overlap, and *vice versa*.

Before the derivation of the Dushinsky matrices, I would like to mention that there is a subtle difference between Sharp and Rosenstock's definition of the Dushinsky Rotation, and that of Watson's. Sharp and Rosenstock define the Dushinsky Rotation as the derivation of the lower state curvi-linear normal modes with respect to their upper state counterparts, in which the ground state normal coordinates are expressed as a linear combination of the excited state normal coordinates: $\mathbf{Q}'' = \mathbf{J}\mathbf{Q}' + \mathbf{K}$. Watson, on the other hand, defines the Dushinsky Rotation as the derivation of the excited-state dimension-less recti-linear normal modes with respect to their ground-state counterparts: $\mathbf{q}' = \mathbf{D}\mathbf{q}'' + \delta + \mathbf{O}(\mathbf{q}''^2)$.

Let us express the Dushinsky matrices in terms of Sharp and Rosenstock's symbols. We have

$$\mathbf{D}'' = \mathbf{L}''\mathbf{Q}'', \quad (6.34)$$

$$\mathbf{D}' = \mathbf{L}'\mathbf{Q}', \quad (6.35)$$

where \mathbf{Q}' and \mathbf{Q}'' are the upper and lower state normal coordinates, respectively, while \mathbf{D}' and \mathbf{D}'' are the respective internal coordinates. \mathbf{L}' and \mathbf{L}'' are the conversion matrices between the two.

$$\mathbf{D}'' = \mathbf{D}' + \Delta\mathbf{D}, \quad (6.36)$$

Combining Eqs. (6.34), (6.35) and (6.36), we obtain

$$\mathbf{L}''\mathbf{Q}'' = \mathbf{L}'\mathbf{Q}' + \Delta\mathbf{D}. \quad (6.37)$$

Therefore,

$$\mathbf{Q}'' = (\mathbf{L}'')^{-1}\mathbf{L}'\mathbf{Q}' + (\mathbf{L}'')^{-1}\Delta\mathbf{D} = \mathbf{J}\mathbf{Q}' + \mathbf{K}, \quad (6.38)$$

where

$$\mathbf{J} = (\mathbf{L}'')^{-1}\mathbf{L}' \quad (6.39)$$

and

$$\mathbf{K} = (\mathbf{L}'')^{-1}\Delta\mathbf{D} = (\mathbf{L}'')^{-1}(\mathbf{D}'' - \mathbf{D}'). \quad (6.40)$$

Now let us derive the Dushinsky matrices according to Watson's definition. Watson uses dimensionless normal coordinates, obtained by substituting $\mathbf{q}' = (\gamma')^{\frac{1}{2}}\mathbf{Q}'$, $\mathbf{q}'' = (\gamma'')^{\frac{1}{2}}\mathbf{Q}''$. Further, substitute $\gamma' = \mathbf{h}c\omega'/\mathbf{h}^2$, and $\gamma'' = \mathbf{h}c\omega''/\mathbf{h}^2$ into Eq. (6.38), and we get

$$(\gamma'')^{-\frac{1}{2}}\mathbf{q}'' = (\mathbf{L}'')^{-1}\mathbf{L}'(\gamma')^{-\frac{1}{2}}\mathbf{q}' + (\mathbf{L}'')^{-1}\Delta\mathbf{D}. \quad (6.41)$$

Hence, we have

$$\mathbf{q}' = (\gamma')^{\frac{1}{2}}(\mathbf{L}')^{-1}\mathbf{L}''(\gamma'')^{-\frac{1}{2}}\mathbf{q}'' - (\gamma')^{\frac{1}{2}}(\mathbf{L}')^{-1}\Delta\mathbf{D} = \mathbf{D}\mathbf{q}'' + \delta + \mathbf{O}(\mathbf{q}''^2) \quad (6.42)$$

where

$$\mathbf{D} = (\gamma')^{\frac{1}{2}}(\mathbf{L}')^{-1}\mathbf{L}''(\gamma'')^{-\frac{1}{2}} \quad (6.43)$$

and

$$\delta = -(\gamma')^{\frac{1}{2}}(\mathbf{L}')^{-1}\Delta\mathbf{D}. \quad (6.44)$$

6.4 Results

The first practical problem to be answered in this section is how to represent the results of multi-dimensional FC calculations. One-Dimensional FC results may simply be represented in 2D figures such as Figure 5-9, this is not the case for multi-dimensional results. In order to present the calculation results comprehensively, displaying the multi-dimensional FC factors as many 2D figures is *not* an option. In this section, we simplify this problem by only listing the calculated FC factors for the CC-stretch and trans-bending modes in the \tilde{X} state, by 3D surface plots, contour diagrams, and simulated spectrum. The choice of these two modes is due to two reasons. First of all, both modes contribute to the intensities for the bright state in the \tilde{X} state polyads, therefore they are the most important modes which contribute to the DF spectral intensities. Secondly, due to the former reason, we have direct measurements of bright state intensities for these modes, which makes direct comparison between theory and experiments possible.

Figure 6-4 contains surface plots for the calculated multi-dimensional FC factors. The four panels display FC factor plots for the zero-point state (upper left), $2\nu'_3$ (upper right), $\nu'_2 + \nu'_3$ (bottom left) and $\nu'_2 + 2\nu'_3$ vibrational states in the \tilde{A} state of $^{12}C_2H_2$. On each plot, the x axis represents the \tilde{X} state CC stretch quantum number, $v''_2 = 0 - 10$, the y axis represents the \tilde{X} state trans bending quantum number, $v''_4 = 0 - 30$. Each grid point on the 2D x-y surface stands for one ground state vibrational level. The \tilde{X} state vibrational levels are therefore the same for all four graphs. The z axis is the calculated FC factor. Observations from these plots include the different excited vibrational level in the \tilde{A} -state lighting up ground state vibrational levels with different Franck-Condon patterns. For example, the two parallel grooves on the $2\nu'_3$ graph stand for the two nodes along the trans-bending coordinate, while the two perpendicular grooves on the $\nu'_2 + \nu'_3$ graph stand for one node in the CC-stretch and one node along the trans-bending. For the FC factors shown in Figure 6-4, no Dushinsky rotation effects have been included in the calculation. Therefore the intensities are simply the product of the CC-stretch FC factors and the trans-bending

FC factors. This is revealed by the fact that all grooves lie parallel to the the x or y axis. Had Dushinsky rotation been taken into account, the nodal “valleys” would not remain parallel to the axes. The FC factors obtained with Dushinsky rotation considered are displayed in Figure 6-5. However, FC factors calculated without considering Dushinsky rotation already manifest the expected nodal structure along the CC stretch and trans-bend. The question is, how accurate are these results compared with the experimentally measured FC factors?

To answer this question, we rely on the contour plots to give us a detailed description of the 2D FC factors. Figure 6-5 displays three columns of FC factors in contour patterns. These plots are the equivalent of the projection of the 3D surface plots in Figure 6-4 onto the xy plane. Among the twelve panels displayed in Figure 6-5, each row stands for the same upper vibrational level in the \tilde{A} state. From top to bottom, they are respectively for the zero-point level, $2\nu'_3$, $\nu'_2 + \nu'_3$, $\nu'_2 + 2\nu'_3$. Similar to Figure 6-4, the x axis on each panel represents the \tilde{X} -state CC-stretch quantum number, ν''_2 , while the y axis represents the \tilde{X} -state trans bending quantum number, ν''_4 . The three columns displayed are respectively, calculated FC factors without considering Dushinsky rotation on the left, calculated FC factors taking into account Dushinsky rotation effect discussed in this chapter on the right column, and the middle column depicts the experimentally measured FC factors. The sloping cut off of the experimental contour is due to absence of measurements above a certain internal energy level, or in the polyad language, above a certain N_{res} . Judging from the appearance of these contour plots, the contours in the left column are more consistent with the experimental measurements, with every nodal point within two quanta away from the minima on the contours in the middle column. The experimental contours display little Dushinsky rotation effects as are depicted in the right column. Nevertheless, based on the intensities obtained from the algorithm described in Chapter 5 and in this chapter, and the frequency information given by Jacobson’s normal mode effective Hamiltonian model, we are able to start to produce some simulated spectra.

Figure 6-6 is an example of such a simulated spectrum. It depicts the observed ground state DF spectrum on the bottom trace and the simulated DF spectrum on

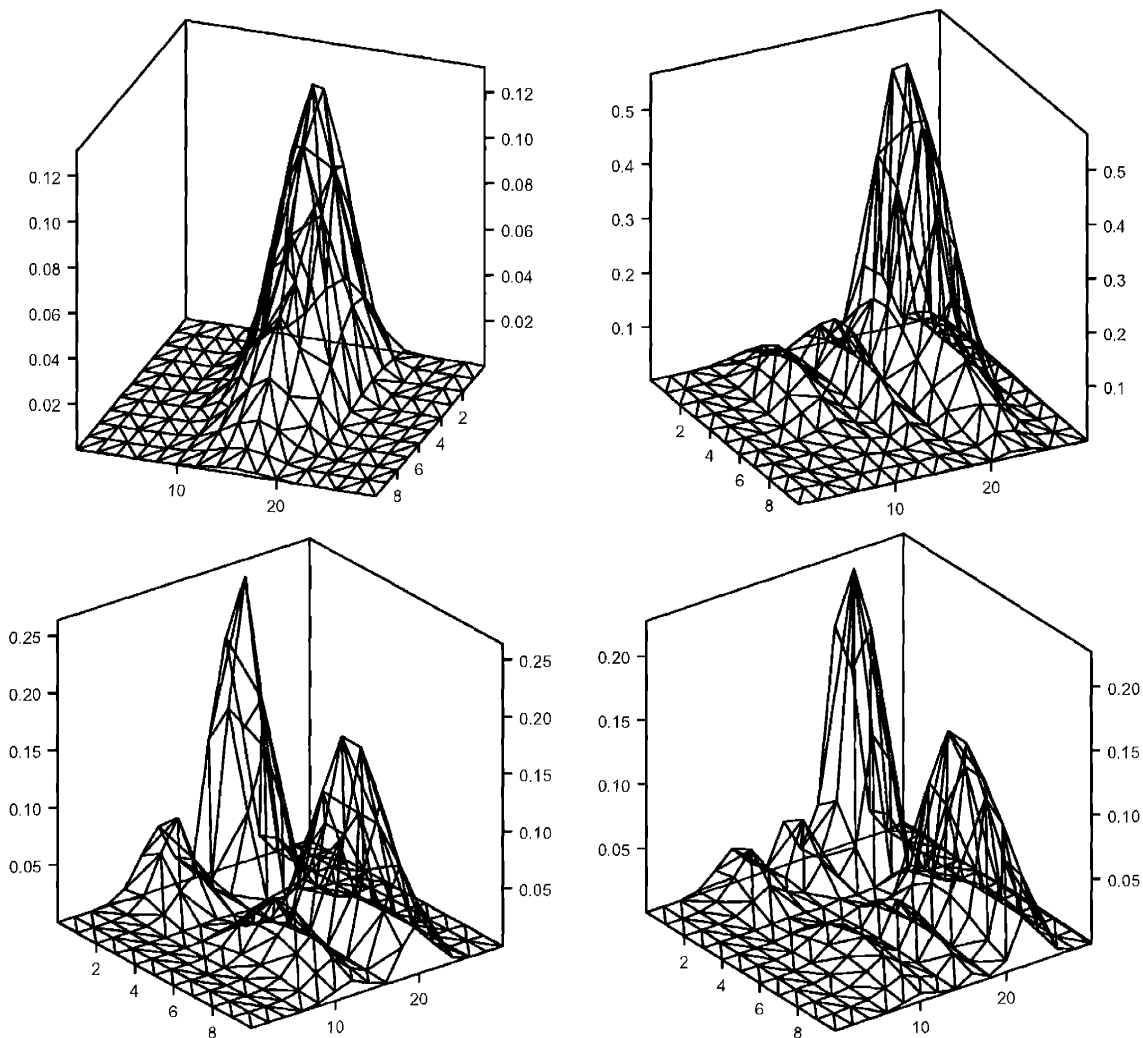


Figure 6-4: Surface plots for the calculated multi-dimensional FC factors. On all graphs, the x axis represents the \tilde{X} state CC stretch quantum number, ν_2'' , the y axis represents the \tilde{X} state trans-bending quantum number, ν_4'' . The z axis is the calculated FC factor. The four graphs are plotted for the zero-point level (upper left), $2\nu_3'$ (upper right), $\nu_2' + \nu_3'$ (bottom left) and $\nu_2' + 2\nu_3'$ vibrational states in the \tilde{A} state. Each grid point on the 2D xy surface stands for one vibrational level, and the ground state levels are the same for all four graphs. However, different excitation patterns in the \tilde{A} state light up these states with different 2D Franck-Condon patterns. For example, the two parallel grooves on the $2\nu_3'$ graph stand for the two nodes in the trans-bending coordinate, while the two perpendicular grooves on the $\nu_2' + \nu_3'$ graph stand for one node in the CC-stretch and one node along the trans-bending.

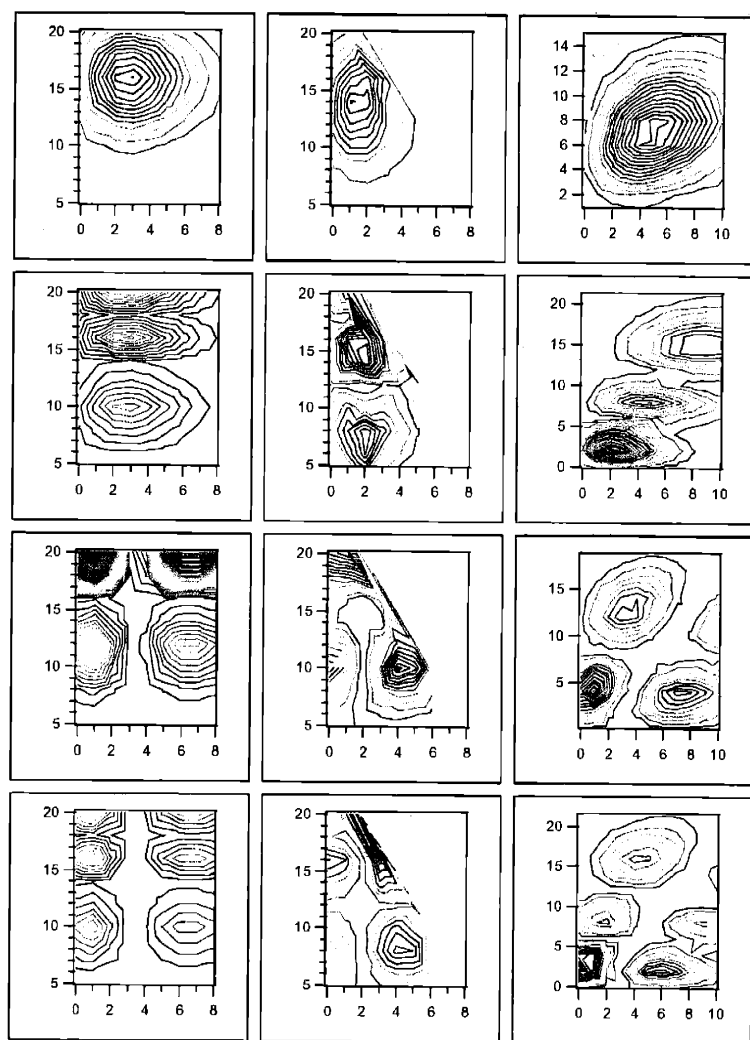


Figure 6-5: Comparison of the multidimensional FC calculation with the experimentally measured FC factors. On each of the twelve plots, the x axis represents the \tilde{X} -state CC-stretch quantum number, ν_2'' , while the y axis represents the \tilde{X} -state trans-bending quantum number, ν_4'' . These plots are contours of the FC factor, in other words, they correspond to the projection of the surfaces in Figure 6-4 onto the xy plane. The left column is the calculated FC factors without considering Dushinsky rotation. The right column depicts the calculated FC factors, taking into account Dushinsky rotations discussed in this chapter. The middle column is the experimentally measured FC factors. The sloping cut off of the experimental contour is due to the absence of measured data above a certain internal energy level. Each row stands for a certain vibrational level in the upper \tilde{A} state. They are, respectively from top to bottom, the zero-point state, $2\nu_3$, $\nu_2 + \nu_3$, $\nu_2 + 2\nu_3$. Judging from the appearance of these contour plots, the contours in the left column are more consistent with the experimental measurements, with every nodal point within two quanta from the minima on the contours in the middle column.

the top trace. The spectrum is simulated frequency-wise by the normal mode effective Hamiltonian model, and intensity-wise by the FC factors reported in this chapter. The simulated spectrum is satisfactorily consistent with the origin band DF spectrum up to $8,000 \text{ cm}^{-1}$, however, discrepancies appear at higher internal energies. My guess is that $8,000 \text{ cm}^{-1}$ is where the harmonic-based, local \leftrightarrow normal ladder operators (described in subsection 5.3.2) start to fail. The spectral simulation brings me to the conclusion that although such a calculation still has some room for improvement before being capable of simulating real DF spectra, the fact that the nodal structures have been successfully reproduced by the multi-dimensional FC calculation is a big step forward compared with traditional, normal mode based FC calculations.

6.5 Comparison with Watson's FC Calculation on Acetylene

In addition to our calculation, we have also compared several numerical methods used to calculate Franck-Condon factors.

The reason we find the Watson calculation significant, is not only because we are calculating the same set of intensity factors for the molecule acetylene, but because we find Watson's algorithm distinctively innovative, and in addition, results from his calculation are reasonably consistent with the experimental observations from our research group. Watson has been quite careful about publishing these results, as his pre-print manuscript existed in our group for more than two years before the paper was submitted to the Journal of Molecular Spectroscopy.

Although many scientists, us included, start the Franck-Condon calculation from individual eigenfunction overlaps, Watson took the approach of a generating function, G . Eq. [26] from the Watson FC paper [113] is:

$$G = 2^{-1/2} \pi^{-9/4} (\det \mathbf{D})^{1/2} \int \int \int dq_1'' dq_2'' d\rho_4'' (\rho_4'')^{1/2}$$

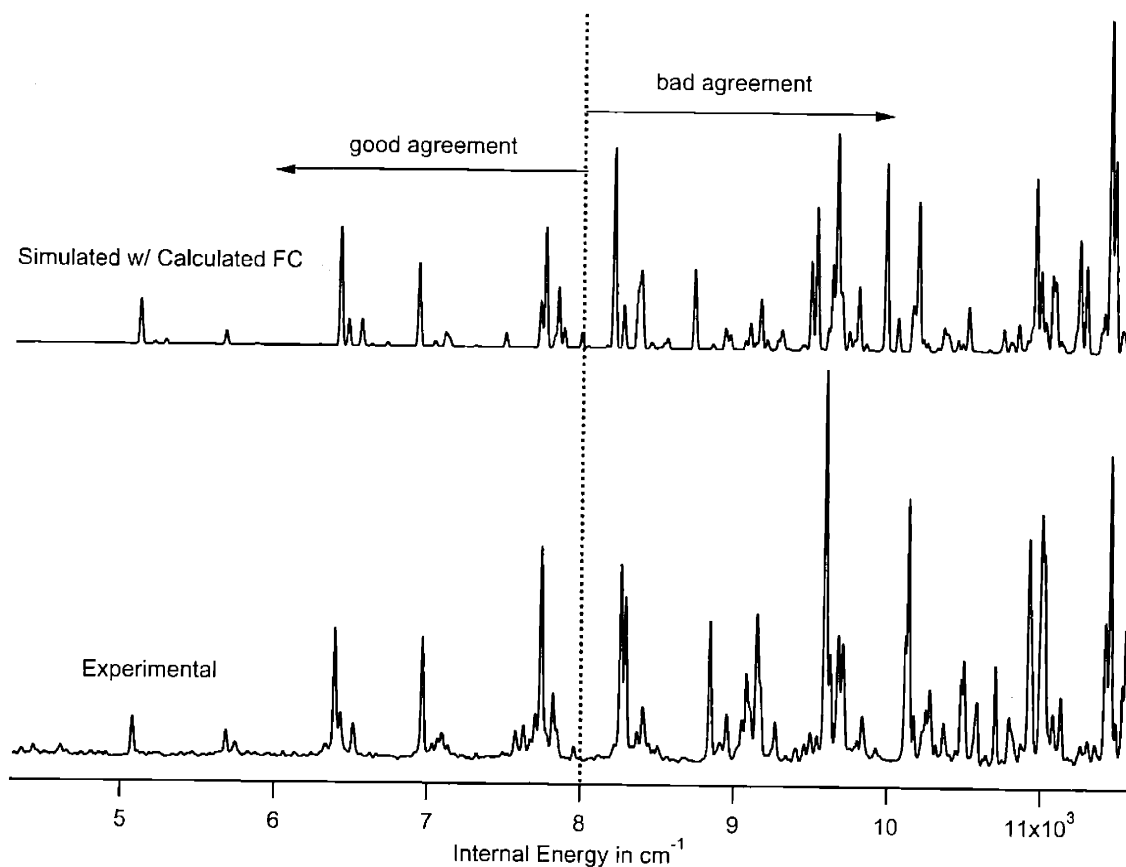


Figure 6-6: Comparison of the simulated origin band DF spectrum with the experimental DF spectrum. The spectrum is simulated frequency-wise by the normal mode effective Hamiltonian model, and intensity-wise by the FC factors reported in this chapter. Up to $8,000 \text{ cm}^{-1}$ the simulated spectrum agrees well with the origin band DF spectrum, however, more discrepancies appear in higher internal energies.

$$\begin{aligned}
& \times \exp[-\tilde{\mathbf{q}}'' \mathbf{A} \mathbf{q}'' - \tilde{\delta} \mathbf{D} \mathbf{q}'' - \frac{1}{2} \tilde{\delta} \delta + \sqrt{2} \tilde{\mathbf{s}} (\mathbf{D} \mathbf{q}'' + \delta) \\
& - \frac{1}{2} \tilde{s} s + \sqrt{2} q_1'' t_1 + \sqrt{2} q_2'' t_2 + \frac{1}{\sqrt{2}} \rho_4'' t_4 (u_4 + u_4^{-1}) - \frac{1}{2} \tilde{t} t] \\
= & \sum_{v'v''} \frac{\langle v'_1 v'_2 v'_3 | v''_1 v''_2 v''_4 l''_4 \rangle}{(v'_1! v'_2! v'_3! v''_1! v''_2! 2^{v''_4})^{1/2}} \times \frac{s_1^{v'_1} s_2^{v'_2} s_3^{v'_3} t_1^{v''_1} t_2^{v''_2} t_4^{v''_4} u_4^{l''_4}}{\{[\frac{1}{2}(v''_4 + l''_4)]! [\frac{1}{2}(v''_4 - l''_4)]!\}^{1/2}}, \quad (6.45)
\end{aligned}$$

In this equation, \mathbf{D} is the transformation matrix between the normal modes of the \tilde{A} state and the \tilde{X} state, corresponding to a Dushinsky Rotation matrix. δ corresponds to the geometric displacement of normal coordinates between the \tilde{A} state and the \tilde{X} state. $s_1, s_2, s_3, t_1, t_2, t_3$ and u_4 are dummy variables, in other words, these can be any values. Matrix \mathbf{A} is derived from the \mathbf{D} matrix, defined by Eq. [13] in the Watson FC paper [113]:

$$\mathbf{A} = \frac{1}{2}(\mathbf{E} + \tilde{\mathbf{D}}\mathbf{D}), \quad (6.46)$$

\mathbf{E} being the identity matrix. Furthermore, Watson examined a special subset from the generation function:

$$\begin{aligned}
v'_1 + v'_2 + v'_3 + v''_1 + v''_2 + v''_4 &= n \\
-v''_4 &\leq l''_4 \leq v''_4. \quad (6.47)
\end{aligned}$$

This poses a constraint on sums over basis function quantum numbers in order to complete a calculation of a value of the Generation function. I agree in part that this is a reasonable criteria, however, some practical difficulties result from the subset constraint, and these will be discussed later in detail.

I personally find the rest of Watson's algorithm extraordinarily interesting. Since the dummy variables, $s_1, s_2, s_3, t_1, t_2, t_3$ and u_4 can be any values, one can sample as many functional value of G upon combinations of the dummy variable, as is necessary. According to Eq. 6.45, one can then run a least square fit of the generation function, using the dummy variables and their resulting G values as data points. The fitted

$\tilde{A}(v_1v_2v_3) \rightarrow \tilde{X}(v_1v_2v_4^l)$	Watson	Our Calc.
(000) \rightarrow (000 ⁰)	1	1
(001) \rightarrow (000 ⁰)	16.27	16.2722
(002) \rightarrow (000 ⁰)	129.5	129.499
(003) \rightarrow (000 ⁰)	671.4	671.38
(004) \rightarrow (000 ⁰)	2548	2548.19
(005) \rightarrow (000 ⁰)	7543	7543.02

Table 6.16: Comparison between Watson’s calculated value and our program for the absorption series, $n\nu'_3 \leftarrow 0$ progression, of the $\tilde{A} \leftarrow \tilde{X}$ system of C_2H_2 . The results reach satisfactory agreement.

values would finally yield the matrix elements, $\langle v'_1v'_2v'_3|v''_1v''_2v''_4l''_4\rangle$, as coefficients.

I have written a program using Watson’s algorithm and his Dushinsky transformation matrixes, \mathbf{D} , and displacement vectors, δ :

$$\mathbf{D} = \begin{bmatrix} 0.7419 & -0.0496 & 1.4542 \\ 0.0294 & 0.8521 & 0.0644 \\ -0.3635 & -0.0075 & 0.9888 \end{bmatrix} \quad \delta = \begin{bmatrix} -4.037 \\ 0.995 \\ -6.477 \end{bmatrix} \quad (6.48)$$

to calculate the Franck-Condon factors that are reported in Watson’s paper, and have obtained satisfactory agreement with his results. The Franck-Condon results are compared in Tables 6.16 and 6.17.

In the course of calculating the Franck-Condon factors according to Watson’s method, we did find a problem in applying the generation function with the special subset defined by Eq. (6.47). To be specific, the number of parameters needed for the fit increases sharply with a slight increase in the quantum numbers of the vibrational modes involved in the calculation. For example, if one needs to calculate the Franck-Condon factor for the transition $1_0^12_0^13^44^1K_1^2$, in this case, the Watson subset defined by Eq. (6.47) leads to $n = 1 + 1 + 4 + 0 + 0 + 1 = 7$. If we consider the possible combinations of these quantum numbers that sum to 7, there are $6^7 = 279,936$ possibilities. This is the number of coefficients that must be obtained by the fit, prior to angular momentum combinations. For this reason, we find it infeasible to use the Watson method to obtain FC factors for acetylene \tilde{X} state polyads, especially those

$\tilde{A}(v_1 v_2 v_3) \rightarrow \tilde{X}(v_1 v_2 v_4^{l_4})$	Watson	Our Calc.
(000) \rightarrow (000 ⁰)	1	1
(000) \rightarrow (001 ¹)	10.74	10.7405
(000) \rightarrow (002 ²)	60.43	60.4344
(000) \rightarrow (002 ⁰)	99.88	99.8807
(000) \rightarrow (003 ³)	236.8	236.805
(000) \rightarrow (003 ¹)	484.8	484.83
(000) \rightarrow (004 ⁴)	725.0	725.028
(000) \rightarrow (004 ²)	1631	1631.17
(000) \rightarrow (004 ⁰)	2022	2022.1
(000) \rightarrow (005 ⁵)	1846	1845.89
(000) \rightarrow (005 ³)	4263	4263.19
(000) \rightarrow (005 ¹)	5814	5814.4

Table 6.17: Comparison between Watson's calculated value and our program for the emission series, $0 \leftarrow n\nu_4''$ progression, of the $\tilde{A} \leftarrow \tilde{X}$ system of C_2H_2 . Results also reach satisfactory agreement.

v_4	l_4	(1, 0, 0, $v_4 - 2, 0$)	(0, 1, 0, $v_4, 0$)
2	0	2.181	69.795
3	1	24.936	337.603
4	0	248.612	1402.340
5	1	1288.13	4016.110
6	0	5777.16	9761.400

Table 6.18: Discrepancy in the 0_0^0 Band. our program based on Watson's FC algorithm using his Dushinsky matrices is predicting another series of bright states $1, 0, 0, v_4'', 0$ beside the only series of bright states that are experimentally confirmed, the $0, 1, 0, v_4'', 0$ series.

containing more than one quantum in the CC stretching mode.

As another simple test of the Watson calculation, we attempted to calculate the FC factors for the series of dark states $(1, 0, 0, v_4 - 2, 0)$ and bright states $(0, 1, 0, v_4, 0)$, which are members of the same polyad. In order to use Watson's subset Eq. (6.47), I only calculated the 0_0^0 band emission to these states. The surprising findings are enlisted in Table 6.18:

As v_4 increases, the intensity of the known dark state $(1, 0, 0, v_4 - 2, 0)$ increases relative to the known bright state $(0, 1, 0, v_4, 0)$. This result contradicts the experimental findings of the single bright state per polyad assumption, first raised by Kellman and

coworkers [42, 47, 48] and confirmed by our DF spectra.

Going back to Watson's paper, we found that the changing in equilibrium distance of the CH bond (the first element) in the δ in Eq. (6.48) is rather large. This can be seen with the following calculation:

From our FG matrix analysis, if we only consider the *gerade* block from the transformation matrix:

$$\mathbf{L}'' = \begin{bmatrix} 1.0254 & 0.1555 & 0 \\ -0.1711 & 0.3706 & 0 \\ 0 & 0 & -1.1047 \end{bmatrix} \quad (6.49)$$

$$\mathbf{L}' = \begin{bmatrix} -1.0353 & -0.0474 & 0.0382 \\ 0.0837 & -0.3682 & 0.1553 \\ 0.0835 & -0.2337 & -1.3159 \end{bmatrix} \quad (6.50)$$

$$\Delta \mathbf{D} = \begin{bmatrix} 1.0605 - 1.097 \\ 1.2033 - 1.375 \\ \left(180 \times \sqrt{1.0605 \times 1.2033} - 122.48 \times \sqrt{1.097 \times 1.375} \right) \times \frac{\pi}{180} \end{bmatrix} (\text{\AA}); \quad (6.51)$$

$$\omega_0 = 2\pi c \times \begin{bmatrix} 3519.3 & 0 & 0 \\ 0 & 1962.9 & 0 \\ 0 & 0 & 746.7 \end{bmatrix} \times 100(\text{Hz}) \quad (6.52)$$

$$\omega_1 = 2\pi c \times \begin{bmatrix} 3002.3 & 0 & 0 \\ 0 & 1420.4 & 0 \\ 0 & 0 & 1065.0 \end{bmatrix} \times 100(\text{Hz}) \quad (6.53)$$

$$\Gamma_0 = \frac{\omega_0}{\hbar} \quad \Gamma_1 = \frac{\omega_1}{\hbar} \quad (6.54)$$

$$\mathbf{J} = \mathbf{L}''^{-1}\mathbf{L}' \quad \mathbf{K} = \mathbf{L}''^{-1}\mathbf{r} \quad (6.55)$$

$$\mathbf{d} = \sqrt{\Gamma_1}\mathbf{J}^{-1}\sqrt{\Gamma_0^{-1}} = \begin{bmatrix} -0.9264 & -0.1240 & 0.0272 \\ 0.1241 & -0.8168 & 0.4588 \\ -0.0541 & 0.1210 & 0.9331 \end{bmatrix} \quad (6.56)$$

$$\delta = -\sqrt{\Gamma_1}\mathbf{J}^{-1}\mathbf{K} = \begin{bmatrix} -0.0102 \\ -1.0303 \\ 4.1025 \end{bmatrix} \quad (6.57)$$

Comparing the d and δ matrices in Eqs. (6.56) and (6.57) that we obtain from FG using the Sharp and Rosenstock's convention [88], and Watson's Dushinsky matrices (Eq. (6.48)), his CH bond length difference (-4.037) is much larger than mine (-0.0102). This is inconsistent with prior knowledge of the electronically excited state geometry, and we believe this is the reason Watson's calculation erroneously predicts an additional series of bright states in each polyad.

6.6 Conclusion

In this chapter, I have listed the necessary steps to expand the 1D, *gerade* mode FC calculations described in the former chapter into a global multi-dimensional FC calculation. Results for the bright states in the \widetilde{X} state of acetylene have been represented, and thoughts on the comparison between my method and Watson's FC calculation are presented. A suggestion for why Watson's calculation is unphysical in predicting another set of bright states in polyads on the \widetilde{X} -state is given by comparing our curvilinear Dushinsky transformation matrices with Watson's.

Chapter 7

Observation of Coriolis Coupling between $\nu_2 + 4\nu_4$ and $7\nu_4$ in Acetylene $\tilde{X}^1\Sigma_g^+$ by Stimulated Emission Pumping Spectroscopy

7.1 Introduction

Coriolis rotationvibration coupling has a long history of being implicated in the vibrational dynamics of small polyatomic molecules. The first such evidence came primarily from rotationally unresolved studies in which the dependencies of rates and extent of intramolecular vibrational redistribution (IVR) on rotation were inferred from changes in spectra or dynamics that accompanied varying amounts of rotational cooling in supersonic jets. Parmenter and co-workers [15], for example, observed significant decreases in the amount of congested fluorescence (not assignable as emission from a single zeroth-order vibrational level) when vibrationally excited levels of S_1 aromatics were excited in supersonic jets rather than at room temperature. Detailed analysis of spectra from paradifluorobenzene [16] indicated that both strong, non-resonant coupling and weak, near-resonant coupling had some degree of rotational

dependence. Similarly, McDonald and co-workers [51] observed that the dilution of CH stretch infrared fluorescence in small polyatomic molecules depended on the rotational temperature of a supersonic expansion, the mixing increasing with increasing rotational temperature. Zewail and co-workers [53, 19] also observed dependencies of quantum beat frequencies on rotational temperature in time- and frequency- resolved fluorescence from S_1 anthracene. Different beat frequencies were found to be more pronounced at different temperatures or when pumping different parts of the rotational contour. This dependence, however, was interpreted as what has been called [54, 3] a “passive” effect of rotations causing different vibrations to tune into and out of resonance due to the vibrational dependence of rotational constants rather than an “active” rotationvibration coupling.

One of the first rotationally resolved demonstrations of the participation of Coriolis coupling in vibrational dynamics came from the study in this laboratory of \widetilde{X}^1A_1 formaldehyde by stimulated emission pumping (SEP) spectroscopy [14]. This study showed that vibrational level mixing rapidly increased with both J and K_a for levels near $E_{vib} = 8000 \text{ cm}^{-1}$. The extent of mixing was shown to be at least qualitatively consistent with Coriolis-coupling matrix elements calculated from a harmonic oscillator basis set.

Another unambiguous demonstration of the dynamic consequences of rotation-vibration coupling came in the rotationally resolved sub-Doppler, two-photon fluorescence excitation studies of S_1 benzene by Riedle and co-workers [78, 86]. In the so-called “channel three” region of benzene, it was seen that rotational levels with $K \neq 0$ were strongly coupled to a manifold of levels that underwent rapid radiation-less decay, the rotational dependence clearly indicating that Coriolis coupling was the first step in the relaxation.

Evidence of rotational involvement has been somewhat more elusive in the numerous studies of IVR at rotational resolution as seen using infrared absorption in the ground electronic state of small polyatomic molecules (reviewed, for example, in Refs. [57] and [72]). Some molecules show little or no dependence of IVR on rotational level. In other molecules, there is a clear change in the width of homoge-

neously broadened single rotational lines or the density of transitions into “clumps” of states (where each clump consists of several eigenstates with a common value of J but mixed vibrational identities) as a function of rotational quantum numbers J and/or K . Unlike the seemingly ubiquitous 2:1 bendstretch resonance observed in CH oscillators with sp^3 [111, 87] or sp^2 [90, 91] hybridization, however, there is little if any evidence for strong, low-order, off-resonance (i.e., separated by an amount much greater than the coherence width in a typical experiment) Coriolis coupling among easily identified vibrational levels. Rather, the evidence seems to point to numerous (but weak) high-order interactions among the near-isoenergetic “bath modes” that lead to dissipative IVR at high state densities. Green et al. [22], for example, have recently shown by infrared microwave double resonance spectroscopy that the rotational spectrum of vibrationally mixed levels in propynol is characterized by a spread of rotational constants that narrow with increasing K_a , indicating extensive Coriolis mixing among the bath modes coupled to the initially excited acetylenic CH stretch.

The numerous studies of IVR in acetylene to date seem to show that Coriolis coupling is relatively unimportant to its vibrational dynamics, at least at relatively short times. The recent dispersed fluorescence (DF) spectra from this laboratory [74, 40, 39] have been assigned on the basis of an effective Hamiltonian that invokes ~ 12 off-diagonal anharmonic resonances in addition to the diagonal anharmonicities of the individual vibrations. Vibrational levels up to $15,000\text{ cm}^{-1}$ in the $\widetilde{X}^1\Sigma_g^+$ state have been fit by this Hamiltonian to an accuracy well within the 5-cm^{-1} resolution of the spectra. The simplicity of this Hamiltonian leads to a block-diagonal structure characterized by a set of three approximately conserved quantum numbers for each block, commonly referred to as a polyad [20, 42, 47]. These quantum numbers are: $N_s = \nu_1 + \nu_2 + \nu_3$, the total number of stretching quanta; $N_{res} = 5\nu_1 + 3\nu_2 + 5\nu_3 + \nu_4 + \nu_5$, which reflects the approximate resonant frequency ratios among the normal modes; and l , the total vibrational angular momentum. (When considering rotations, a polyad is also characterized by the rigorously conserved total angular momentum quantum number J .) The validity of the polyad model at short times is shown by the ability of spectral pattern recognition techniques to disentangle overlapping polyads

and then to extract vibrational assignments from the DF spectra.

Rotationvibration coupling (which, if strong enough, would lead to a breakdown of recognizable polyad structure in the spectrum [102]) has been observed in acetylene previously, but not as a dominant influence on the vibrational level structure. Yang et al. [119], for example, extracted Coriolis coupling parameters for three pairs of vibrational levels (out of a total of 82 levels) in the 12,800-18,500 cm^{-1} range. Each pair has a zero-order separation of $\leq 2 \text{ cm}^{-1}$ and the interacting zero-order levels (when assigned) differ by 10 or more vibrational quanta. Smith and Winn [94] propose one additional “global” Coriolis perturbation of the zero-order state $\nu_2 + 3\nu_3$ by the nearby state $3\nu_3 + \nu_4 + 2\nu_5$. (Alternatively, Zhan et al. [120] have fit this perturbation to a three-level system that involves both anharmonic and rotational l coupling.) The observed states have approximately 11,600 cm^{-1} of vibrational energy with a zero-order energy difference $\leq 1 \text{ cm}^{-1}$. The weak coupling revealed by such accidental degeneracies is unlikely to contribute significantly to IVR in acetylene.

IRUV double-resonance spectroscopy has also revealed perturbations that may be due to Coriolis coupling in the $3\nu_3$ [109] and $\nu_2 + 3\nu_3$ [65, 66] vibrational levels. In the $3\nu_3$ level, however, the perturbations measured by Utz et al. have matrix elements $\leq 0.05 \text{ cm}^{-1}$ and result in mixing that exceeds 10% for only one rotational level. Similarly, even though Milce and Orr have observed unexpected odd ΔJ collision-induced ro-vibrational energy transfer which they attribute to Coriolis coupling among $\nu_2 + 3\nu_3$ and other nearby levels, the mixing is strong for only a small number of rotational states and is not expected to be generally important to acetylene IVR dynamics.

Previous studies of acetylene using SEP [8, 45] also concluded that although anharmonic coupling caused significant scrambling of vibrational levels, rotational levels remained relatively uncoupled from vibrations, at least for $l = 0$ [8] and probably also for $l = 2$ [45]. The improvements in our understanding of the vibrational level structure that have resulted from the DF studies have led us now to reexamine acetylene with SEP to look for specific instances of breakdown of the polyad model that might become apparent at longer time (i.e., at higher resolution). We find that although we can clearly assign one Coriolis interaction (between the zero-order levels $\nu_2 + 4\nu_4$ and

$7\nu_4$), we expect rotationvibration coupling to be generally unimportant to acetylene vibrational dynamics.

7.2 Experimental Details

The experimental apparatus is a descendant of previous SEP setups in this laboratory [45, 49]. Numerous evolutionary changes, however, warrant description. The output of a single XeCl excimer laser (Lambda Physik LPX210icc, typically 200300 mJ/pulse at 308 nm) is divided (roughly 40/60) and used to pump two dye lasers. The first dye laser (Lambda Physik FL2002), the PUMP, is used to excite the sample to a selected rovibronic level in the first excited singlet state (\tilde{A}^1A_u) of acetylene. This laser is fitted with an intracavity etalon and tuned over a 12-cm^{-1} range by varying the intracavity pressure of nitrogen between vacuum and 1 atm. The visible output (Coumarin 450 dye) is frequency-doubled in a β -BBO crystal (CSK crystals) that is manually angle-tuned, giving a typical UV output of a few hundred mJ/pulse in a spectral width of approximately 0.05 cm^{-1} . The second dye laser (Lambda Physik FL3002), the DUMP, stimulates emission from the initially prepared state to high vibrational levels of the ground electronic state ($\tilde{X}^1\Sigma_g^+$). For the experiments described here in the wavelength range 500540 nm, this laser is used primarily with Coumarin 503 dye. The visible output is frequency-doubled in a second β -BBO crystal, producing up to several hundred mJ/pulse of UV. This crystal is used with a homebuilt autotracking system that allows for continuous scanning. For most of the experiments described here, this laser is also used with an intracavity etalon and pressure-tuned, using either nitrogen or SF_6 , so that this laser also has a resolution of approximately 0.05 cm^{-1} . The doubled output of each dye laser is separated from its fundamental by a 60° S1UV fused-silica prism and the second harmonic is then directed parallel to its original path by a second 60° prism. This arrangement is designed to minimize changes in alignment and overlap of the two lasers in the fluorescence viewing regions. A portion of the visible output of each dye laser is directed through a tellurium oven and onto a photodiode. Tellurium ($^{130}\text{Te}_2$) absorption transitions [6] are used to

provide wavenumber calibration for the fundamental of each dye laser with a typical accuracy of 0.02 cm^{-1} .

Acetylene (Matheson purified grade) is stored in a stainless steel bulb with a small amount of acetone to inhibit polymerization. Each day, an acetylene sample (~ 200 mTorr) is prepared by first pumping off any volatile fraction after cooling the storage bulb with liquid nitrogen and then distilling the desired pressure from a pentane slurry (~ 140 K). The sample is transferred to an H-shaped SEP fluorescence cell made primarily of stainless steel and fitted with S1UV quartz windows. The PUMP dye laser beam is divided by a 50/50 beamsplitter, and the two resulting beams are directed through the two parallel arms of the cell. The DUMP beam counterpropagates through one arm of the cell. The PUMP beam is focused with a 25-cm focal-length lens to a spot size of approximately $\frac{1}{4}$ -mm diameter, while the DUMP beam is collimated to a somewhat larger spot size (~ 1 mm) with a Galilean telescope to ensure illumination of the entire PUMP volume by the DUMP laser. Spontaneous $\tilde{A} \rightarrow \tilde{X}$ fluorescence perpendicular to the PUMP laser is detected from both arms of the cell by a set of matched Hamamatsu R331 photomultiplier tubes. A Schott BG-1 filter is placed in front of each photomultiplier to reduce scattered light from both the PUMP and DUMP lasers. The signals from the two photomultipliers are sent directly to separate SRS Model 250 boxcar integrators with gates (100 ns) carefully matched and synchronized. After the PUMP laser is tuned to a selected $\tilde{A} \leftarrow \tilde{X}$ rovibronic transition, the amplitudes of the signals detected from the two arms of the cell are matched by varying shutter openings in front of the two photomultipliers. When obtaining SEP spectra, the DUMP laser frequency is scanned, and integrated signals from the two photomultipliers (and the simultaneously recorded tellurium calibration signal for the DUMP laser) are digitized, compared, and recorded by a personal computer using programs written in LabVIEW. When the DUMP laser is in resonance with an $\tilde{A} \rightarrow \tilde{X}$ fluorescence transition, emission is stimulated in the laser propagation direction, resulting in a decrease in the amount of fluorescence detected by the photomultiplier perpendicular to the DUMP beam. The SEP signal is calculated as the percentage decrease (%dip) in the amount of fluorescence in the

signal (PUMP + DUMP) channel relative to the reference (PUMP-only) channel, i.e.,

$$\%dip = \frac{reference - signal}{reference} \times 100\% \quad (7.1)$$

After calibration, the internal energy of the final state is calculated as the difference between the term value of the pumped state [95] and the DUMP photon energy. The observed transitions can be confirmed to be downward rather than upward (to higher excited states) by verifying term value coincidences after pumping different excited rotational states [44]. Transition wavenumbers (recorded to $\pm 0.01 \text{ cm}^{-1}$) are determined by fitting Lorentzian functions to each peak using the Origin data analysis software package; the fit also yields a value for the linewidth of these transitions. Linewidths of all SEP transitions observed in this experiment are similar ($\sim 0.15 \text{ cm}^{-1}$ FWHM), so relative intensities of transitions within a single scan are estimated from peak heights only.

7.3 Results

A survey of several bands in the low internal energy portion of the acetylene $\tilde{A} \longrightarrow \tilde{X}$ spectrum using SEP ($N_{res} = 711$; vibrational energy approximately 40007000 cm^{-1}) shows that most of the features observed in dispersed fluorescence spectra are, as they had been assigned, single vibrational levels. The so-called “extra transitions” that O'Brien *et al.* [74] were unable to plausibly assign as emission to \tilde{X} -state vibrational levels are completely absent from the SEP spectra, indicating that these transitions are, as proposed, due to some other source¹. Thus, in this low internal energy regime, the SEP spectra reveal little new information about the vibrational dynamics of acetylene.

One notable exception is in the $N_{res} = 7$ region, which is the focus of this work. In the absence of any vibrational or rovibrational coupling, transitions would be expected in this region to the zero-order bright state $\nu_2 + 4\nu_4$. The difference in the

¹The source of these transitions is emission from \tilde{A} state levels populated by K'_a -changing collisional energy transfer, as Chap. indicates.

harmonic frequencies of ν_4 and ν_5 (*trans*- and *cis*-bend, respectively) is such that the DarlingDennison bend resonance with $\nu_2 + 2\nu_4 + 2\nu_5$ should be relatively ineffective for this state, with calculated mixing of less than 1%. Other known anharmonic resonances are expected to have even less influence (less than 0.1% mixing) on the vibrational level structure at this energy. Thus, we would expect the SEP spectrum in this region to be simple. For example, after pumping a single \tilde{A} state rovibronic level with $K'_a = 1$, we would expect the Q-branch region of the SEP spectrum to consist of transitions to \tilde{X} -state levels with vibrational angular momentum $l'' = 0$ and $l'' = 2$ in $\nu_2 + 4\nu_4$, due to the $K'_a l'' = \pm 1$ selection rule for *c*-type transitions. (These transitions would be unresolved in DF spectra, at least for low values of J .) The SEP spectrum from such a level is shown in Fig. 7-1 (bottom), obtained after pumping the Q(5) transition in the $V_0^2 K_0^1$ vibronic band. (In this notation for the vibronic transition, V represents the trans-bending vibration which is ν_4 in the \tilde{X} state and ν_3 in the \tilde{A} state; K represents K_a in the \tilde{A} state and l in the \tilde{X} state.) The Q-branch region of the spectrum actually consists of four resolved rotational transitions: two relatively strong transitions interleaved with two weaker transitions, suggesting the presence of a dark vibrational level gaining oscillator strength through coupling to $\nu_2 + 4\nu_4$. All four transitions are confirmed as belonging to $J'' = 5$ by their observation as R(5) transitions in the SEP spectrum recorded after pumping the P(7) transition.

The only vibrational level expected to be nearly in resonance with $\nu_2 + 4\nu_4$, on the basis of the effective Hamiltonian derived from the DF results [40, 39], is the level $7\nu_4$, calculated to have a zero-order energy within 2 cm^{-1} of $\nu_2 + 4\nu_4$. This level, having an odd number of bending quanta and thus necessarily an odd value for l , is not part of the same polyad and cannot couple to the zero-order bright state by any anharmonic resonance. It can, however, mix with $\nu_2 + 4\nu_4$ by means of a Coriolis interaction. Transitions terminating in the $7\nu_4$ level are also expected to have a small intrinsic intensity due to the axis-switching effect, investigated in detail by Jonas *et al.* [44, 43].

To discover the extent to which each of these two mechanisms, Coriolis coupling and axis-switching, is responsible for the intensity of the extra lines, SEP spectra

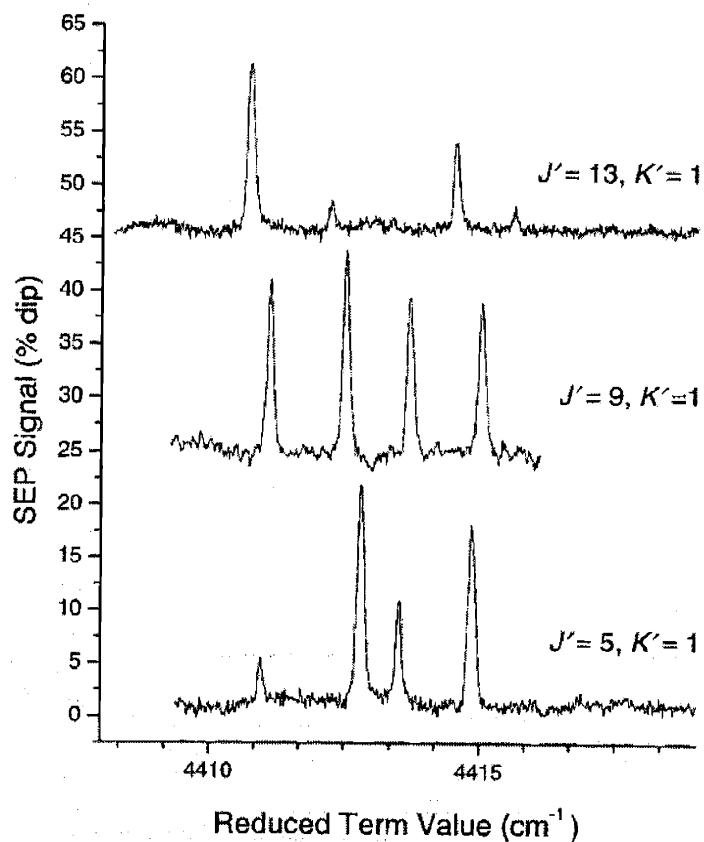


Figure 7-1: Q-branch region of $N_{res} = 7$ SEP spectra recorded after pumping several Q-branch rotational transitions in the $V_0^2 K_0^1$ vibronic band of acetylene: bottom, Q(5) PUMP; middle, Q(9) PUMP; top, Q(13) PUMP. For ease of display, traces have been shifted horizontally by $B_0 J(J+1)$ ($B_0 = 1.176646 \text{ cm}^{-1}$ [102]) and vertically by an arbitrary offset.

were recorded in the Q-branch region after pumping levels with $J' = 113$. Changes in relative transition intensity as a function of J'' were observed and are illustrated in the additional spectra shown in Fig. 7-1. (Note that spectra are plotted as a function of [term value - $B_0 J''(J'' + 1)$], so that they should be vertically aligned except for small variations in the effective rotational constants of different vibrational levels.) At $J'' = 9$ (Fig. 7-1, middle), the spectrum consists of four transitions of roughly equal intensity, and at $J'' = 13$ (Fig. 7-1, top), the intensity has shifted so that the more intense lines are lower in energy than the less intense interlopers. Such changes are reminiscent of the pattern that would be observed in an avoided crossing and are indicative of coupling between two sets of vibrational levels. By contrast, if these were simply two overlapping bands with independent intrinsic intensities, the relative intensities would be expected to remain relatively constant as the levels crossed through each other.

Evidence for coupling is also obtained by examining spectra obtained by pumping an excited state with $K'_a = 0$ (via the $V_1^2 K_1^0$ hot band vibronic transition). The $K'l''$ selection rule indicates that this state should emit only to states with $l'' = 1$, yet the same four states (with different relative intensities) are observed in emission from $K'_a = 1$ and $K'_a = 0$, as shown in Fig. 7-2. Thus the levels observed here must have some admixed character of both even and odd values of l'' .

All of the spectra in Figs. 7-1 and 7-2 probe \widetilde{X} -state levels of e -parity. Levels with f -parity can be reached by a Q-branch PUMP from the zero-point vibrational level followed by a P- or R-branch DUMP. From an excited state level with $K'_a = 1$ and f -parity, only transitions to an f -parity level with $l'' = 2$ would be expected in the P and R branches of the $\nu_2 + 4\nu_4$ vibrational band. (The $l'' = 0$ rotational levels of $\nu_2 + 4\nu_4$ are non-degenerate and belong exclusively to e -parity.) Instead, two transitions are seen in the top spectrum in Fig. 7-3 which presents the P-branch region of the Q(11)-pumped spectrum. As in the e -parity (Q DUMP) spectra, the relative intensities of the two rotational lines change as a function of J_0 ; at high J_0 (as seen in Fig. 7-1), the lower energy level carries more intensity, but below $J'' = 10$, the higher energy level carries more intensity, a pattern similar to that shown by the

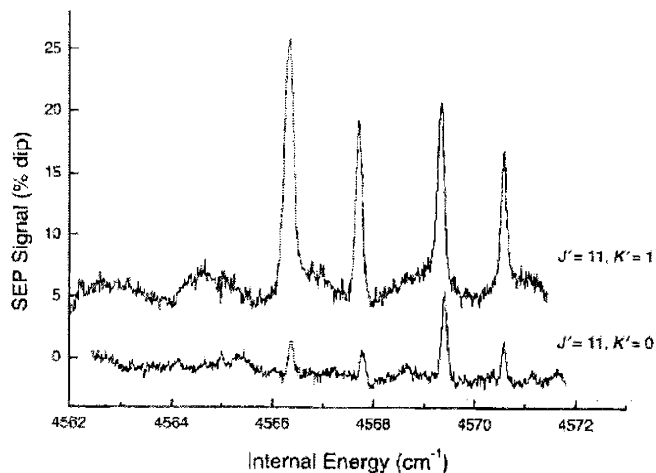


Figure 7-2: Q-branch region of $N_{res} = 7$ SEP spectra recorded after pumping Q(11) rotational transition of two vibronic bands in acetylene: bottom, $K' = 0$ ($V_1^2 K_1^0$ vibronic band); top, $K' = 1$ ($V_0^2 K_0^1$ vibronic band). Intermediate levels differ only in value of K' . Horizontal scale here has not been offset as in Fig. 7-1; to compare, subtract 155.3 cm^{-1} from this horizontal scale.

two pairs of e -parity levels. This region has also been probed from a $K'_a = 0$ excited state, looking for $l'' = 1$ character in the \widetilde{X} state, as shown in the bottom of Fig. 7-3. Only a single transition is seen, and this transition does not coincide with those from $K'_a = 1$, as can be seen by comparing the top and bottom spectra in the figure. Thus $l'' = 1$ character is not significantly mixed into the two levels which carry $l'' = 2$ character. A complete list of all observed term values, organized according to J'' , parity, and nominal l'' value, can be found in Table 7.1.

In summary, if we consider separately the states with e - and f -parity, we observe the following: e -levels appear thoroughly mixed, with character of both even and odd values of l'' distributed over a set of four eigenstates; f -levels with $l'' = 2$ show evidence of mixing with one other state, while f -levels with $l'' = 1$ are relatively unperturbed.

J''	e-state term values (low \rightarrow high energy)		
1			4415.74
2		4419.87(-0.00)	4420.45
3	4424.94(+0.04)	4426.92(+0.01)	4427.52(+0.01)
4	4434.38	4436.28(-0.01)	4436.93
5	4446.18(-0.03)	4448.01(-0.01)	4448.69(-0.03)
6	4460.41(+0.01)	4462.10(+0.01)	4462.88(+0.00)
7	4476.92(-0.02)	4478.52(+0.02)	4479.41(+0.01)
8	4495.83(+0.02)	4497.30(+0.03)	4498.30(-0.01)
9	4517.02(+0.02)	4518.42(+0.02)	4519.59(-0.01)
10	4540.49(-0.01)	4541.86(-0.02)	4543.23(-0.06)
11	4566.30(-0.01)	4567.69(-0.03)	4569.30(-0.08)
12	4594.46(+0.03)	4595.92(+0.02)	4597.83(-0.04)
13	4624.88(+0.01)	4626.39(-0.05)	4628.68(-0.08)

J''	f-state term values (low \rightarrow high energy)		
1			4415.78
2		4419.91(+0.03)	4420.57
3	4424.90	4426.92	4427.75
4	4434.40(+0.02)	4436.31(-0.02)	4437.32
5	4446.22	4448.07(-0.01)	4449.29
6	4460.40(-0.02)	4462.17(-0.02)	4463.66
7	4477.01(+0.02)	4478.68(+0.02)	4480.42
8	4495.90(-0.01)	4497.53(+0.03)	4499.60
9	4517.18(-0.01)	4518.71(+0.02)	4521.18
10	4540.85(+0.02)	4542.27(+0.00)	4545.17
11	4566.84(+0.02)	4568.18(+0.00)	4571.56
12	4595.15(-0.02)	4596.41(-0.07)	4600.54(+0.17) ²
13	4625.92(+0.04)	4627.13(-0.04)	4631.59

Table 7.1: Observed (Observed - Calculated) Term Values (cm^{-1}) for States Observed in the $N_{res} = 7$ Region of Acetylene SEP Spectra. Columns correspond to symbols connected by curves in Fig. 7-4; nominal l values decrease from left to right beginning with $l = 3$. If no state was observed experimentally, the calculated term value is shown in *italics*.

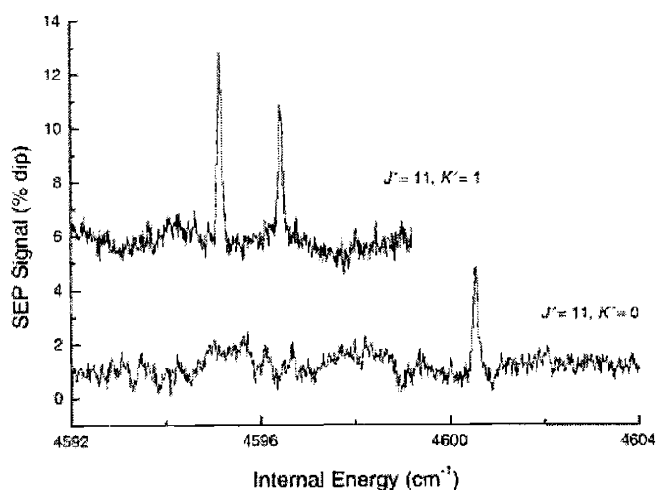


Figure 7-3: P-branch region of $N_{res} = 7$ SEP spectra recorded after pumping Q(11) rotational transition of two vibronic bands in acetylene: bottom, $K' = 0$ ($V_1^2 K_1^0$ vibronic band); top, $K' = 1$ ($V_0^2 K_0^1$ vibronic band). Intermediate levels differ only in value of K' . As in Fig. 7-2, horizontal scale has not been offset.

7.4 Analysis

7.4.1 Frequency Analysis

The most plausible interpretation of the observations above is that two zero-order vibrational states, $\nu_2 + 4\nu_4$ (the bright state) and $7\nu_4$ (the perturber), are being mixed by a Coriolis interaction. These are the only states predicted to lie in this region ($\pm 100 \text{ cm}^{-1}$) by the effective Hamiltonian [40, 39] that has successfully fit acetylene DF spectra up to vibrational energies in excess of $15,000 \text{ cm}^{-1}$. These states are of the correct symmetry to be mixed by a Coriolis interaction, and the mixing is seen to be dependent on J , as would be expected for a Coriolis perturbation. To confirm this interpretation, both the observed energy levels and the relative intensities of transitions from a single excited state rotational level have been calculated from a Coriolis-coupling model.

A least-squares fit has been used to determine the zero-order vibrational energies of the interacting states, the rotational constant for each state, and the magnitude of the Coriolis coupling coefficient. For the purposes of the calculation, the basis states

are assumed to be the harmonic oscillator vibrational states $\nu_2 + 4\nu_4$ and $7\nu_4$ with diagonal energies:

$$\langle v, l, J | H | v, l, J \rangle = T_{v,l} + B_v J(J+1) \quad (7.2)$$

The dependence of the vibrational term value $T_{v,l}$ on l will be discussed in detail below; the rotational constant B_v is not allowed to depend on the value of l in the fit.

The third-order Coriolis coupling matrix element for a linear molecule, in which three quanta of a bending vibration (ν_4 in this case) are exchanged for one quantum of a stretching vibration (ν_2), is given by Maki *et al.* [63] as being of the form (in the signed l basis):

$$\begin{aligned} \langle v_2, v_4, l, J | H | v_2 + 1, v_4 - 3, l \pm 1, J \rangle = & \mp 4\xi \sqrt{[J(J+1) - l(l \pm 1)]} \\ & \times \sqrt{(v_2 + 1)(v_4 \mp l)(v_4 \mp l - 2)(v_4 \pm l)} \end{aligned} \quad (7.3)$$

The Coriolis coupling coefficient ξ is expected to be on the order of $0.00010.001 \text{ cm}^{-1}$ for a $\Delta v = \pm 4$ coupling matrix element [14, 63]. There is, as well, the rotational l resonance which couples states with $\Delta l = \pm 2$ and no changes in other quantum numbers, with the matrix element given by Plva (also in the signed l basis, independent of v_2) [76]:

$$\begin{aligned} \langle v_4, l, J | H | v_4, l \pm 2, J \rangle = & \frac{1}{4} q_4 \sqrt{(v_4 \mp l)(v_4 \pm l + 2)} \\ & \times \sqrt{[J(J+1) - l(l \pm 1)][J(J+1) - (l \pm 1)(l \pm 2)]} \end{aligned} \quad (7.4)$$

The l -doubling coefficient q_4 is calculated from the constants of Kabbadj *et al.* [46]; its value ($q_4 \approx 0.005 \text{ cm}^{-1}$ for the levels under consideration) depends weakly on v_4 and even more weakly on J , the latter effect not being included in the fit.

To simplify the calculations and their interpretation, the terms above were collected and subjected to an orthogonal transformation. This transformation leads to

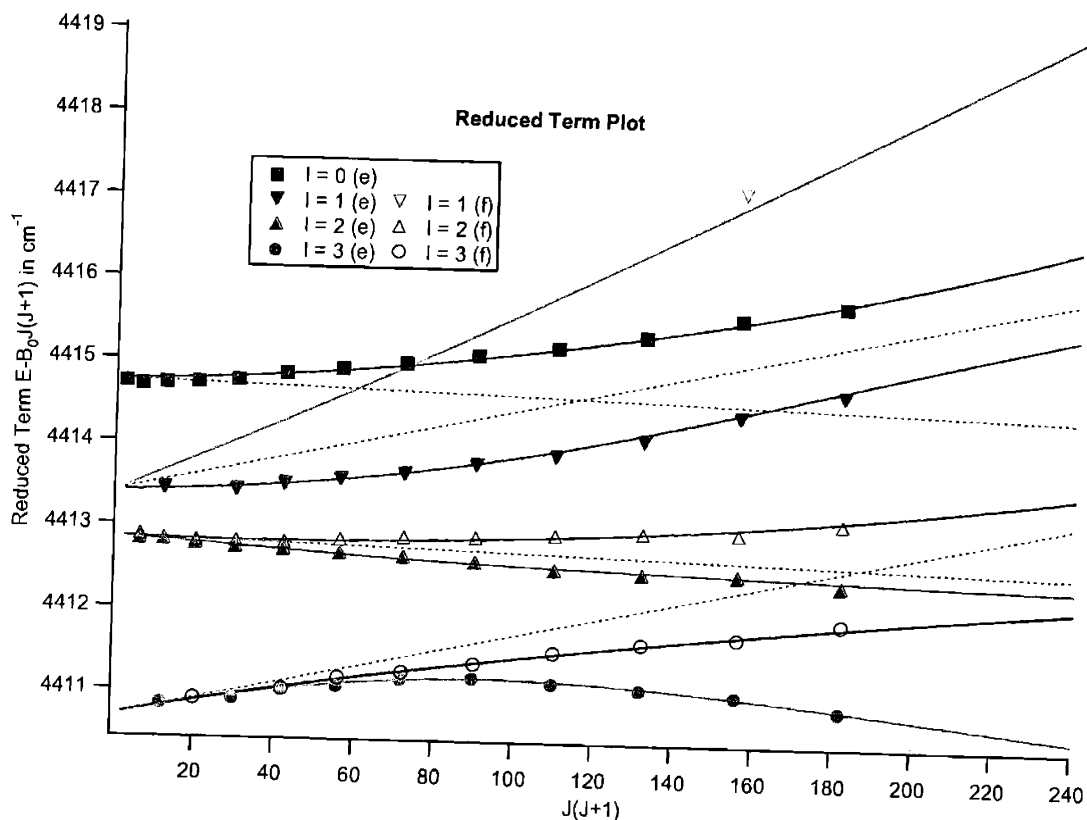


Figure 7-4: Observed (symbols) and calculated (curves) term values (reduced by $B_0J(J+1)$, $B_0 = 1.176646 \text{ cm}^{-1}[102]$) for eigenstates in the $N_{res} = 7$ region of acetylene. Also shown (dotted lines) are deperturbed zero-order energies for the basis states $\nu_2 + 4\nu_4$ and $7\nu_4$ in the absence of rotational l resonance and Coriolis coupling. Filled symbols are e -parity levels and open symbols are f -parity levels with nominal l assignments as indicated in the legend.

a block-diagonal, parity-basis matrix including e -parity basis states with values of $l = 0, 1, \dots, v_4$ and f -parity basis states with values of $l = 1, \dots, v_4$.³ (For low- J values, basis states were limited to the range $l = 0$ or $1, \dots, J$, to conform with the restriction $l \leq J$; in all cases, even- l states have vibrational character of the bright state and odd- l states have vibrational character of the perturber.)

Matrices were set up and diagonalized for values of $J = 113$. The resulting eigenvalues were compared to the 66 observed levels listed in Table 7.1. A least-squares fitting procedure was used to generate the optimized values of the parameters listed

³States with $l > 3$ were not observed experimentally but were found by the calculations to participate (weakly) in the mixing. Therefore, they were included in the fit to minimize errors due to truncation of the basis set.

Parameter	Fit Value (cm ⁻¹)
$T_{bright,l=0}$	4414.73(4)
$T_{bright,l=2}$	4412.84(4)
$T_{perturber,l=1}$	4413.39(6)
$T_{perturber,l=3}$	4410.68(4)
B_{bright}	1.1746(5)
$B_{perturber}$	1.1862(6)
ξ	0.00057(4)

Table 7.2: Model Fit Parameters (Defined in Text) for Coriolis-Coupled Levels $\nu_2 + 4\nu_4$ (Bright) and $7\nu_4$ (Perturber) in $\tilde{X}^1\Sigma_g^+$ Acetylene. The last digit in parentheses specifies 2σ errors.

in Table 7.2. $T_{bright/perturber,l}$ are, respectively, the zero-order vibrational energies of the bright state and the perturber at the indicated values of l (see below), and $B_{bright/perturber}$ are the corresponding B_v values. The results of the fit are displayed graphically in Fig. 7-4, in which the term values for all observed states (symbols), reduced by $B_0J(J+1)$, are plotted vs. $J(J+1)$, along with the reduced eigenvalues calculated from the best fit (smooth curves). In the absence of Coriolis and l -resonance perturbations, the state energies would be represented on this plot by the straight dotted lines, the slopes of which are equal to $(B_v - B_0)$, the change in effective rotational constant due to vibration.

In addition to the visually obvious quality of the fit, there are several consistency checks we may perform on the resulting parameters. The vibrational term values derived from the fit are all within 0.5 cm^{-1} of those predicted by the effective Hamiltonian [40, 39]. The B_v values (or, equivalently, the slopes of the dotted lines) are both within 0.0015 cm^{-1} of those predicted on the basis of the a constants of Aboubou Tamsamani and Herman [102]: B_v is slightly smaller than B_0 for the level with both stretch and bend excitation and significantly larger than B_0 for the level with only bend excitation. The Coriolis coupling parameter, ξ , is of the expected order of magnitude for the states being coupled by this interaction.

Finally, consider the vibrational term values for states differing only in l . These values were allowed to vary independently in the fit, even though their difference could have been constrained to depend on the parameters being fit here (B_v) and other

parameters for which values are proposed elsewhere, specifically the g_{41} parameter from the effective Hamiltonian [40] and the y_4^{44} parameter of Plva [76]. It is our belief that g_{44} and y_4^{44} are probably not sufficiently accurately known to constrain the fit to the data obtained in this experiment. Even so, the differences in energy between the $l = 0, 2$ levels of the bright state and between the $l = 1, 3$ states of the perturber, treated as freely varying parameters, are approximately equal to the values to which they would have been constrained. The best-fit $l = 0, 2$ separation is 1.89 cm^{-1} vs. a predicted value of 1.86 cm^{-1} , and the best-fit $l = 1, 3$ separation is 2.71 cm^{-1} vs. a predicted value of 3.61 cm^{-1} . Calculations based on the effective Hamiltonian [40, 39] suggest that the slightly larger discrepancy in the latter case is due to small changes in the number and position of states coupled by more remote off-diagonal (anharmonic) vibrational interactions which have been neglected in this calculation.

We have also confirmed that Coriolis coupling is necessary for a satisfactory fit. Setting the Coriolis matrix elements to zero leads to a fit that is qualitatively worse, particularly for the high J , and high l states where Coriolis coupling should be strongest.

7.4.2 Relative Intensity Calculations

The relative intensities of transitions within a single Q or P branch were also calculated for comparison with the observed intensities. Caution is required in this comparison for several reasons:

1. Rotational line intensities in SEP are inherently nonlinear [43]. As a result, we are looking primarily for qualitative trends in intensities, most notably the apparent crossing at J'' values of approximately 910 in both the Q- and P-branch regions.
2. The $K'' = 1$ excited state will have transition intensity to both of the coupled $l'' = 0$ and $2e$ levels in the ground state, leading to interference terms in the transition moment [43].

3. Axis-switching effects cause $K' = 1$ rotational levels of the \tilde{A} state to have small amounts of $K' = 0$ and 2 character when expressed in coordinates of the \tilde{X} -state axis system [28]. The $K'l'' = \pm 1$ selection rule then allows for transitions to \tilde{X} -state levels with $l'' = 1$ and 3, as has been seen previously in acetylene SEP spectra [44, 43]. Thus, both the bright state ($l'' = 0$ and 2) and the perturber ($l'' = 1$ and 3) will have intrinsic intensity in the SEP spectrum, leading to additional interference effects.

In the most general case, up to five interfering transition moments could contribute to each observed transition in the Q branch and four in the P branch.

It is also necessary to assign a value to the vibrational portion of the transition moment, i.e., a FranckCondon factor, for the nominally forbidden transition. This value will be nonzero since the selection rule forbidding the transition is based on rotation rather than vibration. It cannot be directly measured from the DF spectrum, but must be estimated by interpolation between known FranckCondon factors for fully allowed transitions. It was estimated that the squared vibrational overlap integrals for the “forbidden” transition and the fully allowed transition were in the ratio of 3:1.

Rotational intensity factors for transitions within a single Q or P branch are accounted for by an M_J sum over products of the usual direction cosine matrix elements [107] with linearly (z) polarized light [43]. Comparisons of relative intensities between branches would require consideration of the relative polarizations of the PUMP and DUMP lasers, since the PUMP produces an anisotropic distribution of M_J states. However, comparisons of intensities within a single branch (regardless of l'' or vibrational identity) are unaffected by the M_J distribution.

The relative intensities within the Q and P branches after pumping levels with $K' = 1$ were calculated and are displayed in Fig. 7-5 (solid curves), along with the experimentally observed values (symbols; tie lines added to emphasize correspondence). For clarity, the e -parity levels are displayed in pairs, even though intensity is shared between all four e -parity levels. We emphasize that the predicted intensities are *not* the result of a fit to observed intensity information, but predictions of intensities based on the eigenvectors derived from a fit to energy levels only.

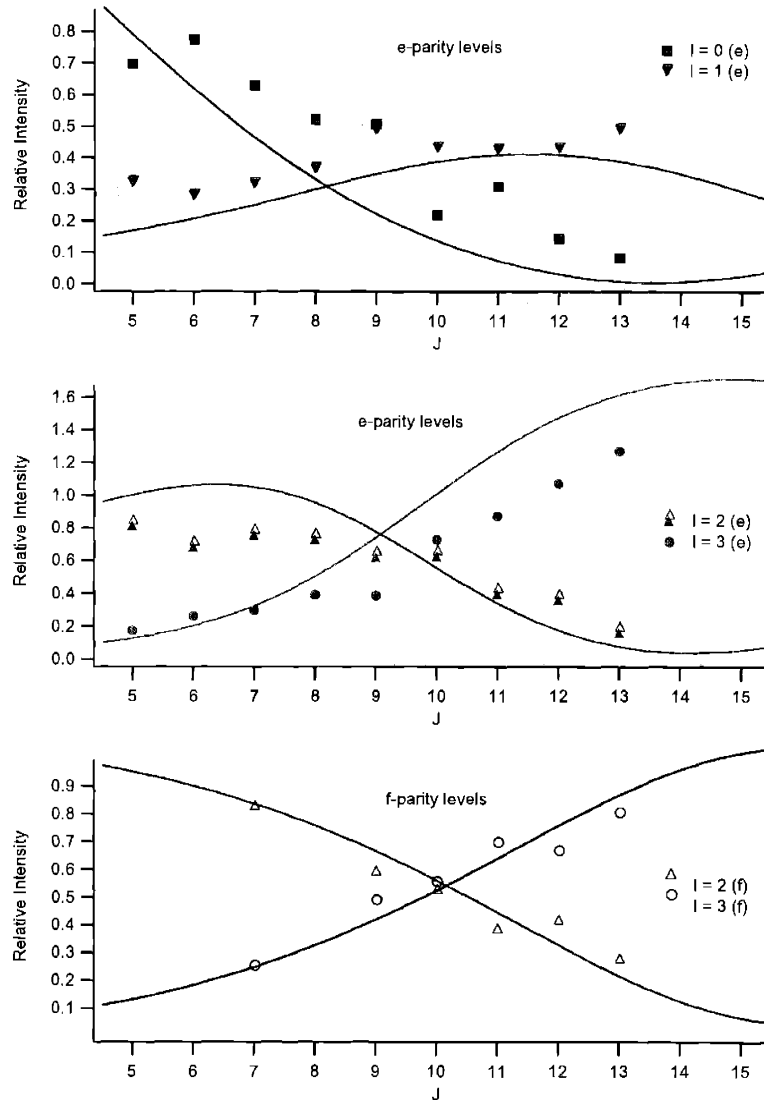


Figure 7-5: Observed (symbols) and calculated (curves) relative intensities for SEP transitions to eigenstates in the $N_{res} = 7$ region of acetylene: top, higher energy pair of e -parity levels (columns 3 and 4 of Table 7.1); middle, lower energy pair of e -parity levels (columns 1 and 2 of Table 7.1); bottom, f -parity levels. Symbols correspond to those in Fig. 7-4.

Given the cautions cited above, the observed and predicted intensities are remarkably consistent. In particular, the calculated intensities for each of the illustrated pairs of e -levels cross at approximately the observed J'' value (± 1), all four e -level intensities are predicted to be similar at $J'' = 9$, and the lowest energy eigenstate is predicted to become dominant at the highest values of J'' investigated. The calculations for the f -parity levels indicate essentially no intensity for the nominal $l'' = 1f$ state (which is pushed far out of resonance with $l'' = 2f$ by the l -doubling term that splits the $l'' = 1f$ and $1e$ states) and show the intensities of the nominal $l'' = 2f$ and $3f$ eigenstates crossing at roughly $J'' = 10$, consistent with the experimental observations.

7.5 Discussion

The DF experiments from this laboratory [74, 40, 39] have revealed a surprisingly simple picture of acetylene vibrational dynamics. At short time scales (≤ 1 ps), IVR in acetylene is mediated by DarlingDennison and Fermi resonance interactions that result in the set of three approximately conserved quantum numbers that define (when combined with the rigorously conserved quantum number J) a polyad. At the resolution of the DF spectra, the polyad model can be used to describe the vibrational energy level structure for energies in excess of $15,000 \text{ cm}^{-1}$.

With the improved resolution of SEP, the time scale for observations of vibrational dynamics is extended by two orders of magnitude. Even so, in most of the lower polyads (up to $N_{res} = 11$), we have seen no evidence for further IVR. The $N_{res} = 7$ region is the only exception that shows something significantly different at longer times. The analysis presented above shows clear evidence for strong rotationvibration coupling that leads to extensive mixing among sets of three or four eigenstates that are divided between the polyads with $N_{res} = 7$ and $N_s = 0$ or 1 . Although evidence for breakdown of the polyad model has been observed in other studies [119, 94, 65, 66], the coupling revealed here is unusual in terms of both the relatively low vibrational energy and the wide range of J values that are strongly coupled.

The mixing even in this case is not necessarily as complete as it would seem by

inspection of the spectra. For example, at $J'' = 10$, the f -parity levels would appear to be almost equal mixtures of the $l'' = 2$ and 3 basis states, but the eigenvectors derived from the best fit show that each level retains about 80% of its primary basis state character. The equal intensities of transitions to these two states result from destructive interference between transition moments to the nominal $l'' = 2$ state and constructive interference for $l'' = 3$. A similar situation applies in the e -parity manifold. Even so, the calculations also indicate that mixing continues to increase with increasing values of J'' , so that there is, for example, nearly complete mixing among the $l'' = 03$ e -parity states at $J'' = 13$.

The strong mixing arises in spite of the fact that the Coriolis matrix element is actually fairly small. Using the $J'' = 10$ states as a benchmark, the Coriolis matrix elements (which scale roughly linearly with J) given by Eq. 7.3 are 0.40, 0.33, and 0.41 cm^{-1} for coupling of $l'' = 01, 12,$ and 23 , respectively. That the resonance is so readily observable in the SEP spectra can be attributed to the near-coincidence of the zero-order vibrational energy levels and the difference in B_v values that cause pairs of zero-order levels to cross as shown by the dashed lines in Fig. 7-4.

Knowledge of the vibrational energy pattern that is extracted from the DF experiments indicates that this resonance will be of negligible importance in higher polyads, as was in fact seen by SEP. As an example, consider the Coriolis coupling that would be expected between levels observed by Jonas et al. [44] in the $N_{res} = 11$ region. The primary level carrying oscillator strength in this region is $\nu_2 + 8\nu_4$; in addition to this level and other members of its polyad ($N_{res} = 11, N_s = 1$), a level was observed and assigned as $2\nu_2 + 5\nu_4$. The transition to this nominally forbidden level in a different polyad ($N_{res} = 11, N_s = 2$) was attributed to axis-switching by Jonas *et al.*, but this level could also couple with $\nu_2 + 8\nu_4$ by the same Coriolis mechanism observed here. The zero-order separation of these two levels is roughly 14 cm^{-1} and their B_v values are such that the levels will separate rather than cross at high J'' , so the value 15 cm^{-1} can be used as an estimate of the energy gap at $J'' = 10$. Matrix elements for coupling among the various l states of these vibrational levels, calculated from Eq. 7.3, are on the order of 0.6 cm^{-1} , so the first-order perturbation theory estimate

of the mixing coefficient as matrix element divided by energy gap may be used to predict that the bright state character in the mixed eigenstate will be on the order of $(0.6/15)^2 = 0.0016$ or 0.16%. Clearly the attribution of the observed transition intensity to axis-switching is correct and Coriolis coupling is not an important contributor to the vibrational dynamics of these levels.

It is not surprising that this particular Coriolis coupling channel will be generally unimportant to IVR in acetylene. The typical matrix elements are $\leq 1 \text{ cm}^{-1}$, consistent with the change in vibrational quantum numbers for this process. What is perhaps more surprising is that this is one of only a few Coriolis coupling interactions so far observed in acetylene that is strong enough to substantially mix levels from different polyads over a wide range of J'' values, and the only such case observed below $E_{vib} = 10,000 \text{ cm}^{-1}$. The SEP spectra of formaldehyde [14], on the other hand, showed pervasive evidence of rotationvibration coupling at $E_{vib} \approx 8000 \text{ cm}^{-1}$. As mentioned in the Introduction, the evidence for involvement of rotations in IVR is mixed in other systems as well. Is there any generalization that can be made from these results?

We believe that in the particular case of acetylene, the observations reflect the gross mismatch in frequencies for low $|\Delta v|$ Coriolis coupling. The symmetry-allowed $|\Delta v| = 2$ couplings in acetylene would lead to mixing between ν_1 or ν_2 and ν_4 and also between ν_3 and ν_5 . (The orthogonal components of the doubly degenerate bending modes, ν_4 and ν_5 , are each coupled by the Coriolis force, but this coupling is accounted for by the splitting of internal angular momentum states within the polyad model). The smallest frequency difference among these possibilities ($\nu_2\nu_4$) is greater than 1000 cm^{-1} , and all other differences are greater than 2000 cm^{-1} . Coriolis matrix elements as large as tens of reciprocal centimeters will be totally ineffective over such a large energy gap. By contrast, in formaldehyde, ν_3 and ν_6 (in-plane bends) both couple with ν_4 (out-of-plane bend) with frequency mismatches of 400 and 100 cm^{-1} , respectively. Thus, although acetylene and formaldehyde are of similar vibrational complexity (four nuclei; two H, two heavy), the symmetries of the vibrational modes of these two molecules are such that Coriolis interactions are a much more important

aspect of the dynamics of formaldehyde than acetylene.

Acetylene may actually be somewhat distinctive in its relative lack of rotationvibration coupling. Larger polyatomics are perhaps more likely to have one or more small $|\Delta v|$ couplings allowed by symmetry. Even the rearrangement of the same four atoms to form the meta-stable acetylene isomer vinylidene will result in a system with normal modes that resemble those of formaldehyde and should provide a more favorable situation for low-order Coriolis coupling.

It has been suggested previously that the number and strength of such low-order resonances will have a dominant influence on IVR dynamics. For example, in a study of absorption linewidths for the fundamental and first overtone of the acetylenic CH stretch of a series of isotopically and chemically substituted *t*-butyl acetylenes, Gambogi *et al.* [21] noted that IVR rates are uncorrelated with total densities of states, but seem to be related to the density of states linked by low-order couplings. Subsequently, Stuchebrukhov and Marcus [100] were able to reproduce most aspects of the experimental trends in IVR rates in this series with a tier model that includes only third- and fourth-order coupling between subsequent tiers of states. Thus, as a general rule, one should look for large contributions of Coriolis coupling to vibrational dynamics only in systems where the symmetries and frequencies of vibrations are favorable for strong, low-order Coriolis coupling.

It is possible that at sufficiently high energies even weak, large $|\Delta v|$ Coriolis coupling will become effective at promoting IVR in acetylene. Matrix elements will certainly scale with vibrational quantum numbers, and the density of states will equally certainly increase so that small energy gaps should compensate for small matrix elements. Under these circumstances, a global breakdown of the polyad structure might be expected at sufficiently long times. Nevertheless, it seems clear that the short-time dynamics in acetylene will continue to be dominated by anharmonic couplings described by the polyad model well into the region of chemically significant energy.

Chapter 8

Ongoing Projects

8.1 Introduction

In this chapter I intend to list all the ongoing projects as investigations on the singlet electronic states of acetylene are continuing. The chapter includes three projects, each of which has some special importance toward a better understanding of acetylene.

In addition to regular acetylene, can HCCD, with its unique asymmetry, give us some new insights into the local mode dynamics on both the \tilde{A} -state and the \tilde{X} -state? I have collected a systematic series of DF data from various vibrational levels of the S_1 electronic state, the analysis of which is complicated by multiple bright state in the S_0 potential. However, would a systematic LIF dataset help in determining the \tilde{A} state structure? Will C_2D_2 provide us with additional insights? A section will be devoted to the discussion of each of these questions.

The *cis* well on the \tilde{A} state surface has never been investigated. I designed an IR-UV double resonance CRD scheme for this purpose. Feasibility calculations suggest that the experiment is feasible.

As studies of the \tilde{A} state of acetylene continue, we wish to find interpretations for the perturbation in the $3\nu'_3$ vibrational state observed by DF. Further assistance of this project can be provided by analysis from the JWU *ungerade* jet-cooled LIF spectra. Theoretical calculations of the Coriolis interaction between the asymmetric bending modes and the torsional modes will be decisive in yielding some insights into

the \tilde{A} state dynamics. Expanding the LIF dataset into higher energy regions in the \tilde{A} state would also help in making some new assignments of the $n\nu'_{bend}$ polyads.

8.2 Dispersed Fluorescence of HCCD

8.2.1 Background and Motivation

By fitting the overall unzipped polyad patterns from DF spectra in $^{12}\text{C}_2\text{H}_2$, Jacobson [35] convinced me that there exist stable local modes at high internal energy of $^{12}\text{C}_2\text{H}_2$. Interest in non-symmetric isotopomer, C_2HD , is therefore stimulated.

The logic is, if in a symmetric molecule such as $^{12}\text{C}_2\text{H}_2$, its eigenstates exhibit local bend, in a non-symmetric molecule such as HCCD , one expects the onset of local mode types of motion to occur much lower internal energy than in its symmetric isotopomer. The different bending frequencies of the CCH and CCD bonds de-tunes what is the equivalent of the normal mode *trans* bending motion in regular acetylene into a dominant CD local bending motion, and similarly, *cis* bending into a dominant CH local bending. The fact that the normal modes themselves resemble local modes adds to our belief that it ought to be easier to observe the isomerization through a local bend in HCCD , provided that spectra covering the isomerization energy can be recorded and decoded.

However, as always, there are complications in the study of C_2HD . In C_2H_2 , the *trans* bending motion in the upper electronic state is symmetric with respect to inversion; while the *cis* bending motion in the ground electronic state is anti-symmetric; thus there will be no direct transition from the *trans* bending excited states in the upper electronic state to the *cis* bending states in the ground electronic state (in other words, the *cis*-bend is dark). That is one of the fundamental reasons why in C_2H_2 there is only one bright state per polyad. However, this statement is no longer valid for C_2HD – since C_2HD no longer has a molecular center of symmetry, the inversion operation no longer exists. Consequently, we will have multiple bright states in a polyad (if polyads exist). Therefore we anticipate much more congested

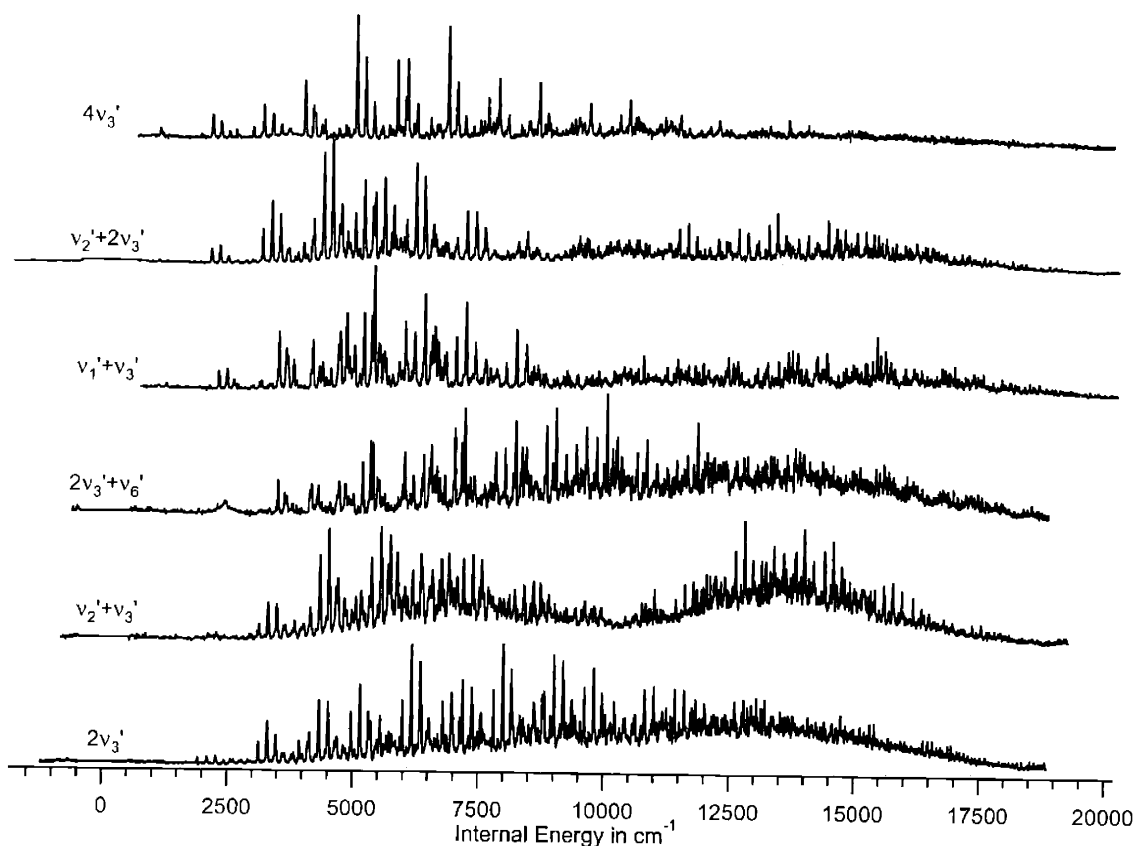


Figure 8-1: Raw DF spectra at 18 cm^{-1} resolution recorded from the $4\nu_3'$, $\nu_2'+2\nu_3'$, $\nu_1'+\nu_3'$, $2\nu_3'+\nu_6'$, $\nu_2'+\nu_3'$, and $2\nu_3'$ levels of the \tilde{A} state of $HCCD$. The undulating baseline is the Quasi continuous baseline described in Chapter 4. All spectra are carefully calibrated and concatenated. Therefore, the frequency information contained in every spectrum is identical, while the intensity information contained in each spectrum is related to the Franck-Condon factor from the individual upper vibrational states.

and complicated $HCCD$ DF spectra. XCC, which works well for C_2H_2 in unzipping the polyad patterns in DF spectra, cannot be applied to $HCCD$ due to the failure of the one-bright-state-polyad assumption on which it is based.

8.2.2 Experimental

Despite the expected complications, six carefully calibrated DF spectra have been recorded for C_2HD (Fig. 8-1).

The DF spectra that sample the vibrational dynamics in the electronic ground state of $HCCD$ were recorded from several vibrational levels of the \tilde{A} state. The

data set consists of DF spectra excited via the ${}^rQ_0(1)$ lines of the $4\nu'_3$, $\nu'_2 + 2\nu'_3$, $\nu'_1 + \nu'_3$, $2\nu'_3 + \nu'_6$, $\nu'_2 + \nu'_3$, and $2\nu'_3$ vibrational levels.

The reason the ${}^rQ_0(1)$ line is chosen is to minimize Coriolis effects and to simplify the rotational structure in the spectra. Despite the population advantage of choosing a higher- J' line as the intermediate state, the higher J' is in the intermediate upper state, the larger the spacing between the P, Q, R transitions in the Dispersed Fluorescence spectra. Eventually when the PQR spacing exceeds the DF resolution, those rotational transitions would show up in our spectra as several lines, which would result in a much more congested spectrum, and would bring unnecessary complexity into the assignment process. As the DF spectral intensity is sufficient when excited via a $J' = 1$ line, higher J' has more disadvantages than advantages.

The DF spectra were recorded at 18 cm^{-1} resolution. The experimental methodology for recording these spectra has been reported previously [74, 73] and is briefly reviewed here. The output of a XeCl excimer (Lambda-Physik LPX- 210icc), 250 mJ/pulse at 60 Hz, pumped Lambda-Physik FL2002 dye laser (10 mJ/pulse), operated with Coumarin 440 or 450 dye, was frequency doubled to produce about 1 mJ/pulse of radiation tunable from 215 to 230 nm with a spectral width $\leq 0.05\text{ cm}^{-1}$. The beam of fundamental radiation was separated from the doubled light and subsequently passed through a ${}^{130}\text{Te}_2$ (500 C) cell used for frequency calibration. The frequency doubled dye laser output was locked onto the ${}^rQ_0(1)$ line of each $\tilde{A} \leftarrow \tilde{X}$ vibronic band. The UV beam was passed through a static cell containing 1.0 Torr of *HCCD* (Cambridge Isotope Laboratories, 99% pure) which was subject to several freeze-pump-thaw cycles before it was distilled into the sample cell using a pentane-liquid N_2 slurry (-129.7 C). Before the fill, the gas cell was pre-conditioned by 1:1 $H_2O:D_2O$ mixtures. The fluorescence was imaged onto the slit of a monochromator (JobinYvon HR640mm, 1200 g/mm grating, borrowed from Professor Mounji Bawendi, returned in year 2000) equipped with a Princeton Instruments intensified charge coupled device (ICCD), Model 1024-M059413, to record the dispersed fluorescence spectra. The entrance slit width of the monochromator was set to $100\ \mu\text{m}$ and the grating was used in first order.

At each grating position, frequency calibration was performed using the emission from a series of atomic lamps (Fe, Kr, Ar, Xe, Hg, Ne) prior or subsequent to recording the acetylene fluorescence. Each DF segment (recorded at a particular grating angle) was recorded twice to permit the removal of spurious signals such as those due to cosmic rays. The grating positions were chosen such that each segment of spectrum overlapped with at least half of each adjacent segment. Previously, the DF segments were recorded such that the individual segments had minimal ($\leq 10\%$) overlap. That procedure enabled spectra to be recorded more rapidly, but made intensity calibration more difficult. Previously, in order to make meaningful comparisons between the intensities of peaks in adjacent segments, fluctuations in the laser power had to be monitored and accounted for in the concatenation of spectral segments. However, the current methodology permits superior intensity and frequency calibration, and improved signal to noise ratio. Intensity calibration is straightforward and virtually effortless due to the duplication of each segment of the spectrum. Direct comparison of the intensities of the replicated peaks in each segment eliminates the need to normalize each segment with respect to fluctuations in laser power. This comparison of intensities is accomplished in a statistically optimal way by creating a recursion map [37, 10] of the two frequency calibrated overlapping segments. The intensity ratio of the segments is given by the slope of the line of the recursion map (the slope is generally close to 1) and a least squares fit of the recursion map slope is used to optimally scale the relative intensities of the segments. It is worth mentioning that this method is almost identical to the intensity calibration method used for LIF spectra discussed in Chapter 2.

Improvement of the intensity calibration was not the only benefit from recording the segments in this 50% overlapped fashion. A trivial benefit is an improved signal-to-noise-ratio, since fluorescence emission at each wavelength was recorded twice and could be averaged. Furthermore, each segment was frequency calibrated independently. This eliminated gross calibration errors. Excess spectra (those portions of the segments which overlap by more than 50%) could be discarded. Frequency calibration error is determined to be $\pm 0.93 \text{ cm}^{-1}$ (as determined by comparing the frequencies of

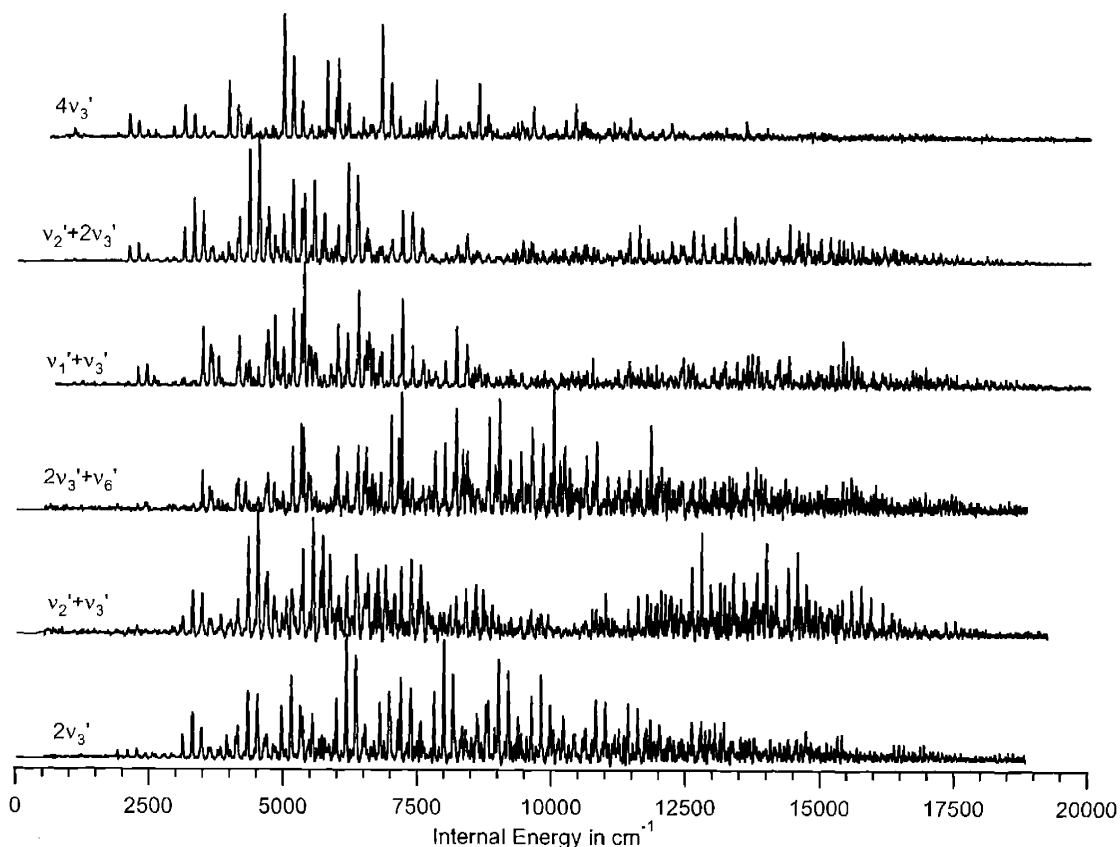


Figure 8-2: HCCD DF spectra with baseline correction. The baseline removal tool is listed in the appendix, the algorithm for which is based on a paper by Ruckstuhl *et al* [81].

lines in two independently recorded and calibrated segments).

8.2.3 Spectra

As quasi-continuous baselines are present in almost all spectra in Figure 8-1. In this chapter, since we are less interested in the detailed kinetics behind our DF spectra than the spectral features themselves, I wrote a small igor program to remove the baseline in the spectra (appendix). The baseline-removed spectra are depicted in Fig. 8-2.

One obvious observation is that the *HCCD* DF spectra look much more complicated than those of its symmetric counterparts', namely, $^{12}\text{C}_2\text{H}_2$ and $^{13}\text{C}_2\text{H}_2$. This

is believed to be caused by multiple bright states, as mentioned earlier. As the $4\nu'_3$ DF spectrum looks least congested among all six spectra, we have a better chance to assign the lines in this spectrum. It is the only band that I have successfully, though not completely, assigned up to $10,000\text{ cm}^{-1}$.

8.2.4 Assignment

In spite of the complicated appearance of the spectra, and the very congested nature of the spectra addressed above, we were able to assign normal mode quantum numbers to almost all peaks observed in the $4\nu'_3$ DF spectrum below $10,000\text{ cm}^{-1}$. Table 8.1 gives a listing of all the peaks that I was able to assign, based on the vibrational term value fourth-order Dunham expansion (3.1) listed in the HCCD paper by Herman and coworkers [59] and the constants therein:

$$G_v^0 = \sum_i \omega_i^0 v_i + \sum_{i \leq j} x_{ij}^0 v_i v_j + \sum_{i \leq j \leq k} y_{ijk}^0 v_i v_j v_k + \sum_{i \leq j \leq k \leq l} z_{ijkl}^0 v_i v_j v_k v_l + \sum_{t \leq t'} g_{tt'}^0 l_t l_{t'} \quad (8.1)$$

Assignments of the $4\nu'_3$ spectrum extend to $10,000\text{ cm}^{-1}$ in internal energy. I would like to point out three interesting observations from the assigned lines:

1. Depicted in Fig. 8-3, the clusters of four or three peaks are groups of states between the neighboring two of which exchange one quantum of dominant CD bending for one quantum of dominant CH bending.
2. Of the states that have been observed, although the CD bend can sometimes reach up to 11 quanta, the spectra contain features with very few (0-3) quanta of CH bend. This is counter-intuitive, as the excited states, $4\nu'_3$, have four quanta in CH bending. Naively, the DF spectrum ought to contain high quanta in the dominant CH bending instead of the CD bending. Notice also that the lowest member of each cluster has the most CD bending character, and its intensity is often twice as large as the second member in that cluster, which has one fewer quanta in the CD bending and one more in the CH bending. These

CH Stretch 3383.91 cm ⁻¹	CC Stretch 1859.34 cm ⁻¹	CD Stretch 2606.83 cm ⁻¹	CD Bend 516.65 cm ⁻¹	CH Bend 677.19 cm ⁻¹	l ₄	l ₅	Obs. in cm ⁻¹	Calc. in cm ⁻¹
0	1	0	5	1	1	1	5125.418	5126.861
0	1	0	4	2	2	0	5291.001	5297.379
0	0	0	9	1	1	1	5374.953	5378.412
0	1	0	3	3	1	1	5463.822	5458.535
0	0	1	6	0	0	0	5598.586	5599.409
0	0	1	6	0	2	0	5605.102	5607.816
0	0	0	7	3	1	1	5715.982	5715.540
0	2	0	4	0	2	0	5754.430	5748.791
0	0	1	5	1	1	1	5798.059	5795.333
0	2	0	3	1	1	1	5921.843	5923.133
0	1	0	8	0	0	0	5966.440	5977.393
0	2	0	2	2	2	0	6081.899	6092.504
0	1	0	7	1	1	1	6156.377	6162.870
0	1	0	6	2	0	0	6322.437	6326.561
0	0	0	11	1	1	1	6426.781	6424.404
0	1	0	5	3	1	1	6493.672	6497.703
0	3	0	2	0	2	0	6557.253	6550.060
0	0	0	10	2	2	0	6606.323	6599.229
0	0	1	8	0	0	0	6613.316	6608.622
0	2	0	6	0	2	0	6778.385	6775.255
0	2	0	5	1	1	1	6955.284	6951.177
0	2	0	4	2	2	0	7115.841	7122.128
0	2	0	3	3	1	1	7285.827	7283.716
0	3	0	4	0	2	0	7573.891	7568.560
0	2	0	8	0	0	0	7790.964	7795.331
0	2	0	7	1	1	1	7976.165	7981.240
0	1	0	11	1	1	1	8234.496	8240.943
0	4	0	2	0	2	0	8384.282	8365.713
0	3	0	6	0	2	0	8591.836	8589.077
0	3	0	5	1	1	1	8762.897	8765.431
0	4	0	4	0	2	0	9383.906	9378.266
0	3	0	8	0	2	0	9606.533	9611.614
0	3	0	7	1	1	1	9783.273	9789.547

Table 8.1: Assignments of the *HCCD* DF Spectrum Recorded from $4\nu_3$ in the 5,000-10,000 cm⁻¹ Range. The calculation is performed according to constants published by Herman and coworkers [59]. Of the states that have been observed, although 2-11 quanta of CD bend are present, very few (0-3) quanta of CH bend are observable. This effect can be accounted for by a simple Franck-Condon argument.

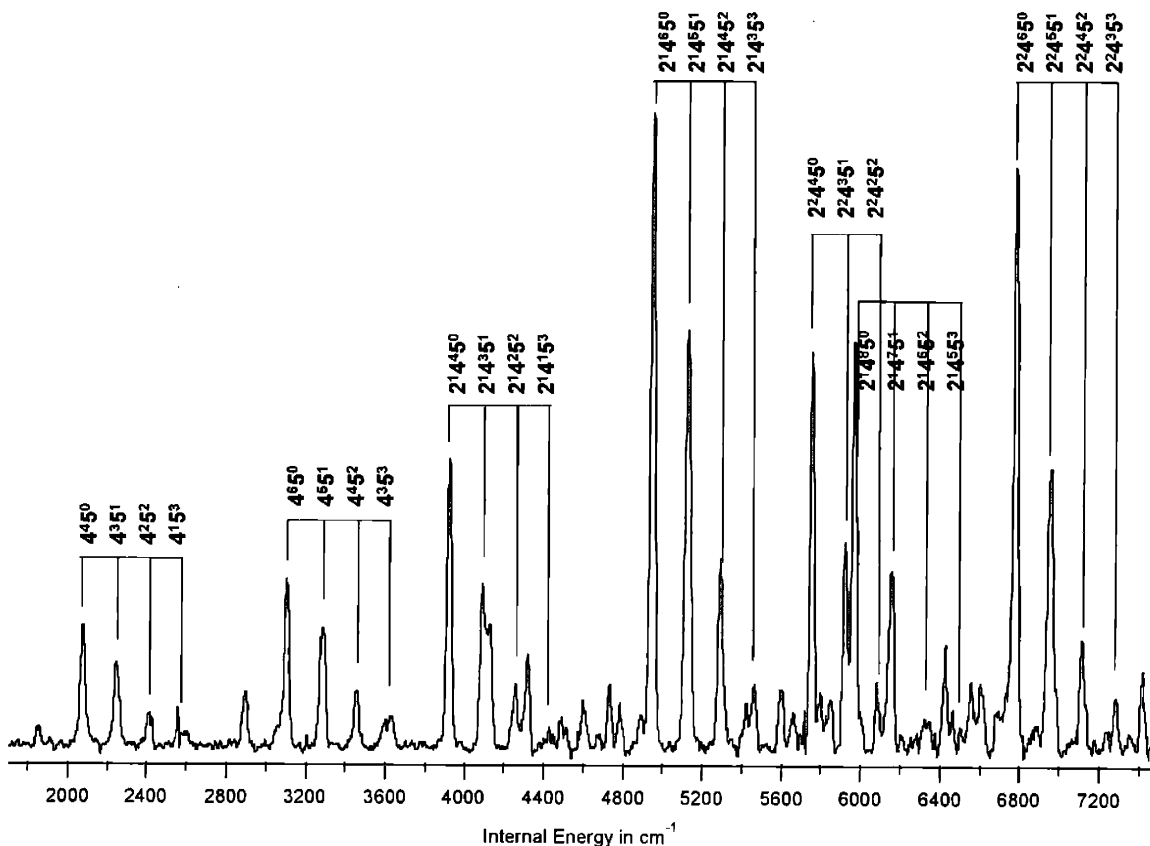


Figure 8-3: A subset of assignments for the $4\nu_3'$ DF spectrum of *HCCD*. The repeated clusters of four or three close lying peaks are unique features in *HCCD*. These are the result of exchange of one quantum of dominant CD bending with one quantum in dominant CH bending. Notice that the strongest peak in the cluster is always the one with most quanta in mode 4 (dominant CD bending), and zero in mode 5 (dominant CH bending). Notice also that the quantum number in mode 5, ν_5'' , never exceeds 3, giving no more than four members for every cluster, no matter how many quanta in mode 4 to start with. Both of these observations suggest that the CH bending mode has smaller Franck-Condon factor than CD bending mode, when the excitation is via $4\nu_3'$ in the \tilde{A} state. This seems counter-intuitive, because the ν_3' mode in the \tilde{A} -state is dominant CH bending. A qualitative Franck-Condon explanation of this phenomenon is given in Fig 8-4.

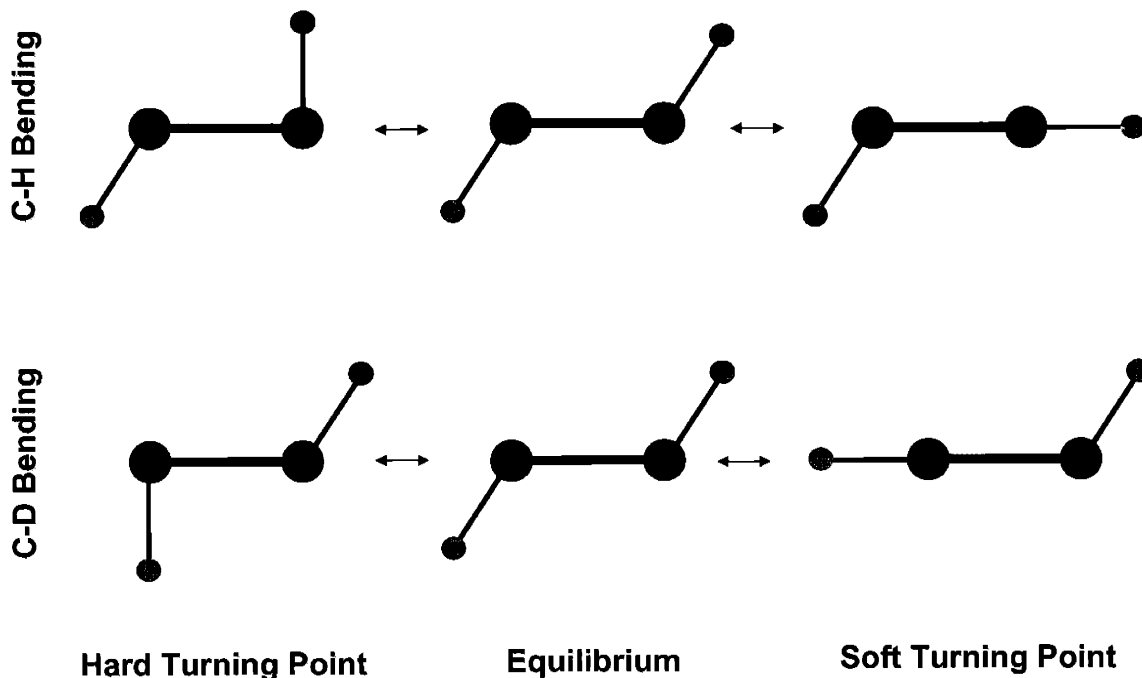


Figure 8-4: A qualitative account for the spectral observation in HCCD. In the plot, the black nuclei stand for Carbons, red stands for the Deuterium nucleus, and green stands for the Hydrogen nucleus. The top row depicts the two turning points while $HCCD$ in the \tilde{A} state is undergoing dominant CH bend, while the bottom depicts for the CD-bend. While neither the hard turning point for the CH bend nor that for the CD bend resembles the geometry of the ground state, the soft turning point for the dominant CH bend resembles an extreme, half-linear, local CD bend geometry downstairs, and *vice versa*. This is the reason why I believe in the observations made in the $4\nu_3$ DF spectral analysis for HCCD.

observations can be simply accounted for by a Franck-Condon argument. As Fig. 8-4 indicates, while neither the hard turning point for the upper state CH bend nor that for the CD bend resembles the geometry of the ground state, the soft turning point for the dominant CH bend resembles an extreme, half-linear, local CD bend geometry in the \tilde{X} state, and *vice versa*. This is why I believe that the intensity observations made for the cluster features in the $4\nu_3$ DF spectral analysis for HCCD.

- Fig. 8-5 depicts our strategy in making as many probable assignments as possible. To do this, I have made a synthetic spectrum (the green trace in the top

panel) with all the spectral lines that have been assigned. In order to uncover the unassigned features, I subtract the synthetic “known” spectrum from the original, baseline-removed, $4\nu'_3$ DF spectrum. The red trace in the top panel is the result after the subtraction. The spectrum in the bottom panel contains a zoom-in view of the residual “unknown” features from such a subtraction. A first observation of this residual is that it is *very* congested. Needless to explain, this is caused by the multiple-bright-state caused by the destruction of the center of symmetry and g , u symmetry. A second observation is that there are unexplainable lines as low as $4,000\text{ cm}^{-1}$, where not too many vibrational states ought to be present, but the spectral congestion exceeds that expectation. At this point, I do not have an explanation for this phenomenon.

To conclude, although most sharp features were assignable in the $4\nu'_3$ DF spectrum, some weak peaks do not seem to fall into any of the “apparent” bright modes (that is, the CC stretch, ν''_2 , the dominant CD bending, ν''_4 , and the dominant CH bending, ν''_5). I name these “apparent” bright modes due to the expectation that the CH stretches are not FC active in the DF spectrum, based on the observation that no stretching modes were involved in the assigned lines in the $4\nu'_3$ DF of HCCD (Table 8.1). In order to assign the “unknown” residuals further, one would need to make full use of the intensity information. Given the spectral congestion, a near-perfect Franck-Condon calculation is needed for that purpose. The FC algorithm described in Chapters 5 and 6 would provide a good start in such a pursuit.

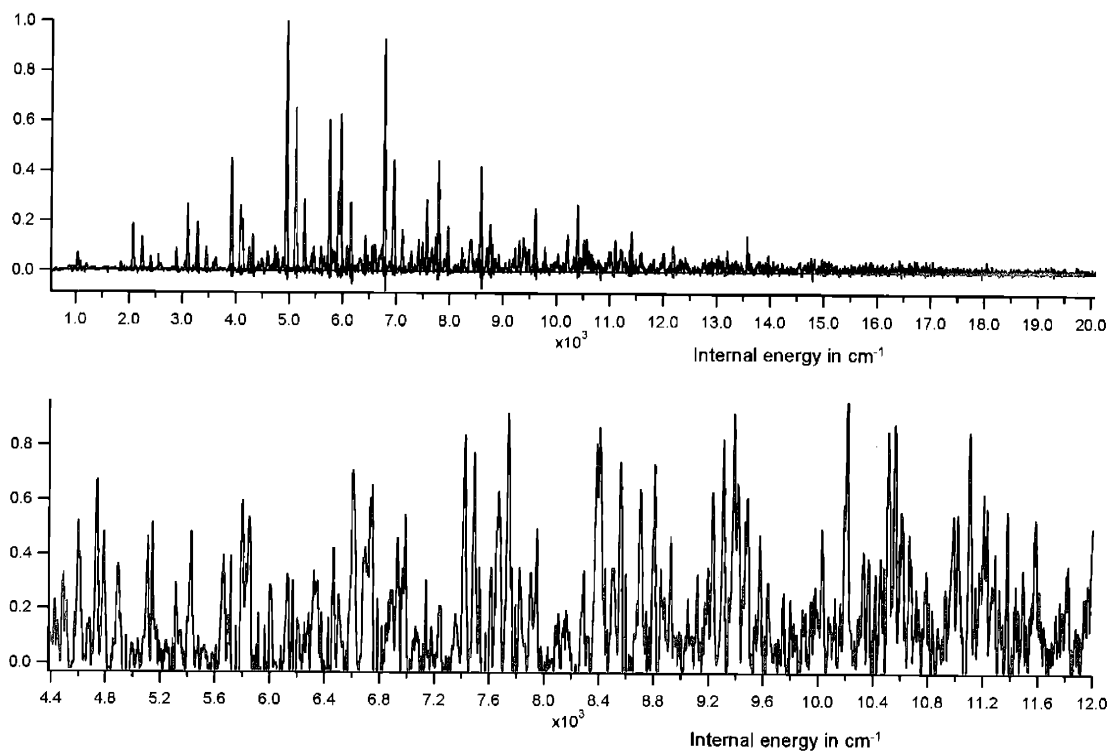


Figure 8-5: In order to uncover as many unassigned features as possible, a synthetic “known” spectrum (green) is subtracted from the original, baseline-removed, $4\nu_3$ DF spectrum. The red trace in the top panel is the result after the subtraction. The spectrum in the bottom panel contains a zoom-in view of the residual “unknown” features (the red trace in the top panel). Spectral congestion in the residual is high, and there are unexplainable lines as low as $4,000 \text{ cm}^{-1}$, where not too many vibrational states ought to be present. The spectral congestion exceeds that expectation.

8.3 A Proposal on Investigation of the *cis*-well of S_1 state of C_2H_2

8.3.1 Overview

Motivation

The S_1 state of Acetylene contains three local minima whose equilibrium configurations correspond to *cis*-Acetylene, *trans*-Acetylene and Vinylidene. Although many experiments have been performed to study the *trans*-well, no spectroscopic observation of the *cis*-well has been reported. Observing the *cis*-well will give rise to an understanding of *cis* \longleftrightarrow *trans* isomerization on the S_1 potential surface. The experimental research proposed here will exploit a double resonance cavity-ringdown experiment which will directly excite molecules into the *cis*-well, with discussions of why we should be able to observe what had been previously unobservable. A detailed feasibility calculation for the experiment is also provided.

Previous work

Stanton *et al.* [97] calculated the zero-point energy of each of the three local minima and the isomerization barrier between *cis* and *trans* (Fig.1-1). The *cis* well is an extremely shallow well of around 1110 cm^{-1} depth. The zero-point of the *cis*-well is above H-CCH dissociation energy according to Mordaunt and Ashfold [67]. In the energy region of the low vibrational levels of the *cis*-well, there are vibrational levels with a high density of one level per ten cm^{-1} in the *trans*-well. In addition, the transition from S_0 to S_1 (*cis*) is electronically *forbidden*. These three factors may explain why the levels of the *cis*-well on the S_1 surface have never been observed.

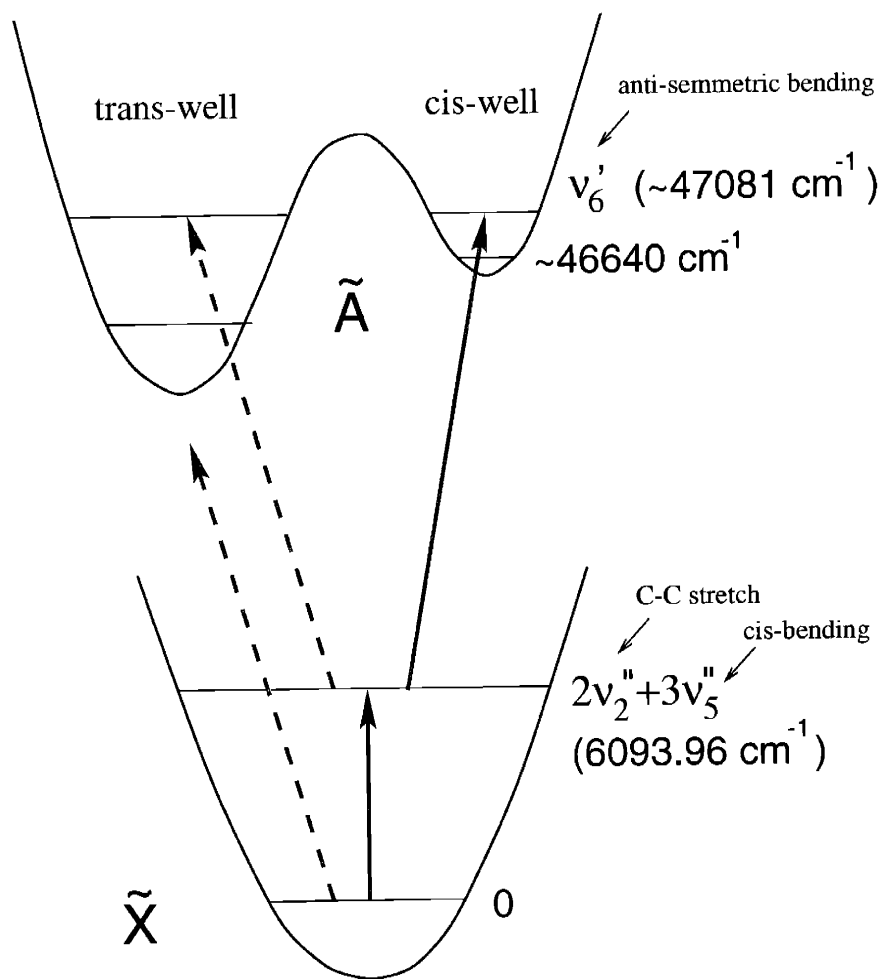


Figure 8-6: IR-UV double-resonance transition diagram

8.3.2 Experiment

Transition

Fig.1-2 shows the normal modes for the three Acetylene equilibrium geometries involved in the experiment. Note that ν_6 of *cis*-Acetylene is of most importance for *cis* \longleftrightarrow *trans* isomerization. We will emphasize upon probing the ν_6 fundamental of the *cis*-well.

In the transition diagram (Fig.8-6), an IR beam excites the $2\nu_2'' + 3\nu_5''$ (6093.96 cm^{-1}) band (Calculated by Herman *et al* [103]) of the S_0 state, from which population will be pumped into the *cis*-well ν_6' state by a UV beam. The choice of the intermediate state is specially designed. Three quanta of ν_5'' selectively enhances the Franck-Condon overlap with levels of S_1 (*cis*), the combination with two quanta of ν_2'' (no transition strength) pushes the transition into a region easily accessible by one laser, and further enhances the Franck-Condon overlap. The energy of this intermediate level is sufficiently high to eliminate the possibility of the UV laser pumping population from the S_0 ground vibrational state into the S_1 *trans*-well.

Experimental Setup

Two lasers are involved in this experiment (Fig.8-7), an injection seeded Lambda-Physik OPPO and a Lambda-Physik 3002 dye laser. In order to make sure that the IR laser is tuned to exact resonance with the desired intermediate state, an opto-acoustic cell is used. The ringdown mirrors are highly UV reflective, but highly IR transmissive, so that the IR pump-beam will pass through the cell only once. On the other hand, the UV beam will circulate within the cell, be absorbed by the pre-excited molecules, and thus give ringdown signals which will then be collected by a photodiode. In addition, a PMT is used for collecting fluorescence from the side window. In order to get the total fluorescence on a more accurate basis, a calibration gas, nitric oxide, will be used. The \tilde{A} state of nitric oxide was used by Suzuki *et al* [101] to calibrate the absolute intensities of acetylene *linear* $\tilde{X}^1\Sigma_g^+ \longleftrightarrow \textit{trans}\tilde{A}^1A_u$ vibrational bands.

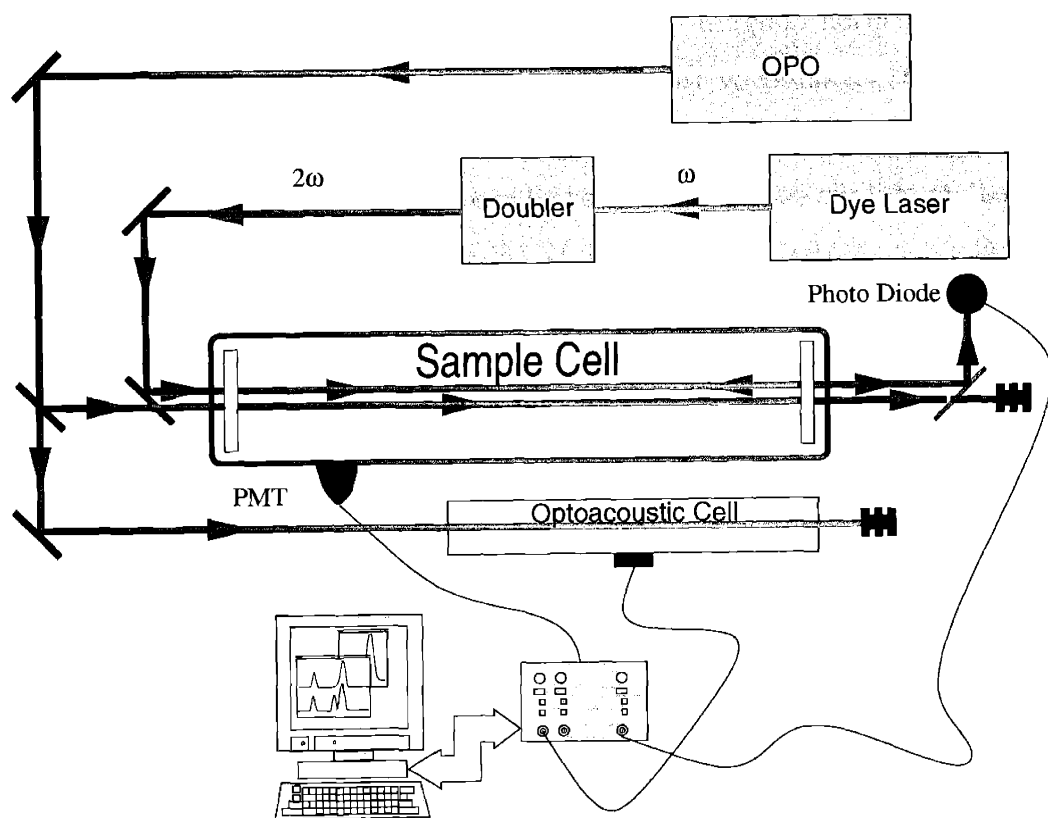


Figure 8-7: IR-UV double-resonance CRD setup

Since CRD is an absorption-based technique, it is useful for observing pre-dissociated states. A further advantage of this experiment is it can measure the absolute fluorescence quantum yield from the excitation, thus provide a good way to verify theoretical predictions. This is an experiment that has never been done before, and no absolute quantum yield for the *linear* \rightarrow *trans* or the *linear* \rightarrow *cis* transitions has been experimentally obtained. Success of this experiment will establish an innovative way to study pre-dissociated states and a practically simple scheme to measure absolute quantum yield.

There is still the potential problem of the spectral overlap with transitions into the *trans*-well. However, the B constants for these two geometries are different by 5%, as is shown in Table 8.2 (Calculated by molecular constants provided in [97]).

	A	B	C
<i>cis</i>	14.766	1.157	1.073
<i>trans</i>	19.243	1.085	1.027

Table 8.2: The rotational constants of *cis* and *trans*

8.3.3 Feasibility

Pressure Analysis and Line Broadening

Although use of a higher pressure would yield a stronger absorption, the decreased lifetime of the intermediate state would result in no change in the ringdown signal. With a 2.25-meter-long cell, one round trip period is around 15ns. Collisional depopulation occurs at a rate of 10 MHz per torr. In order to keep our intermediate state populated during the experiment, we select pressure to allow 1 collision every ringdown lifetime. $1/10^{-6}\text{s}=1\text{MHz}$, thus 100 mTorr will be an ideal pressure to be used.

At 100 mTorr, the pressure broadening of the lineshape (in cm^{-1}) is:

$$\Delta\nu_P = \frac{\text{Collisional Frequency}}{\text{Speed of Light}} = \frac{10^6 \text{ Hz}}{3 \times 10^{10} \text{ cm/s}} = 3 \times 10^{-5} \text{ cm}^{-1}$$

Let's also calculate the Doppler width of the two transitions:

For the pump transition $(00000)^0 \longleftrightarrow (02003)^1$ (6093.96cm^{-1}), the Doppler width is:

$$\Delta\nu_D = 7.1 \times 10^{-7} \times \nu_0 \sqrt{\frac{T}{M}} = 7.1 \times 10^{-7} \times 6093.96\text{cm}^{-1} \times \sqrt{\frac{300}{26}} = 0.0147\text{cm}^{-1}$$

For the probe transition $2\nu_2'' + 3\nu_5''$ (*linear* $\tilde{X}^1\Sigma_g^+$) $\longleftrightarrow \nu_6''$ (*cis* \tilde{A}^1A_2) (40987.04cm^{-1}), the Doppler width is:

$$\Delta\nu_D = 7.1 \times 10^{-7} \times \nu_0 \sqrt{\frac{T}{M}} = 7.1 \times 10^{-7} \times 40987.04\text{cm}^{-1} \times \sqrt{\frac{300}{26}} = 0.0989\text{cm}^{-1}$$

In the visible and UV regions, the natural linewidth at zero pressure is around 10^{-5} to 10^{-6}cm^{-1} ; for IR it's around 10^{-6} to 10^{-9}cm^{-1} . In both cases, the natural broadening can be ignored relative to the much larger Doppler linewidth.

For the pump transition, it is advantageous to have the laser resolution match the transition linewidth. In fact, a Nd:YAG-seeded OPPO has a linewidth of 0.01cm^{-1} . In this case, the laser selects a restricted velocity group of the molecules to be excited and the Doppler lineshape can actually be resolved.

For the probe transition, we will first run a grating scan then an Etalon scan:

Grating Scan: Dye laser resolution 0.3cm^{-1} . This is broader than any of the lineshapes, so only 5% of the photons will have the frequency appropriate for exciting the transitions.

Etalon Scan: Dye laser resolution 0.01cm^{-1} , which is much smaller than the Doppler width.

Ringdown Cell

The reflectivity of the mirror in the UV transition region has to be chosen so that the empty cell ringdown lifetime is around $1\mu\text{s}$. Suppose there is no cavity loss except that due to the transmission (1-R) of the mirrors, the *i*-th round trip yields a signal

of:

$$I(i) = I(0)R^{2i}, 2iL = ct$$

Thus the ringdown lifetime τ (when $I=I(0)/e$) is:

$$\tau = \frac{L}{-c \times \ln(R)}$$

Consequently, with a two-meter-long cell, in order to have τ equal to $1\mu s$, one needs a mirror reflectivity of 99.25%.

Transition Probability and Laser Pulse Energy

The probability of the pump transition $(02003)^1 \longleftrightarrow (00000)^0$ is decisive in determining the number of pre-excited molecules that can be further excited into the *cis* well. No intensity information has been reported for this transition. Our goal is to excite as many molecules in the $2\nu_2'' + 3\nu_5''$ level as possible. The integrated absorption of $5\nu_3$, which exemplifies a weak band, has been reported by Lehmann as 38 cm/mole [56], which corresponds to 6.31×10^{-23} cm/molecule, divided by the Doppler width at $5\nu_3$ (0.0397 cm^{-1}), the absorption cross section for each molecule is $1.59 \times 10^{-21} \text{ cm}^2$. Let D be the beam diameter (.9mm), the number of photons needed to excite 1% of the molecules is:

$$0.01 \times \frac{\pi(\frac{D}{2})^2}{\sigma} = 4 \times 10^{16}$$

These photons have a total energy of:

$$N_{photons}h\nu = 4 \times 10^{16} \times 6.63 \times 10^{-34} \times 3.00 \times 10^{10} \times 6094 = 4.8(mJ)$$

In order to excite 1% of the molecules onto the intermediate state, the pulse energy needed from the OPPO output is 4.8 mJ.

Detection Threshold

In order to calculate how many molecules need to be excited in order for the absorption to be detectable, one needs to know the absorption cross section for transition $2\nu_2'' + 3\nu_5''$ (linear $\tilde{X}^1\Sigma_g^+$) \longleftrightarrow ν_6' (cis \tilde{A}^1A_2). In comparison to 0 (linear $\tilde{X}^1\Sigma_g^+$) \longleftrightarrow ν_3' (trans \tilde{A}^1A_u) transition, assume that electronic forbiddenness degrades the oscillator strength by a factor of 100, but the more favorable Franck-Condon enhances the oscillator strength by a factor of 100 [113], the oscillator strength should be comparable in terms of magnitude. For the 0 (linear $\tilde{X}^1\Sigma_g^+$) \longleftrightarrow ν_3' (trans \tilde{A}^1A_u) transition, Ingold and King [33] has reported its oscillator strength as 4.2×10^{-8} . To convert from oscillator strength to integrated cross section [26], one get:

$$\sigma_{integrated} = \frac{f}{1.1 \times 10^{12}} = 3.8 \times 10^{-20} (cm)$$

The peak cross section, therefore, is the integrated cross section divided by the linewidth, in our case, mainly the Doppler width.

$$\sigma_{peak} = \sigma_{integrated} / \Delta\nu_D = 3.8 \times 10^{-20} / 0.0989 = 3.9 \times 10^{-19} (cm^2)$$

Select $J = 9$ as the most populated rotational level ($f_{J=9}=0.096$) at room temperature, thus $N_{J=9}=0.096N_{total}$. Within $1\mu s$, the beam travels $l = 3 \times 10^{10} \times 10^{-6} = 30000$ (cm). A sensitivity of $\frac{\Delta\tau}{\tau} = 10^{-3}$ at $\tau = 1\mu s$ has been achieved by the current CRD setup [17]. Thus the detection threshold is 0.1% absorption at $t=\tau$,

$$0.001 = \sigma_{peak} \times 0.096 \times N_{total} \times l$$

We get $N_{total}=8.99 \times 10^{11}$ molecules/cm³. Under room temperature and 100mTorr,

$$N = \frac{P}{kT} = \frac{1.01 \times 10^5 \times 0.1}{1.38 \times 10^{-23} \times 300 \times 760} = 3.21 \times 10^{21} (m^{-3}) = 3.21 \times 10^{15} (cm^{-3})$$

This shows that we only need to have $\frac{8.99 \times 10^{11}}{3.21 \times 10^{15}} = 2.8 \times 10^{-4} = 0.03\%$ of molecules pre-excited to the intermediate state to reach the detection threshold.

8.3.4 Ringdown Signal

The double resonance ringdown signal will be different from a conventional exponential decay. This is due to the absorption species (molecules pre-excited to the intermediate state) decays over time. Namely,

$$[\text{preexcitedmolecules}] = [\text{preexcitedmolecules}]_0 \times e^{\frac{-t}{\tau_{decay}}}$$

As a result,

$$\alpha = \alpha_0 \times e^{\frac{-t}{\tau_{decay}}}$$

The derivative of the intensity I in terms of distance is:

$$-\frac{dI}{dx} = I\alpha = I\alpha_0 \times e^{\frac{-t}{\tau_{decay}}}, x = ct$$

Solve for I:

$$I = I_0 \exp[-\alpha_0 c \tau_{decay} (1 - e^{-\frac{t}{\tau_{decay}}})]$$

If τ_{decay} is long compared to t , $\frac{t}{\tau_{decay}}$ approximates $1 - e^{-\frac{t}{\tau_{decay}}}$, thus

$$I = I_0 e^{-\alpha_0 c t}$$

The same as Beer-Lambert's Law.

8.3.5 Discussion

Selection Rules

Listed (Tab.8.3, Tab.8.4 and Tab.8.5) are character tables for C_{2v} point group (*cis* \tilde{A}^1A_2), C_{2h} point group (*trans* \tilde{A}^1A_u) and $D_{\infty h}$ point group (*linear* $\tilde{X}^1\Sigma_g^+$).

Fig.8-8 shows the relation between the rotational axes and body-fixed Cartesian coordinates for the three types of Acetylene configurations.

As mentioned, the rotational structure of the *linear* \longleftrightarrow *trans* transition will be different from that of the *linear* \longleftrightarrow *cis* transition. This is shown as the following:

C_{2v}	I	$C_2(b)$	σ_{bc}	σ_{ab}	
A_1	1	1	1	1	T_b
A_2	1	1	-1	-1	R_b
B_1	1	-1	1	-1	$T_c; R_a$
B_2	1	-1	-1	1	$T_a; R_c$

Table 8.3: The character table for C_{2v} point group (*cis* \tilde{A}^1A_2)

C_{2h}	I	$C_2(c)$	σ_{ab}	i	
A_g	1	1	1	1	R_c
A_u	1	1	-1	-1	T_c
B_g	1	-1	-1	1	$R_a; R_b$
B_u	1	-1	1	-1	$T_a; T_b$

Table 8.4: The character table for C_{2h} point group (*trans* \tilde{A}^1A_u)

$D_{\infty h}$	I	C_2^∞	σ_{ab}^∞	i
Σ_g^+	1	1	1	1
Σ_u^-	1	1	-1	-1
Σ_g^-	1	-1	-1	1
Σ_u^+	1	-1	1	-1

Table 8.5: The character table for $D_{\infty h}$ point group (*linear* $\tilde{X}^1\Sigma_g^+$)

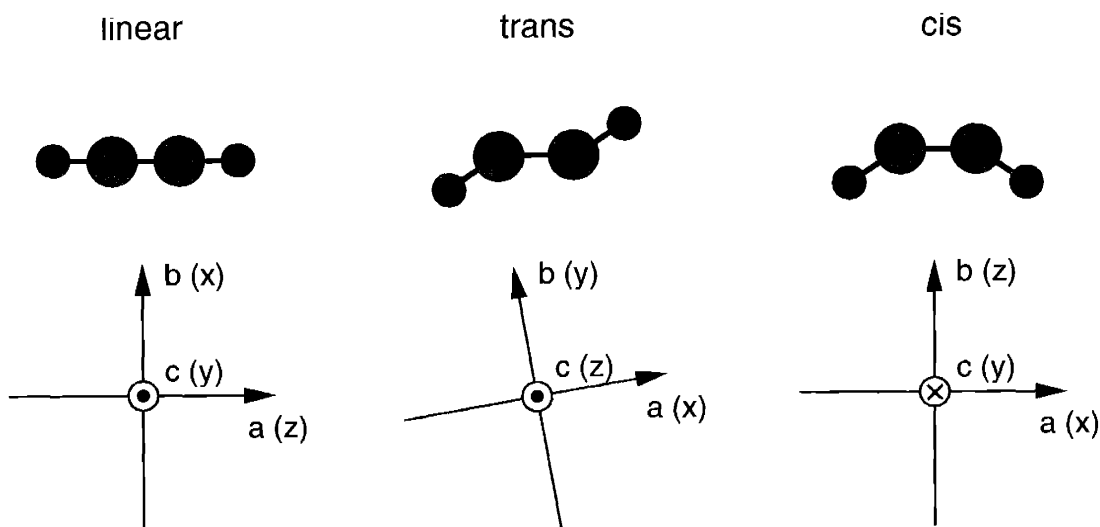


Figure 8-8: Principal-axes vs. body-fixed Cartesian axes

On one hand, the *linear* \longleftrightarrow *trans* transition is of C-type:

$$\Sigma_g^+ \otimes A_u = A_g \otimes A_u = A_u \longrightarrow T_c \implies C - type \quad (8.2)$$

On the other hand, *linear* \longleftrightarrow *cis* transition is *electronically forbidden*:

$$\Sigma_g^+ \otimes A_2 = A_1 \otimes A_2 = A_2 \longrightarrow R_b \implies forbidden$$

However, vibronic coupling lends oscillator strength to transitions involving certain nontotally symmetric vibrational levels. From the ground $\widetilde{X}^1\Sigma_g^+$ state of linear Acetylene, only $^1\Sigma_u^+$ and $^1\Pi_u$ are electronically allowed transitions. $^1\Sigma_u^+$ corresponds to B_1 in C_{2v} , and Π_u corresponds to A_1 or B_1 , depending on whether the π vibration is along the b-axis or the c-axis. The intermediate state that we are going to excite, $\nu_2'' + 3\nu_5''$, is also of Π_u symmetry. ν_6' is of symmetry B_2 . Thus, the vibronic symmetry of ν_6' is:

$$\nu_6' : A_2 \otimes B_2 = B_1$$

ν_6' can borrow oscillator strength from $^1\Sigma_u^+$ (Upper state vibronic coupling). Reached via P or R branch pumping from the ν_0 level, the vibration of $\nu_2'' + 3\nu_5''$ is along the b-axis, a C-type transition into the S_1 state occurs:

$$A_1 \otimes B_1 = B_1 \longrightarrow T_c \implies C - type \quad (8.3)$$

Through Q branch pumping, the vibration of $\nu_2'' + 3\nu_5''$ is along the c-axis, the transition into the S_1 *cis*-state is of B-type:

$$B_1 \otimes B_1 = A_1 \longrightarrow T_b \implies B - type \quad (8.4)$$

Summarizing (8.2), (8.3) and (8.4), *linear* \longrightarrow *trans* transitions are of C-type, while *linear* \longrightarrow *cis* transitions are either of C-type or B-type.

Signature of *linear*→*cis* transitions

Tab.8.2 shows the computed rotational constants for both the *cis* and the *trans* states, based on the molecular constants from Stanton [97]. The B and C rotational constants do not differ from each other by a large amount for the *cis* acetylene. However, there is a 7% difference between the *cis* isomer rotational B constant and the *trans* isomer rotational B constant, which will be revealed in the J-progressions. That is, by measuring the B constant of a particular transition, one could say something about whether the upper state is likely in the *trans*-well, or *vice versa*.

8.4 Study of Perturbations in the $3\nu'_3$ State of C_2H_2

8.4.1 Goal

The $3\nu'_3$ state of the \tilde{A} state of acetylene is known to exhibit perturbations. Among these perturbations, the best known is the fairly weak singlet – triplet coupling, or otherwise termed “Inter-System Crossing”. Ochi and Tsuchiya [75] and Dupré *et al.* [18] each proposed that the inter-system crossing of the $3\nu'_3$ vibrational levels is mediated by a sparse manifold of states from the triplet T_3 electronic surface. The SEELEM spectrum recorded by the triplet project team in our group indicates that, in fact, the Inter-System Crossing of $3\nu'_3$ may be mediated by a single T_3 vibrational state, and coupling of the singlet $3\nu'_3$ basis state to the other triplet states occurs primarily through this T_3 “doorway” state.

There is another perturbation in the $3\nu'_3$ band of acetylene that is not as well known. Crim and coworkers [110] assigned some low-J lines in the R-branch as belonging to the $4\nu'_6$ polyad. Since the torsional frequency, $\nu'_4 = 764.9 \text{ cm}^{-1}$, and the asymmetric in-plane bending frequency, $\nu'_6 = 768.3 \text{ cm}^{-1}$, only differ by 3.4 cm^{-1} , $4\nu'_6$ therefore is a vibrational polyad containing a combination of ν'_4 and ν'_6 . The members of this polyad are expected to be profoundly mixed by anharmonic and Coriolis couplings. There are a total of five (ν'_4, ν'_6) basis states in the $4\nu'_6$ polyad — (0,4), (1,3), (2,2), (3,1), and (4,0). Since torsion is of a_u symmetry and asymmetric bending is of

b_u symmetry, among the five members, the three eigenstates comprising (0,4), (2,2), and (4,0) will have a_g vibrational symmetry, and will therefore be able to interact via anharmonic coupling with $3\nu'_3$. The other two basis states, (1,3) and (3,1), would be able to interact with the former three basis through Coriolis couplings. Pursuant to the goal of the project described in this section, we would like to attempt to answer two questions – what additional evidence can we obtain about the $3\nu'_3$ perturber, and, which eigenstate of this $4\nu'_6$ polyad is interacting with $3\nu'_3$?

I believe that the answer to the second question will provide a key observation concerning the isomerization path in the \tilde{A} state. Since the *trans* \leftrightarrow *cis* isomerization saddle point is predicted by Stanton to be only 5550 cm^{-1} above the zero point in the *trans* well of the \tilde{A} state, four quanta of the fundamental frequency of ν'_6 ($4\nu'_6 \approx 3066\text{ cm}^{-1}$) is already 55% of the way to the saddle point. What would happen if the rest of the modes continue to follow the anharmonic term value rules, while the isomerization mode approaches the isomerization saddle point with a steadily decreasing spacing? If it turns out that the spread of the $n\nu'_6$ polyad is steadily increasing as n increases, there is a big chance that the lowest member of the polyad is undergoing isomerization.

8.4.2 Experiments

As additional $\tilde{A} \leftarrow \tilde{X}$ LIF spectroscopic studies on the $3\nu'_3$ level itself has little chance of identifying the nature of the perturbers beyond what has been previously established¹, an alternative probe scheme can be devised. As described in the introduction to this thesis, it is my belief that the study of the \tilde{A} -state isomerization is closely related to the study of isomerization in the \tilde{X} state. Therefore, *the present knowledge about the \tilde{X} -state can be used to provide additional information for the \tilde{A} -state perturbations.* Dispersed Fluorescence from the perturbed lines will provide this kind of information.

The idea is to launch DF probes from a number of perturbed lines in the $3\nu'_3$ vibrational level, and monitor the fluorescence patterns in the \tilde{X} state that result

¹though it is obvious that further LIF studies on other vibrational levels in the \tilde{A} state *will* help in the investigation process.

from the perturbed upper state.

There are a number of things to expect from a DF probe scheme such as that proposed here. Due to the fact that no direct transitions of the type triplet \rightarrow singlet is allowed by electronic spin symmetry, if a chosen \tilde{A} state eigenstate contains a mixture of singlet and triplet characters, the DF pattern resulting from this line should be indistinguishable from what would normally result from an unperturbed $3\nu'_3$ line, other than decreased overall intensity. However, a singlet perturber would result in entirely new vibrational patterns in the DF spectrum, because new classes of bright states are illuminated. Before I recorded the DF spectrum, there was hardly any information as to what the DF patterns from the usually inaccessible vibrational levels in the \tilde{A} state would look like, since we were previously unable to directly excite into neither the torsional mode nor the asymmetric bending mode. However, it turns out that the vibrational patterns in the DF spectrum appear to be very different from those that are assignable from the normally excited symmetric bending levels.

Figure 8-9 depicts a segment of the $3\nu'_3$ LIF spectrum. The two peaks at 45305.3 cm^{-1} and 45305.0 cm^{-1} have been assigned as the R(1) "main" (whose eigenstate contains more than 50% singlet $3\nu'_3$ character) and the R(1) "extra" (whose eigenstate contains more of the perturber character) features respectively. With the excitation laser locked onto each of these R(1) transitions, we recorded two DF spectra, one from the "main" level and one from the "extra" level, as shown in Figure 8-10.

The spectrum originating from the "extra" level exhibits a distinctively different vibrational pattern than that from the "main" level. As the dispersed fluorescence spectrum of the unperturbed $n\nu'_3$ levels is well characterized [35], we know that fluorescence from the $3\nu'_3$ state contains primarily progressions of transitions terminating in trans-bending and CC-stretch vibrational states on the ground electronic surface. The intensity of each transition is governed by the Franck-Condon overlap between the excited state vibrational wavefunction and the vibrational wavefunction on the ground electronic surface. As a result, the intensity patterns in the DF spectrum are sensitive to the characteristics of the excited state vibrational wavefunction. If the perturbing state is singlet, the DF spectrum will contain different features from the

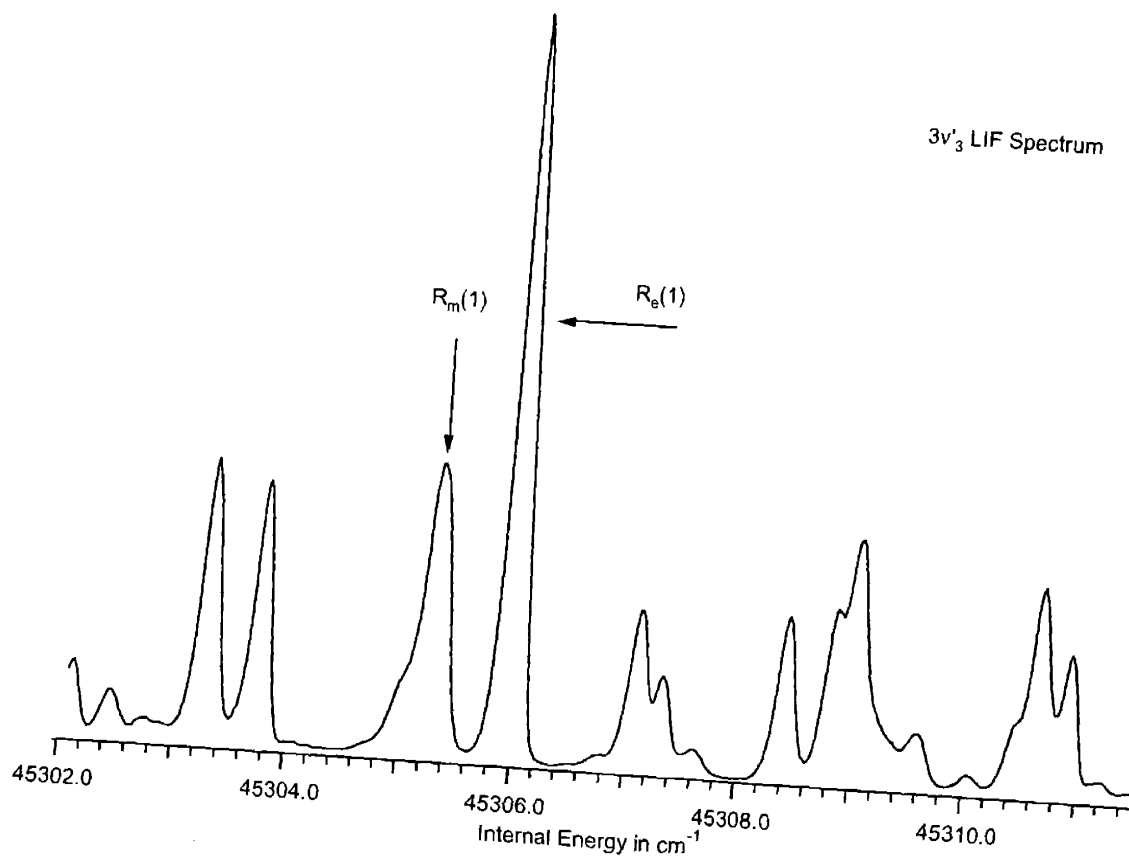


Figure 8-9: The $3\nu_3$ LIF spectrum. The peaks at 45305.3 cm^{-1} and 45306.0 cm^{-1} were assigned as the R(1) "main" and the R(1) "extra" features, respectively. Utz et al [110] suggested that this perturbation pair is caused by a singlet perturber which is a member of the $4\nu_6'$ polyad.

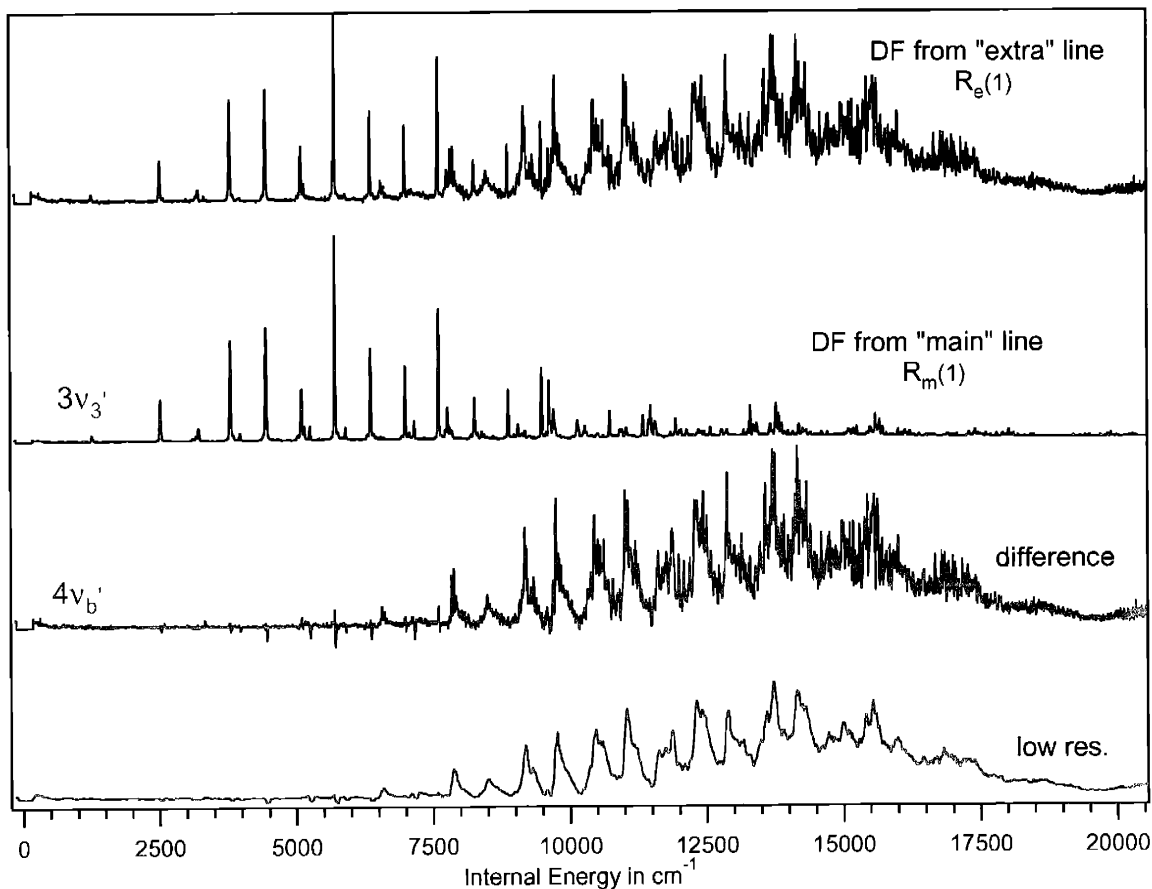


Figure 8-10: The top two DF spectra were recorded from the R(1) “main” line and the R(1) “extra” lines. From 0 to 7500 cm^{-1} of internal energy, these two DF spectra look similar, however, the “extra” line DF spectrum starts to display extra vibrational features above 7500 cm^{-1} . A simple subtraction of the two DF spectra results in the third trace, which indicates that there is virtually no Franck-Condon overlap between the singlet perturber of the $3\nu_3'$ state and the linear geometry (manifested in the low internal energy region of the DF spectrum) from the \bar{X} state. The bottom trace is a gaussian-convoluted, lower resolution version of the third trace. Its pattern manifests a strong similarity to the “ $6\nu_3$ ” DF pattern reported by Tsuji *et al* (Fig. 3 from [108]), which led us to the belief that what was assigned as “ $6\nu_3$ ” should instead be a member of some $n\nu_b'$ polyad. ($n=7-9$)

unperturbed spectrum in a way that should help to identify the vibrational nature of the perturbing state. If the perturbing state is a triplet, the DF spectrum will display the same features as the DF spectrum of a pure singlet state because emission from the triplet states to the ground state is spin-forbidden, and the Franck-Condon factors for the $T \rightarrow S_0$ transition are irrelevant to the observed vibrational level intensities.

In the $3\nu'_3$ energy region, there are two possible singlet vibrational states with the correct symmetry. $4\nu'_6$ and ν'_1 , which has a frequency of 2880.5 cm^{-1} (ref. to Chapter 3). In order to understand the extra vibrational features from the perturber, a simple subtraction is made between the “main” line DF spectrum and the “extra” line DF spectrum. This is a legitimate approach, because we observe the exact “main” line DF patterns repeated in the “extra” line, but not the other way around. Based on the difference between the “main” line and “extra” line DF spectral patterns (the 3rd and the 4th traces in Figure 8-10), the following observations are made:

1. Franck-Condon overlap between the \tilde{A} state perturber and the low- ν''_4 region in the ground state is almost non-existent below 7500 cm^{-1} . If the perturber of the R(1) line of $3\nu'_3$ were ν'_1 , ν''_1 in the \tilde{X} -state should be bright. All transitions should terminate in combination levels built on one quantum of ν''_1 . This contradicts the observation. Thus ν'_1 can be excluded as a possible candidate for this perturber.
2. The perturber feature contains apparent “lumps”. Based on Jacobson’s analysis, these are polyad structures lit up by one or more (“more” because the upper state is no longer pure $3\nu'_3$) bright states. The bright state intensity gets distributed within each polyad through anharmonic couplings, and eventually the entire polyad is illuminated. In the low resolution trace (bottom trace on Figure 8-10) the polyads appear as “lumps”.
3. The fact that the unique vibrational patterns for the perturber only start to emerge in the DF about 7500 cm^{-1} of internal energy indicates that either the Franck-Condon overlap is poor between the perturber and low internal energy states, or a new class of vibrational motions emerges from the ground state

above 7500 cm^{-1} . The latter deduction is consistent with the emergence of local bending and counter-rotating type of motions in Jacobson's [35] DF analysis. In other words, the perturber on $3\nu'_3$ may be lighting up the local bending states or the counter-rotation in the X state, but which one?

4. A strong piece of evidence that supports the local bend assumption is that a sharp edge of every lump in the low resolution trace (the 3rd and 4th trace in Figure 8-10) appears on the low energy edge of the polyad. Based on Jacobson's effective Hamiltonian model [35], the lowest eigenstate for each polyad evolves from trans bend to local bend as the internal energies increases. I believe, therefore, the $3\nu'_3$ perturber, in this case, very likely a member of the $4\nu'_b$ polyad, is lighting up the local bend, which would eventually lead to isomerization.

5. Interestingly, there is a strong similarity between the perturber DF pattern (bottom trace in Figure 8-10) and the claimed " $6\nu'_3$ " DF pattern reported by Tsuji *et al* (Fig. 3 from [108]), which led us to the belief that what was assigned as " $6\nu'_3$ " by Tsuji *et al* should be reassigned as a member of a certain $n\nu'_b$ ($n=7-9$)² considering that the $6\nu'_3$ is twice in vibrational energy as that of $3\nu'_3$, and the perturber for $3\nu'_3$ is $4\nu'_b$, the reported " $6\nu'_3$ " is most likely a member of the $8\nu'_b$ polyad. However, strong anharmonicity is anticipated as the energy approaches *trans* \leftrightarrow *cis* isomerization, we do not want to make the exclusive conclusion of $8\nu'_b$ too soon. Normally, we expect the DF pattern from $6\nu'_3$ would look similar to that from the R(1) "main" line of $3\nu'_3$. The question then is, "How could Tsuji observe directly a $n\nu'_b$ polyad if not through its anharmonic interaction with the regular bright mode, $m\nu'_2 + n\nu'_3$?" The answer to this question might reveal some important dynamics in the $6\nu'_3$ region of the \tilde{A} state, which lies in the heart of the *trans* \leftrightarrow *cis* isomerization.

²C

8.4.3 Conclusion

To conclude, this project is ongoing in a sense that we are lacking precise Franck-Condon calculations to quantitatively test our assignments. Nevertheless, the DF spectra clearly identify the perturber that is responsible for the extra line in the $3\nu'_3$ level as $4\nu'_b$, which is consistent with the assignments made by Crim and co-workers [110]. This project has also provided clear evidence that contradicts the assignment of $6\nu'_3$ by Tsuji *et al.*

Bibliography

- [1] E. Abramson, R.W. Field, D. Imre, K. K. Innes, and J. L. Kinsey. Fluorescence and stimulated emission $s_1 \rightarrow s_0$ spectra of acetylene: Regular and ergodic regions. *J. Chem. Phys.*, page 453, 1985.
- [2] J. Vander Auwera, T. R. Huet, M. Herman, C. Hamilton, J. L. Kinsey, and R. W. Field. The \tilde{A}^1a'' electronic state of monodeuterated acetylene. *J. Mol. Spectrosc.*, page 381, 1989.
- [3] G. A. Bethardy and D. S. Perry. Rate and mechanism of intramolecular vibrational redistribution in the $\nu(16)$ asymmetric methyl stretch band of 1-butyne. *J. Chem. Phys.*, 98:6651, 1993.
- [4] L. E. Brus. Acetylene fluorescence. *J. Mol. Spectrosc.*, 75:245, 1979.
- [5] A. Campargue, M. Abbouti Tamsamani, and M. Herman. The absorption spectrum of $^{12}C_2H_2$ between 12,800 and 18,500 cm^{-1} . *Mol. Phys.*, page 793, 1997.
- [6] J. Cariou and P. Luc. *Atlas du Spectre d'Absorption de la Molecule de Tellure*, Editions du C.N.R.S. Orsay, 1979.
- [7] R. Q. Chen, H. Guo, L. Liu, and J. T. Muckerman. Symmetry-adapted filter diagonalization: Calculation of the vibrational spectrum of planar acetylene from correlation functions. *J. Chem. Phys.*, page 7128, 1998.
- [8] Y. Chen, S. Halle, D. M. Jonas, J. L. Kinsey, and R. W. Field. Stimulated-emission pumping studies of acetylene $\tilde{X}^1\sigma_g^+$ in the 11,400-15,700 cm^{-1} region: the onset of mixing. *J. Opt. Soc. Am. B*, page 1805, 1990.

- [9] C. Cohen-Tannoudji, B. Diu, and F. Laloe. *Quantum Mechanics*. Hermann, 1973.
- [10] S. L. Coy, M. P. Jacobson, and R. W. Field. Identifying patterns in multi-component signals by extended cross correlation. *J. Chem. Phys.*, 107:8357, 1997.
- [11] J. C. Van Craen, R. Colin, M. Herman, and J. K. G. Watson. The $\tilde{A} - \tilde{X}$ band system of acetylene: Analysis of medium-wavelength bands, and vibration-rotation constants for the levels $n\nu'_3$ ($n = 4 - 6$), $\nu'_2 + n\nu'_3$ ($n = 3 - 5$), and $\nu'_1 + n\nu'_3$ ($n = 2, 3$). *J. Mol. Spectrosc.*, page 185, 1985.
- [12] J. C. Van Craen, M. Herman, R. Colin, and J. K. G. Watson. The $\tilde{A} - \tilde{X}$ band system of acetylene: Bands of the short-wavelength region. *J. Mol. Spectrosc.*, page 137, 1986.
- [13] H. W. Cruse, P. J. Dagdigian, and R. N. Zare. Crossed-beam reactions of barium with hydrogen halides. measurement of internal state distributions by laser-induced fluorescence. *Faraday Discuss*, 55:277, 1973.
- [14] H. L. Dai, C. L. Korpa, J. L. Kinsey, and R. W. Field. Rotation-induced vibrational mixing in formaldehyde - non-negligible dynamical consequences of rotation. *J. Chem. Phys.*, 82:1688, 1985.
- [15] D. A. Dolson, K. W. Holtzclaw, S. H. Lee, S. Munchak, C. S. Parmenter, and A. E. W. Knight. Intramolecular vibrational redistribution at low state densities in s_1 aromatics. evidence for rotational contributions. *Laser Chem*, 2:271, 1983.
- [16] D. A. Dolson, K. W. Holtzclaw, D. B. Moss, and C. S. Parmenter. Chemical timing 4. the rovibronic level structure associated with intramolecular vibrational redistribution in s_1 *p*-difluorobenzene. *J. Chem. Phys.*, 84:1119, 1986.
- [17] Ilia A. Dubinsky. *Application of Highly Sensitive Spectroscopic Techniques to the Study of Intramolecular Dynamics and Remote Sensing*. PhD thesis, Massachusetts Institute of Technology, 1998.

- [18] P. Dupré, R. Jost, M. Lombardi, P. G. Green, E. Abramson, and R. W. Field. Anomalous behavior of the anticrossing density as a function of excitation energy in the c_2h_2 molecule. *Chem. Phys.*, 152:293, 1991.
- [19] P. M. Felker and A. H. Zewail. Dynamics of intramolecular vibrational-energy redistribution (ivr) .3. role of molecular rotations. *J. Chem. Phys.*, 82:2994, 1985.
- [20] L. E. Fried and G. S. Ezra. Semiclassical quantization using classical perturbation theory: Algebraic quantization of multidimensional systems. *J. Chem. Phys.*, page 6270, 1987.
- [21] J. E. Gambogi, R. P. L'Esperance, K. K. Lehmann, B. H. Pate, and G. Scoles. Influence of methyl group deuteration on the rate of intramolecular vibrational energy relaxation. *J. Chem. Phys.*, page 1116, 1993.
- [22] D. Green, R. Holmberg, C. Y. Lee, D. A. McWhorter, and B. H. Pate. The rotational spectrum of highly vibrationally mixed quantum states of propynol near 3330 cm^{-1} . *J. Chem. Phys.*, page 4407, 1998.
- [23] M. Herman, J. Lievin, J. Vander Auwera, and A. Campargue. Advances in chemical physics - global and accurate vibration hamiltonians from high-resolution molecular spectroscopy - general introduction. *Adv. Chem. Phys.*, 108:1, 1999.
- [24] G. Herzberg. *Molecular Spectra and Molecular Structure: Electronic Spectra and Electronic Structure of Polyatomic Molecules*. Krieger, 1991.
- [25] G. Herzberg. Determination of the structures of simple polyatomic molecules and radicals in electronically excited states. twelfth spiens memorial lecture. *Discuss. Faraday Soc.*, page 7, 1963.
- [26] R. C. Hilborn. Einstein coefficients, cross-sections, f values, dipole-moments, and all that. *Am. J. Phys.*, 50:982, 1982.

- [27] K. Hoshina, A. Iwasaki, K. Yamanouchi, M. P. Jacobson, and R. W. Field. The infrared-ultraviolet dispersed fluorescence spectrum of acetylene: New classes of bright states. *J. Chem. Phys.*, 114:7424, 2001.
- [28] J. T. Hougen and J. K. G. Watson. Anomalous rotational line intensities in electronic transitions of polyatomic molecules: Axis switching. *Can. J. Phys.*, page 298, 1965.
- [29] T. R. Huet and M. Herman. The $\tilde{A}-\tilde{X}$ band system of acetylene- d_2 : Vibration-rotation constants for the \tilde{A}^1a_u state. *J. Mol. Spectrosc.*, page 396, 1989.
- [30] F. Iachello, F. Pérez-Bernal, T. Muller, and P. H. Vaccaro. A quantitative study of non-condon effects in the $s_2o \tilde{C} \rightarrow \tilde{X}$ emission spectrum. *J. Chem. Phys.*, page 6507, 2000.
- [31] M. I. El Idrissi, J. Lievin, A. Campargue, and M. Herman. The vibrational energy pattern in acetylene (iv): Updated global vibration constants for $^{12}c_2h_2$. *J. Chem. Phys.*, 110:2074, 1999.
- [32] C. K. Ingold and G. W. King. Excited states of acetylene. *J. Chem. Soc.*, 1953:2702, 1953.
- [33] C. K. Ingold and G. W. King. Excited states of c_2h_2 . iv. description and analysis of the near-ultraviolet absorption spectra of c_2h_2 and c_2d_2 : Nature of the excited state. *J. Chem. Soc.*, page 2725, 1953.
- [34] K. K. Innes. Analysis of the near-ultraviolet absorption spectrum of acetylene. *J. Chem. Phys.*, page 863, 1954.
- [35] M. P. Jacobson. *Spectroscopic Patterns Encode Unimolecular Dynamics*. PhD thesis, Massachusetts Institute of Technology, 1999.
- [36] M. P. Jacobson and M. S. Child. Spectroscopic signatures of bond-breaking internal rotation. i. saddle point induced polyad breaking. *J. Chem. Phys.*, page 250, 2001.

- [37] M. P. Jacobson, S. L. Coy, and R. W. Field. Extended cross correlation: A technique for spectroscopic pattern recognition. *J. Chem. Phys.*, 107:8349, 1997.
- [38] M. P. Jacobson and R. W. Field. Acetylene at the threshold of isomerization. *J. Phys. Chem.*, page 3073, 2000.
- [39] M. P. Jacobson, J. P. O'Brien, and R. W. Field. Anomalously slow intramolecular vibrational redistribution in the acetylene \tilde{X} state above 10,000 cm^{-1} of internal energy. *J. Chem. Phys.*, 109:3831, 1998.
- [40] M. P. Jacobson, J. P. OBrien, R. J. Silbey, and R. W. Field. Pure bending dynamics in the acetylene $\tilde{X}^1\sigma_g^+$ state up to 15,000 cm^{-1} of internal energy. *J. Chem. Phys.*, 109:121, 1998.
- [41] M. P. Jacobson, Robert J. Silbey, and Robert W. Field. Local mode behavior in the acetylene bending system. *J. Chem. Phys.*, page 845, 1999.
- [42] C. Jaffe and M. E. Kellman. Localized chaos and partial assignability of dynamical constants of motion in the transition to molecular chaos. *J. Chem. Phys.*, page 7196, 1990.
- [43] D. M. Jonas. *Spectroscopy of Vibrationally Hot Molecules: Hydrogen Cyanide and Acetylene*. PhD thesis, Massachusetts Institute of Technology, 1992.
- [44] D. M. Jonas, S. A. B. Solina, B. Rajaram, R. J. Silbey, R. W. Field, K. Yamanouchi, and S. Tsuchiya. Intramolecular vibrational relaxation and forbidden transitions in the sep spectrum of acetylene. *J. Chem. Phys.*, 97:2813, 1992.
- [45] D. M. Jonas, S. A. B. Solina, B. Rajaram, R. J. Silbey, R. W. Field, K. Yamanouchi, and S. Tsuchiya. Intramolecular vibrational redistribution of energy in the stimulated emission pumping spectrum of acetylene. *J. Chem. Phys.*, page 7350, 1993.
- [46] Y. Kabbadj, M. Herman, G. Di Lonardo, L. Fusina, and J. W. C. Johns. The bending energy levels of acetylene. *J. Mol. Spectrosc.*, page 535, 1991.

- [47] M. E. Kellman. Approximate constants of motion for vibrational spectra of many-oscillator systems with multiple anharmonic resonances. *J. Chem. Phys.*, page 6630, 1990.
- [48] M. E. Kellman and G. Chen. Approximate constants of motion and energy transfer pathways in highly excited acetylene. *J. Chem. Phys.*, page 8671, 1991.
- [49] C. Kittrell, E. Abramson, J. L. Kinsey, S. A. McDonald, D. E. Reisner, R. W. Field, and D. H. Katayama. Selective vibrational excitation by stimulated emission pumping. *J. Chem. Phys.*, page 2056, 1981.
- [50] O. Klein. Calculation of potential curves of diatomic molecules with the aid of spectral terms. *Z. Physik*, 76:226, 1932.
- [51] T. J. Kulp, H. L. Kim, and J. D. McDonald. Rotational effects on intramolecular vibrational relaxation in dimethyl ether and 1,4 dioxane. *J. Chem. Phys.*, 85:211, 1986.
- [52] *Lambda Physik FL2002 Dye Laser Operation Manual*.
- [53] W. R. Lambert, P. M. Felker, and A. H. Zewail. Picosecond excitation and selective intramolecular rates in supersonic molecular-beams 2. intramolecular quantum beats and ivr. *J. Chem. Phys.*, 81:2217, 1984.
- [54] W. D. Lawrance and A. E. W. Knight. Rotational mechanisms in intramolecular vibrational-energy redistribution - an examination of centrifugal and coriolis coupling and the states contributing to time dynamical measurements. *J. Phys. Chem.*, 92:5900, 1988.
- [55] H. Lefebvre-Brion and R. W. Field. *Perturbations in the Spectra of Diatomic Molecules*. Academic Press, 1986.
- [56] K. K. Lehmann. The absolute intensity of visible overtone bands of acetylene. *J. Chem. Phys.*, 91:2759, 1989.

- [57] K. K. Lehmann, G. Scoles, and B. H. Pate. Intramolecular dynamics from eigenstate-resolved infrared spectra. *Ann. Rev. Phys. Chem.*, 45:241, 1994.
- [58] Ira N. Levine. *Molecular Spectroscopy*. Wiley, 1975.
- [59] J. Lievin, M. Abbouti Temsamani, P. Gaspard, and M. Herman. Overtone spectroscopy and dynamics in monodeuteroacetylene (c_2hd). *Chemical Physics*, 190:419, 1995.
- [60] Yaoming Liu, Jian Li, Dieyan Chen, Li Li, Kevin M. Jones, Bing Ji, and Robert J. Le Roy. Molecular constants and rydberg-klein-rees (rkr) potential curve for the $na_2 1^3\sigma_g^-$ state. *J. Chem. Phys.*, 111:3494, 1999.
- [61] Yaoming Liu, Jian Li, Dieyan Chen, Li Li, Kevin M. Jones, Bing Ji, and Robert J. Le Roy. Molecular constants and rydberg-klein-rees (rkr) potential curve for the $na_2 1^3\sigma_g^-$ state [j. chem. phys. 111, 3494 (1999)]. *J. Chem. Phys.*, 117:6380, 2002.
- [62] T. H. Maiman. Stimulated optical emission in fluorescent solids. ii. spectroscopy and stimulated emission in ruby. *Nature*, page 493, 1960.
- [63] A. G. Maki, W. B. Olson, and R. L. Sams. Hcn rotational-vibrational energy levels and intensity anomalies determined from infrared measurements. *J. Mol. Spectrosc.*, page 433, 1970.
- [64] D. A. McQuarrie. *Statistical Mechanics*. University Science Books, 2000.
- [65] A. P. Milce and B. J. Orr. Symmetry-breaking perturbations in the $\nu_2 + 3\nu_3$ rovibrational manifold of acetylene: Spectroscopic and energy-transfer effects. *J. Chem. Phys.*, page 6423, 1996.
- [66] A. P. Milce and B. J. Orr. The $\nu_c c + 3\nu_c h$ rovibrational manifold of acetylene. i. collision-induced state-to-state transfer kinetics. *J. Chem. Phys.*, page 3592, 1997.

- [67] David H. Mordaunt and Michael N. R. Ashfold. Near-ultraviolet photolysis of C_2H_2 : A precise determination of $d_0(\text{hcc-h})$. *J. Chem. Phys.*, 101:2630, 1994.
- [68] David B. Moss, Zicheng Duan, Matthew P. Jacobson, Jonathan P. O'Brien, and Robert W. Field. Observation of coriolis coupling between $\nu_2 + 4\nu_4$ and $7\nu_4$ in acetylene $\widetilde{X}^1\sigma_g^+$ by stimulated emission pumping spectroscopy. *J. Mol. Spectrosc.*, 199:265, 2000.
- [69] T. Muller, P. Dupré, P. H. Vaccaro, F. Pérez-Bernal, M. Ibrahim, and F. Iachello. Algebraic approach for the calculation of polyatomic franck-condon factors. application to the vibronically resolved emission spectrum of s_2o . *Chem. Phys. Lett.*, page 243, 1998.
- [70] T. Muller, P. H. Vaccaro, F. Pérez-Bernal, and F. Iachello. The vibronically-resolved emission spectrum of disulfur monoxide (s_2o): An algebraic calculation and quantitative interpretation of franck-condon transition intensities. *J. Chem. Phys.*, page 5038, 1999.
- [71] T. Muller, P. H. Vaccaro, F. Pérez-Bernal, and F. Iachello. Algebraic approach for the calculation of polyatomic franck-condon factors: Application to the vibronically resolved absorption spectrum of disulfur monoxide (s_2o). *Chem. Phys. Lett.*, page 271, 2000.
- [72] D. J. Nesbitt and R. W. Field. Vibrational energy flow in highly excited molecules: Role of intramolecular vibrational redistribution. *J. Phys. Chem.*, 100:12735, 1996.
- [73] J. P. O'Brien. *Acetylene – Dispersed Fluorescence Spectroscopy and Intramolecular Dynamics*. PhD thesis, Massachusetts Institute of Technology, 1997.
- [74] J. P. O'Brien, M. P. Jacobson, J. J. Sokol, S. L. Coy, and R. W. Field. Numerical pattern recognition in acetylene dispersed fluorescence spectra. *J. Chem. Phys.*, 108:7100, 1998.

- [75] Nobuaki Ochi and Soji Tsuchiya. Rovibronic level structure of electronically excited acetylene (\tilde{A}^1a_u) in a supersonic jet as studied by laser-induced fluorescence and zeeman quantum beat spectroscopy. *Chem. Phys.*, 152:319, 1991.
- [76] J. Plva. Molecular constants for the bending modes of acetylene $^{12}C_2H_2$. *J. Mol. Spectrosc.*, page 165, 1972.
- [77] A. L. G. Rees. The calculation of potential-energy curves from band-spectroscopic data. *Prec. Phys. Soc. (London)*, 59:998, 1947.
- [78] E. Riedle, H. J. Neusser, and E. W. Schlag. Sub-doppler high-resolution spectra of C_6H_6 - anomalous results in the channel 3 region. *J. Phys. Chem.*, 86:4847, 1982.
- [79] H. Romanowski, R. B. Gerber, and M. A. Ratner. The anharmonic stretching-bending potential of carbon dioxide from inversion of spectroscopic data. *J. Chem. Phys.*, 88:6757, 1988.
- [80] R. M. Roth, Mark A. Ratner, and R. B. Gerber. Inversion of polyatomic rovibration spectra into a molecular potential energy surface: Application to carbon dioxide. *Physical Review Letters*, 52:1288, 1984.
- [81] A. F. Ruckstuhl, M. P. Jacobson, R. W. Field, and J. A. Dodd. Baseline subtraction using robust local regression estimation. *Journal of Quantitative Spectroscopy & Radiative Transfer*, 68:179, 2000.
- [82] Ragnar Rydberg. Graphical representation of some results of band spectroscopy. *Z. Physik*, 73:376, 1931.
- [83] Ragnar Rydberg. Some potential curves of mercury hydride. *Z. Physik*, 80:514, 1933.
- [84] G. J. Scherer, Y. Chen, R. L. Redington, J. L. Kinsey, and R. W. Field. An unsuspected fermi perturbation in the acetylene \tilde{A}^1a_u $3\nu_3$ level. *J. Chem. Phys.*, 85:6315, 1986.

- [85] J. J. Scherer, K. K. Lehmann, and W. Klemperer. the high-resolution visible overtone spectrum of acetylene. *J. Chem. Phys.*, page 2817, 1983.
- [86] U. Schubert, E. Riedle, H. J. Neusser, and E. W. Schlag. Lifetimes of single rotational states in the channel 3 region of c_6h_6 . *J. Chem. Phys.*, 84:6182, 1986.
- [87] J. Segall, R. N. Zare, H.-R. Dubal, M. Lewcenz, and M. Quack. Tridiagonal fermi resonance structure in the vibrational spectrum of the ch chromophore in chf_3 . 2. visible spectra. *J. Chem. Phys.*, page 634, 1987.
- [88] T. E. Sharp and H. M. Rosenstock. Franck-condon factors for polyatomic molecules. *J. Chem. Phys.*, 41:3453, 1964.
- [89] C. David Sherrill, George Vacek, Yukio Yamaguchi, Henry F. Schaefer III, John F. Stanton, and Jurgen Gauss. The \tilde{A}^1a_u state and the t_2 potential surface of acetylene: Implications for triplet perturbations in the fluorescence spectra of the \tilde{A} state. *J. Chem. Phys.*, 104:8507, 1996.
- [90] E. L. Sibert, W. P. Reinhardt, and J. T. Hynes. Intramolecular vibrational-relaxation of ch overtones in benzene. *Chem. Phys. Lett.*, page 455, 1982.
- [91] E. L. Sibert, W. P. Reinhardt, and J. T. Hynes. Intramolecular vibrational-relaxation and spectra of ch and cd overtones in benzene and perdeuterobenzene. *J. Chem. Phys.*, page 1115, 1984.
- [92] M. L. Silva, M. P. Jacobson, Z. Duan, and R. W. Field. Anomalous simplicity of the $\tilde{A} \rightarrow \tilde{X}$ dispersed fluorescence spectrum of $^{13}c_2h_2$. *Journal of Molecular Structure*, page 87, 2001.
- [93] M. L. Silva, M. P. Jacobson, Z. Duan, and R. W. Field. Unexpected simplicity in the $s_1v_{s_0}$ dispersed fluorescence spectra of $^{13}c_2h_2$. *J. Chem. Phys.*, page 7939, 2002.
- [94] B. C. Smith and J. S. Winn. The overtone dynamics of acetylene above 10,000 cm^{-1} . *J. Chem. Phys.*, page 4120, 1991.

- [95] S. A. B. Solina. *Intramolecular Dynamics of Acetylene*. PhD thesis, Massachusetts Institute of Technology, 1996.
- [96] S. A. B. Solina, J. P. O'Brien, R. W. Field, and W. F. Polik. Dispersed fluorescence spectrum of acetylene from the \tilde{A}^1a_u origin: Recognition of polyads and test of multiresonant effective hamiltonian model for the \tilde{X} state. *J. Phys. Chem.*, 100:7797, 1996.
- [97] John F. Stanton and Chang-Ming Huang. Stationary points on the s_1 potential energy surface of c_2h_2 . *J. Chem. Phys.*, 101:356, 1994.
- [98] J. C. Stephenson, J. A. Blazy, and D. S. King. Spectroscopy and collisional quenching rates for \tilde{A} C_2H_2 ($v'_3=0, 1, 2$). *Chem. Phys.*, 85:31, 1984.
- [99] G. Strey and I. M. Mills. Anharmonic force field of acetylene. *J. Mol. Spectrosc.*, page 103, 1976.
- [100] A. A. Stuchebrukhov and R. A. Marcus. Theoretical study of intramolecular vibrational relaxation of acetylene ch vibration for $\nu=1$ and 2 in large polyatomic molecules (cx_3). *J. Chem. Phys.*, page 6044, 1993.
- [101] Suzuki. Electronic relaxation and predissociation dynamics of acetylene, internal publication, 1996.
- [102] M. Abbouti Tamsamani and M. Herman. The vibrational energy pattern in $^{12}c_2h_2$ (ii): Vibrational clustering and rotational structure. *J. Chem. Phys.*, page 1355, 1996.
- [103] Mohammed Abbouti Tamsamani and Michel Herman. The vibrational energy levels in acetylene $^{12}c_2h_2$: Towards a regular pattern at higher energies. *J. Chem. Phys.*, 102:6371, 1995.
- [104] J. D. Tobiasson. *Laser Double-Resonance Studies of Electronic Spectroscopy and State-Resolved Collisional Relaxation in Highly Vibrationally Excited Acetylene*. PhD thesis, University of Wisconsin-Madison, 1992.

- [105] J. D. Tobiason, A. L. Utz, and F. F. Crim. The direct observation, assignment, and partial deperturbation of ν_5 and $\nu_3 + \nu_5$ in \tilde{A}^1a_u acetylene (c_2h_2). *J. Chem. Phys.*, page 928, 1993.
- [106] J. D. Tobiason, A. L. Utz, E. L. Sibert III, and F. F. Crim. Normal modes analysis of \tilde{A} acetylene based on directly observed fundamental vibrations. *J. Chem. Phys.*, page 5762, 1993.
- [107] C. H. Townes and A. L. Schawlow. *Microwave Spectroscopy*. Dover, 1975.
- [108] Kazuhide Tsuji, Chiaki Terauchi, Kazuhiko Shibuya, and Soji Tsuchiya. *Trans* isomerization of acetylene in the \tilde{A}^1a_u state as studied by dispersed fluorescence spectroscopy. *Chemical Physics Letters*, 306:41, 1999.
- [109] A. L. Utz, E. Carrasquillo M., J. D. Tobiason, and F. F. Crim. Direct observation of weak state mixing in highly vibrationally excited acetylene. *Chem. Phys.*, page 311, 1995.
- [110] A. L. Utz, J. D. Tobiason, E. Carrasquillo M., L. J. Sanders, and F. F. Crim. The direct observation, assignment, and partial deperturbation of the ν_4 and ν_6 vibrational fundamentals in \tilde{A}^1a_u acetylene (c_2h_2). *J. Chem. Phys.*, page 2742, 1993.
- [111] K. von Puttkamer, H.-R. Dubal, and M. Quack. Time-dependent processes in polyatomic molecules during and after intense infrared irradiation. *Faraday Disc. Chem. Soc.*, page 197, 1983.
- [112] J. K. G. Watson. *Vibrational Spectra and Structure, a Series of Advances*, page 1. Elsevier, New York/Amsterdam, 1977.
- [113] J. K. G. Watson. Calculated vibrational intensities in the $\tilde{A} - \tilde{X}$ electronic transition of acetylene. *J. Mol. Spectrosc.*, 207:276, 2001.
- [114] J. K. G. Watson, M. Herman, J.C. van Craen, and R. Colin. The $\tilde{A} - \tilde{X}$ band system of acetylene – analysis of long-wavelength bands, and vibration-rotation

constants for the levels $0 - 4 - \nu_4''$, $0 - 3 - \nu_3'$, and $\nu_2' + 0 - 2 - \nu_3'$. *J. Mol. Spectrosc.*, 95:101, 1982.

- [115] D. G. Xu, G. H. Li, D. Q. Xie, and H. Guo. Full-dimensional quantum calculations of vibrational energy levels of acetylene (hcch) up to $13,000 \text{ cm}^{-1}$. *Chem. Phys. Lett.*, page 480, 2002.
- [116] N. Yamakita, S. Iwamoto, and S. Tsuchiya. a. submitted for publication.
- [117] N. Yamakita, S. Tsuchiya, A. J. Merer, Z. Duan, and R.W. Field. a. to be published.
- [118] K. Yamanouchi, N. Ikeda, S. Tsuchiya, D. M. Jonas, J. K. Lundberg, G. W. Adamson, and R. W. Field. Vibrationally highly excited acetylene as studied by dispersed fluorescence and stimulated emission pumping spectroscopy: Vibrational assignment of the feature states. *J. Chem. Phys.*, 95:6330, 1991.
- [119] S. F. Yang, L. Biennier, A. Campargue, M. Abbouti Tamsamani, and M. Herman. The absorption spectrum of $^{12}\text{C}_2\text{H}_2$ between $12,800$ and $18,500 \text{ cm}^{-1}$ ii. rotational analysis. *Mol. Phys.*, page 807, 1997.
- [120] X. Zhan, O. Vaittinen, and L. Halonen. High resolution photoacoustic study of acetylene between $11,500$ and $11,900 \text{ cm}^{-1}$ using a titanium:sapphire ring laser. *J. Mol. Spectrosc.*, page 172, 1993.

Curriculum Vitae

EDUCATION: University of Science and Technology of China, Sc.B. (1996); Massachusetts Institute of Technology, Ph.D. expected February 2003.

HONORS AND AWARDS: Member of the Colblentz Society, 2002; Finalist in Chinese Olympic Competitions of Mathematics, Physics and Optics, 1992.

PUBLICATIONS AND PRESENTATIONS:

D. B. Moss, Z. Duan, M. P. Jacobson, J. P. O'Brien, and R. W. Field, "Observation of Coriolis Coupling between $\nu_2+4\nu_4$ and $7\nu_4$ in Acetylene $\widetilde{X}^1\Sigma_g^+$ by Stimulated Emission Pumping Spectroscopy", *Journal of Molecular Spectroscopy*, **199** (2): 265-274 (FEB 2000).

M. P. Jacobson, R. W. Field, Michelle L. Silva, and Z. Duan, "Acetylene at the Threshold of Isomerization", *Abstracts of Papers of the American Chemical Society*, **219**: 76-PHYS Part 2 (MAR 26 2000).

Michelle L. Silva, M. P. Jacobson, Z. Duan, and R. W. Field, "Anomalous Simplicity of the $\widetilde{A} \rightarrow \widetilde{X}$ Dispersed Fluorescence Spectrum of $^{13}\text{C}_2\text{H}_2$ ", *Journal of Molecular Structure*, **565**: 87-91 Sp. Iss. SI (MAY 30 2001).

Michelle L. Silva, M. P. Jacobson, Z. Duan, and R. W. Field, "Unexpected Simplicity in the $S_1 - S_0$ Dispersed Fluorescence Spectra of $^{13}\text{C}_2\text{H}_2$ ", *Journal of Chemical Physics*, **116** (18): 7939-7947 (MAY 8 2002).

A. J. Merer, N. Yamakita, S. Tsuchiya, J. F. Stanton, Z. Duan, and R. W. Field, "New Vibrational Assignments in the $\widetilde{A}^1A_u - \widetilde{X}^1\Sigma_g^+$ Electronic Transition of Acetylene, C_2H_2 ; the ν'_1 Frequency", *Molecular Physics*; special issue to honour Ian Mills, *submitted*.